De invloed van afschrik- en partitioneerparameters op de microstructuur en op de mechanische eigenschappen van geavanceerde hoogsterktestaalsoorten

Influence of Quenching and Partitioning Parameters on the Microstructure and Mechanical Properties of Advanced High Strength Steels

Dorien De Knijf

Promotoren: prof. dr. ir. R. Petrov, prof. dr. ir. L. Kestens
Proefschrift ingediend tot het behalen van de graad van
Doctor in de Ingenieurswetenschappen: Materiaalkunde

Vakgroep Toegepaste Materiaalwetenschappen
Voorzitter: prof. dr. ir. J. Degrieck
Faculteit Ingenieurswetenschappen en Architectuur
Academiejaar 2014 - 2015

UNIVERSITEIT
GENT

ISBN 978-90-8578-805-8
NUR 971
Wettelijk depot: D/2015/10.500/49

Dankwoord

Veel mensen hebben meegeholpen aan de realisatie van deze thesis. Ik wil graag van de gelegenheid gebruik maken om hen te bedanken voor hun steun, inzet en vertrouwen.

Eerst en vooral zou ik graag mijn promotor, Prof. Dr. Ir. Roumen Petrov, willen bedanken voor zijn encyclopedische kennis, onuitputbare ideeën, inzet en aangename babbels. Graag dank ik ook mijn co-promotor, Prof. Dr. Ir. Leo Kestens, voor de getoonde interesse, discussies en ondersteuning. Mijn begeleidster van OCAS, Cecilia Föjer, dank ik van harte voor haar luisterend oor, aanmoedigingen en industriële input.

Alle techniekers van OCAS wil ik bedanken voor assistentie met de testen. Ook Vitaliy Bliznuk en Hui Shi ben ik dankbaar omdat zij de TEM experimenten voor hun rekening genomen hebben. Graag bedank ik ook Jurij Sidor en Tuan Nguyen Minh voor hun modelleerwerk en Irene Diego-de-Calderón voor de DIC en nano-indentatie testen. Bovendien wil ik alle leden van het RFCS project 'NewQP' bedanken voor de samenwerking, raadgevingen en gezellige bijeenkomsten. Hierbij wil ik voornamelijk Maria Santofimia bedanken voor haar advies.

Verder wil ik mijn collega's van de vakgroep bedanken voor de aangename momenten binnen en buiten de werkuren. Hierbij wil ik speciaal An Verdiere, Evelien De Wilde, Athina Puype, Elisabete Pinto Da Silva, Aurélie Laureys en Irene Diego-de-Calderón bedanken voor hun vriendschap en steun.

Daarnaast wil ik mijn ouders bedanken voor hun vertrouwen. Zij hebben mij deze kansen gegeven en gesteund doorheen moeilijke momenten.

In het bijzonder ook ontzettend veel dank aan mijn man, Bram, voor zijn raad, geduld en zijn geloof in mij.

Dorien

SUMMARY

The development of advanced high strength steel (AHSS) grades was largely driven by the demands of the automotive industry. To reduce fuel consumption, without compromising the safety of the passengers, weight reduction of the steel car body is required by using thinner and therefore necessarily stronger and tougher materials. The goal of development of these AHSS steels was hence to increase strength without compromising ductility and formability. This is possible by employing new approaches for heat treatment by which a required balance of hard and ductile phases could be obtained.

The first generation of AHSS were developed in lean compositions and ferritic-based multi-phase microstructures e.g. Dual Phase (DP) and Transformation Induced Plasticity (TRIP) steel. The second generation were austenitic steel grades e.g. Twinning Induced Plasticity (TWIP) steel, which were highly alloyed and much more expensive. The third generation AHSS was investigated to cover the property range between the first and second generation while reducing the alloying levels of the second generation.

So far, no steel exists that meets all the requirements for combinations of strength and formability of the third generation if the strength criteria include not only tensile strength, but also yield strength and if the concept of formability includes uniform elongation as well as hole expansion. Nevertheless, there are several prospective candidates that demonstrate high combinations of strength and formability.

One of these candidates is Quenching and Partitioning (Q&P) steel proposed in 2003 by John Speer. The Q&P treatment starts with full austenitisation or intercritical annealing followed by quenching to a temperature below the martensite start temperature (M_s) and above the martensite finish temperature (M_f). At this temperature, the microstructure of steel consists of controlled fractions of martensite and austenite. During the isothermal holding between M_s and M_f or after increasing the temperature above M_s, diffusion of carbon from the supersaturated martensite to the untransformed austenite (carbon partitioning) occurs. The final microstructure after quenching and partitioning will consist of ferrite in the case of intercritical annealing, retained austenite and possibly of two types of martensite: the one formed during the first quench (tempered martensite) and the other formed during the final quench (fresh martensite). In the Q&P process, carbon partitioning and microstructure development are decoupled. The phase fractions and morphologies are controlled by an

athermal martensite transformation while partitioning is controlled in an isothermal stage, implying an independent and complete control during Q&P processing. Such an approach allows creating large varieties of microstructures in Q&P steels and correspondingly large ranges of mechanical properties.

In this work, a new steel grade 0.25C1.5Si3Mn (wt.%) was developed to meet the technical requirements of the heat treatment parameters. The microstructural evolution and mechanical properties were studied as a function of partitioning time for different quenching and partitioning temperatures with X-ray diffraction (XRD), scanning electron microscopy (SEM) and electron backscattered diffraction (EBSD). XRD analysis on samples with consecutive partitioning times enabled to track the evolution of the retained austenite fraction and its %C-content. SEM and EBSD analysis were conducted on selective samples to follow the microstructural evolution during partitioning allowing to quantitatively study the phase fractions of retained austenite, fresh and tempered martensite.

The stabilized retained austenite fraction was found to be relatively independent upon variation of the quenching temperature presumably due to the lower diffusion coefficient of C in austenite, creating pile-ups near the martensite-austenite interfaces. The fresh martensite fraction however was larger at higher quenching temperatures because of insufficient (partial) stabilisation. The partitioning temperature range was determined by avoiding competing reactions as precipitation, bainite formation and decomposition of austenite, which were investigated by dilatometry. The evolution of the microstructure and mechanical properties as a function of partitioning time illustrated, in the absence of competing reactions, that more austenite was stabilized at higher temperatures and at longer times replacing fresh martensite which was present at shorter times. A linear correspondence could be found between the total elongation and retained austenite fraction multiplied with the C-concentration, indicating the importance of both high retained austenite fraction and sufficient C-content. The yielding behaviour was observed to be continuous at short partitioning times but changed to a more discrete yield point for longer times due to martensitic tempering. This tempering effect also explained the evolution of the ultimate tensile strength.

Fundamental information regarding the microstructural evolution during partitioning was obtained via high resolution transmission electron microscopy (HR-TEM) during in-situ partitioning. The possibility of interface migration was studied by following an austenite lath in between two martensite grains. A high-C steel was produced in order to retain sufficient austenite at room temperature after full austenitisation. After selection of an appropriate area with an alternating microstructure of lath martensite with interlath austenite, a foil prepared in

focussed ion beam (FIB) was mounted on a heating holder inside a HR-TEM. The width change of the austenite grain versus partitioning time was followed and modelled with a partitioning model taking grain boundary movement into account. From this model, the activation energy was found to correspond with a semi-coherent nature of austenite-martensite interfaces during partitioning.

The reaction of a Q&P microstructure upon tensile deformation with the main focus on austenite to martensite transformation (TRIP-effect) was investigated. A selection of two samples treated to obtain microstructures with and without fresh martensite was subjected to tensile testing combined with EBSD analysis at the same pre-selected area. From these data, information regarding the influence of the surrounding matrix, the austenite grain size, morphology, and crystallographic orientation on the austenite stability was obtained. It was observed that fresh martensite altered the strain distribution in the microstructure by inhibiting the amount of deformation accommodated in the tempered martensite matrix, and influenced the fracture mechanism by triggering void formation. Besides, this constraining effect decreased the austenite transformation stability, defined as the exponential factor of the retained austenite fraction versus strain interpolation. Consequently, fresh martensite caused an initial higher strain hardening due to substantial austenite transformation at low strains. The parameters influencing the stability inherently related to the austenite were studied. The microstructural parameters that have effect on the retained austenite stability in a decreasing order of importance were found to be: (1) austenite grain size, (2) morphology and (3) crystallographic orientation. Besides, an attempt was made to model the stress-strain curves of these samples by a simple rule of mixture.

Ultra-fast flash annealing was applied as a possible way to improve the mechanical properties obtained by conventional Q&P. It was found that by increasing the heating rate, the austenite grains, nucleated in a non-recrystallized matrix, refined significantly and that the carbides were not dissolved completely. The complex microstructural interactions during ultra-fast heating resulted in an improvement of both ultimate tensile strength and total elongation compared to conventional heating rates.

SAMENVATTING

De ontwikkeling van geavanceerde hoogsterkte staal (AHSS) kwaliteiten werd grotendeels gedreven door de eisen van de automobielindustrie. Om het brandstofverbruik te verminderen, zonder afbreuk te doen aan de veiligheid van de passagiers, wordt gewichtsreductie van de stalen carrosserie vereist door het gebruik van dunnere en dus per definitie sterkere en taaiere materialen. Het doel van deze AHSS staalsoorten was dus om de sterkte te verhogen, zonder afbreuk te doen aan de taaiheid en vervormbaarheid. Dit is mogelijk door toepassing van nieuwe warmtebehandelingscycli waarbij een vereist evenwicht van harde en ductiele fasen wordt verkregen.

De eerste generatie AHSS werd ontwikkeld met samenstellingen die een minimum aan legeringselementen bevatten met ferritisch gebaseerde multi-fase microstructuren bv. Dual Phase (DP) en Transformation Induced Plasticity (TRIP) staal. De tweede generatie waren austenitische staalsoorten bv. Twinning Induced Plasticity (TWIP) staal, die sterk werden gelegeerd wat resulteerde in een aanzienlijke toename van de kosten. Daarom werd de derde generatie AHSS ontwikkeld om de kloof tussen de eigenschappen van de eerste en tweede generatie te dekken maar met minder legeringselementen dan de tweede generatie.

Tot dusver bestaat er geen staal dat voldoet aan alle eisen met betrekking tot combinaties van sterkte en vervormbaarheid van de derde generatie als de sterktecriteria niet alleen treksterkte maar ook vloeisterkte bevatten en als het concept van vormbaarheid zowel uniforme rek als dieptrekbaarheid omvatten. Niettemin zijn er verschillende potentiële kandidaten die uitstekende combinaties van sterkte en vervormbaarheid hebben.

Eén van deze kandidaten is afschrik- en partitioneerstaal (Q&P) voorgesteld door John Speer in 2003. De Q&P behandeling begint met volledig austenitiseren of interkritisch gloeien gevolgd door afschrikken tot een temperatuur onder de martensiet starttemperatuur (M_s) en boven de martensiet eindtemperatuur (M_f). Bij deze temperatuur bestaat de microstructuur uit gecontroleerde fracties van martensiet en austeniet. Tijdens het isotherm houden op een temperatuur tussen M_s en M_f of na het verhogen van de temperatuur boven M_s, diffundeert koolstof uit de oververzadigde martensiet naar austeniet d.i. koolstof partitionering, dewelke (gedeeltelijk) stabiel blijft bij afschikken tot op kamertemperatuur. De uiteindelijke microstructuur na afschrikken en partitioneren bestaat uit ferriet bij interkritisch gloeien, austeniet en eventueel twee soorten martensiet: de ene gevormd tijdens het eerste afschikken (ontlaten martensiet) en de andere gevormd tijdens het finale afschrikken (nieuwe martensiet).

Samenvatting

In het Q&P-proces worden koolstof partitionering en microstructuurontwikkeling ontkoppeld. De fase fracties en morfologie worden gecontroleerd door een athermische martensiet transformatie terwijl partitionering wordt gecontroleerd in een isotherm stadium, wat neerkomt op een onafhankelijke en volledige controle tijdens de productie. Een dergelijke methode maakt het produceren van grote variaties aan microstructuren en overeenkomstige mechanische eigenschappen in Q&P staal mogelijk.

In dit werk werd een nieuw staalsoort, 0.25C1.5Si3Mn (gew.%), ontwikkeld om aan de technische eisen van de warmtebehandeling parameters te voldoen. De microstructurele veranderingen en mechanische eigenschappen werden onderzocht als functie van de partitioneertijd voor verschillende afschrik- en partitioneertemperaturen met X-stralen diffractie (XRD), scanning elektronenmicroscopie (SEM) en elektronen teruggekaatste diffractie (EBSD). XRD analyse van monsters met opeenvolgende partitioneertijden lieten toe om de evolutie van de austeniet fractie en het % C-gehalte te volgen. SEM en EBSD analyses werden uitgevoerd op selectieve monsters om de microstructurele veranderingen tijdens het partitioneren kwantitatief te onderzoeken. Hieruit konden de fase fracties van austeniet, nieuwe en ontlaten martensiet bepaald worden.

De gestabiliseerde austeniet fractie was niet sterk afhankelijk van variaties in de afschriktemperatuur, waarschijnlijk door de lagere diffusiecoëfficiënt van C in austeniet wat leidde tot een C-opstapeling nabij de martensiet-austeniet korrelgrenzen. De nieuwe martensiet fractie werd echter groter bij hogere afschirktemperaturen als gevolg van onvoldoende (gedeeltelijke) stabilisatie. Het partitioneertemperatuursbereik werd bepaald door competitieve reacties als carbide precipitatie, bainiet vorming en austeniet ontbinding dewelke bestudeerd werden met dilatometer experimenten. De evolutie van de microstructuur en mechanische eigenschappen als functie van de partitioneertijd toonde aan dat meer austeniet werd gestabiliseerd bij hogere temperaturen en langere tijden, in afwezigheid van competitieve reacties. Bij kortere tijden transformeerde een deel van de austeniet door onvoldoende C-stabilisatie naar nieuwe martensiet. Een lineaire verband tussen de totale verlenging en de austeniet fractie vermenigvuldigd met de C-concentratie werd gevonden, hetgeen het belang met het oog op goede ductiliteit van zowel een hoge austeniet fractie als voldoende C-gehalte benadrukt. Het vloeigedrag was continu bij korte partitioneertijden, maar veranderde in een hoger, meer discreet vloeipunt voor langere tijden als gevolg van het ontlaten van de martensiet. Dit ontlaateffect verklaarde ook de evolutie van de treksterkte.

Fundamentele informatie over de microstructurele veranderingen tijdens partitioneren werd bekomen in een hoge resolutie transmissie elektronen microscoop (HR-TEM) tijdens in-situ

partitioneren. De mogelijkheid tot korrelgrens beweging werd bestudeerd door de afmetingen van een austenietkorrel tussen twee martensietlatten te volgen. Om voldoende austeniet bij kamertemperatuur te behouden na volledige austenitisatie, werd een hoog-C staal ontwikkeld. Na selectie van een geschikte zone met een microstructuur van afwisselende lat-martensiet met tussenlat-austeniet, werd een monster, geproduceerd met een gefocuste ionen straal, in een verwarmde houder in de HR-TEM gemonteerd. De breedte verandering van de austenietkorrel versus partitioneertijd werd bepaald en gemodelleerd met een partitioneermodel waarbij korrelgrens beweging in rekening werd gebracht. Vanuit dit model werd een activatie-energie voor de mobiliteit bekomen dat overeenkomt met een semi-coherente aard van de austeniet-martensiet korrelgrenzen tijdens partitioneren.

De reactie van een Q&P microstructuur op trekvervorming met de nadruk op austeniet-naar-martensiet transformatie (TRIP-effect) werd onderzocht. Een selectie van twee warmtebehandelingen met als resultaat een microstructuur met en één zonder nieuwe martensiet werden onderworpen aan trektesten gecombineerd met EBSD analyse op eenzelfde vooraf geselecteerd gebied. Uit deze gegevens werd informatie omtrent de invloed van de omringende matrix, de austeniet korrelgrootte, morfologie en kristallografische oriëntatie op de austeniet stabiliteit verkregen. Er werd waargenomen dat nieuwe martensiet de spanningsdistributie in de microstructuur veranderde waardoor minder vervorming kon ondergebracht worden in de ontlaten martensiet, en dat holtevorming in het breuk mechanisme werd bevorderd. Door dit beperkend effect daalde de austeniet transformatie stabiliteit, gedefinieerd als de exponentiële factor van de austeniet fractie versus verlenging. Bijgevolg veroorzaakt nieuwe martensiet een initiële hogere koudversteviging door aanzienlijke transformatie van austeniet naar martensiet bij lagere vervormingen. Wat betreft de parameters inherent verbonden met austeniet, bleken de volgende factoren in een afnemende volgorde van belang een rol te spelen: (1) austeniet korrelgrootte, (2) morfologie en (3) kristallografische oriëntatie. Bovendien werd een poging ondernomen om de spanning-rek krommen van deze monsters te modelleren door een eenvoudige meng-regel.

Tenslotte werd ultrasnel gloeien toegepast als een manier om de mechanische eigenschappen verkregen met het gebruikelijke Q&P proces te verbeteren. Door het verhogen van de opwarmsnelheid verfijnden de austeniet korrels, gekiemd in een niet-gerekristalliseerde matrix, aanzienlijk en losten de carbides niet volledig op. De complexe microstructurele interacties tijdens ultrasnelle opwarming resulteerden in een verbetering van zowel treksterkte als totale verlenging.

List of publications

Publications in international journal of the Science Citation Index (A1)

1. D. De Knijf, R. Petrov, C. Föjer, and L. A. I. Kestens: 'Effect of fresh martensite on the stability of retained austenite in quenching and partitioning steel', *Materials Science and Engineering: A*, 2014, 615, 107-115.

2. D. De Knijf, T. Nguyen-Minh, R. Petrov, L. A. I. Kestens, and J. J. Jonas: 'Orientation dependence of the martensite transformation in a quenched and partitioning steel subjected to uniaxial tension', *Journal of Applied Crystallography*, 2014, 47, 1261-1266.

3. D. De Knijf, E. Pinto Da Silva, C. Föjer, and R. Petrov: 'Study of heat treatment parameters and kinetics of Quenching and Partitioning cycles', *Materials Science and Technology*, 2015.

4. D. De Knijf, A. Puype, C. Föjer, and R. Petrov: 'The influence of ultra-fast annealing prior to Quenching and Partitioning on the microstructure and mechanical properties', *Materials Science and Engineering A*, 2015, 627, 182-190.

5. D. De Knijf, M. J. Santofimia, H. Shi, W. Xu, C. Föjer and R. Petrov: 'In-situ austenite-martensite interface mobility study during annealing', *Acta Materialia*, 2015, 90, 161-168.

6. D. De Knijf, C. Föjer, L.A.I. Kestens and R. Petrov: 'Factors influencing the austenite stability during tensile testing of Quenching and Partitioning steel determined via in-situ Electron Backscattered Diffraction', *Materials Science and Engineering: A*, 2015, 638, 219-227.

7. E. P. da Silva, D. De Knijf, W. Xu, C. Föjer, Y. Houbaert, J. Sietsma, R. Petrov: 'Isothermal transformations in advanced high strength steels below martensite start temperature', *Materials Science and Technology*, 2015.

8. I. de Diego-Calderón , D. De Knijf, J.M. Molina-Aldareguia ,I. Sabirov, C. Föjer, R.H. Petrov: 'Effect of Q&P parameters on microstructure development and mechanical behavior of Q&P steels', *Revista de Metalurgia*, 2015, 51(1), 1-12.

9. I. de Diego-Calderón , D. De Knijf, M.A. Monclús, J.M. Molina-Aldareguia ,I. Sabirov, C. Föjer, R.H. Petrov: 'Global and local deformation behavior and mechanical properties of individual phases in a quenched and partitioned steel', *Materials Science and Engineering: A*, 2015, 630, 27-35.

Publications in international conference proceedings (C1)

10. D. De Knijf, R. Petrov, C. Föjer, and L. A. I. Kestens: 'Optimization and Characterization of a Quenching and Partitioning heat treatment on a Low Carbon Steel', Proceedings of MS&T: Steel Product Metallurgy and Applications, Pittsburgh, 2012, 275-286.

11. D. De Knijf, R. Petrov, C. Föjer, and L. A. I. Kestens: 'Austenite Stability Study by Micro-tensile Testing of Q&P Steel', Proceedings of International Symposium on New Developments in Advance High Strength Sheet Steels, Colorado, 2013, 185-195.

List of abbreviations

A	Austenite
A_{C1}	Onset of austenite formation during heating
A_{C3}	End of austenite formation during heating
AFM	Atomic force microscopy
AHSS	Advanced High Strength Steels
APT	Atom probe tomography
B	Bainite
CCE	Carbon Constrained Equilibrium
CCT	Continuous Cooling Transformation diagram
CI	Confidence index
DA	Decomposed austenite
DIC	Digital image correlation
DSC	Differential scanning calorimetry
E_{act}	Activation energy
EBSD	Electron backscattered diffraction
EDS	Energy dispersive spectrometry
EPMA	Electron probe micro-analyser
f	Fraction
FEG	Field emission gun
FEM	Finite element modelling
FIB	Focussed ion beam
FM	Fresh martensite
GPa	Giga Pascal
GROD	Grain reference orientation deviation
HEM	Homogeneous effective medium
HR-TEM	High resolution transmission electron microscopy
ICP-MS	Inductive coupled plasma mass spectrometry
ICP-OES	Inductive coupled plasma optical emission spectroscopy
IPF	Inverse pole figure

IQ	Image quality
JMAK	Johnson-Mehl-Avrami-Kolmogorov
KAM	Kernel average misorientation
K-M	Koistinen-Marburger
kV	Kilovolts
M	Martensite
mA	Milliampere
MAO	Major axis orientation
M_f	Martensite finish temperature
MPa	Megapascal
M_s	Martensite start temperature
NA	Newly formed austenite
ND	Normal direction
OIM	Orientation image microscopy
OM	Optical microscopy
OQT	Optimum quenching temperature
PT	Partitioning temperature
Pt	Partitioning time
PTMC	Phenomenological theory of martensite crystallography
Q&P	Quenching and Partitioning
Q&T	Quenched and Tempered
QT	Quenching temperature
RA	Retained austenite
RD	Rolling direction
rpm	Revolutions per minute
SEM	Scanning electron microscopy
TD	Transverse direction
TKD	Transmission Kikuchi diffraction
TM	Tempered martensite
TRIP	Transformation Induced Plasticity
TTT	Time Temperature Transformation diagram
TWIP	Twinning induced plasticity

UFA	Ultra-fast annealing
UTS	Ultimate tensile strength
VPSC	Visco-plasticity self-consistent
x	Mole fraction
XRD	X-ray diffraction
XRF	X-ray fluorescence
YS	Yield strength
α'	Martensite phase
γ	Austenite phase
ε_u	Uniform elongation
μ	Chemical potential

TABLE OF CONTENTS

INTRODUCTION

INTRODUCTION

The goal of this PhD work was to gain fundamental knowledge of microstructural evolutions during partitioning and mechanical testing of "Quenching and Partitioning" (Q&P) steel.

Q&P is a thermal process, proposed in 2003 by Speer *et al.* [1-3], aimed at stabilizing retained austenite. The process involves an initial partial or full austenitization, followed by quenching to a temperature between the martensite start (M_s) and finish (M_f) temperature to create a controlled fraction of martensite. This step is called *quenching* step. Then, the steel is held isothermally or reheated to a higher temperature to allow carbon diffusion from martensite into the remaining austenite. This step is called *partitioning* step. Enhanced carbon levels stabilize the austenite at room temperature after final quenching. Competing reactions during the partitioning step (such as carbide precipitation, dislocation trapping of carbon or decomposition of austenite to bainitic ferrite) have been identified by previous contributors [4-7]. Additionally, evidence of interface migration has been reported [8, 9], which contradicts previous assumptions of an immobile austenite-martensite interface [1].

This study aims to fundamentally understand the physical metallurgy mechanisms behind the process and to optimize the Q&P heat treatment cycle. However, this optimization requires fundamental comprehension of the partitioning process itself as well as the relationship between the microstructure and the mechanical properties. Specifically, the goals of this project were to:

1. Understand the relationship between microstructure and mechanical properties
2. Study the microstructural changes upon deformation
3. Provide insight into the mobility of the martensite/austenite interface during partitioning

It is envisioned that gaining a more fundamental understanding of Q&P steels will ultimately help to obtain more efficient processing and even more attractive property combinations than those already observed.

Industrial relevance

The use of advanced high-strength steels (AHSS) has increased significantly in recent years. Particularly in the automotive industry, mass reduction is an important tool to reduce the fuel consumption without compromising the passenger's safety. Thus, steels that can offer the same structural performance with thinner steel products are required. Therefore, AHSS are attractive due to their increased levels of strength whilst maintaining formability necessary for industrial applications. Quenched and partitioned steels with a martensite and austenite based microstructure were calculated theoretically to have a promising combination of elongation and strength lying in the future opportunity of third generation AHSS, cfr. Figure 1.

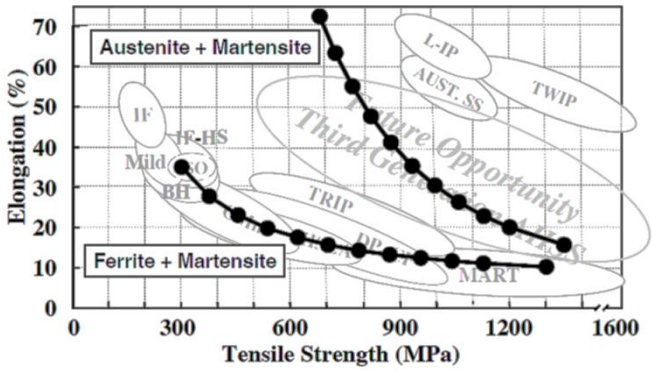

Figure 1: Total elongation vs. tensile strength of ferrite + martensite and austenite + martensite steel grades with Q&P lying in the third generation steels area [10]

It has been shown experimentally that such steels exhibit excellent combinations of strength and ductility [11, 12]. In some cases, the strength of Q&P steels has been shown to exceed that of Transformation Induced Plasticity (TRIP) aided steels possessing the same level of ductility [13]. Research aimed at understanding of the Q&P process will enhance the metallurgy field by enabling another type of steel that offers slightly different property combinations than those currently employed.

Quenching and Partitioning steels

Q&P steels are processed via a thermal profile shown schematically in Figure 2. First, the steel is reheated in the intercritical temperature range or above the A_{C3}-temperature to obtain a partially or fully austenitic microstructure respectively. Then the material is quenched between the martensite start temperature, M_s and the martensite finish temperature, M_f. After quenching, the microstructure consists out of controlled fractions of martensite,

austenite and ferrite in the case of intercritical annealing. In order to stabilize the remaining austenite during the final quench, its M_s-temperature must decrease at least until room temperature. This condition can be fulfilled by carbon enrichment during the *partitioning* step by carbon diffusion from the supersaturated martensite into the austenite. The partitioning step can be conducted at the quenching temperature or at a higher temperature to enhance diffusion kinetics. The above partitioning processes are indicated as *one-step* and *two-step* Q&P heat treatment respectively.

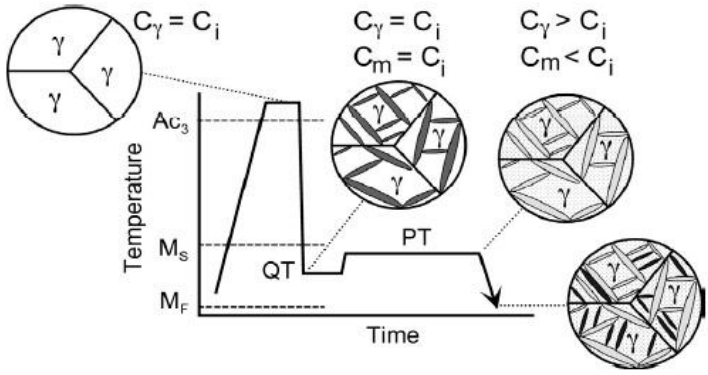

Figure 2: General heat treatment cycle of Q&P-steels [3]

After intercritical annealing, the main mechanism of carbon enrichment besides partitioning is epitaxial growth of ferrite during the first quench. This ferrite can be distinguished from the old one by a different etching colour, as observed by Santofimia *et al.* [14]. This contrast in etching colour was attributed to a different concentration of alloying elements due to a paraequilibrium condition with the austenite during growth of the ferrite. By this mechanism, carbon will be expelled into the remaining austenite during the growth stage of the ferrite in which the carbon solubility is lower.

Additionally, competing reactions may take place during the partitioning step. These competing reactions include conventional tempering reactions, carbon atom trapping at defects in the martensite and decomposition of austenite into other transformation products such as bainite, which in the form of a carbide-free constituent can also promote carbon enrichment of austenite.

After the final quench, the microstructure contains retained austenite, ferrite if annealing was conducted in the intercritical regime and possibly two types of martensite: the one formed during the first quench (referred to as “old” or “tempered” martensite) and

possibly the one formed during the final quench (referred to as "fresh", "new" or "untempered" martensite) [15].

Significant austenite fractions in Q&P steel can contribute to ductility and work hardening in the same manner as in the TRIP steels; that is, upon the application of strain, the austenite transforms to martensite, which is associated with a volume expansion and work hardening leading to postponed necking formation, enhanced formability and tensile strength [7, 11, 13, 16-18].

Advantages of Q&P processing

In the Q&P process, carbon partitioning and microstructure development are decoupled. The phase fractions and morphologies are controlled by athermal martensite transformation while partitioning is controlled in an isothermal stage, implying an independent and complete control during Q&P processing. This is a fundamental and very important difference with conventional heat treatments. Of course, this decoupling has some major implications [1, 2] :

1. Carbon enrichment of austenite is more effective compared to conventional carbide-free bainite formation.

2. Due to independent control, new possibilities arise to influence the final properties. An increase in strength in comparison to conventional bainitic processing is possible due to the presence of substantial quantities of lath martensite in Q&P microstructures.

3. During conventional bainitic transformation, carbon diffusion and ferrite nucleation/growth has to be controlled. Because only carbon diffusion needs to be controlled during Q&P partitioning treatment, its time dependence is different and allows more flexibility in the partitioning stage.

4. Q&P processing allows carbon enrichment of austenite in traditionally martensitic, rather than only bainitic microstructures.

The advantages of this heat treatment are mainly a higher potential for carbon enrichment of austenite, the decoupling of the bainitic ferrite growth kinetics from the carbon partitioning process, and the increased strength via formation of lath martensite in the microstructure. These advantages could make the Q&P heat treatment a very promising opportunity in steel production.

References

1. J. G. Speer, D. K. Matlock, B. C. De Cooman, and J. G. Schroth: 'Carbon partitioning into austenite after martensite transformation', *Acta Materialia*, 2003, **51**, 2611-2622.

2. J. G. Speer, D. V. Edmonds, F. C. Rizzo, and D. K. Matlock: 'Partitioning of carbon from supersaturated plates of ferrite, with application to steel processing and fundamentals of the bainite transformation', *Materials Science*, 2004, **8**, 219-237.

3. J. G. Speer, F. C. R. Assunção, D. K. Matlock, and D. V. Edmonds: 'The "quenching and partitioning" process: Background and recent progress', *Materials Research*, 2005, **8**, 417-423.

4. H. Y. Li, X. W. Lu, X. C. Wu, Y. A. Min, and X. J. Jin: 'Bainitic transformation during the two-step quenching and partitioning process in a medium carbon steel containing silicon', *Materials Science and engineering*, 2010, **527**, 6255-6259.

5. A. J. Clarke, J. G. Speer, M. K. Miller, R. E. Hackenberg, D. V. Edmonds, D. K. Matlock, F. C. Rizzo, K. D. Clarke, and E. D. Moor: 'Carbon partitioning to austenite from martensite or bainite during the quench and partition process: A critical assessment', *Acta Materialia*, 2008, **56**, 16-22.

6. D. V. Edmonds, K. He, F. C. Rizzo, B. C. D. Cooman, D. K. Matlock, and J. G. Speer: 'Quenching and partitioning martensite—a novel steel heat treatment', *Materials Science and engineering*, 2006, **438-440**, 25-34.

7. D. V. Edmonds, D. K. Matlock, and J. G. Speer: 'The recent development of steels with carbide-free acicular microstructures containing retained austenite', *Metallugia Italiana*, 2011, **1**, 41-49.

8. N. Zhong, X. Wang, Y. Rong, and L. Wang: 'Interface migration between martenisite and austenite during quenching and partitioning (q&p) process', *Materials Science and Technology*, 2006, **22**(6), 4.

9. M. J. Santofimia, J. G. Speer, A. J. Clarke, L. Zhao, and J. Sietsma: 'Influence of interface mobility on the evolution of austenite–martensite grain assemblies during annealing', *Acta Materialia*, 2009, **57**, 4548-4557.

10. D. K. Matlock and J. G. Speer: 'Design considerations of the next generation of advanced high strength sheet steels', Proceedings of the 3rd International Conference on Structural Steels, Seoul, Korea, 2006, The Korean Institute of Metals and Materials, 774-781.

11. E. De Moor, J. G. Speer, D. K. Matlock, J.-H. Kwak, and S.-B. Lee: 'Effect of carbon and manganese on the quenching and partitioning response of cmnsi steels', *ISIJ International*, 2011, **51**, 137-144.

12. M. Bohuslav, J. Hana, H. Daniela, K. Ludmila, and K. Danuse: 'The effect of mn and si on the properties of advanced high strength steels processed by quenching and partitioning', *Materials Science Forum*, 2010, **654-656**, 94-97.

13. E. De Moor, S. Lacroix, A. J. Clarke, J. Penning, and J. Speer: 'Effect of retained austenite stabilized via quenching and partitioning on the strain hardening of martensitic steels', *Metallurgical and Materials Transactions A*, 2008, **39A**, 2586-2595.

14. M. J. Santofimia, L. Zhao, R. Petrov, and J. Sietsma: 'Characterization of the microstructure obtained by the quenching and partitioning process in a low-carbon steel', *Materials Characterization*, 2008, **59**, 1758-1764.

15. C. Y. Wang, J. Shi, W. Q. Cao, and H. Dong: 'Characterization of microstructure obtained by quenching and partitioning process in low alloy martensitic steel', *Materials Science and engineering*, 2010, **527**, 3442-3449.

16. C. Zhao, D. Tang, H.-T. Jiang, S.-S. Jhao, and H. Li: 'Process simulation and microstructure analysis of low carbon si-mn quenched and partitioned steel', *Journal of Iron and Steel Research, International*, 2008, **15**(4), 82-85.

17. X. D. Wang, Z. H. Guo, and Y. H. Rong: 'Mechanism exploration of an ultrahigh strength steel by quenching-partitioning-tempering process', *Materials Science and engineering*, 2010.

18. A. Dimatteo, G. Lovicu, R. Valentini, M. DeSanctis, and M. R. Pinasco: 'The strain-hardening behaviour of q&p steels', 2010.

CHAPTER I

LITERATURE STUDY

I. LITERATURE STUDY

I.1. Carbon partitioning

The central concept in Q&P steels is the *partitioning* stage. Little attention has been given to this concept because most of the production processes do not consider carbon diffusion after displacive or martensitic transformations. In conventional quenched steels, the microstructure consists almost completely out of martensite where the supersaturation is eliminated by precipitation, using a tempering heat treatment [1]. Besides, the quenching temperatures are usually too low to have substantial amounts of carbon diffusion [2]. There is, however, evidence that carbon partitioning from martensite to austenite happens to thin interlath films during cooling [3] or isothermal holding [4].

This stabilization of the remaining austenite during partitioning was assumed by Speer *et al.* [5-9] to possibly play an important role if alloying elements which suppress carbide formation were added. They developed a thermodynamic model to predict the endpoint of complete or *ideal* partitioning at a given temperature, described by the "Constrained Carbon Equilibrium" (CCE) condition.

I.1.1. Constrained carbon equilibrium

The constrained carbon equilibrium condition (CCE) is defined by absence of iron or substitutional diffusion, and the freedom of carbon to migrate over distances greater than the Fe unit cell. The big difference with paraequilibrium [10] is that grain boundary movement is precluded by short-range iron or substitutional diffusion.

Two conditions describe the model completely. First, carbon diffusion occurs until its chemical potential is the same in the austenite (γ) and martensite (α'):

$$\mu_C^{\gamma} = \mu_C^{\alpha'} \tag{1}$$

Ignoring the effects of alloying elements on the carbon activity, this can be represented as [11, 12]:

$$x_C^{\gamma} = x_C^{\alpha'} . e^{\frac{76.789 - 43.8 \cdot T - (169.105 - 120.4 \cdot T) \cdot x_C^{\gamma}}{R \cdot T}} \tag{2}$$

where $x_C^{\alpha'}$ and x_C^{γ} are the mole fractions of carbon in martensite and austenite respectively.

If the only requirement would be the equalisation of the chemical potential of C in both phases, an infinite number of solutions would exist. This is schematically illustrated in Figure I-1 by the molar Gibbs free energy vs. composition diagram. Two constrained carbon equilibrium conditions (I and II) are possible at this particular temperature. Therefore, a second criterion needs to be fulfilled to limit the number of solutions to retain one.

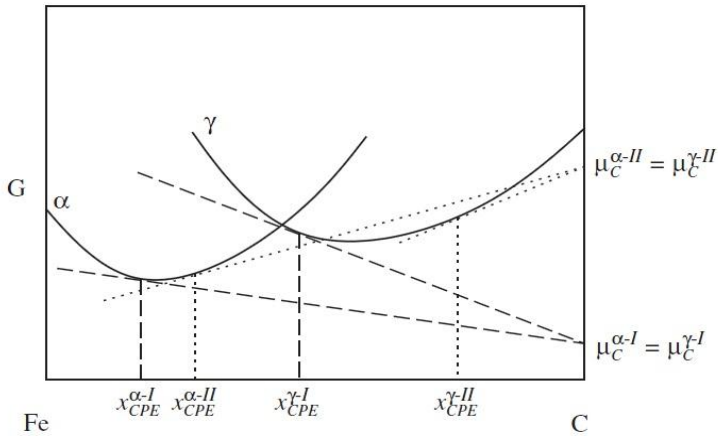

Figure I-1: Schematic molar Gibbs free energy vs. composition diagram illustrating metastable equilibrium at a particular temperature between ferrite and austenite in the Fe-C binary system with two possible constrained carbon equilibrium conditions (I and II) [5]

The second restriction is that the number of iron atoms must be conserved in each phase. For an as-quenched condition, i.e. before any partitioning, the martensite and austenite have the same carbon content, i.e. both equal to the overall carbon content x_C^{alloy}. Mathematically, the matter balance for iron in austenite can be presented by:

$$f_{CCE}^{\gamma}\left(1 - x_{C_{CCE}}^{\gamma}\right) = f_i^{\gamma}\left(1 - x_C^{alloy}\right) \tag{3}$$

where x_C^{alloy} is the overall carbon content of the steel in mole fraction, f_i^{γ} is the mole fraction of the retained austenite before partitioning begins, and f_{CCE}^{γ} and $x_{C_{CCE}}^{\gamma}$ represent the austenite fraction and the carbon concentration at constrained carbon equilibrium when carbon partitioning is completed. Changes in phase fractions during partitioning may seem in contradiction with the assumption of an immobile α'/γ interface. However it makes sense given that the change in phase fractions is not caused by movement of iron or substitutional atoms but by exchange of carbon atoms. This change in the total number of atoms leads to slightly adjusted mole fractions of the phases.

Together with the following equations the equilibrium is completely defined:

$$f_{CCE}^{\alpha'} x_{C_{CCE}}^{\alpha'} + f_{CCE}^{\gamma} x_{C_{CCE}}^{\gamma} = x_C^{alloy} \quad (4)$$

$$f_{CCE}^{\alpha'} + f_{CCE}^{\gamma} = 1 \quad (5)$$

Most of the carbon will diffuse into the austenite, because the solubility of carbon in ferrite is small [6]. For the ease of calculations, the carbon concentration in martensite $x_{C_{CCE}}^{\alpha'}$ is often set equal to zero. This is what is called *ideal partitioning*. Example calculations given by Speer *et al.* [5], illustrate that the austenite composition at constrained carbon equilibrium can indeed be closely approximated by assuming that virtually all of the carbon in the martensite partitions into the austenite.

I.1.2. Interface mobility

One of the restrictions in the constrained carbon equilibrium model is that interface migration is precluded. The occurrence of interface migration was however proposed by Zhong *et al.* [13] to explain changes in the curvature of austenite grains before and after partitioning. Expected motion of the interface during partitioning, due to a chemical potential difference of iron, was qualitatively examined by Speer *et al.* [14] and quantitatively by Santofimia *et al.* [15, 16].

Zhong *et al.* [13] stated that scanning electron microscopy (SEM) images illustrated the loss of the original plate-like appearance of martensite after partitioning. Besides, transmission electron microscopy (TEM) images as reproduced in Figure I-2, showed that the interfaces of martensite/austenite with almost straight appearances became curved after partitioning with increasing tempering time, without nucleation of bainite at the interfaces.

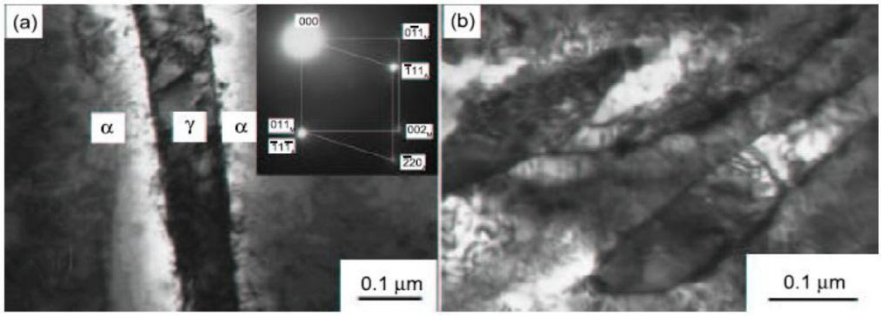

Figure I-2: TEM of samples partitioned at 480°C for (a) 6s and (b) 80s [13] illustrating the change in interface from a straight to a curved interface with increasing partitioning time

This interface migration was a suggestion for the presence of Fe-atom migration, and in this case the CCE concept does not strictly apply since this assumes a stationary or

constrained martensite/austenite interface. Zhong *et al.* stated that the "endpoint" of the carbon constraint equilibrium model is the "startpoint" of Fe-diffusion or interface migration.

The direction of Fe-diffusion depends on the chemical potential of Fe in martensite and austenite after the equalization of the chemical potentials of carbon by the constraint carbon equilibrium. If the interface is enriched in carbon relative to the equilibrium, then the chemical potential of Fe in martensite will be higher than in austenite. Hence, iron will diffuse from the martensite to the austenite resulting in grain boundary movement in the opposite direction. If the interface is depleted in carbon, the reverse will happen. Additionally, carbide precipitation during partitioning will decrease the amount of carbon in austenite and in turn decrease its chemical potential in the two phases. Therefore, this will not only decrease the austenite fraction by decomposition but also by interface migration.

This was also discussed by Speer *et al.* [14] and quantitatively analysed by Santofimia *et al.* [15] illustrating a bidirectional movement of the interface. The calculations were made under the assumption of an incoherent interface nevertheless its semi-coherent nature [17]. Therefore, Santofimia *et al.* assumed in [16] different mobilities related to the activation energy for iron migration to simulate the microstructural evolution during partitioning: *(i)* completely immobile ($E_{act} = \infty$), *(ii)* limited mobile representing a semi-coherent interface ($E_{act} = 180\frac{kJ}{mol}$), and *(iii)* highly mobile representing an incoherent interface ($E_{act} = 140\frac{kJ}{mol}$). The alloy of interest was a binary Fe-0.25C (wt. %) alloy with a film–like morphology of martensite and austenite. The martensite lath was considered to have a fixed width of 0.2µm [18] whereas the austenite film width changed according to varying quenching temperatures.

In general, Santofimia *et al.* [15, 16] calculated a sharp increase of the carbon content in the austenite near the interface for short partitioning times, stabilizing a small fraction with a high C-content. This peak was progressively reduced with increasing partitioning time.

The interface change and %C in the austenite are shown in Figure I-3 (a) and (b) respectively. A positive interface change represents a grain boundary movement from martensite to austenite, whereas a negative interface change refers to the opposite movement. An immobile interface results in stabilization of more austenite with decreasing C-content due to homogenisation, reaching the equilibrium C-content for increasing partitioning times. For a semi-coherent interface, the carbon concentration profiles were similar to those for an immobile interface for short times. However, longer partitioning times lead to the initiation of interface migration and enrichment of carbon at the interface until full equilibrium was

reached. For a coherent interface, the carbon profiles and evolution of the interface were coupled during the partitioning process leading to a bidirectional movement of the interface prior to achieving equilibrium, cfr. Figure I-3 (a). Carbon partitioning started with an increase of the carbon content in the austenite which is compensated by the movement of the interface from the austenite to the martensite. Once the carbon content is lower than the equilibrium value, the interface reverses its direction.

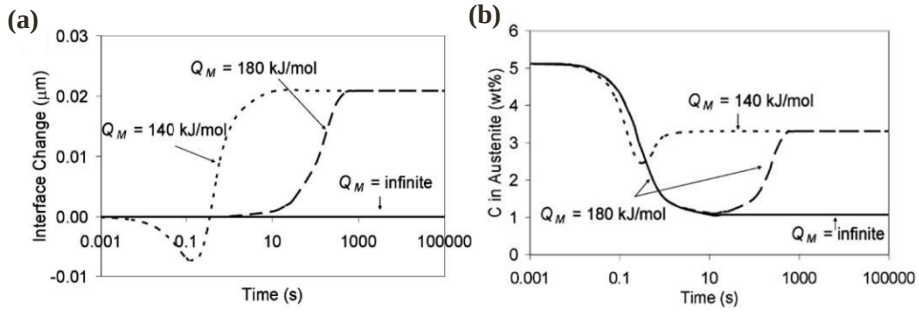

Figure I-3: (a) Interface change (μm) with partitioning time and (b) carbon content of the austenite (wt. %) as a function of partitioning time for three different activation energies/mobilities of the austenite/martensite interface for QT = 300°C and PT = 400°C [16]

Phase field simulation was addressed by Takahama *et al.* [19] to show details of carbon redistribution as well as possible interface migration. The peak in the local carbon content in austenite close to the grain boundary with martensite was calculated to be higher than the paraequilibrium value, which created a driving force for the movement of the interface, causing growth of austenite. This is consistent with the observations of Santofimia *et al.* [16] for an incoherent interface.

Toij *et al.* [20] conducted atom probe tomography experiments on Q&P steels and observed that Mn partitioned from martensite into austenite after C-partitioning. This phenomenon was explained by two possible mechanisms being diffusion of Mn after C-partitioning due to a slower kinetics or interface migration.

Finally, Tan *et al.* [21] observed a thickening of the martensite laths during partitioning. This was explained to be caused either by coalescence of lath-boundaries or interface migration.

I.1.3. Optimum Quench temperature

A methodology for obtaining the maximal retained austenite fraction after Q&P as a function of the quenching temperature was developed [7]. The model ignores kinetic effects, assumes ideal partitioning and supposes that carbide precipitation is avoided. It predicts the fraction of retained austenite as a function of the quenching temperature whereby the quenching temperature at which the model yields a maximum amount of retained austenite is defined as the optimum quench temperature.

The volume fractions of austenite and martensite at the quenching temperature can be calculated based on the undercooling below M_s according to the Koistinen-Marburger relationship [22]:

$$f_{\alpha'} = 1 - e^{-\alpha \cdot (M_s - QT)} \tag{6}$$

where $f_{\alpha'}$ is the fraction of austenite that transforms into martensite during the first quench. The martensite start temperature M_s can be calculated from equations in literature e.g. with an exponential relationship with respect to the carbon content [23]:

$$M_s(°C) = 565 - (31 \cdot x_{Mn} + 13 \cdot x_{Si} + 10 \cdot x_{Cr} + 18 \cdot x_{Ni} + 12 \cdot x_{xMo}) - 600 \cdot (1 - e^{-0.96 \cdot x_C}) \tag{7}$$

The rate parameter α, controls the kinetics of martensite formation [23]:

$$\alpha\ (10^{-3} K^{-1}) = 27.2 - (0.14 \cdot x_{Mn} + 0.21 \cdot x_{Si} + 0.11 \cdot x_{Cr} + 0.08 \cdot x_{Ni} + 0.05 \cdot x_{Mo}) - 19.8 \cdot (1 - e^{-1.56 \cdot x_C}) \tag{8}$$

The carbon content of austenite is approximated by assuming that all carbon is homogeneously contained in the austenite during annealing.

The M_s temperature of the remaining austenite is calculated by supposing complete, ideal partitioning. Then, the Koistinen-Marburger calculation is repeated for the final quench until room temperature resulting in the overall evolution of the retained austenite fraction versus quenching temperature as illustrated in Figure I-4.

The peak temperature is the optimum quenching temperature at which all the austenite is stabilized after ideal partitioning. If the quenching temperature is lower, the available austenite is completely stabilized however the fraction is lower due to too much martensite formation during the first quench. If the quenching temperature is higher, there will be a lack of carbon to stabilize all the austenite and part of it will transform to fresh martensite during final quenching.

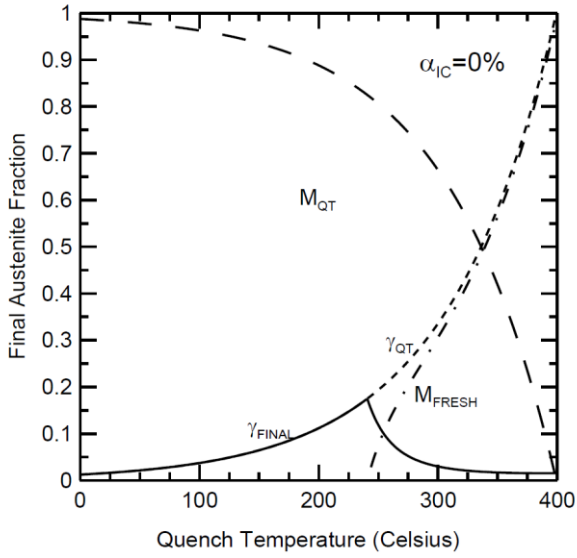

Figure I-4: Calculated austenite fraction as a function of quench temperature for a 0.19C-10.59Mn-1.63Si (wt.%) steel. M_{QT} and γ_{QT} correspond to the amount of martensite and austenite present after the initial quench to the quenching temperature. M_{FRESH} is the amount of fresh martensite that forms during final quenching to room temperature and γ_{FINAL} predicts the final austenite weight fraction at room temperature [24]

Experimental values can differ from the model due to non-ideal partitioning by kinetic effects [8] or competing reactions e.g. bainite formation [25-28] or carbide precipitation [8, 24, 26, 29].

I.1.4. Kinetics

The kinetics of partitioning is determined by diffusion of carbon inside austenite and martensite. C-diffusion in austenite is the time-limiting step since it is much slower than in martensite [26]. Short partitioning times are associated with significant carbon enrichment in austenite near the interface; these levels of enrichment however decrease progressively as time increases [9, 16, 24].

If an immobile grain boundary is supposed, the partitioning kinetics can be included in the Koistinen-Marburger relationship by incorporating the local carbon concentration profiles in austenite and martensite relative to the α'/γ interface as a function of time [9]. This profile in austenite is used to estimate the local stability, providing insight regarding the final austenite fraction as a function of partitioning time for a given set of processing conditions. Simulations were done using DICTRA with a ferrite cell with a width of 0.2 µm [18],

simulating a martensite lath and an adjacent austenite film with a width between 15nm and 145nm, depending on the quenching temperature.

The predictions of the model follow the results without kinetic aspects very well at temperatures lower than or equal to the optimum quenching temperature, cfr. Figure I-5. The optimal final austenite fraction is already obtained after 1s. At higher quenching temperatures, the retained austenite fraction is predicted to be larger than modelled without the influence of kinetics. This can be explained by a faster C-diffusion in martensite than in austenite, creating a pile-up of carbon in the austenite grains near the grain boundaries. This austenite will be stabilized locally. Thus, the final fraction will be less sensitive to a higher quenching temperature as was also observed experimentally [30]. Besides, this phenomenon explains the film-like morphology of austenite [31-33] frequently present in the final microstructure. At longer partitioning times, the fraction decreased again due to homogenisation of the C-content in the austenite and next transformation to martensite during the final quench because of insufficient C-stabilisation.

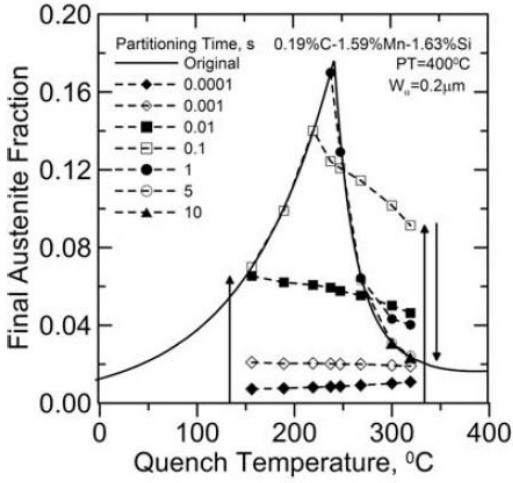

Figure I-5: Calculated final austenite fraction as a function of the quenching temperature for 0.19C-1.59Mn-1.63Si [9]

The model of Santofimia *et al*. [16] predicted the volume fraction of retained austenite after the final quench for a semi-coherent and coherent interface, cfr. Figure I-6. The evolution of the retained austenite fraction for a semi-mobile interface is similar to an immobile interface at short partitioning times until the optimum fraction is reached. Afterwards, for quenching temperatures lower than the optimum, the retained austenite fraction decreases again to the full equilibrium value. For quenching temperatures higher than

the optimum, it first increases then decreases and after that increases again to the equilibrium value. For a mobile interface, the austenite fraction increases with annealing time until it reaches its maximum and then it decreases again to the value corresponding with full equilibrium.

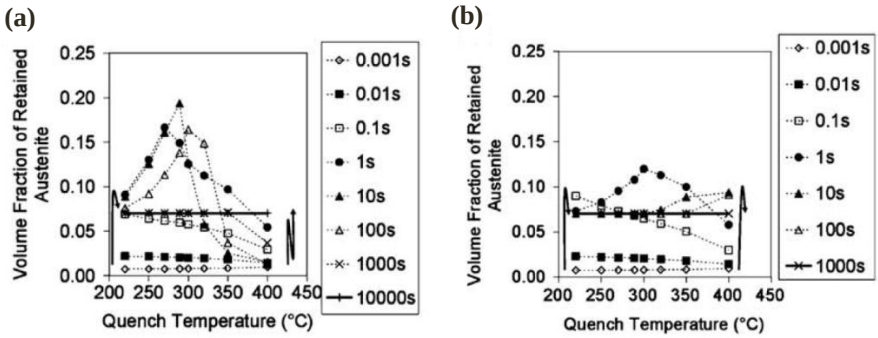

Figure I-6: Predicted volume fraction of retained austenite as a function of the quenching temperature for different annealing times at 400°C for a (a) semi-mobile interface and (b) mobile interface [16]

I.1.5. Experimental observation of partitioning

Several researchers have studied the phenomenon of carbon partitioning from martensite to austenite [34, 35]. Bigg *et al.* [34] have most recently shown evidence of carbon partitioning by studying steels containing 0.64C-4.57Mn-1.30Si (wt. %) using XRD and neutron diffraction by a high resolution powder diffractometer. For this study, the samples were austenitized at 1000 °C for 7.5 min and then quenched into water. Samples were then partitioned at 400 °C for various times and the austenite fractions and lattice parameters of austenite and martensite were measured. The first stage consisted of a reduction in the lattice parameter of martensite but not of austenite which was attributed to internal partitioning of carbon to low-energy sites around defects and the formation of epsilon-carbides. At longer times, a clear increase in the austenite lattice parameter was observed which was assigned to carbon partitioning.

De Moor *et al.* [35] have shown indirect evidence for carbon partitioning by differential scanning calorimetry measurements on a 0.2C-1.63Mn-1.63Si steel. The steel was reheated to 600°C after a short partitioning heat treatment. Two exothermic peaks were observed of which one was associated with austenite decomposition. The presence of the other peak could not be explained by classical tempering reactions. The activation energy was close to the activation energy for carbon diffusion in ferrite. Additional XRD measurements

on the sample after reheating above the peak illustrated an increase in carbon content in the austenite. Hence, De Moor *et al.* concluded that this peak could be associated with carbon partitioning.

Partitioning of carbon into austenite during martensitic tempering was first highlighted by atom probe tomography by Bernard *et al.* [36]. Experimental evidence of carbon partitioning from bainitic ferrite to austenite [37] and from martensite to austenite in Q&P steel [8, 20, 38] was also addressed by this technique. Gouné *et al.* [38] used a 0.4C-25Ni (wt.%) alloy which was quenched in liquid nitrogen and tempered at 75°C for 1h. A carbon-depleted zone in the martensite and a carbon-enriched zone in the austenite in the vicinity of the interface were observed supporting diffusion controlled carbon partitioning process from martensite to austenite. Toji *et al.* [20] observed besides carbon partitioning also Mn partitioning from martensite to austenite. This may indicate interface migration, as discussed previously or slow Mn partitioning after C-diffusion.

I.2. Other mechanisms

Ideal partitioning makes the assumption that all available carbon partitions into austenite and that no competing reactions such as carbide precipitation or bainite formation occur [5]. Depending on the steel composition and the particular heat treatment, formation of ferrite, bainite [25-28], isothermal martensite [39-41] and carbides [8, 24, 26, 29] during Q&P processing can overlap with carbon partitioning, reducing its effectiveness.

I.2.1. Carbon trapping in dislocations

Low carbon lath martensite has a very high dislocation density. The stress-fields around dislocations cause the interstitial sites to be even lower in energy as compared to the same zones in the bulk. Therefore, carbon atoms tend to redistribute to these preferential sites and become “trapped” by the dislocations [42-44]. This occurs especially at low temperatures. At higher temperatures this trapping is only a transition phase in time because recovery occurs which reduces the number of dislocations in the material and the trapping probability.

I.2.2. Carbide precipitation

The defects within the martensite are believed to become saturated with carbon before transition carbide precipitation begins [43]. At lower partitioning temperatures (< 300°C) the transition ε-carbide which has a hexagonal close packed structure and chemical formula of $Fe_{2.4}C$, can be formed [24, 26, 29, 45]. At higher partitioning temperatures, cementite [24] can precipitate and previously formed epsilon carbides can dissolve again [46]. It is important to avoid carbide precipitation because it will reduce the available carbon content for stabilizing austenite. Cementite precipitation can be suppressed by alloying with silicon. Silicon changes the controlling reaction from carbon diffusion towards the diffusion of silicon away from the interface due to a low solubility in cementite [47]. The silicon forms a barrier around this cementite, and suppresses the growth of the carbide [48]. Nevertheless, Edmonds *et al.* [24] reported that silicon stabilizes epsilon carbides.

I.2.3. Bainite transformation

Austenite can also transform during partitioning into different morphologies of bainite, depending on the chemical composition. Santofimia et al. [25, 49] attributed the length-increase during partitioning to the development of bainite.

If the material is alloyed with silicon, cementite formation is suppressed. However, part of the austenite can transform into carbide-free bainite [25] or bainite with epsilon carbides [26]. Because of the low solubility of carbon in this bainitic ferrite, it is (partially) expelled to the austenite. As such, it might be considered a complimentary mechanism to explain carbon enrichment of austenite. Clarke et al. [8, 9] showed, however, that bainitic ferrite formation cannot be the sole contributor to carbon enrichment of austenite in Q&P.

Clarke et al. [8, 9] performed theoretical calculations to assess the levels of austenite that might be retained via expulsion of C due to carbide-free bainite formation. As seen in Figure I-7, the experimental austenite volume fractions measured using XRD are two to four times higher than the levels predicted based on carbide-free bainite formation. Therefore, Clarke et al. concluded that carbide-free bainite formation was not able to explain the experimentally observed levels of retained austenite, while predictions based on carbon partitioning, were able to account for the levels of retained austenite observed. However, deviations from the predicted levels of austenite indicate that the partitioning was incomplete.

Hence, the formation of bainite cannot be completely ignored. It should be noted that the bainite formation kinetics is enhanced by the strains induced by martensite transformation [50].

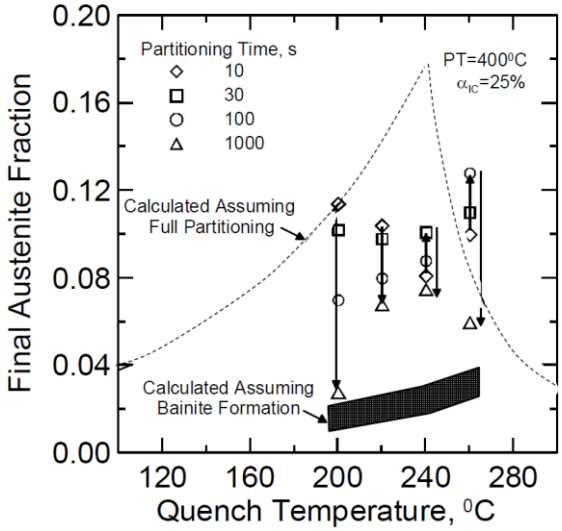

Figure I-7: Austenite volume fraction as a function of the quenching temperature for different partitioning times for intercritical annealed samples at 820°C for 180s, quenched and partitioned at 400°C for 10-30-100-1000s. The arrows indicate the kinetics of the experiments, and the calculated austenite fraction assuming full partitioning and assuming carbide less bainite formation are shown [8, 9]

I.2.4. Isothermal transformations below M_s

An isothermal transformation at the quenching temperature was reported by Kim *et al.* [39, 41] by dilatometric analyses of Q&P processes. Averbach *et al.* [51] were the first to report isothermal decomposition of austenite into martensite in a 1 wt.% C tool steel. In 1969, Pati and Cohen [52] concluded that the isothermal transformation was martensitic in nature and that the nucleation was affected by autocatalysis due to stresses and strains in the austenite. Oka and Okamoto [50] showed the existence of thin, plate-like and leaf-like isothermal martensite with midrib in TEM.

After analysis of isothermal transformations by means of dilatometry, Kim *et al.* [39, 41] reported a swing-back phenomenon. This effect was reported before [50, 53] and addressed on one hand to an acceleration effect on the nucleation of bainite in the adjacent austenite due to the presence of thin plate-type martensite [50] or on the other hand to a thin platelike isothermal product [53].

The kinetics above the M_s temperature was found to correspond with diffusion controlled growth of needles with one long dimension, whereas the kinetics below the M_s temperature matched with the thickening of long needles or plates. The transformation was not observed to be thermally activated, but driven by a small activation energy which was lower than the reported one for a diffusion-controlled process. This activation energy was correlated with the movement of interfacial transformation dislocations [54]. Hence, they concluded that the isothermal transformation below M_s was not a continuation of the bainite transformation above M_s.

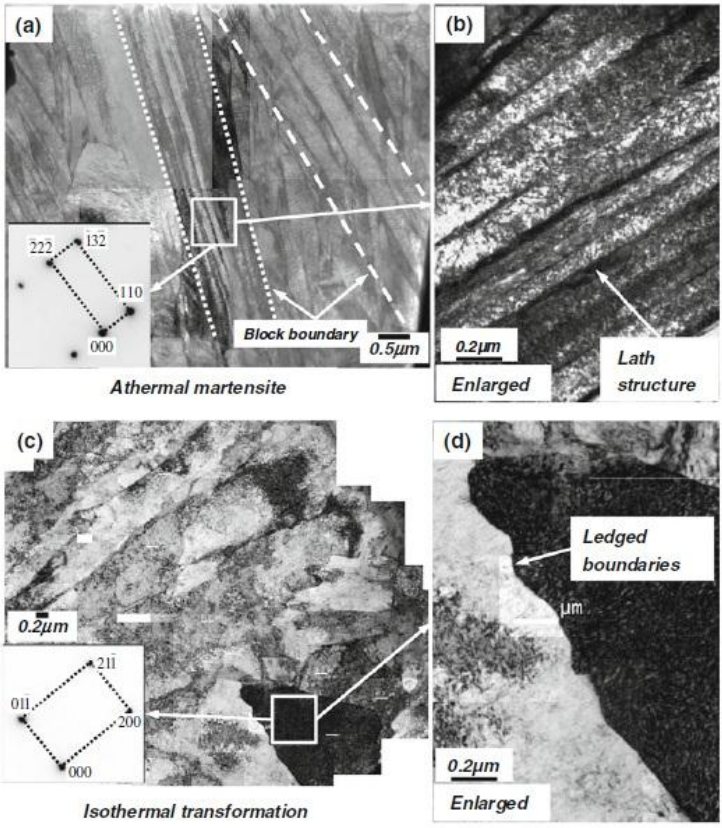

Figure I-8: (a-b) Athermal martensite and (c-d) isothermal martensite [39]

The main morphological differences [39] between the two transformation products were that athermal martensite consisted of well-developed laths with straight boundaries, a width of 0.2μm and a misorientation of less than 5° between the laths. The isothermal component had wavy edges, a lath width of a magnitude larger, 2 μm and a misorientation of more than 10°, cfr. Figure I-8.

The orientation relationship between martensite and its parent austenite grain is Kurdjumov-Sachs [55] e.g. in Figure I-9. However, a small difference in the low range of the misorientation angle distribution was observed for isothermal martensite, athermal martensite and bainite. In contrast to the athermal martensite (and lower bainite) with almost no peaks in the lower angle range, about 12% of the misorientation angles were seen around 10° in the case of the isothermal transformation product [41].

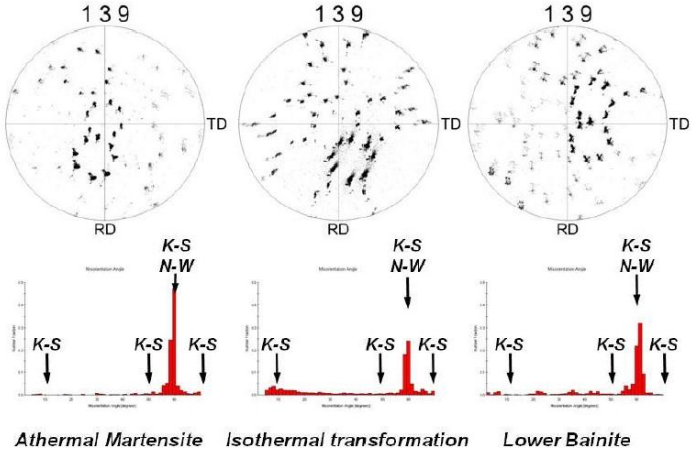

Figure I-9: Pole figures and misorientation angles for athermal martensite-isothermal martensite and lower bainite [41]

The difference between both types of martensite concerning their mechanical properties is related to their dislocation structure. These differences were showed quantitatively by internal friction measurements. Assuming that both athermal and isothermal martensite transformation products contain the same amount of carbon in solution, the difference in peak intensities must be related to a difference in mobile dislocation density. This is due to the diffusion of carbon to the strain field of the dislocations and some degree of recovery during isothermal transformation. In addition, less transformation-induced dislocations were generated. Because of this, the mobile dislocation density was lower which lead to a lower strength and n-value for isothermal martensite compared to athermal martensite.

Li *et al.* [45] also concluded that the observed length increase during one-step Q&P at 100°C below M_s could not be attributed to bainite formation but could be assigned to isothermal martensite.

I.3. TRIP effect

Q&P steels are multi-phase steels consisting of a hard phase (martensite and possibly bainite) and a soft phase (retained austenite); if intercritical annealing is employed then ferrite may also be present. It is reasonable to consider that the behaviour of Q&P steel under mechanical testing may give similar responses as TRIP-assisted steels, which consist of ferrite, bainite, retained austenite and possibly hard martensite. The mechanism by which steels with retained austenite exhibit their combination of strength and ductility was proposed in 1967 by Zackay *et al.* [56] to occur by a strain hardening process.

The reason behind the favourable mechanical properties of TRIP-assisted steels due to TRIP effect has been postulated to occur by two mechanisms [57] : (1) transformation of austenite to martensite and (2) the plastic straining of the phases surrounding the austenite due to the volume and shape changes associated with the displacive transformation [58].

Before large scale macroscopic yielding, the austenite grains already bear a significant larger load than the matrix [59]. If austenite transformation occurs at this stage, it is referred to as stress-induced [60]. Macroscopic yielding then takes place through a simultaneous collaborative activity of strain-induced [60] austenite-to-martensite transformation and plastic deformation in the matrix [60, 61]. The martensitic transformation of finely dispersed retained austenite assists the plastic deformability of TRIP steels. At the same time however, since the retained austenite is harder than the ferritic matrix, it acts as an effective reinforcement responsible for large macroscopic stresses [62] creating a strain hardening effect. These effects postpone further deformation in this area and move the martensitic transformation to neighbouring areas, leading to a delay in the onset of macroscopic necking and consequently, to higher values of uniform and total elongation.

Bhadeshia [63] stated that the effect of martensite transformation cannot contribute for more than 2% to the total ductility of TRIP-steels. He concluded that the composite like deformation behaviour in which the austenite controls the strain distribution is responsible for the high strength and ductility. These results are consistent with the observations of Jacques *et al.* [64], who observed good ductility with limited retained austenite fractions.

This TRIP effect results in an increased ductility of Q&P steel [33]. Martensite and austenite have a different yielding point and during plastic deformation yielding and work hardening of the austenite takes place [65]. This will transport the stress to the martensite which breaks consequently in a plastic way. The type of martensite is very important: the first

formed martensite with a lath structure is ductile and though owing to its dislocation substructure. In contrast, the martensite formed during the final quench is brittle and hard.

Experimental evidence of TRIP-assisted behaviour in Q&P steel was observed by Zhao *et al*. [33] by a decreased austenite fraction measured with X-ray diffraction before and after tensile testing. Dimatteo *et al*. [66] and other researchers [42, 66, 67] assigned this effect to the occurrence of a plateau in the instantaneous n-value versus strain chart. De Moor *et al.* [30] reported that the strain hardening behaviour of Q&P steels is dependent on the partitioning conditions being intermediate between quench and tempered (Q&T) and austempered (TRIP) steels with the same tempering conditions as the partitioning treatment. Q&P heat treatments with lower partitioning temperatures and shorter partitioning times have a strain hardening curve closer to Q&T steels with a decreasing n-value; whereas the increasing n-values of a better partitioning treatment are in close correspondence with TRIP steels suggesting an effective contribution of austenite to martensite transformation to the strain hardening of Q&P steels.

I.3.1. Austenite stability

A good ductility-strength balance is attained when the strain-induced transformation of austenite develops gradually during plastic straining.

In TRIP-steel several experimental studies have been carried out, showing that the transformation stability of austenite is affected by *(i)* the local carbon content in the austenite [68-71], *(ii)* the grain volume of the retained austenite [71-74], *(iii)* morphology [73, 75, 76], *(iv)* the constraining effect of the phases surrounding the austenite [76-79], and *(v)* the crystallographic orientation [68, 80, 81] of the austenite with respect to the loading direction. Besides transformation to martensite, austenite grains were found to rotate to accommodate deformation [68, 82].

I.3.1.1. Carbon content

Increasing the carbon concentration has the effect of reducing the tendency of retained austenite to transform to martensite under loading. Jimenez-Melero *et al*. [70, 71] evaluated the thermal stability of retained austenite and found that carbon enrichment was the dominant influence in the stability of large austenite grains (> 20 μm^3). Several authors [21, 68, 83] have observed an increase in average the C-content during plastic deformation indicating that the austenite with higher C-content remained stable until later deformation stages. Increasing the austenite C-content, increases the deformation induced martensite (M_d)

temperature and the stacking fault energy and as a consequence decreases the nucleation rate and hence the transformation rate to martensite [84].

I.3.1.2. Grain size

Besides the carbon content, austenite stability can be enhanced by a fine grain size. This is due to the absence of substructures in the austenite, for example stacking faults and other defects, which provide nucleation sites for martensitic transformation. Jeong *et al.* [85] observed experimentally in studies of multiphase TRIP steels that the retained austenite with smaller grain size has a higher resistance to martensitic transformation. Jimenez-Melero *et al.* [70, 71] found out that below 20 μm^3 the grain volume plays an increasing role in austenite stability.

I.3.1.3. Morphology

Austenite in TRIP steels exists in two forms, isolated austenite grains in ferrite outside of bainite and film-like austenite in between bainitic ferrite plates. The latter type of austenite is generally observed to be more stable during deformation than the former [73, 75, 76, 79]. This is attributed both to the morphology of the retained austenite [75] and the surrounding phases [79].

In Q&P steel, investigations on the austenite stability related to its morphology revealed that high-carbon blocky grains were less stable than low carbon lath-type or film-like austenite, despite their lower carbon content [86, 87]. Xiong et al. [86] performed interrupted tensile tests combined with synchrotron XRD experiments on Q&P produced by intercritical annealing. A decrease of the retained austenite fraction with increasing strain was observed. The austenite peaks were deconvoluted into two peaks, one was assigned to high-C, blocky austenite and the other to low-C, film-like austenite. The peak associated with high-C, blocky austenite grains transformed faster. This observation made them suggest that the morphology of retained austenite was a more determining factor for stability than the C-content.

Two intrinsic mechanisms were employed to explain these results: (i) the high yield strength of the lath martensite surrounding the film-austenite compared to the pro-eutectoid ferrite surrounding the blocky austenite grains; (ii) a higher hydrostatic stress on the lath-austenite induced by the residual stress of the martensitic transformation of the surroundings. Xie et al. [87] observed with EBSD analysis of tensile strained samples that granular retained austenite transformed to martensite at a tensile strain of 2%, whereas film-like austenite only transformed at a tensile strain of 12%. This gradual transformation of austenite with different

stabilities to strain-induced martensite continuously increased the instantaneous work hardening and delayed necking, leading to excellent ductility.

I.3.1.4. Phases surrounding austenite

The strength of the phases surrounding the austenite influences the austenite resistance to martensitic transformation. Jacques et al. [79] studied the influence of C-content and surrounding phases on the austenite stability in TRIP-steels. He concluded that harder phases can shield the austenite from the externally applied load and hence the mechanical stability of retained austenite was not solely related to the decrease of the M_s temperature by carbon enrichment.

I.3.1.5. Crystallographic orientation

Kruijver *et al.* [81] studied austenite stability in TRIP steel during tensile testing via X-ray diffraction in a synchrotron. By dividing the angles of the measurements into different sections, the influence of the austenite orientation with respect to the tensile axis was studied. The study revealed that the austenite grains with angles of 0° and 90° between the tensile direction and the normal direction of the diffracting {200} plane were least stable to martensitic transformation during tensile testing. Blondé *et al.* [68] observed as well that austenite grains with their {200} planes oriented in the tensile direction experienced the highest critical resolved shear stress and transformed first. At higher strains, combined preferential transformation and grain rotation sustained the deformation.

Tirumalassetty *et al.* [82] observed that depending on the stress state of the austenite grains, they can undergo rotation prior to transformation. The rotation angles were found to depend on their crystallographic orientation with respect to the straining direction. The driving force for this rotation was assigned to a lowering of the Schmid factor. Besides transformation to martensite, grain rotation was suggested to play an important role in contributing to the ductility of TRIP steels.

Recently, in-situ synchrotron experiments on Q&P steels have been started with the aim to study the influence of grain size, carbon content and crystallographic orientation on austenite stability [88, 89].

I.4. Recent developments for approaching the targets of the third generation of advanced high-strength sheet steels

The first generation AHSS concepts were developed in lean compositions and ferritic-based multi-phase microstructures, cfr. Introduction Figure 1. The second generation were austenitic steel grades which were highly alloyed resulting in a significant cost increase. Therefore, the third generation AHSS was investigated to cover the property range between the first and second generation reducing the alloying levels of the second generation.

So far, no steel exists that meets all the requirements of combinations of strength and formability of the third generation if the strength criteria include not only tensile strength, but also yield strength and if the concept of formability includes uniform elongation as well as hole expansion. Nevertheless, there are several prospective candidates that demonstrate high combinations of strength and formability.

I.4.1. Modified TRIP steels

Matsumura *et al.* [90, 91] investigated high-C grades with properties approaching those of third generation AHSS. Grain refinement by micro-alloying [92, 93] has also been investigated as a possible way to achieve higher strength levels (1GPa) and high ductility (20% total elongation). Other studies [94] focussed on changing the isothermal holding temperature after full austenitisation. Decreasing this temperature resulted in a higher strength at the expense of ductility with less strain hardening.

I.4.2. Ultrafine bainite

Ultrafine bainite [95, 96] is produced by long isothermal holding at temperatures in the range between 125°C – 325°C. For industrial purposes, this isothermal holding time is too long and therefore further work [97] was conducted on improving the bainite transformation kinetics. A fine-scale (nm) microstructure and absence of large blocks of untransformed austenite lead to an excellent combination of strength and toughness.

I.4.3. Rapid heating and cooling

Flash processing [98] with very high heating and cooling rates has been investigated to refine the microstructure. Lolla *et al.* [99] observed after flash processing a distribution of

large and small carbides which were suggested to be undissolved and inherited from the prior microstructure due to the very high heating rates and short austenitisation times. Besides, a fine microstructure of the prior austenite grains was obtained. It has been postulated that the incomplete dissolution of carbides and non-homogeneous redistribution of carbon leads to a complex interaction of recrystallization and austenitisation [100-103] resulting in a fine austenitic microstructure and different transformation products. If an industrial applicable heat treatment line is possible, a new way of producing steel with a combination of high strength and ductility levels will be opened.

I.4.4. Medium Mn-steel

Merwin *et al*. [104-107] proposed an alternative way to produce a duplex ferrite-austenite microstructure with medium manganese (4-10 wt.%) and low carbon (0.1 wt.%) levels. These levels are higher than conventional TRIP and lower than TWIP steels. Reverse transformation of martensite to austenite and manganese partitioning at the intercritical annealing temperatures results in an ultrafine microstructure consisting of ferrite, high-manganese austenite which is retained at room temperature, and possibly martensite. The mechanical properties are extremely sensitive to the annealing temperature reducing the processing window. Austenite fractions up to 17-38% were measured resulting in a pronounced strain hardening behaviour. The ductility did not correlate directly with the total amount of retained austenite, but also depended on its stability. The unstable portions of austenite, as well as very stable film-type austenite do not contribute to TRIP effect. Medium Mn-steels with strength below 1200MPa have good elongation. At higher strength levels, which was achieved through a higher fraction of martensite, elongation decreases drastically below 10% [104, 105]. The mechanisms contributing to ductility are combinations of TRIP and TWIP.

I.4.5. Quenching and Partitioning

New ways of processing Q&P are recently being proposed as interesting routes to obtain the desired mechanical properties e.g. by conducting intercritical annealing after Q&P to stabilize the austenite laths by reversion [108], by pre-quenching prior to Q&P to refine the microstructure [109], by dynamical partitioning resulting in austenite with inhomogeneous C-distributions and a more homogeneous transformation during straining (high strain hardening) compared to normal Q&P [21], by adding Nb to have grain refinement and an additional precipitation strengthening [110-112] , etc…

I.5. Conclusions

No clear relationship between the retained austenite fraction, its carbon content, and the resulting mechanical properties was found in the literature for Q&P steel. Besides, non-ideal partitioning conditions were observed experimentally. As a consequence, more fundamental research is required to understand the coupling of microstructural evolution during partitioning related to austenite decomposition and partitioning kinetics, and ensuing mechanical properties of Q&P steel.

To understand the deformation behaviour which connects the microstructural evolution with the mechanical properties, the response of the microstructure under different loading conditions needs to be studied. In TRIP-steels a lot of research was conducted on the parameters influencing austenite stability focussing mainly on the carbon content in austenite, grain size and crystallographic orientation. In Q&P steel, little information regarding the parameters influencing the austenite stability is known. Research on the influence of % C, grain size and morphology is on-going. However, data concerning the effect of the surrounding phases on the microstructural response as austenite stability are still lacking.

The exact mechanism of austenite stabilisation is still an issue. Some studies were conducted on interface movement, but direct evidences like in-situ experimental observations of the austenite–martensite interface movement during partitioning are still missing. Experimental evidence of interface movement will provide fundamental information regarding the activation energy and hence the underlying mechanisms of carbon partitioning.

References

1. M. Cohen, G. B. Olson, and W. S. Owen: 'Martensite: A tribute to morris cohen', 1992, ASM International.
2. D. A. Porter, K. E. Easterling, and M. Sherif: 'Phase transformations in metals and alloys, third edition (revised reprint)', 2009, Taylor & Francis.
3. M. Sarikaya, G. Thomas, J. W. Steeds, S. J. Barnard, and G. D. W. Smith: 'Solute element partitioning and austenite stabilization in steels ', International conference on solid to solid phase transformations, 1982, Warrendale, 1421-1425.
4. M. F. Gallagher, J. Speer, D. K. Matlock, and N. M. Fonstein: 'Microstructure development in trip-sheet steels containing si, al and p', 44th Mechanical Working and Steel conference, 2002, Warrendale, 153-172.
5. J. G. Speer, D. K. Matlock, B. C. De Cooman, and J. G. Schroth: 'Carbon partitioning into austenite after martensite transformation', *Acta Materialia*, 2003, **51**, 2611-2622.

6. J. G. Speer, D. V. Edmonds, F. C. Rizzo, and D. K. Matlock: 'Partitioning of carbon from supersaturated plates of ferrite, with application to steel processing and fundamentals of the bainite transformation', *Materials Science*, 2004, **8**, 219-237.

7. J. G. Speer, F. C. R. Assunção, D. K. Matlock, and D. V. Edmonds: 'The "quenching and partitioning" process: Background and recent progress', *Materials Research*, 2005, **8**, 417-423.

8. A. J. Clarke, J. G. Speer, M. K. Miller, R. E. Hackenberg, D. V. Edmonds, D. K. Matlock, F. C. Rizzo, K. D. Clarke, and E. D. Moor: 'Carbon partitioning to austenite from martensite or bainite during the quench and partition process: A critical assessment', *Acta Materialia*, 2008, **56**, 16-22.

9. A. J. Clarke, J. G. Speer, D. K. Matlock, F. C. Rizzo, D. V. Edmonds, and M. J. Santofimia: 'Influence of carbon partitioning kinetics on final austenite fraction during quenching and partitioning', *Scripta Materialia*, 2009, **61**, 149-152.

10. M. Hillert and J. Agren: 'On the definitions of paraequilibrium and orthoequilibrium', *Scripta Materialia*, 2004, **50**, 697-699.

11. J. A. Lobo and G. H. Geiger: 'Thermodynamics and solubility of carbon in ferrite and ferritic fe-mo alloys', *Metallurgical Transactions A*, 1976, **7A**, 1347-1357.

12. J. A. Lobo and G. H. Geiger: 'Thermodynamics of carbon in austenite and fe-mo austenite', *metallurgical Transactions A*, 1976, **7A**, 1359-1364.

13. N. Zhong, X. Wang, Y. Rong, and L. Wang: 'Interface migration between martenisite and austenite during quenching and partitioning (q&p) process', *Materials Science and Technology*, 2006, **22**(6), 4.

14. J. G. Speer, R. E. Hackenberg, B. C. De Cooman, and D. K. Matlock: 'Influence of interface migration during annealing of martensite/austenite mixtures', *Philosophical Magazine Letters*, 2007, **87**(6), 379-382.

15. M. J. Santofimia, L. Zhao, and J. Sietsma: 'Model for the interaction between interface migration and carbon diffusion during annealing of martensite–austenite microstructures in steels', *Scripta Materialia*, 2008, **59**(2), 159-162.

16. M. J. Santofimia, J. G. Speer, A. J. Clarke, L. Zhao, and J. Sietsma: 'Influence of interface mobility on the evolution of austenite–martensite grain assemblies during annealing', *Acta Materialia*, 2009, **57**, 4548-4557.

17. J. W. Christian: 'Chapter 21 - characteristics of martensitic transformations', in 'The theory of transformations in metals and alloys', (ed. J. W. Christian), 961-991; 2002, Oxford, Pergamon.

18. C. A. Apple, R. N. Caron, and G. Krauss: 'Packet microstructure in fe-0.2c pct c martensite', *MT*, 1974, **5**(3), 593-999.

19. Y. Takahama, M. J. Santofimia, M. G. Mecozzi, L. Zhao, and J. Sietsma: 'Phase field simulation of the carbon redistribution during the quenching and partitioning process in a low-carbon steel', *Acta Materialia*, 2012, **60**(6–7), 2916-2926.

20. Y. Toji, H. Matsuda, M. Herbig, P.-P. Choi, and D. Raabe: 'Atomic-scale analysis of carbon partitioning between martensite and austenite by atom probe tomography and correlative transmission electron microscopy', *Acta Materialia*, 2014, **65**(0), 215-228.

21. X. Tan, Y. Xu, X. Yang, Z. Liu, and D. Wu: 'Effect of partitioning procedure on microstructure and mechanical properties of a hot-rolled directly quenched and partitioned steel', *Materials Science and Engineering: A*, 2014, **594**(0), 149-160.

22. D. P. Koistinen and R. E. Marburger: 'A general equation prescribing extend of austenite-martensite tranformation in pure fe-c alloys and plain carbon steels', *Acta Materialia*, 1959, **7**, 59.

23. S. M. C. van Bohemen: 'The bainite and martensite start temperature calculated with an exponential carbon dependence', *Materials Science and Technology*, 2012, **28**(4), 487-495.

24. D. V. Edmonds, K. He, F. C. Rizzo, B. C. D. Cooman, D. K. Matlock, and J. G. Speer: 'Quenching and partitioning martensite—a novel steel heat treatment', *Materials Science and engineering*, 2006, **438-440**, 25-34.

25. M. J. Santofimia, T. Nguyen-Minh, L. Zhao, R. Petrov, I. Sabirov, and J. Sietsma: 'New low carbon q&p steels containing film-like intercritical ferrite', *Materials Science and engineering*, 2010, **527**, 6429-6439.

26. H. Y. Li, X. W. Lu, X. C. Wu, Y. A. Min, and X. J. Jin: 'Bainitic transformation during the two-step quenching and partitioning process in a medium carbon steel containing silicon', *Materials Science and engineering*, 2010, **527**, 6255-6259.

27. S. Chupatanakul and P. Nash: 'Dilatometric measurement of carbon enrichment in austenite during bainite transformation', *J Mater Sci*, 2006, **41**, 4965–4969.

28. S. M. C. van Bohemen, M. J. Santofimia, and J. Sietsma: 'Experimental evidence for bainite formation below ms in fe–0.66c', *Scripta Materialia*, 2008, **58**(6), 488-491.

29. S. S. Nayak, R. Anumolu, R. D. K. Misra, K. H. Kim, and D. L. Lee: 'Microstructure–hardness relationship in quenched and partitioned medium-carbon and high-carbon steels containing silicon', *Materials Science and engineering*, 2008, **498**, 442-456.

30. E. De Moor, S. Lacroix, A. J. Clarke, J. Penning, and J. Speer: 'Effect of retained austenite stabilized via quenching and partitioning on the strain hardening of martensitic steels', *Metallurgical and Materials Transactions A*, 2008, **39A**, 2586-2595.

31. G. Thomas, J. G. Speer, D. Matlock, and J. Michael: 'Application of electron backscatter diifraction techniques to quenched and partitioned steels', *Microscopy and Microanalysis*, 2011, **17**, 368-373.

32. C. Y. Wang, J. Shi, W. Q. Cao, and H. Dong: 'Characterization of microstructure obtained by quenching and partitioning process in low alloy martensitic steel', *Materials Science and engineering*, 2010, **527**, 3442-3449.

33. C. Zhao, D. Tang, H.-T. Jiang, S.-S. Jhao, and H. Li: 'Process simulation and microstructure analysis of low carbon si-mn quenched and partitioned steel', *Journal of Iron and Steel Research, International*, 2008, **15**(4), 82-85.

34. T. D. Bigg, D. V. Edmonds, and E. S. Eardley: 'Real-time structural analysis of quenching and partitioning (q&p) in an experimental martensitic steel', *Journal of Alloys and Compounds*, 2013, **577, Supplement 1**(0), S695-S698.

35. E. De Moor, C. Föjer, J. Penning, A. J. Clarke, and J. G. Speer: 'Calometric study of carbon partitioning from martensite into austenite', *Physical Review B*, 2010, **82**, 104-210.

36. S. J. Barnard, G. D. W. Smith, M. Sarikaya, and G. Thomas: 'Carbon atom distribution in a dual phase steel: An atom probe study', *Scripta Metallurgica*, 1981, **15**(4), 387-392.

37. F. G. Caballero, M. K. Miller, A. J. Clarke, and C. Garcia-Mateo: 'Examination of carbon partitioning into austenite during tempering of bainite', *Scripta Materialia*, 2010, **63**(4), 442-445.

38. M. Gouné, F. Danoix, S. Allain, and O. Bouaziz: 'Unambiguous carbon partitioning from martensite to austenite in fe–c–ni alloys during quenching and partitioning', *Scripta Materialia*, 2013, **68**(12), 1004-1007.

39. D. Kim, J. G. Speer, and B. C. De Cooman: 'Isothermal transformation of a cmnsi steel below the ms temperature', *Metallurgical and Materials Transactions A*, 2010, **42**, 1575-1585.

40. H. K. Dong, J. G. Speer, and H. S. Kim: 'Observation of an isothermal transformation during quenching and partitioning processing', *Metallurgical and materials transactions A- Physical metallurgy and materials science*, 2009, **40A**, 2048-2060.

41. D. Kim, J. G. Speer, and B. C. De Cooman: 'The isothermal transformation of low-alloy low-c cmnsi steels below ms', *Materials Science Forum*, 2010, **654-656**, 98-101.

42. D. V. Edmonds, D. K. Matlock, and J. G. Speer: 'The recent development of steels with carbide-free acicular microstructures containing retained austenite', *Metallugia Italiana*, 2011, **1**, 41-49.

43. G. R. Speich and W. C. Leslie: 'Tempering of steel', *MT*, 1972, **3**(5), 1043-1054.

44. F. L. H. Gerdemann: 'Microstructure and hardness of 9260 steel heat-treated by the quenching and partitioning process', Aachen University of Technology, Germany, 2004.

45. H. Y. Li, X. W. Lu, W. J. Li, and X. J. Jin: 'Microstructure and mechanical properties of an ultrahigh-strength 40simnnicr steel during the one-step quenching and partitioning process', *Metallurgical and Materials Transactions A*, 2010, **41**(5), 1284-1300.

46. F. L. H. Gerdemann: 'Microstructure and hardness of 9260 steel heat-treated by the quenching and partitioning process ', Aachen University of Technology, Germany, 2004.

47. W. S. Owen: 'The effect of silicon on the kinetics of tempering', *Transactions of the ASM*, 1954, **46**, 812-828.

48. L. Chang and G. D. W. Smith: 'The silicon effect in the tempering of martensite in steels', *Journal de Physique*, 1984, **45**, 397-401.

49. M. J. Santofimia, L. Zhao, R. Petrov, C. Kwakernaak, W. G. Sloof, and J. Sietsma: 'Microstructural development during the quenching and partitioning process in a newly designed low-carbon steel', *Acta Materialia*, 2011, **59**, 6059-6068.

50. M. Oka and H. Okamoto: 'Swing back in kinetics near ms in hypereutectoid steels', *Metallurgical Transactions a-Physical Metallurgy and Materials Science*, 1988, **19**(3), 447-452.

51. C. H. Shih, B. L. Averbach, and M. Cohen: 'Some characteristics of the isothermal martensitic transformation', *Transactions of the American Institute of Mining and Metallurgical Engineers*, 1955, **203**(1), 183-187.

52. S. R. Pati and M. Cohen: 'Nucleation of the isothermal martensitic transformation', *Acta Metallurgica*, 1969, **17**(3), 189-199.

53. R. T. Howard and M. Cohen: *Transactions of the American Institute of Mining and Metallurgical Engineers*, 1948, **176**, 384-400.

54. A. Borgenstam and M. Hillert: 'Activation energy for isothermal martensite in ferrous alloys', *Acta Materialia*, 1997, **45**(2), 651-662.

55. S. Morito, H. Tanaka, R. Konishi, T. Furuhara, and T. Maki: 'The morphology and crystallography of lath martensite in fe-c alloys', *Acta Materialia*, 2003, **51**(6), 1789-1799.

56. V. F. Zackay, E. R. Parker, D. Fahr, and R. Bush: *Trans. ASM*, 1967, **60**, 252.

57. F. Marketz and F. D. Fischer: 'A mesoscale study on the thermodynamic effect of stress on martensitic transformation', *Metallurgical and Materials Transactions A*, 1995, **26**(2), 267-278.

58. G. W. Greenwood and R. H. Johnson: 'The deformation of metals under small stresses during phase transformations', *Proceedings of the Royal Society of London. Series A. Mathematical and Physical Sciences*, 1965, **283**(1394), 403-422.

59. E. Jimenez-Melero, N. H. van Dijk, L. Zhao, J. Sietsma, J. P. Wright, and S. van der Zwaag: 'In situ synchrotron study on the interplay between martensite formation, texture evolution and load partitioning in low-alloyed trip steels', *Materials Science and Engineering: A*, 2011, **528**(21), 6407-6416.

60. J. Jung, H. Kim, and B. C. De Cooman: 'Yielding behavior of nb micro-alloyed c-mn-si trip steel studied by in-situ synchrotron x-ray diffraction', *ISIJ International*, 2010, **50**(4), 620-629.

61. S. Cheng , X. Wang, Z. Feng, C. B., H. Choo, and P. Liaw: 'Probing the characteristic deformation behaviors of transformation-induced plasticity steels', *Metallurgical and Materials Transactions A*, 2008, **39A**, 3105-3112.

62. O. Muransky, P. Sittner, J. Zrnik, and E. C. Oliver: 'In situ neutron diffraction investigation of the collaborative deformation-transformation mechanism in trip-assisted steels at room and elevated temperatures', *Acta Materialia*, 2008, **56**(14), 3367-3379.

63. H. K. D. H. Bhadeshia: 'Trip-assisted steels?', *ISIJ International*, 2002, **42**, 1059-1060.

64. P. J. Jacques, E. Girault, A. Mertens, B. Verlinden, J. Van Humbeeck, and F. Delannay: 'The developments of cold-rolled trip-assisted multiphase steels. Al-alloyed trip-assisted multiphase steels', *ISIJ international*, 2001, **41**(9), 1068-1074.

65. X. D. Wang, Z. H. Guo, and Y. H. Rong: 'Mechanism exploration of an ultrahigh strength steel by quenching-partitioning-tempering process', *Materials Science and engineering*, 2010.

66. A. Dimatteo, G. Lovicu, R. Valentini, M. DeSanctis, and M. R. Pinasco: 'The strain-hardening behaviour of q&p steels', 2010.

67. E. De Moor, J. G. Speer, D. K. Matlock, J.-H. Kwak, and S.-B. Lee: 'Effect of carbon and manganese on the quenching and partitioning response of cmnsi steels', *ISIJ International*, 2011, **51**, 137-144.

68. R. Blondé, E. Jimenez-Melero, L. Zhao, J. P. Wright, E. Brück, S. van der Zwaag, and N. H. van Dijk: 'High-energy x-ray diffraction study on the temperature-dependent mechanical stability of retained austenite in low-alloyed trip steels', *Acta Materialia*, 2012, **60**(2), 565-577.

69. N. H. van Dijk, A. M. Butt, L. Zhao, J. Sietsma, S. E. Offerman, J. P. Wright, and S. van der Zwaag: 'Thermal stability of retained austenite in trip steels studied by synchrotron x-ray diffraction during cooling', *Acta Materialia*, 2005, **53**, 5439-5447.

70. E. Jimenez-Melero, N. H. van Dijk, L. Zhao, J. Sietsma, S. E. Offerman, J. P. Wright, and S. van der Zwaag: 'The effect of aluminium and phosphorus on the stability of individual austenite grains in trip steels', *Acta Materialia*, 2009, **57**(2), 533-543.

71. E. Jimenez-Melero, N. H. van Dijk, L. Zhao, J. Sietsma, S. E. Offerman, J. P. Wright, and S. van der Zwaag: 'Characterization of individual retained austenite grains and their stability in low-alloyed trip steels', *Acta Materialia*, 2007, **55**(20), 6713-6723.

72. J. Wang and S. Van Der Zwaag: 'Stabilization mechanisms of retained austenite in transformation-induced plasticity steel', *Metallurgical and Materials Transactions A*, 2001, **32**(6), 1527-1539.

73. I. B. Timokhina, P. D. Hodgons, and E. V. Pereloma: 'Effect of microstructure on the stability of retained austenite in transformation-induced-plasticity steels', *Metallurgical and Materials Transactions A*, 2004, **35**, 2331-2340.

74. E. Jimenez-Melero, N. H. van Dijk, L. Zhao, J. Sietsma, S. E. Offerman, J. P. Wright, and S. van der Zwaag: 'Martensitic transformation of individual grains in low-alloyed trip steels', *Scripta Materialia*, 2007, **56**(5), 421-424.

75. K. Sugimoto, N. Usui, S. Kobayashi, and S. Hashimoto: *ISIJ International*, 1992, **32**(12).

76. J. Chiang, B. Lawrence, J. D. Boyd, and A. K. Pilkey: 'Effect of microstructure on retained austenite stability and work hardening of trip steels', *Materials Science and Engineering: A*, 2011, **528**(13–14), 4516-4521.

77. Timokhina I.B., Hodgons P.D., and P. E.V.: 'Effect of microstructure on the stability of retained austenite in transformation-induced-plasticity steels', *Metallurgical and Materials Transactions A*, 2004, **35**, 2331-2340.

78. D. De Knijf, R. Petrov, C. Föjer, and L. A. I. Kestens: 'Effect of fresh martensite on the stability of retained austenite in quenching & partitioning steel', *Materials Science and engineering A*, 2014, **615**(0), 107-115.

79. P. J. Jacques, J. Ladriere, and F. Delannay: 'On the influence of interactions between phases on the mechanical stability of retained austenite in transformation-induced plasticity multiphase steels', *Metallurgical and Materials Transactions A - Physical Metallurgy and Materials Science*, 2001, **32**(11), 2759-2768.

80. P. Hilkhuijsen, H. J. M. Geijselaers, T. C. Bor, E. S. Perdahcıoğlu, A. H. vd Boogaard, and R. Akkerman: 'Strain direction dependency of martensitic transformation in austenitic stainless steels: The effect of', *Materials Science and Engineering: A*, 2013, **573**(0), 100-105.

81. S. O. Kruijver, L. Zhao, J. Sietsma, S. E. Offerman, N. H. van Dijk, E. M. Lauridsen, L. Margulies, S. Grigull, H. F. Poulsen, and S. van der Zwaag: 'In situ observations on the mechanical stability of austenite in trip steel', *Journal de Physique*, 2003, **IV**(104), 499-502.

82. G. K. Tirumalasetty, M. A. Van Huis, C. Kwakernaak, J. Sietsma, W. G. Sloof, and H. W. Zandbergen: 'Deformation-induced austenite grain rotation and transformation in trip-assisted steel', *Acta Materialia*, 2012, **60**, 1311-1321.

83. A. Itami, M. Takahshi, and K. Ushioda: 'Plastic stability of retained austenite in the cold-rolled 0.14%c-1.9%si-1.7%mn sheet steel', *ISIJ International*, 1995, **35**(9), 1121-1127.

84. L. Samek, E. De Moor, J. Penning, and B. De Cooman: 'Influence of alloying elements on the kinetics of strain-induced martensitic nucleation in low-alloy, multiphase high-strength steels', *Metallurgical and Materials Transactions A*, 2006, **37**(1), 109-124.

85. W. C. Jeong, D. K. Matlock, and G. Krauss: 'Observation of deformation and transformation behavior of retained austenite in a 0.14c-1.2si-1.5mn steel with ferrite-bainite-austenite structure', *Materials Science and Engineering: A*, 1993, **165**(1), 1-8.

86. X. C. Xiong, B. Chen, M. X. Huang, J. F. Wang, and L. Wang: 'The effect of morpholohy on the stability of retained austenite in a quenched and partitioned steel', *Scripta Materialia*, 2013, **68**(5), 321-324.

87. Z. J. Xie, Y. Q. Ren, W. H. Zhou, J. R. Yang, C. J. Shang, and R. D. K. Misra: 'Stability of retained austenite in multi-phase microstructure during austempering and its effect on the ductility of a low carbon steel', *Materials Science and Engineering: A*, 2014, **603**(0), 69-75.

88. T. Rieger, K. Herrmann, D. Carmele, S. Meyer, T. Lippman, A. Stark, W. Bleck, and U. Klemradt: 'Quenching and partitioning - an in-situ approach to characterize he process kinetics and final microstructure of trip-assisted steel', THERMEC, 2011.

89. D. Carmele, T. Rieger, K. Herrmann, S. Meyer, T. Lippman, A. Stark, W. Bleck, and U. Klemradt: 'Very hard synchotron x-ray radiation as an advanced characterization method applied to advanced high strength steels', THERMEC, 2011.

90. O. Matsumura, Y. Sakuma, and H. Takechi: 'Trip and its kinetic aspects in austempered 0.4c-1.5si-0.8mn steel.', *Scripta Metallurgica*, 1987, **27**, 1301–1306.

91. O. Matsumura, Y. Sakuma, Y. Ishii, and J. Zhao: 'Effect of retained austenite on formability of high strength sheet steels', *ISIJ International*, 1992, **32**(10), 1110-1116.

92. M. Zhang, L. Li, R. Y. Fu, D. Krizan, and B. C. De Cooman: 'Continuous cooling transformation diagrams and properties of micro-alloyed trip steels', *Materials Science and Engineering: A*, 2006, **438–440**(0), 296-299.

93. A. Z. Hanzaki, P. D. Hodgson, and S. Yue: 'Hot deformation characteristics of si-mn trip steels with and without nb microalloy additions', *ISIJ International*, 1995, **35**(3), 324-331.

94. K.-i. Sugimoto, T. Iida, J. Sakaguchi, and T. Kashima: 'Retained austenite characteristics and tensile properties in a trip type bainitic sheet steel', *ISIJ International*, 2000, **40**(9), 902-908.

95. F. G. Caballero, M. K. Miller, S. S. Babu, and C. Garcia-Mateo: 'Atomic scale observations of bainite transformation in a high carbon high silicon steel', *Acta Materialia*, 2007, **55**(1), 381-390.

96. F. G. Caballero and H. K. D. H. Bhadeshia: 'Very strong bainite', *Current Opinion in Solid State and Materials Science*, 2004, **8**(3–4), 251-257.

97. H. K. D. H. Bhadeshia, F. García Caballero, and C. García Mateo: 'Acceleration of low-temperature bainite', 2003.

98. A. Arlazarov, G. Lujzn Brollo, and C. Maga: 'Influence of heating rate on the microstructure and mechanical properties of annealed low carbon steels', METAL2014, 2014.

99. T. Lolla, G. Cola, B. Narayanan, B. Alexandrov, and S. S. Babu: 'Developement of rapid heating and cooling (flash processing) process to produce advanced high strength steel microstructures', *Materials Science and Technology*, 2011, **27**(5), 863-875.

100. R. Petrov, J. Sidor, and L. A. I. Kestens: 'Texture formation in high strength low alloy steel reheated with ultrafast heating rates', *Materials Science Forum*, 2012, **702-703**, 798-801.

101. R. Petrov, F. Hajyakbary, J. Sidor, M. J. Santofimia, S. J., and L. A. I. Kestens: 'Ultra-fast annealing of high strength steel', 9th International Congress on Machnies Technologies, Materials (MTM-2012), 2012.

102. R. Petrov, L. Kestens, W. Kaluba, and Y. Houbaert: 'Recrystallization and austenite formation in a cold rolled trip steel during ultra fast heating', in 'Steel Grips', 289-294; 2003.

103. R. Petrov, F. Hajyakbary, j. Sidor, M. J. Santofimia, J. Sietsma, and L. Kestens: 'Ultra-fast annealing of high strength steel', *MTM International Virtual Journal*, 2012(11), 72-81.

104. M. J. Merwin: 'Microstructure and properties of cold rolled and annealed low-carbon manganese trip steels', *Iron & steel technology*, 2008, **5**, 66-84.

105. M. J. Merwin: 'Low-carbon manganese trip steels', *Materials Science Forum*, 2007, **539-543**, 4327.

106. S. W. Lee, K. Y. Lee, and B. C. De Cooman: 'Ultra fine-grained 6wt% manganese trip steel', in 'Materials Science Forum', (eds. J.-F. Nie, et al.), 654-656; 2010.

107. A. Arlazarov, M. Gouné, O. Bouaziz, A. Hazotte, G. Petitgand, and P. Barges: 'Evolution of microstructure and mechanical properties of medium mn steels during double annealing', *Materials Science and Engineering: A*, 2012, **542**(0), 31-39.

108. R. Ding, D. Tang, and A. Zhao: 'A novel design to enhance the amount of retained austenite and mechanical properties in low-alloyed steel', *Scripta Materialia*, 2014.

109. J. Zhang, H. Ding, R. D. K. Misra, and C. Wang: 'Enhanced stability or retained austenite and consequenct work hardening rate through pre-quenching prior to quenching and partitioning in a q&p microalloyed steel', *Materials Science & Engineering A*, 2014.

110. N. Zhong, X.D.Wang, L. Wang, and Y. H. Rong: 'Enhancement of the mechanical properties of a nb-microalloyed advanced high-strength steel treated by quenching–partitioning–tempering process', *Materials Science and engineering*, 2009, **506**, 111-116.

111. Y. Rong, H. Yu, and Z. Shi: 'The design principle and enigneering realization of novel super-high strength q-p-t steels'.

112. X. D. Wang, W. Z. Xu, Z. H. Guo, L. Wang, and Y. H. Rong: 'Carbide characterization in a nb-microalloyed advanced ultrahigh strength steel after quenching–partitioning–tempering process', *Materials Science and engineering*, 2010, **527**, 3373-3378.

CHAPTER II

EXPERIMENTAL MATERIALS AND TECHNIQUES

II. EXPERIMENTAL MATERIALS AND TECHNIQUES

II.1. Experimental material

Low-C and high-C Q&P steel grades were studied in this work. The low-C grade was employed in the whole thesis except in Chapter VI. In this chapter the grain boundary mobility during partitioning was studied inside a TEM. To make this possible, the quenching temperature of the steel should be suppressed until room temperature. This was done by increasing the carbon content of the model Q&P steel and the steel was denominated as high–C Q&P steel.

II.1.1. Casting

The low-C steel grade was produced as a 100 kg ingot with a nominal composition of 0.25C-1.5Si-3Mn (wt. %) in a laboratory vacuum induction furnace. The actual chemical composition determined with a combination of techniques - X-ray fluorescence (XRF), inductively coupled plasma mass spectrometry (ICP-MS) and inductively coupled plasma optical emission spectrometry (ICP-OES) - is given in Table II-1.

Table II-1: Chemical composition of the steel studied (*: below the detection limit)

%C	% Mn	% Si	% P	% Al	% Ti	% Nb	% Cu	% Cr	% Ni	% W	% Sn	% Mo	% Zr	% V
0.248	2.8	1.5	0.0019	0.021	0.0006	< *	0.0033	0.0086	0.0073	0.0023	0.0012	0.0005	0.0002	0.0008

The high-C steel grade was produced according to the same method with a nominal composition of 1C-1.5Si-3Mn (wt.%).

II.1.2. Rolling

After casting, steel blocks with a thickness of 40 mm were heated to 1250°C and hot rolled to a final thickness of 2.5 mm in 7 reduction passes according to the schedule given in Table II-2. Next, the sheets were accelerated cooled by water jets to 600°C and transferred to a furnace for coiling simulations at 560°C.

Table II-2: Hot rolling schedule with 7 reduction passes after reheating to 1250°C

Temperature	**1200°C**	**1150°C**	**1100°C**	**1050°C**	**1000°C**	**950°C**	**900°C**
Reduction	40%	40%	38%	30%	27%	25%	25%

The low-C hot rolled sheets were pickled and cold rolled to a thickness of 1 mm imposing a total reduction in thickness of 60%.

II.1.3. Heat treatments

Dilatometer experiments were carried out in a Bähr DIL 805 A/D dilatometer on hot rolled rectangular samples. The samples had dimensions of 2.5 x 3.5 x 10 mm with the longest axis parallel to the sheet rolling direction.

Strips of the cold-rolled sheets were subjected to Q&P thermal treatments in a Gleeble™ 3500 thermo-mechanical simulator. The temperature variations along the heat treated length of the samples were in the range of 10°C. This approach ensures enough large standard size samples with homogeneous heat treated zone for tensile tests.

II.2. Microstructural and mechanical characterization

II.2.1. Microstructural characterization techniques applied to Q&P steel to resolve the different phase fractions

Wide accepted opinion is that the austenite plays a crucial role in enhancing ductility of Quenching and Partitioning (Q&P) steel by transforming to martensite under strain [1-5]. Hence the qualitative and quantitative characterization of austenite (and its surrounding microstructure) is important to understand the link between mechanical properties and microstructure. Well-known and new techniques to characterize austenite are discussed and compared with respect to their resolution and reliability ranging from optical microscopy (OM), scanning electron microscopy (SEM), electron backscattered diffraction (EBSD), X-ray diffraction (XRD), transmission electron microscopy (TEM) and transmission Kikuchi diffraction (TKD-SEM). A link to correlate the retained austenite fractions obtained from XRD and EBSD experiments was proposed.

II.2.1-1 Introduction

In 2008, the first Q&P steels were characterized by means of optical microscopy, scanning and transmission electron microscopy, X-ray diffraction and magnetic measurements [1, 6, 7]. The resolution of optical microscopy is below the requirement to resolve fine austenite grains and depending on the used etchant, fresh martensite could not be distinguished from the austenite [6]. Hence by using this technique to determine the volume fraction of retained austenite, an underestimation by not resolving the fine austenite or overestimation by wrongly assigning fresh martensite as austenite was obtained as compared to other quantitative methods as X-ray diffraction and magnetic measurements [6]. SEM was used to study the martensite laths and carbide precipitation conditions whereas TEM resolved interlath austenite (in the range of 10 nm) but with a very low statistical relevance.

From 2010 on, EBSD started to become a currently used technique to study the microstructure of Q&P steel [8-12]. It is a very powerful technique to resolve larger (µm-range) austenite grains and to study the morphology of martensite. A trade-off between resolution and statistical relevance exists with this technique. Moreover, part of the retained austenite lying between the martensite laths is hardly detectable [1].

Transmission Kikuchi diffraction (TKD-SEM) was proposed by Keller and Geiss [13] to offer better spatial resolution than conventional EBSD [14]. This powerful method was proven to resolve nano-austenite grains by a more convenient technique than TEM.

An accurate description of the microstructure is essential for better understanding of its formation and control of the final properties. Therefore, in this work different characterization techniques were employed to resolve and quantify the retained austenite of the *same* Q&P sample (QT = 224°C, PT = 400°C, Pt = 500s). The samples for microstructural characterization were prepared by mechanical grinding and polishing following the classical preparation routes.

II.2.1-2 Optical microscopy

For optical microscopy, 2% Nital etching for 10s and a colour etchant, LePera [15] were applied. The latter consists of 4% picral and 1% sodium metabisulphite in a 2:3 proportion. The sample was immersed for 20s, rinsed with methanol and finally dried with compressed air. With this etchant the fresh martensite and austenite appear in white colour [6], the tempered martensite and ferrite phases are mostly coloured orange-brown [6] and the darker phases are assigned to bainite and/or pearlite [15]. The microstructures were analysed by bright field light optical microscopy as illustrated in Figure II-1.

Nital-etching, cfr. Figure II-1(a), reveals martensite laths formed during the first quenching (TM), and large retained austenite (RA) and fresh martensite (FM) as white equiaxed grains. The difference in grey-intensity is related to their etching response. Tempered martensite is etched more than the retained austenite and the high-carbon untempered, blocky martensite [4, 16].

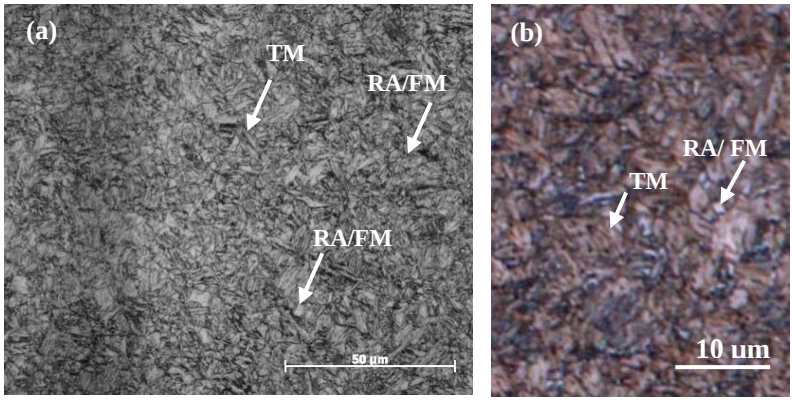

Figure II-1: (a) 2% Nital etch (b) LePera etch highlighting the retained austenite (RA), tempered martensite (TM) and fresh martensite (FM)

LePera etching colours retained austenite and possibly fresh martensite formed during final quenching white, and tempered martensite laths brown/grey, cfr. Figure II-1(b). From these pictures, the fraction of retained austenite and possibly fresh martensite was estimated to be 5.9% with an average grain size of 0.7µm in diameter, determined with ImageJ™ software based on a threshold value for the brightness. The smallest reliable grain size was set at 0.1µm² to avoid artefacts. This fraction represents the RA and FM grains with diameters larger than 0.3µm as calculated with respect to the resolution of the optical microscope. The reliability and reproducibility of this technique is relatively low due to the determination of the threshold value and etching response [6].

II.2.1-3 X-ray diffraction

The volume fractions of austenite at room temperature and the average carbon contents were determined from X-ray diffraction (XRD) experiments performed on a Siemens Kristalloflex D5000 diffractometer equipped with Mo-K_α source operating at 40kV and 40mA. A 2θ-range of 0° to 45° was scanned using step sizes between 0.01° and 0.02°, dwell-times of 1-2s and a rotation speed of 15rpm. This 2θ-range contains the (111), (200), (220) and (311) fcc reflections and the (110), (200), (211) bcc reflections. The data were post-processed by subtracting the background radiation and $K\alpha_2$ influence.

Austenite fractions were calculated by the formula of Cullity [17] and the austenite lattice parameter a_γ is determined from the extrapolation function of the lattice parameter vs. $\cos^2(\theta)/\sin(\theta)$ of the (200), (220) and (311) austenite peaks [8, 18]. The carbon concentration x_C was obtained from the following well-accepted equation [8, 19]: $a_\gamma = 0.3556 + 0.00453x_C + 0.000095x_{Mn}$ where a_γ is the austenite lattice parameter in nm and, x_C and x_{Mn} are the concentrations of carbon and manganese in austenite in wt. %. If paraequilibrium conditions are assumed, no diffusion of manganese during partitioning occurs and the average manganese content in the steel can be used. The equation does not include silicon since the literature contains limited data about its effect on the lattice parameter of austenite. Besides, the silicon has a negligible effect on the lattice parameter compared to carbon.

The wavelength of X-rays determines the resolution of the system through Bragg's law [17]. The used Mo-K_α source can resolve lattices with a spacing of 0.036nm. The detectable size and volume fraction of retained austenite are in the range of 10 Å and 0.5 vol.% respectively [20]. The austenite fraction was calculated from the diffraction pattern in Figure II-2 as 20.6 ± 0.4%. Besides, additional information regarding its carbon content, being 1.25 ± 0.1wt.% can be obtained. Because of the high resolution, it determines the RA fraction highest of all techniques due to a favourable combination of statistical and spatial reliability.

The difference between the retained austenite fractions determined with optical microscopy (5.9%) and XRD (20.6%) suggests that most of the austenite is present as small or interlath grains which require techniques with higher resolution.

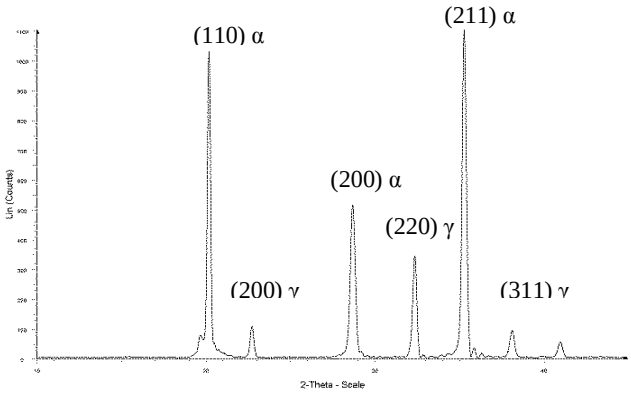

Figure II-2: X-ray diffraction pattern with indication of the austenite and martensite peaks

II.2.1-4 Scanning electron microscopy

Scanning electron microscopy analysis was carried out by means of a FEI Quanta™ 450-FEG (field emission gun)-SEM. The images were acquired with an accelerating voltage of 20 kV and a spot size of 5 nm. This technique can be used to identify the phases of a microstructure and to provide additional information regarding the morphology of the constituents as shown in Figure II-3 for Q&P steel.

Tempered martensite (TM) and carbides can be distinguished [9]. Retained austenite (RA) and fresh martensite (FM) on the other hand are less susceptible to 2% Nital etching. Consequently, they can be identified as the constituents lying topographically higher in the image [4, 16]. Nevertheless, substructures can be resolved inside the fresh martensite grains [9, 21]. Based on these micrographs, the separation of the phases is difficult and hence it is not straightforward to quantify the fractions.

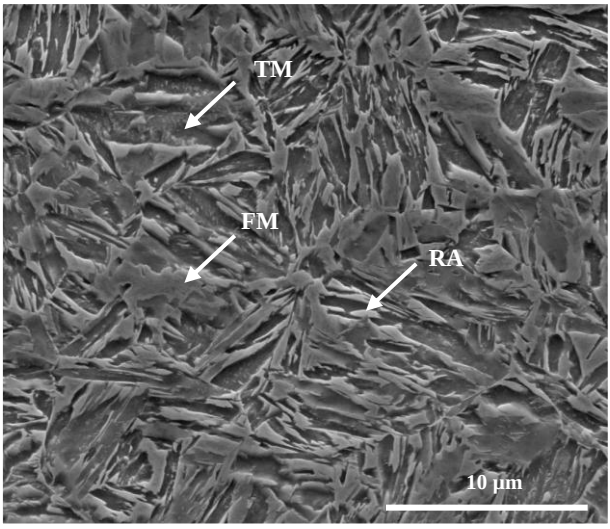

Figure II-3: SEM image of Q&P steel with retained austenite (RA), tempered martensite (TM) and fresh martensite (FM)

II.2.1-5 Electron Backscattered Diffraction

Electron backscattered diffraction (EBSD) analysis were carried out by means of a FEI Quanta™ 450-FEG-SEM equipped with a Hikari detector controlled by the EDAX-TSL OIM-Data Collection version 6.2® software. The EBSD data were acquired on a hexagonal scan grid using an accelerating voltage of 20 kV, a working distance of 16 mm and tilt angle of 70°. The orientation data were post-processed with TSL-OIM Analysis 6.2® software.

The raw data were cleaned according to the following procedure. First, a *confidence index* (*CI) standardization* with a minimum grain size of 4 pixels was applied. This clean up algorithm changes the CI of all points in a grain to the maximum CI found among all points belonging to that grain. Afterwards, the *neighbour CI correlation* algorithm was employed, which implies that if a particular point has a CI below 0.1 then the CI of the nearest neighbours are checked to find the neighbour with the highest CI. The orientation and CI of the particular point are reassigned to match the orientation and CI of the neighbour with the maximum CI. Finally, if the majority of neighbours of a particular grain smaller than 4 pixels with a grain tolerance angle of 5° belong to the same grain, then the orientation of the particular grain is changed to match that of the majority grain, i.e. a *grain dilation* algorithm was applied.

The austenite fraction determined with EBSD on three different areas with a step size of 60 nm was 14.3 ± 1.4%. By the clean-up procedure, austenite grains smaller than 1.44 µm² were removed in the scan. Hence, about 5% of the reference austenite fraction, determined with XRD, is lost with this technique.

EBSD measurements can be performed with (cfr. Figure II-4) or without (cfr. Figure II-5) electrolytic polishing. Electrolytic polishing is advisable for conducting EBSD measurements since it removes the deformed surface layer after mechanical polishing which could give bad Kikuchi patterns. However in multi-phase material, the response of the different components upon this mild etching differs, resulting in surface roughness. This surface relief leads to misindexed points close to the irregularities by shadowing part of the phosphorus screen which detects the diffracting Kikuchi bands under an angle of 20° with respect to the sample's surface. Since small interlath austenite grains between the martensite laths are usually present in Q&P steel [1, 5, 22], their detection is often difficult by the unevenness. This is illustrated in Figure II-4 by the grains inside the white boxes.

If the material is only mechanically polished with a colloidal silica suspension (OP-U), almost no surface relief (Figure II-5(a)) is observed. To remove the deformation induced by the previous grinding and polishing steps, this final step needs to be done with low pressure and for a sufficient long time (20-40 min). As a consequence, the EBSD measurement resolves the austenite laths and smaller grains better as can be seen from the uncleaned phase map in Figure II-5(b). The Kurdjumov-Sachs orientation relationship $\{110\}_{\alpha}$ // $\{111\}_{\gamma}$ also describes the orientation relation between small austenite grains and the matrix reliably in the uncleaned scan suggesting that these austenite data points are real.

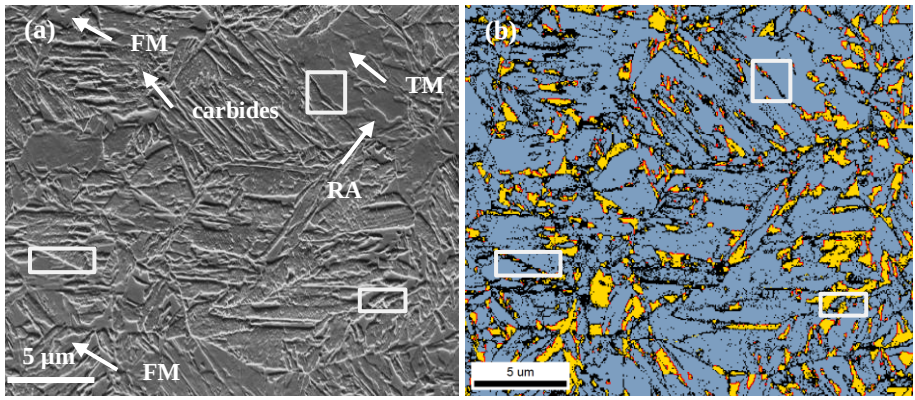

Figure II-4: (a) SEM image after electrolytic polishing with indication of retained austenite (RA), fresh martensite (FM), tempered martensite (TM) and carbides (b) uncleaned phase map with yellow fcc and blue bcc, in red are shown axis- angle grain boundaries that fulfil the Kurdjumov-Sachs orientation relationship

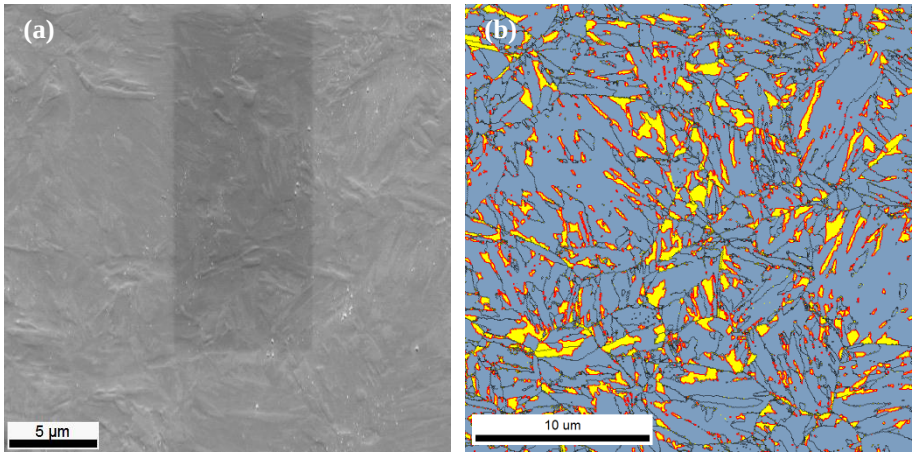

Figure II-5: (a) SEM image after OP-U polishing (b) uncleaned phase map with yellow and blue representing the fcc and bcc phase respectively, red illustrates the Kurdjumov-Sachs orientation relationship

Next to sample preparation, the quality of the EBSD scan is determined by the setting parameters. The accelerating voltage and spot size determine the quality of the pattern. Also the actual step size of the scan defines the reliability of the detection of small austenite grains. Choosing the step size for an EBSD measurement is a trade-off between statistics and resolution, depending on the aimed result. The step size could be set at very low values which should be able to resolve fine austenite grains. However the best spatial resolution in EBSD is between 20 nm and 40 nm because it is affected by the interaction volume between the primary electrons and the sample [14]. When analysing a sample with small grains or sub-grains, the patterns of two grains could overlap resulting in bad indexation and a lower

achievable spatial resolution. Therefore, TEM and TKD-SEM can give better information regarding the remaining 5% interlath austenite.

II.2.1-6 Transmission Electron Microscopy

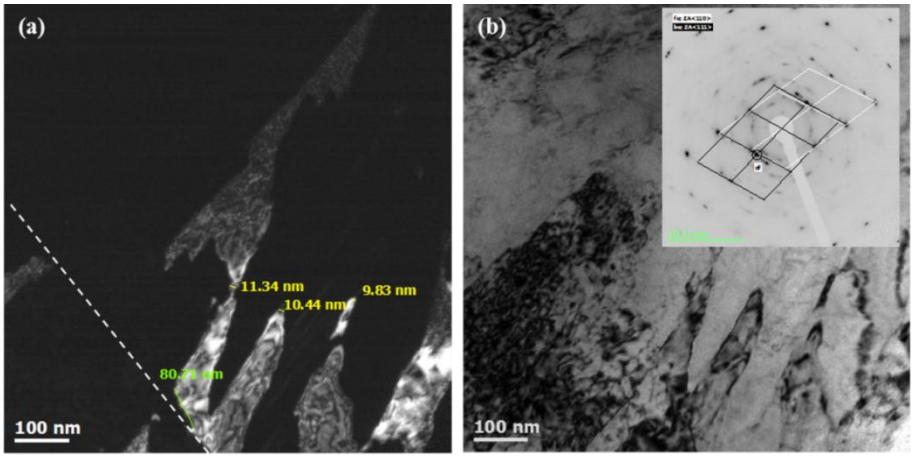

Figure II-6: (a) Dark field image of retained austenite (b) corresponding bright field image with the diffraction pattern

Transmissions electron microscopy foils were prepared by thinning the sample to 0.08mm by grinding with SiC papers. The punched disks were twin-jet electropolished using a 4% perchloric acid solution with a 20 V potential at room temperature. A JEOL JEM-2200FS high resolution TEM was used for the characterization. Figure II-6 (a) and (b) illustrate a bright field and corresponding dark field image of interlath retained austenite. The advantage of TEM is that it resolves the retained austenite to several nm but the timeframe required to make a statistical estimation of the retained austenite fraction is very large.

II.2.1-7 Transmission Kikuchi Diffraction

TEM foils and FIB-samples were also analysed by transmission Kikuchi diffraction (TKD-SEM) in the FEI Quanta™ 450-FEG-SEM. The transmission data were acquired with a spot size of 5 nm, an accelerating voltage of 30 kV, a working distance of 6 mm and a tilt angle of -10°. The orientation data were post-processed with TSL-OIM Analysis 6.2® software. For these measurements, the clean-up procedure was different from the standard EBSD measurements. In general the confidence index of the TKD scans is lower than acquired with standard EBSD. Hence a *neighbour CI correlation* procedure was applied with a minimum CI of 0.05 instead of 0.1 for a standard EBSD scan. Besides, the minimum grain size retained in the scan was increased to e.g. 7 pixels depending on the step size (typically 10-20nm) used.

Transmission Kikuchi Diffraction in a scanning electron microscope has significantly better spatial resolution than conventional EBSD, enabling to characterize nano-sized austenite grains. The used parameters were optimized with respect to the step size, accelerating voltage and working distance to maximize the resolution [23]. Because of the geometry of this technique, the lateral spatial resolution of TKD is one order of magnitude better than conventional EBSD. Since forward-scattered beams scatter among small angles, many high-energy electrons reach the exit surface reducing the interaction volume. The resolution of the technique can be estimated in the range of 5 nm to 10 nm [14]. The angular resolution of TKD [24] i.e. the accuracy with which the relative orientation between adjacent data points within the same crystal can be determined, is similar to EBSD [24, 25] and is between 0.5° and 1°.

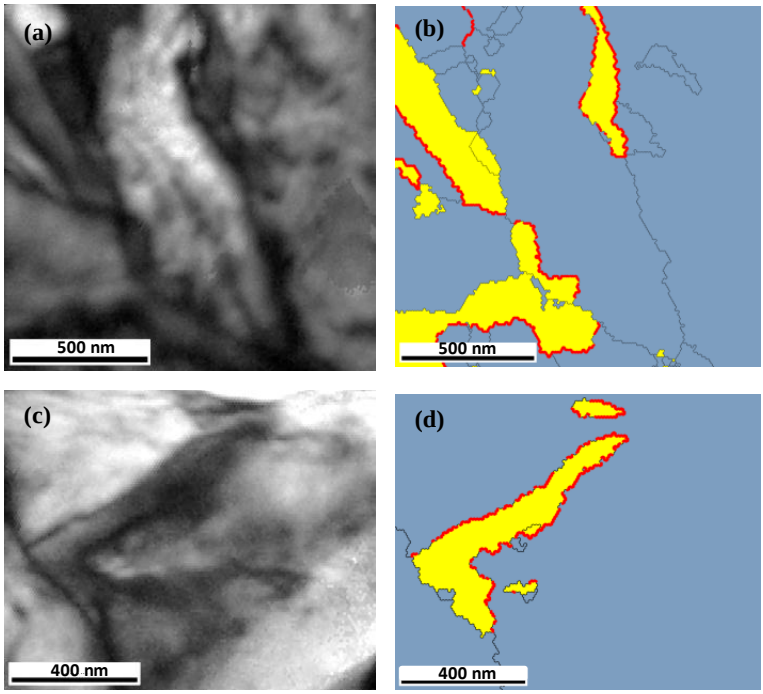

Figure II-7: (a-c) Image quality map (b-d) phase map with retained austenite in yellow, martensite in blue and the Kurdjumov-Sachs orientation relationship in red

The phase maps resolve small interlath austenite grains as shown in Figure II-7 (b) and (d) respectively. They demonstrate that austenite grains of several nm can be detected. The Kurdjumov-Sachs orientation relationship is plotted in red confirming the reliability of the measurement. Besides, the substructures of the martensite grains are shown in the image quality map in Figure II-7 (a).

II.2.1-8 Link between retained austenite fractions obtained from EBSD vs. XRD

The difference between retained austenite fractions obtained by EBSD and XRD depends on two factors: *(i)* the spatial and *(ii)* statistical resolution. Based on knowledge of high-resolution e.g. TEM or TKD images, an estimation of the contributing retained austenite fraction related to the undetectable fraction linked with the limited spatial resolution of EBSD can be made.

The uncleaned EBSD scan illustrates that high angle grain boundaries inside the martensite grains contain individual fcc indexed points, cfr. Figure II-8(a). Though some of these points have a CI of 0, it does not mean that they are wrongly indexed. It only means that they may belong with equal probability to fcc or to bcc structures. However after the cleaning procedure, they partially disappeared as illustrated in Figure II-8(b). Although this does not necessarily mean that these austenite grains are not present in the real microstructure.

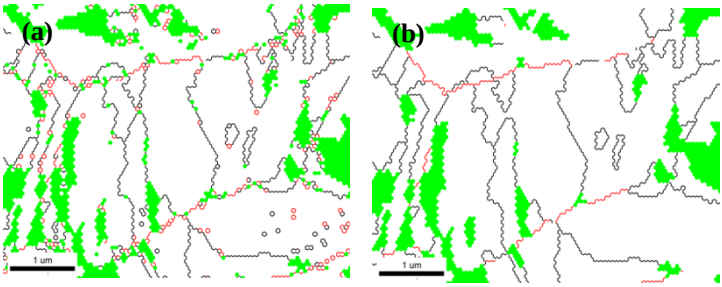

Figure II-8: (a) Uncleaned (b) cleaned phase map with austenite in green

The austenite interlath grains are widest at the prior austenite grain boundary and continue inside the martensitic parent grain with a decreasing width, cfr. Figure II-6. In an ideal abstraction, the austenite grains were simplified as trapezoids touching each other at the length of the radius of the prior austenite grain, as illustrated schematically in Figure II-9.

The average width of the laths (*Wav*) approximated by a rectangle can be calculated as follows:

$$Wav \cdot \frac{D_{PAG}}{2} = 2 \cdot \left[\frac{\left(\frac{Wmax - Wmin}{2} \cdot \frac{D_{PAG}}{2} \right)}{2} \right] + Wmin \cdot \frac{D_{PAG}}{2} \quad (1)$$

This can be simplified to:

$$Wav = \frac{Wmax + Wmin}{2} \quad (2)$$

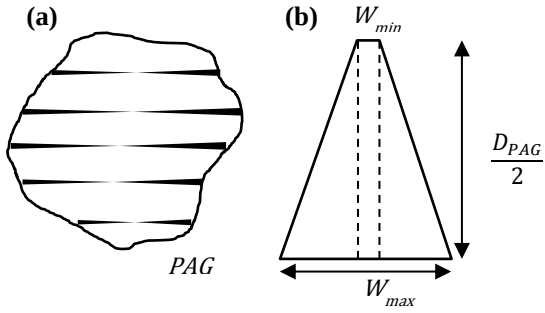

Figure II-9: Schematic of a (a) prior austenite grain with retained austenite grains in between the martensite laths (b) simplified austenite lath

The top width of the grains, *Wmin*, was estimated to be around 10 nm as illustrated in Figure II-6 (a). The maximum undetectable width, *Wmax*, depends on the step size, scan grid and cleaning procedure of the EBSD scan and was estimated as:

$$Wmax = \frac{3}{2}\, Step\ size \tag{3}$$

This is illustrated in Figure II-10 by an abstraction of an austenite lath with a width of 3/2*step size, represented by the coloured rectangles. For different orientations of the austenite lath with respect to the hexagonal scan grid, the 4 pixels which are indexed as austenite are highlighted in the corresponding colour. Consequently these grains are just retained after the cleaning procedure.

The final area of austenite laths is calculated by multiplying the average width with the grain boundary length in the martensite higher than 47° [26]. Prior austenite grain boundaries are assumed not to contain undetectable austenite laths, cfr. Figure II-9. Therefore, these boundaries are excluded from the calculation and only high angle grain boundaries between 48° and 180° are considered relevant:

$$A_{lath} = Wav \cdot GB\_L_{>47^\circ} \tag{4}$$

The total undetectable austenite fraction can be obtained by dividing this area with the total area of the EBSD scan:

$$f_{lath} = \frac{A_{lath}}{A_{EBSD}} \tag{5}$$

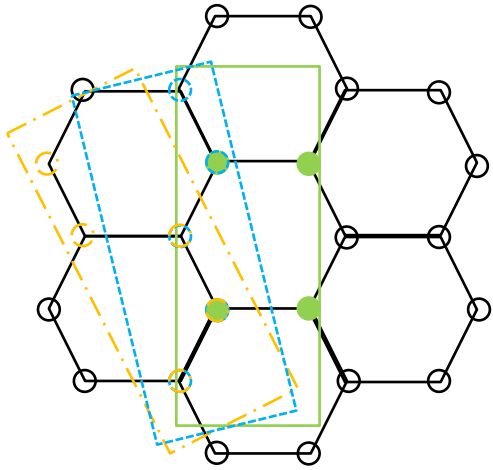

Figure II-10: Schematic representation of the scan grid with austenite laths having a width of 3/2*step size

The results for several Q&P heat treated materials with various step sizes are given in Table II-3. Six samples were analysed with EBSD (f_{EBSD}) with different step sizes and with XRD (f_{XRD}) with differences in austenite fractions ($\Delta_{XRD-EBSD}$) up to 10.9%. If the calculated fraction interlath austenite (f_{lath}) was taken into account, the maximum difference dropped to 2.9%. Hence, a better correspondence between the austenite fractions obtained with XRD and EBSD was found if the undetectable interlath fraction was included. This fraction which is similar for the same step sizes, reduces with smaller step sizes due to a better experimental resolution.

Table II-3: The austenite fraction obtained from the cleaned EBSD scan (f_{EBSD} (%)) and measured by XRD (f_{XRD} (%)) and their difference ($\Delta_{XRD-EBSD}$).The calculated fraction in between the martensite laths (f_{lath} (%)) and the sum ($f_{EBSD+lath}$ (%)) which is compared with the XRD values ($\Delta_{XRD-(EBSD+lath)}$)

Sample	Step size	f_{EBSD} (%)	f_{XRD} (%)	$\Delta_{XRD-EBSD}$	f_{lath} (%)	$f_{EBSD+lath}$ (%)	$\Delta_{XRD-(EBSD+lath)}$
1	**60**	12.8	20.6	7.8	7.7	20.5	0.1
2	**60**	8.4	18.4	10	7.3	15.7	2.7
3	**30**	15.7	17.9	2.2	2.8	18.5	-0.6
	50	9.6		8.3	6.7	16.3	1.6
4	**40**	9.6	18.3	8.7	6.8	16.4	1.9
	50	7.4		10.9	8	15.4	2.9
	70	8.2		10.1	7.8	16	2.3
5	**50**	8.5	14.4	5.9	7.1	15.6	-1.2
	70	7.2		7.2	8.1	15.3	-0.9
6	**50**	5	14.2	9.2	7	12	2.2

II.2.1-9 Conclusion

Different characterization techniques were tested on Q&P steel to resolve the present phases. Optical microscopy seemed not appropriate for detailed characterization while SEM can give a first qualitative indication of the constituents present in the sample with information regarding the precipitation condition. A combination of EBSD and TEM is advisable to detect and qualitatively study the austenite grains of all sizes. However for quantification, a method as XRD that characterizes the bulk microstructure is required. A link between the austenite fractions determined with EBSD and XRD was proposed to estimate the austenite fractions quantitatively based on EBSD measurements. TKD was applied successfully to resolve interlath austenite in between the martensite grains and its ease in use, speed of acquisition and accessibility make the technique favourable compared to TEM.

II.2.1-10 Other characterization techniques

Atomic force microscopy (AFM) topography scans were performed in contact mode using a Park XE150 instrument to visualize nano-indentations in Chapter VI.

For digital image correlation (DIC) analysis, tensile tests were carried out in a Carl Zeiss SEM EVO MA15 operating at an accelerating voltage of 20 kV.

Differential scanning calorimetry (DSC) was carried out using a Netzsch 4040C apparatus whereby alumina crucibles with He-gas flow to prevent oxidation were used. The baseline was determined by running the same program with two empty crucibles. Flat samples with a mass between 70-90 mg were carefully cut with a water-cooled disk. The exact parameters of the DSC scans are mentioned when the data are discussed.

II.2.2. Mechanical characterization

Dog-boned A50, A25 and micro-tensile samples were prepared by water jet cutting from the central area of the Gleeble™ specimens (assuring a well-controlled and known thermal cycle). The dimensions of the micro-tensile specimens satisfy the ASTM standard conditions and to ensure that the specimen failed within the parallel length, the ratio of the grip width to the parallel width was equal to or greater than 1.5 [27].

Tensile tests were carried out on A50 standard size samples according to norm NBN EN ISO 6892-1 on a Zwick Z250 tensile test machine at room temperature with two different speeds. First the position was determined with 20 MPa/s from start to yield point, followed by an elongation rate of 0.006 mm/s from yield point to fracture.

Tensile tests on A25 samples (ASTM E8/E8M) were performed at room temperature in a MTS819 tensile test machine at strain rates 0.083 mm/s and 0.208 mm/s before and after an elongation of 2.5 mm respectively.

To study the local deformation behaviour with EBSD, interrupted micro-tensile tests were conducted on a Deben Microtest 5000N® Tensile Stage device at a constant cross head speed of 0.5 mm/s. Microtest™ software was used for control of the test parameters and data acquisition. For DIC analysis, the micro-tensile tests were performed on a load Kammrath &Weiss module installed inside the SEM chamber. Tensile specimens were deformed to failure with the constant cross-head speed corresponding to the initial strain rate of 10^{-3} s^{-1}. VicSNAP Vic-2D 2009 Digital Image Correlation software was used for full-field strain analysis and generation of deformation maps.

Specimens for nanoindentation experiments were electropolished with a solution of 5% $HClO_4$ and 95% acetic acid kept at 15°C under a potential of 40 V. The tests were carried out using the Hysitron TriboIndenter TI 950 in displacement control testing mode, at a constant strain rate $\dot{\varepsilon} = \dot{h}/h$ of 0.07 s^{-1}, where h is the penetration depth and $\dot{h}$ is the penetration rate of the indenter. Indentations were performed at an imposed maximum depth of 100 nm using a Berkovich type indenter.

References

1. C. Zhao, D. Tang, H.-T. Jiang, S.-S. Jhao, and H. Li: 'Process simulation and microstructure analysis of low carbon si-mn quenched and partitioned steel', *Journal of Iron and Steel Research, International*, 2008, **15**(4), 82-85.
2. A. Dimatteo, G. Lovicu, R. Valentini, M. DeSanctis, and M. R. Pinasco: 'The strain-hardening behaviour of q&p steels', 2010.
3. D. V. Edmonds, D. K. Matlock, and J. G. Speer: 'The recent development of steels with carbide-free acicular microstructures containing retained austenite', *Metallugia Italiana*, 2011, **1**, 41-49.
4. E. De Moor, J. G. Speer, D. K. Matlock, J.-H. Kwak, and S.-B. Lee: 'Effect of carbon and manganese on the quenching and partitioning response of cmnsi steels', *ISIJ International*, 2011, **51**, 137-144.
5. E. De Moor, S. Lacroix, A. J. Clarke, J. Penning, and J. Speer: 'Effect of retained austenite stabilized via quenching and partitioning on the strain hardening of martensitic steels', *Metallurgical and Materials Transactions A*, 2008, **39A**, 2586-2595.
6. M. J. Santofimia, L. Zhao, R. Petrov, and J. Sietsma: 'Characterization of the microstructure obtained by the quenching and partitioning process in a low-carbon steel', *Materials Characterization*, 2008, **59**, 1758-1764.
7. S. S. Nayak, R. Anumolu, R. D. K. Misra, K. H. Kim, and D. L. Lee: 'Microstructure–hardness relationship in quenched and partitioned medium-carbon and high-carbon steels containing silicon', *Materials Science and engineering*, 2008, **498**, 442-456.

8. M. J. Santofimia, T. Nguyen-Minh, L. Zhao, R. Petrov, I. Sabirov, and J. Sietsma: 'New low carbon q&p steels containing film-like intercritical ferrite', *Materials Science and engineering*, 2010, **527**, 6429-6439.

9. C. Y. Wang, J. Shi, W. Q. Cao, and H. Dong: 'Characterization of microstructure obtained by quenching and partitioning process in low alloy martensitic steel', *Materials Science and engineering*, 2010, **527**, 3442-3449.

10. M. J. Santofimia, L. Zhao, R. Petrov, C. Kwakernaak, W. G. Sloof, and J. Sietsma: 'Microstructural development during the quenching and partitioning process in a newly designed low-carbon steel', *Acta Materialia*, 2011, **59**, 6059-6068.

11. M. J. Santofimia, R. H. Petrov, L. Zhao, and J. Sietsma: 'Microstructural analysis of martensite constituents in quenching and partitioning steels', *Materials Characterization*, 2014, **92**(0), 91-95.

12. G. Thomas, J. G. Speer, D. Matlock, and J. Michael: 'Application of electron backscatter diifraction techniques to quenched and partitioned steels', *Microscopy and Microanalysis*, 2011, **17**, 368-373.

13. R. R. Keller and R. H. Geiss: 'Transmission ebsd from 10 nm domains in a scanning electron microscope', *Journal of Microscopy*, 2012, **245**(3), 245-251.

14. P. W. Trimby: 'Orientation mapping of nanostructured materials using transmission kikuchi diffraction in the scanning electron microscope', *Ultramicroscopy*, 2012, **120**(0), 16-24.

15. F. S. LePera: 'Improved etching technique for the determination of percent martensite in high-strength dual-phase steels', *Metallography*, 1979, **12**, 263-268.

16. N. Maheswari, S. Ghosh Chowdhury, K. C. Hari Kumar, and S. Sankaran: 'Inluence of alloying elements on the microstructure evolution and mechanical properties in quenched and partitioned steels', *Materials Science and Engineering A*, 2014, **600**, 12-20.

17. B. D. Cullity: 'Elements of x-ray diffraction', 1956, New Jersey, USA, Addison-Wesley Publishing Company, Inc.

18. C. Suryanarayana and M. G. Norton: 'X-ray diffraction: A practical approach', 1998, New York, Plenum Publishing Corporation.

19. N. H. van Dijk, A. M. Butt, L. Zhao, J. Sietsma, S. E. Offerman, J. P. Wright, and S. van der Zwaag: 'Thermal stability of retained austenite in trip steels studied by synchrotron x-ray diffraction during cooling', *Acta Materialia*, 2005, **53**, 5439-5447.

20. S. H. Magner, R. J. De Angelis, W. N. Weins, and J. D. Makinson: 'A historical review of retained austenite and its measurement by x-ray diffraction', *Advances in X-ray Analysis*, 2002, **45**, 92-97.

21. E. Girault, P. J. Jacques, P. Harlet, K. Mols, J. Van Humbeeck, E. Aernoudt, and F. Delannay: 'Metallographic methods for revealing the multiphase microstructure of trip-assisted steels'.

22. D. V. Edmonds, K. He, F. C. Rizzo, B. C. D. Cooman, D. K. Matlock, and J. G. Speer: 'Quenching and partitioning martensite—a novel steel heat treatment', *Materials Science and engineering*, 2006, **438-440**, 25-34.

23. R. Serret: 'Investigation of heavily deformed and dual phase materials by means of transmission kikuchi diffraction', Ghent University, 2013.

24. P. W. Trimby, Y. Cao, Z. Chen, S. Han, K. J. Hemker, J. Lian, X. Liao, P. Rottmann, S. Samudrala, J. Sunb, J. T. Wang, J. Wheeler, and J. M. Cairneya: 'Characterizing deformed ultrafine-grained and nanocrystalline materials using transmission kikuchi diffraction in a scanning electron microscope', *Acta Materialia*, 2014, **62**, 69-80.

25. S. Suzuki: 'Features of transmission ebsd and its applications', *JOM*, 2013, **65**(9), 1254-1263.

26. N. Bernier, L. Bracke, L. Malet, and S. Godet: 'An alternative to the crystallographic reconstruction of austenite in steels', *Materials Characterization*, 2014, **89**, 23-32.

27. M. Maringa: 'Dimensioning of dog bone specimens and numerical analysis of the effects of different fillet radii, clamp area and pinhole loading on the stresses in such specimens', *African Journal of Science and Technology* 2004, **5**(2), 60-72.

CHAPTER III

STUDY OF HEAT TREATMENT PARAMETERS AND KINETICS OF QUENCHING AND PARTITIONING CYCLES

Extended version of

D. De Knijf, E. Pinto Da Silva, C. Föjer, and R. Petrov: 'Study of heat treatment parameters and kinetics of Quenching and Partitioning cycles', Materials Science and Technology, 2015.

III. STUDY OF HEAT TREATMENT PARAMETERS AND KINETICS OF QUENCHING AND PARTITIONING CYCLES

III.1. Abstract

Cold rolled sheets of a low carbon Quenching and Partitioning (Q&P) steel grade were subjected to heat treatment cycles which were designed by dilatometric experiments and optimized with respect to the quenching temperature, partitioning temperature and partitioning time. Characterisation of the retained austenite was carried out by Electron Backscattered Diffraction (EBSD), whereas the carbides were studied by Scanning Electron Microscopy (SEM) and Differential Scanning Calorimetry (DSC). The mechanical properties were evaluated by tensile testing and linked with retained austenite fractions and carbon contents, determined by X-ray diffraction (XRD). Conclusions are drawn concerning the influence of the kinetics of partitioning for different partitioning and quenching temperatures on the microstructure in terms of optimal austenite fraction in the martensitic matrix, its C-content and ensuing mechanical properties. These results contribute to an optimal design of Q&P heat treatments, producing microstructures with desired balance of strength and ductility.

III.2. Introduction

A new concept for processing of advanced high strength steel called "Quenching and Partitioning" (Q&P) has been developed. It was proposed by Speer et al [1] in 2003 as a method to produce low carbon high strength steels with a mixed microstructure of martensite and retained austenite. Additions of Si and Al in the steel compositions were used to inhibit cementite precipitation, opening the possibility to obtain carbon-enriched austenite at room temperature (i.e. with improved stability) by carbon partitioning from a supersaturated martensite [1-3].

The Q&P heat treatment consists of full or partial austenitization (intercritical annealing) followed by quenching to a pre-determined temperature (QT) within the martensite start (M_s) and finish (M_f) temperature range. At this temperature, the microstructure consists of controlled fractions of martensite and austenite. The second step of the Q&P heat treatment is either isothermal holding at the quench temperature (QT) or isothermal holding at increased temperatures to promote carbon diffusion. This step, referred to as a partitioning stage,

induces carbon depletion of the martensite and diffusion to the untransformed austenite, resulting in its stabilization [3]. After final quenching to room temperature, the microstructure consists of ferrite -if the austenitization was in the intercritical temperature range-, retained austenite and two types of martensite: the one formed during the first quench (referred to as "partitioned" or "tempered" martensite) and possibly the one formed during the final quench (referred to as "fresh", "new" or "untempered" martensite) [4].

Q&P heat treatment holds promise to produce a wide range of mechanical properties by appropriate control of the martensite and the austenite fractions and the carbon enrichment of the austenite. The final retained austenite fraction depends on several factors: the quench temperature (QT), the partitioning temperature (PT) and the partitioning time (Pt) [5]. Besides, ideal partitioning makes the assumption that all of the available carbon partitions into the austenite and that no competing reactions such as carbide precipitation or bainite formation occur [1]. Depending on the steel composition and the particular heat treatments, formation of ferrite, bainite [6], isothermal martensite [7, 8] and carbides during the Q&P process can occur in addition to carbon partitioning, reducing the effectiveness of this heat treatment. Knowledge of these mechanisms, as will be addressed in this work, will lead to a better control of these phenomena and optimization of the Q&P cycle.

III.3. Experimental Procedure

III.3.1. Chemical Composition

The selection of appropriate alloying elements was based on three main requirements [9]: (i) avoiding ferrite, pearlite or bainite during quenching and bainite during partitioning; (ii) suppressing carbide precipitation; and (iii) stabilizing the austenite during final quenching.

Manganese is effective in fulfilling the first requirement [10]. However, high concentrations result in segregation banding [11]and therefore the Mn-content was limited to 3wt.%. According to literature [12-15], 1.5wt.% Si is adequate to suppress cementite formation during partitioning since it changes the carbide precipitation kinetics from carbon diffusion control to silicon diffusion control, away from the carbide interface [16]. The carbon content was chosen between 0.25wt.% and 0.3wt.% to ensure austenite stability [17].

Different concentrations of these elements influence the Time Temperature Transformation (TTT) diagram [18], cfr. Figure III-1.

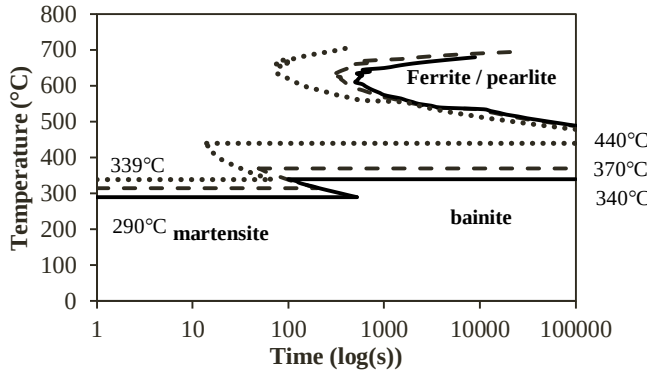

Figure III-1: TTT diagrams modelled with mucg-83 [18] software for different compositions: 0.25C – 2.5Mn – 1.5Si (wt.%) by dotted lines; 0.25C – 3Mn – 1.5Si (wt.%) by small stripes; 0.3C – 3Mn – 1.5Si (wt.%) by the full line

Increasing the Mn-concentration from 2.5wt.% to 3wt.% shifts the ferrite/pearlite transformation to the right and the bainite onset temperature down from 440°C to 370°C. The influence of increasing the carbon content from 0.25wt.% to 0.3wt.% is similar; however, the effect is less pronounced. Therefore, the combination of 3wt.% Mn with 0.25wt.% C fulfils the requirements of high hardenability, bainite suppression during partitioning and austenite stabilization [12-15]. Based on this, a steel with a nominal composition of 0.25C-1.5Si-3Mn (wt.%) was produced in a laboratory vacuum induction furnace. Its phase diagram calculated by Thermocalc™, represents the mass fraction of the equilibrium phases as a function of temperature, cfr. Figure III-2.

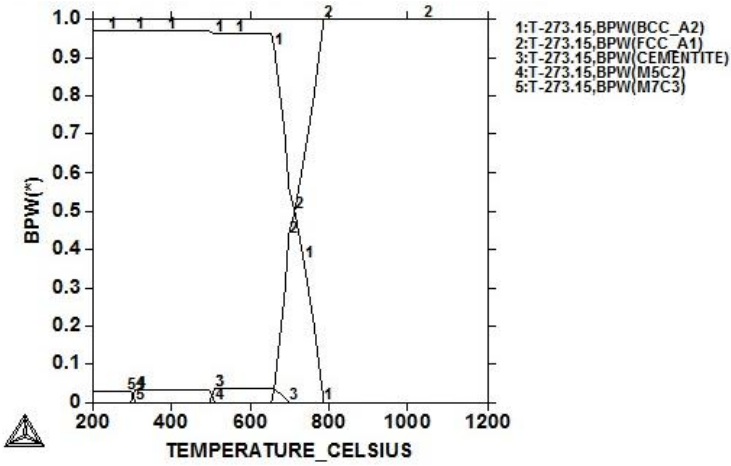

Figure III-2: Mass fraction of phases as a function of temperature for 0.25C-1.5Si-3Mn calculated with Thermocalc™

An A_{e3} temperature of 785°C was obtained and three types of precipitates namely cementite, M_5C_2 and M_7C_3 can be formed below the respective temperatures of 695°C, 510°C and 306°C. The equilibrium composition of the carbides contains Mn and Fe with an increasing fraction of Mn at higher temperatures.

After casting, the steel blocks were hot rolled to a final thickness of 2.5 mm, accelerated cooled by water jets to 600°C and transferred to a furnace for coiling simulations at 560°C. During cooling and isothermal holding, austenite transformed completely into pearlite, cfr. the optical and SEM images in Figure III-3(a) and (b-c) respectively. The image quality map in Figure III-3(d) illustrates a bimodal distribution of the bcc grain size with an average diameter of approximately 4.5µm.

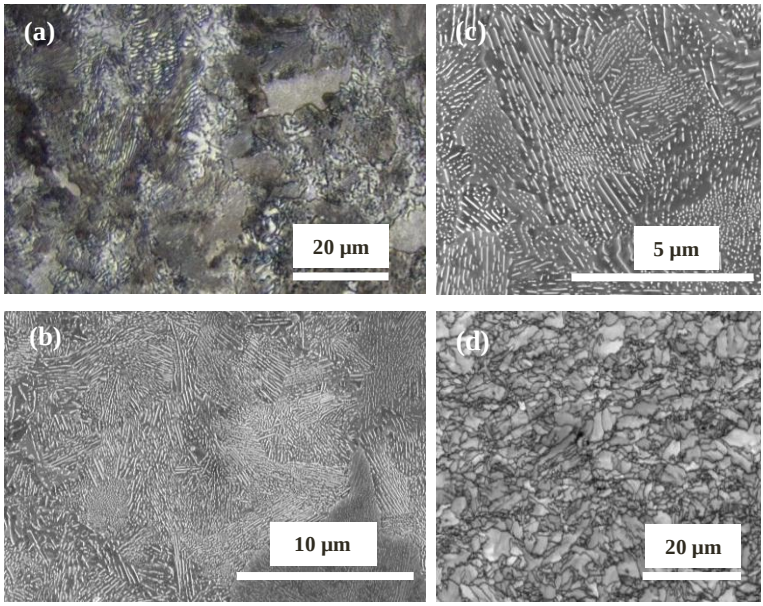

Figure III-3: (a) Optical image, (b-c) SEM images, (d) image quality map of the hot rolled material

Segregation bands were detected in the hot rolled pearlitic microstructure, cfr. Figure III-4 (a-b). The optical images are superimposed with an electron probe micro-analyser (EPMA) profile of manganese illustrating that high Mn-areas appear as darker bands with an average width of 13.9 ± 4.6 µm. Silicon segregated according to the same profile as manganese, cfr. Figure III-4 (c-d) but no significant segregation of carbon was detected.

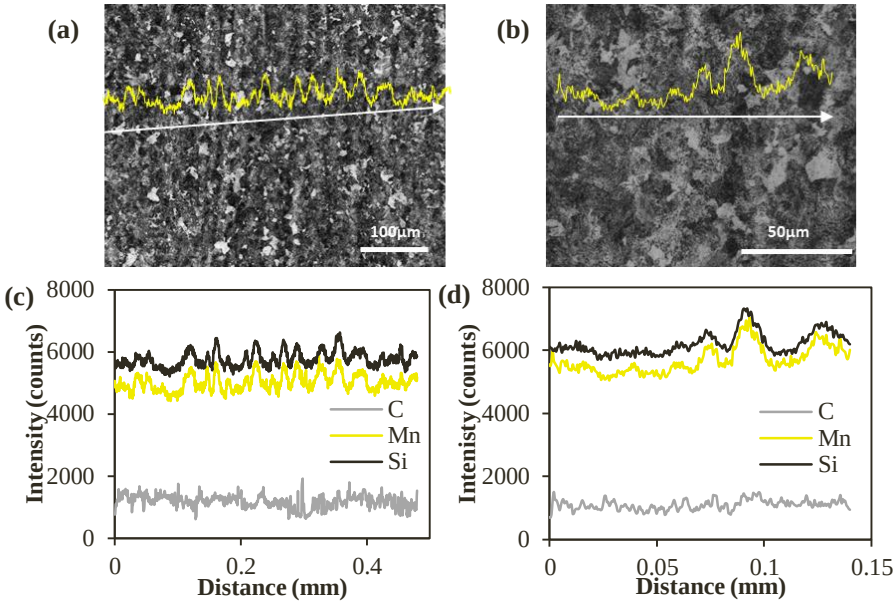

Figure III-4: (a)-(b) Optical images of hot rolled material illustrating segregation bands superimposed with corresponding EPMA line-scans of Mn; the intensity profiles of C, Si and Mn versus the distance in the EPMA scan are given in (c) and (d) corresponding with (a) and (b) respectively

Increasing the Mn and Si content refines the spacing and thickness of the cementite lamellae in pearlite [19]. Manganese is an austenite stabilizing element and reduces the transformation temperature to pearlite. This implies a lower undercooling temperature and more cementite nuclei. Silicon on the other hand inhibits growth of cementite explaining the darker appearance of the high Mn/Si bands by thinner lamellae. This segregation originated from solidification and hot rolling since the last liquid fraction was calculated with Thermocalc™ to be enriched in Mn and Si up to levels of 10% and 3% respectively, cfr. Figure III-5. The segregation bands remain in the material during the entire processing cycle which could alter microstructural evolutions locally e.g. in retained austenite fractions and carbide precipitation conditions.

The hot rolled sheets were pickled and cold rolled to a thickness of 1 mm imposing a total reduction in thickness of 60%. The microstructure consisted of deformed pearlitic grains with partially fragmented cementite lamellae as shown in the micrographs in Figure III-6.

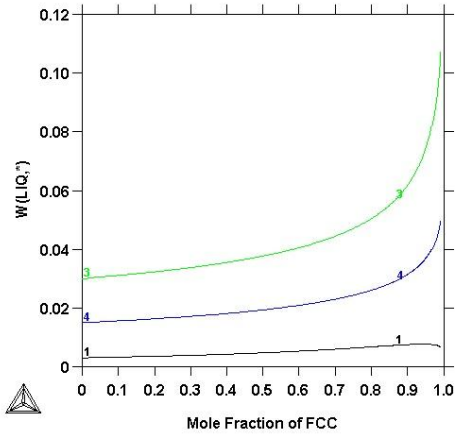

Figure III-5: Weight fraction of C in black, Si in blue, and Mn in green in the liquid phase during solidification as a function of the solidified fcc fraction, simulated with Thermocalc™ (Scheil calculation with C as a fast diffusing element)

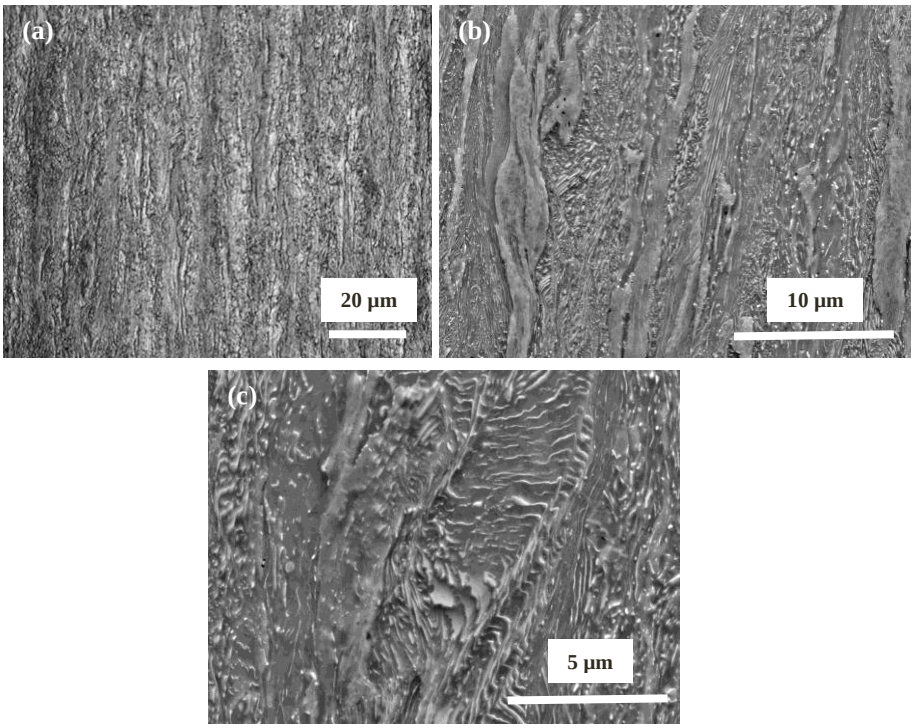

Figure III-6: (a) Optical image (b-c) SEM images of cold rolled material

The hot rolled texture, illustrated in Figure III-7(a), contained the typical transformation products of deformed austenite having Copper {211}‹111›, Goss {110}‹001›, S {123}‹634› and Brass {011}‹112› orientations. After 60% cold rolling, the deformation γ-

fibre increased its intensity from 2 to a maximum of 8 mrd (multiples of a random distribution) for the F-component {111}‹112›, cfr. Figure III-7(b).

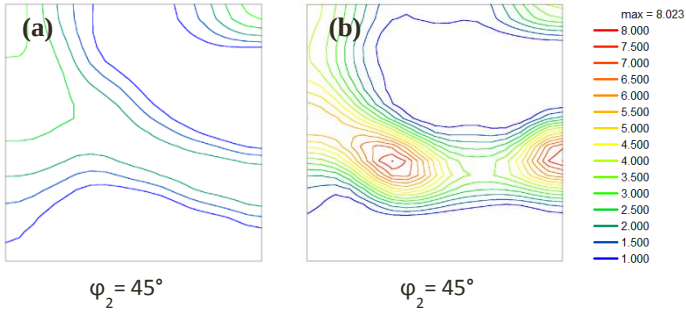

Figure III-7: Orientation distribution figure in section ϕ_2= 45° of (a) the hot rolled material (b) cold rolled material

III.3.2. Heat treatment experiments

Dilatometer experiments were carried out in a Bähr DIL 805 A/D on hot rolled rectangular samples with dimensions of 2.5 x 3.5 x 10mm, with the longest axis parallel to the plate rolling direction.

The samples were heated at 20°C/s to 850°C, which is 35°C above the measured Ac_3 temperature, for full austenitisation. Cooling rates between 1°C/s and 100°C/s were applied and the dilation data were analysed in order to determine part of the CCT diagram.

Additional Q&P experiments with long isothermal partitioning treatments at 300°C, 350°C and 400°C were performed to study the isothermal transformation via the length change.

Based on these dilatometric experiments, the required cooling rate, quenching and partitioning temperatures were examined and chosen for the final Q&P heat treatments. The final heat treatments were carried out on cold rolled samples which were cut perpendicular to the rolling direction and heat treated in a Gleeble™ thermo-mechanical simulator.

III.3.3. Mechanical characterization

Tensile tests were carried out on A50 tensile specimens, conform norm NBN EN ISO 6892-1 on a Zwick Z250 tensile test machine at room temperature. The samples were cut out of the central part of the heat treated samples experiencing a uniform thermal history.

III.3.4. Microstructural characterization

The samples for microstructural characterization were prepared by mechanical grinding and polishing following the classical preparation routes. The austenite volume fractions and the average carbon contents were determined at room temperature with XRD experiments performed on a Siemens Kristalloflex D5000 diffractometer equipped with Mo-Kα source operating at 40kV and 40mA. A 2θ-range of 25° to 45° was scanned using a step size of 0.01°, dwell-time of 2s and rotation speed of 15rpm. The diffraction data were post-processed by subtracting the background radiation and $K_{\alpha 2}$ influence. The retained austenite volume fractions were determined with the formula of Cullity [20] using the intensity of the $(220)\alpha$, $(311)_{\alpha}$, $(200)_{\gamma}$ and $(211)_{\gamma}$ reflections. The carbon content was obtained using the positions of both austenite peaks [12, 21].

The EBSD analysis was carried out by means of a FEI Quanta™ 450-FEG-SEM equipped with a Hikari EBSD detector controlled by the EDAX-TSL OIM-Data Collection software. The EBSD data were acquired on a hexagonal scan grid using an accelerating voltage of 20kV, a working distance of 16 mm, a tilt angle of 70° and a step size of 60nm. The orientation data were post-processed with TSL-OIM Analysis 6.2® software. The raw data were cleaned according to the following procedure. First, a confidence index (CI) standardization with a minimum grain size of 4 pixels or 1.44 µm² was applied. This clean up algorithm changes the CI of all points in a grain to the maximum CI found among all points belonging to that grain. Afterwards, the neighbour CI correlation algorithm was employed, which implies that if a particular point has a CI below 0.1 then the CI of the nearest neighbours are checked to find the neighbour with the highest CI. The orientation and CI of the particular point are reassigned to match the orientation and CI of the neighbour with the maximum CI. Finally, if the majority of neighbours of a particular grain smaller than 4 pixels with a grain tolerance angle of 5° belong to the same grain, then the orientation of the particular grain is changed to match that of the majority grain, i.e. a grain dilation algorithm was applied.

Differential Scanning Calorimetry (DSC) was carried out using a Netzsch 4040C apparatus whereby alumina crucibles with He-gas flow to prevent oxidation were used. The baseline was determined by running the same program with two empty crucibles. Flat samples with a mass between 70 and 90 mg were carefully cut with a water-cooled disk. A Kissinger-type kinetic [22] analysis was applied to determine the activation energies of the processes

which take place during heating: $\ln\left(\frac{T^2}{\varphi}\right) = \frac{E}{RT} + \ln\left(\frac{E}{R}\right) - \ln(A)$, where E is the activation energy in [J/mol], A is the pre-exponential factor, T is the peak temperature [K], and φ is the heating rate [K/min].

III.4. Study of the heat treatment parameters

In the first part of this work, the critical cooling rate required to have a fully martensitic microstructure, the optimal quenching and partitioning temperatures were determined by dilatometric measurements on hot rolled material.

III.4.1. Results and discussion

The experimentally derived Continuous Cooling Transformation (CCT) diagram was used to determine the critical cooling rate after full austenitisation. The diagram is shown in Figure III-8 and illustrates the formation of bainite for cooling rates between 1°C/s and 5°C/s. Hence, a cooling rate of 10°C/s is sufficient to have a completely martensitic microstructure. However, in order to completely avoid bainite formation, cooling with 20°C/s was applied. The experimentally derived martensite start temperature was 301°C.

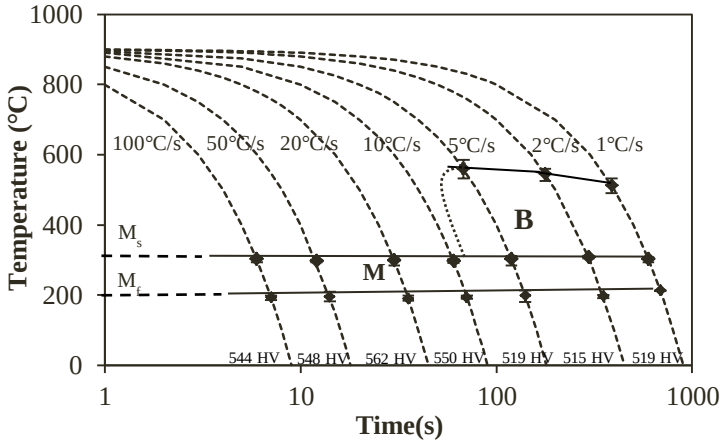

Figure III-8: Experimentally derived CCT diagram for 0.25C-3Mn-1.5Si with B – bainite and M – martensite

Quenching was intentionally interrupted at the quenching temperature (QT) [5]. The Koistinen-Marburger (K-M) relationship [23], based on ideal C-partitioning without diffusion of substitutional elements, predicts the final retained austenite fraction as a function of the

quenching temperature. The optimum quenching temperature (OQT) is defined as the temperature at which the fraction of retained austenite is maximal, meaning that this austenite fraction is stabilized to room temperature through the available carbon without formation of fresh martensite during final quenching. In this work, the theoretical M_s-temperature and α-parameter are determined with formulas having an exponential carbon dependence [24] resulting in a theoretical optimum quenching temperature of 242°C with the stabilization of 19% retained austenite. This can be determined more accurately if two experimentally derived parameters are employed in the calculation.

First, by using the experimentally derived M_s, an OQT of 219°C was predicted, being 23°C below the theoretical value. Secondly, the martensite fraction for the first quench was replaced by fitting the true martensite fraction obtained from dilatometric measurements. This gives an average OQT of 244°C, which is in very close correspondence with the calculated value. To verify this optimum quenching temperature value, hot rolled material was austenitized and quenched to 244°C, at which it was held for 300s prior to quenching to room temperature. The purpose of this isothermal holding was to temper the first formed martensite and hence to estimate the fraction of austenite at the quenching temperature.

The image quality map superimposed with the austenite grains in green is shown in Figure III-9 (a). Isothermal holding at 244°C seems to trigger sufficient carbon diffusion to stabilize 6.2% austenite. From the experimental dilation data, 28.7% austenite should remain at this temperature. As a consequence, the fractions of fresh and tempered martensite can be estimated to be 22.5% and 71.3% respectively.

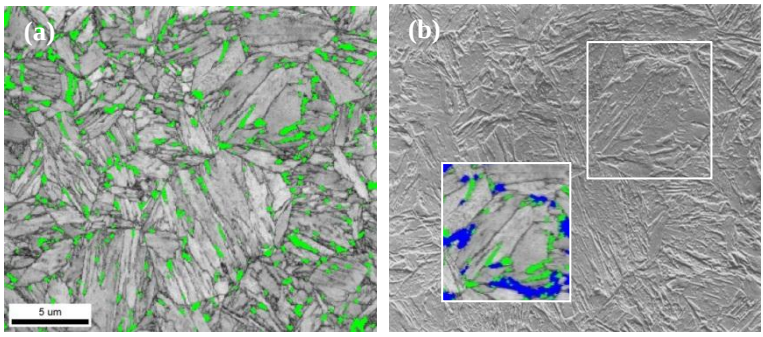

Figure III-9: (a) Image quality map superimposed with the retained austenite in green (b) SEM image of the scanned area with the fraction austenite remaining in green and transformed during final quenching in blue of the area in the boxed area

A technique developed by Wu et al. [25] and repeated by Santofimia [26], predicts the tempered and fresh martensite fractions by deconvoluting the number of bcc pixels versus

image quality, cfr. Figure III-10. Via integrating the fitted curves, the fractions tempered and fresh martensite were determined to be 77.5% and 22.5% respectively. Taking the austenite volume fraction into account, this results in 6.2% RA, 72.7% tempered martensite and 21.2% fresh martensite. This is in close correspondence with the fractions predicted from the dilation data.

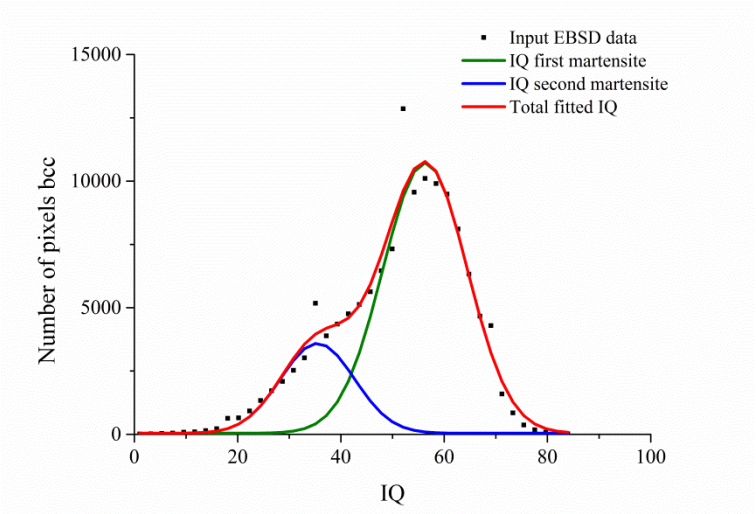

Figure III-10: Number of pixels versus image quality fitted by the deconvolution method

To distinguish fresh martensite in the SEM-image, the number of pixels with a lower grain average image quality was highlighted, as illustrated by the blue coloured grains in the inset of Figure III-9(b). The retained austenite in green and fresh martensite in blue can be associated with the less etched constituents in the SEM image. According to the Koistinen-Marburger relationship, the maximum amount of retained austenite that can be stabilized in an ideal partitioning condition is approximately 19%. However at 244°C, 28.7% austenite is present. Therefore, this temperature is most likely too high for complete stabilisation.

The partitioning stage consists of reheating the partially quenched steel to the partitioning temperature (PT) and isothermal holding where carbon diffusion occurs from the martensite towards the untransformed austenite.

After full austenitisation and quenching to 244°C, the dilatometer samples were reheated at 10°C/s [27] to different partitioning temperatures. The temperatures selected were above 300°C since unwanted ε-carbides start dissolving above this temperature [10, 28, 29]. The upper limit of the PT was set at 400°C to avoid competing reactions such as decomposition of the austenite into ferrite and coarse carbides [10] or carbide precipitation [30]. The theoretically

determined bainite start temperature is 370°C (cfr. Figure III-1) indicating that between 300°C and 370°C decomposition of austenite to bainite can occur after longer partitioning times.

In Figure III-11 (a), the relative change in length as a function of time during partitioning illustrates that partitioning at 400°C results in a small length decrease, whereas at 300°C and 350°C the length increases. The length decrease might be associated with tempering of the martensite [31] or growth of the existing austenite by interface movement [32]. Additionally, the length increase could be due to the formation of bainite or isothermal growth of martensite [8] by martensite to austenite interface migration [32].

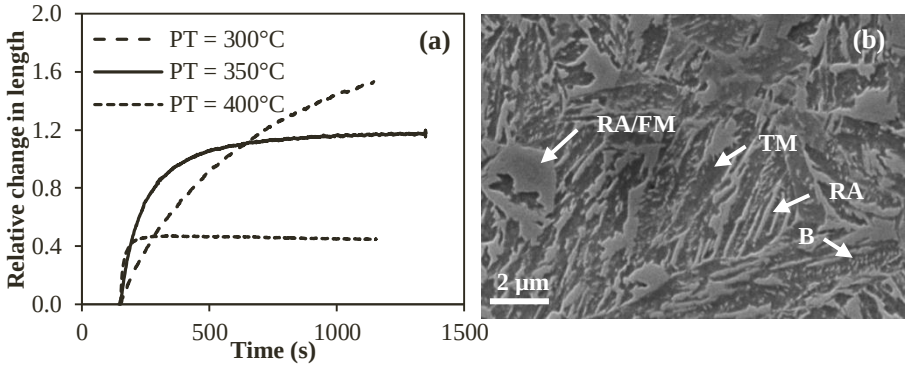

Figure III-11: (a) Relative change in length during partitioning at 300°C, 350°C and 400°C; (b) SEM image of sample partitioned at 350°C with retained austenite (RA), tempered martensite (TM), bainite (B) and fresh martensite (FM)

In Figure III-11 (b), the SEM image after partitioning at 350°C reveals retained austenite (RA), bainite (B), tempered (TM) and fresh martensite (FM). The presence of bainite in the microstructure could explain the increase in length although the total dilatation response is a result of all the above mentioned effects.

The retained austenite fraction evaluated by XRD, cfr. Table III-1, was 13.2 ± 0.8 % for partitioning at 300°C, and indicates that austenite is effectively retained during final quenching. Nevertheless, its transformation stability based on the C-content is expected to be rather low (0.83 ± 0.1 % C) [33, 34]. The austenite fraction determined with EBSD is 7.4 % (cfr. Table III-1 and Figure III-12(a)). Although the resolution of the EBSD technique is reasonably high, film-like austenite grains between the martensite laths are not resolved reliably. With a step size of 60 nm, these laths of 10-100 nm [35] are indexed with maximum 2 points and hence removed by the applied cleaning procedure.

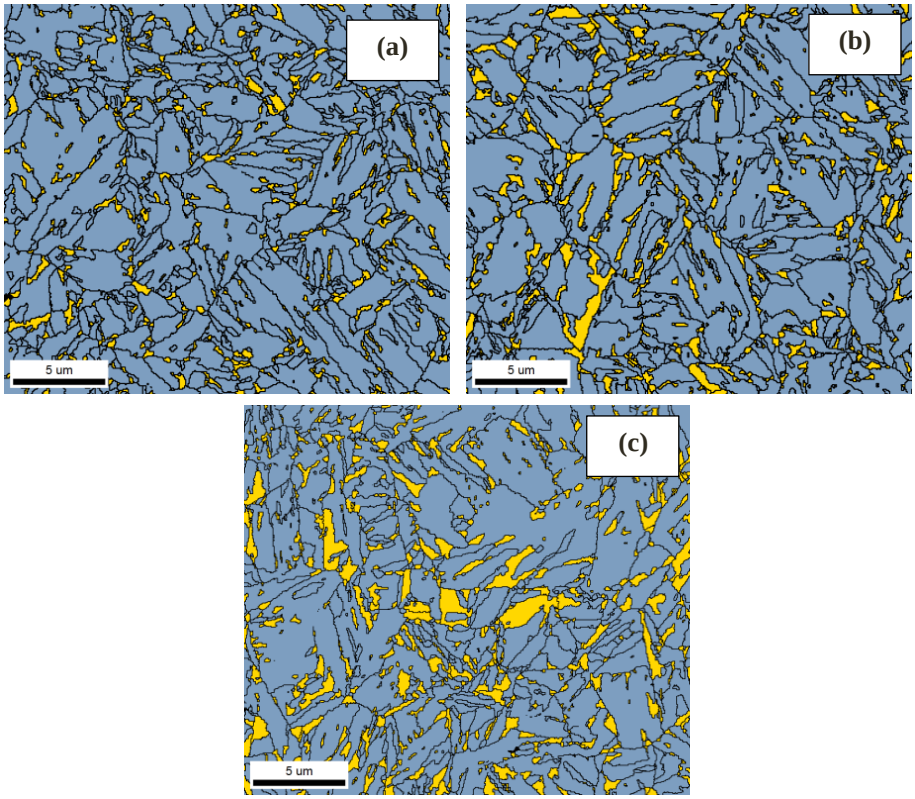

Figure III-12: EBSD phase map with austenite in yellow and martensite in blue for partitioning at (a) 300°C (b) 350°C and (c) 400°C

Table III-1: Retained austenite fraction (%) and its C-content (wt.%) determined with XRD and the retained austenite fraction (%) obtained from EBSD for Q&P steel quenched to 244°C and partitioned at 300°C, 350°C and 400°C

	XRD RA (%)	**XRD C (wt. %)**	**EBSD RA (%)**
300°C	13.2 ± 0.8	0.83 ± 0.1	7.4
350°C	11.4 ± 0.8	1.34 ± 0.1	11.0
400°C	18.7 ± 0.8	0.92 ± 0.1	16.0

After annealing at 350°C, the austenite fraction decreased to 11.4 ± 0.8 % with a C-content of 1.34 ± 0.1 %. Transformation to bainite low in carbides explains the lower austenite fraction, whereas higher carbon diffusivity and possibly C-expulsion from the bainite clarify its higher stability. The austenite fraction of 11% determined by EBSD is

similar to the value of XRD due to larger, and easy detectable interlath lamellar austenite grains.

After partitioning at 400°C, the retained austenite fraction was 18.7 ± 0.8 % , which is similar to the theoretically predicted value. The carbon content of 0.92 ± 0.1 % C suggests ideal partitioning conditions related to high C-diffusivity without competing reactions. The EBSD phase map (cfr. Figure III-12 (c)) illustrates that, after this partitioning treatment, besides the interlath lamellar austenite, blocky austenite grains were stabilized as well.

DSC experiments were performed on the hot rolled material after austenitization and quenching, cfr. Figure III-13 (a). By heating the sample at different speeds, 10°C/min and 30°C/min, the activation energy for carbide precipitation could be obtained.

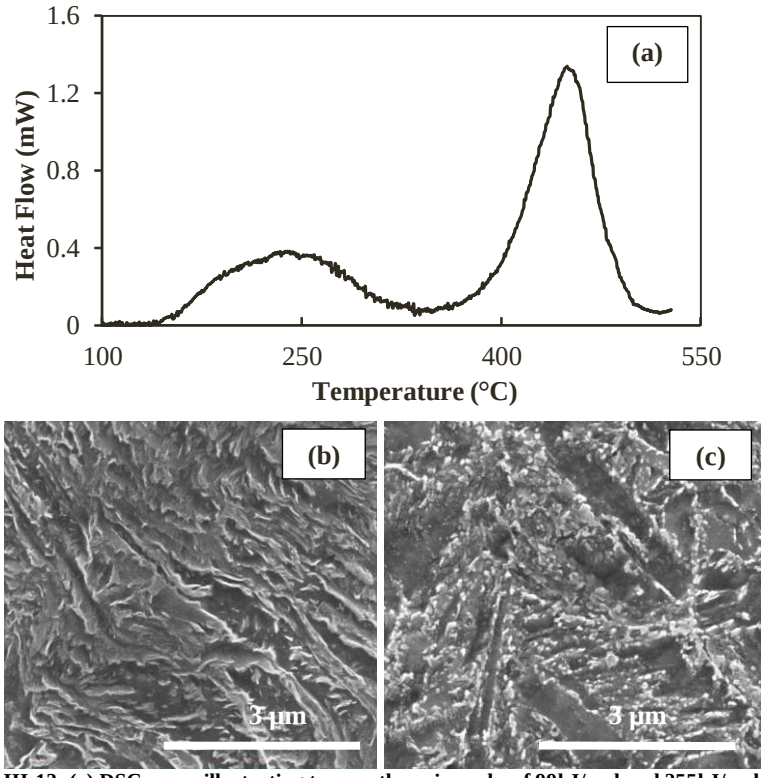

Figure III-13: (a) DSC curve illustrating two exothermic peaks of 99kJ/mol and 255kJ/mol during reheating at 10°C/min after full austenitisation and quenching of hot rolled material; SEM images of a sample heated to (b) 350°C and to (c) 550°C and quenched to room temperature

The first exothermal peak was observed between 150°C and 300°C with an activation energy of 99 kJ/mol. It was associated with the formation of epsilon-carbides [10, 30, 36]. The second peak was detected between 400°C and 525°C with an activation energy of

255kJ/mol and it was associated with cementite formation [10, 30]. Figure III-13 (b) and (c) show the SEM micrographs of the quenched dilatometer samples after heating to 350°C and 550°C respectively. Figure III-13 (b) illustrates the lath-type epsilon-carbides formed during the first peak, whereas Figure III-13 (c) shows larger, globular cementite linked with the second peak.

III.5. Study of the partitioning kinetics and mechanical properties for different partitioning and quenching temperatures

III.5.1. Q&P of cold rolled steel

Variations in the Q&P parameters have an important influence on the partitioning kinetics and hence on the phase fractions and mechanical properties. According to the CCT-diagram, our composition allows a non-severe cooling rate of 20°C/s after full austenitisation at 850°C.

The sensitivity of the heat treatment cycle to the quenching temperature (QT) was studied in a temperature range of ± 20°C around 244°C. The isothermal holding time at this temperature was kept short to avoid isothermal transformation products below M_s [8].

The partitioning temperatures (PT) were selected in the range between 300 to 450°C. The lowest temperature, 300°C, was selected just above the ε-carbide dissolution temperature. Additionally, to analyse the effect of bainite formation on the partitioning kinetics and mechanical properties, partitioning at 350°C was conducted. The length decrease during partitioning and the measured 18.7% retained austenite suggest that 400°C is the best partitioning temperature, having the highest C-diffusivity without competitive reactions. Besides ideal partitioning, 450°C was applied to study the effect of austenite decomposition to ferrite and coarse cementite [10] on mechanical properties. The heat treatment cycles were conducted for identical holding times of 10s, 50s, 100s, 250s, 500s and 1000s for all partitioning temperatures.

III.5.2. Results

Quenching and Partitioning microstructures consist of tempered martensite, retained austenite and fresh martensite in the case of incomplete austenite stabilization. An EBSD image quality map, superimposed with retained austenite (in green), is shown in Figure III-14.

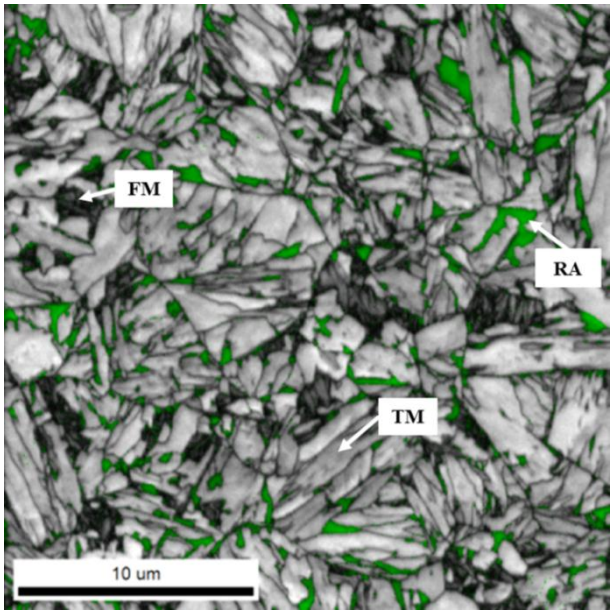

Figure III-14: EBSD image quality map of a typical Q&P microstructure illustrating the fresh martensite (FM), tempered martensite (TM) and retained austenite (RA) in green

Any distortions to the crystal lattice within the diffracting volume will produce lower quality (more diffuse or less sharp) diffraction patterns. This enables the IQ parameter to be used for a qualitative description of the strain distribution in a microstructure [37]. Hence, fresh martensite has a lower image quality compared to tempered martensite due to its higher carbon content and untempered microstructure [26].

Different combinations of these microstructural features influence the mechanical properties, since the harder fresh martensite alters the strain distribution between the tempered martensite and austenite. The fractions of these phases and the C-content of the austenite produced by different heat treatment conditions, determine the final mechanical properties.

The time limiting step determining the kinetics of Q&P is C diffusion in austenite [6, 32]. The average diffusion distance of C in austenite as a function of time, t, can be estimated by the equation [10]:

$$x_{\gamma}^{C} = \sqrt{6.D_{\gamma}.t}$$

$D_{\gamma} = D_{\gamma 0} \exp(-\frac{Q_{\gamma}}{RT})$ is the diffusion coefficient of C in austenite where $D_{\gamma 0}$ is a constant [38] ($D_{\gamma 0} = 0.1\ 10^{-4} m^2/s$), Q_{γ} is the activation energy for C diffusion [38] ($Q_{\gamma} = 135.7\ kJ/mol$), R is the gas constant and T is the absolute temperature. Figure III-15 shows

the diffusion distance of C in austenite as a function of partitioning time for the different partitioning temperatures considered in this work.

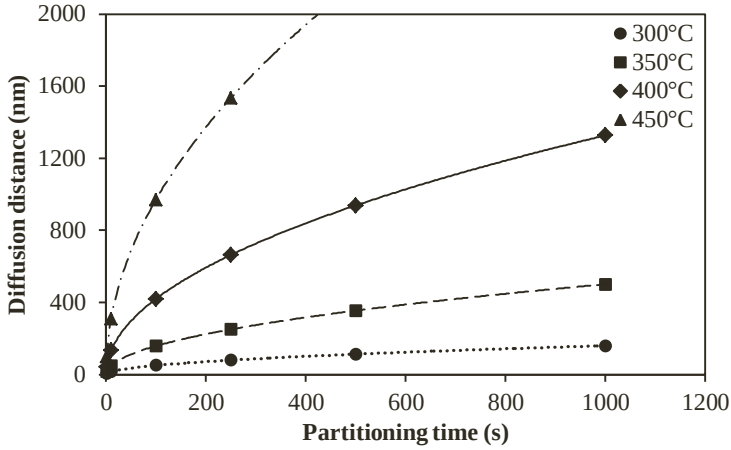

Figure III-15: Diffusion path (nm) of C in austenite for different partitioning temperatures (PT = 300°C, 350°C, 400°C, 450°C) as a function of partitioning time

In general, the ultimate tensile strength and total elongation are correlated with a reverse relationship, whereby strength increases as ductility decreases (cfr. Figure III-16 for this work).

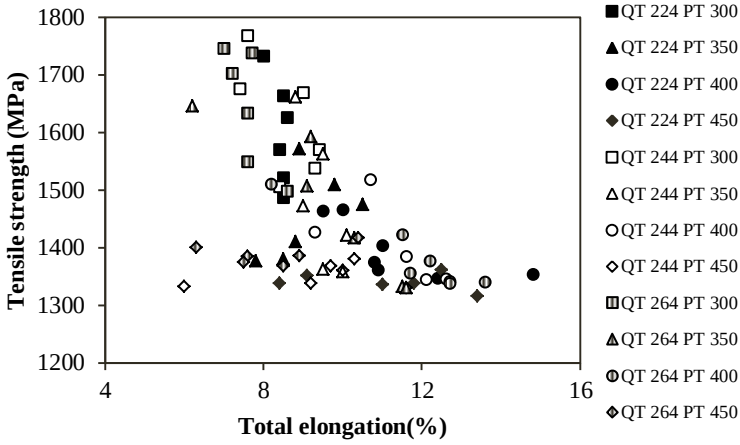

Figure III-16: Ultimate tensile strength (MPa) versus total elongation (%) curve for the Q&P heat treated materials in this work

III.5.3. Discussion

III.5.3.1 The partitioning kinetics and mechanical properties at different partitioning temperatures

The plots of elongation and stabilized austenite fraction versus partitioning time for quenching to 224°C and different partitioning temperatures, shown in Figure III-17 (a) and (c), illustrates that a PT of 300°C was actually too low to have sufficient carbon diffusion and austenite stabilization. Only in the first 100s, the elongation increased due to tempering of martensite and stabilization of around 5% austenite through limited carbon diffusion at the boundaries of the austenite grains, cfr. Figure III-15.

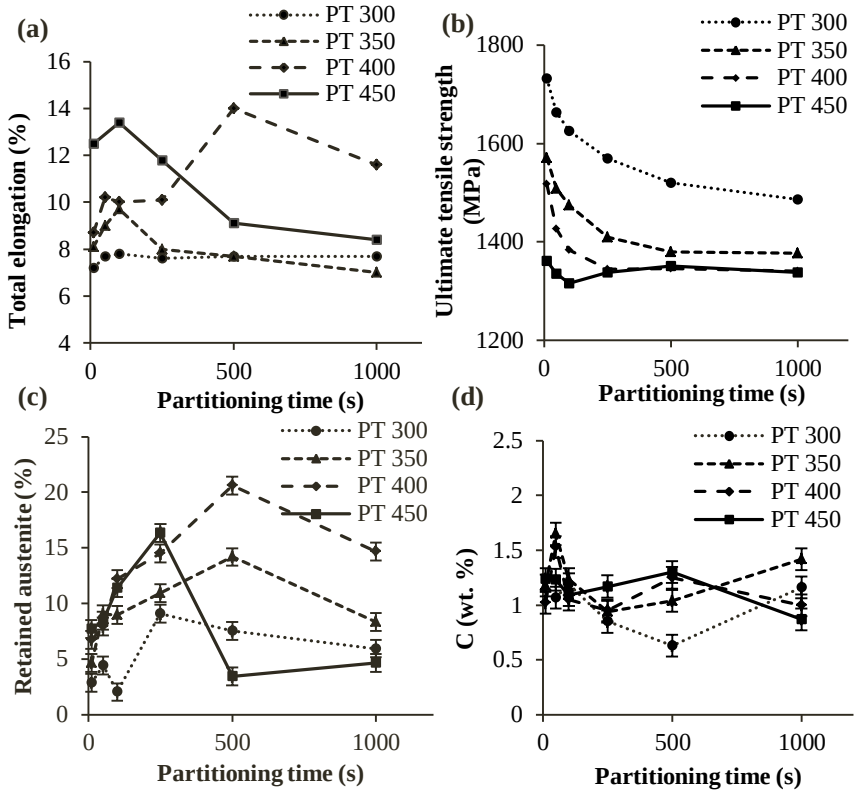

Figure III-17: (a) Total elongation (%), (b) ultimate tensile strength (MPa), (c) retained austenite fraction (%) and (d) C-content (wt.%) of the RA versus partitioning time for Q&P steel quenched to 224°C and partitioned at different temperatures: 300°C - 350°C - 400°C - 450°C

After 250s, the fraction of stabilized austenite increased to almost 10%. However, the ductility of the Q&P steel remained unchanged due to low mechanical stability of the austenite caused by its low carbon content of 0.85 ± 0.1% (cfr. Figure III-17 (d)) [33, 34]. Afterwards, the RA fraction remained constant with an increasing C-content indicating that C-diffusion giving mechanical stability to the austenite occurs *after* its stabilization. This difference in austenite stability is reflected in the stress-strain curves by the instantaneous strain hardening exponent in Figure III-18 (a) and (b) respectively.

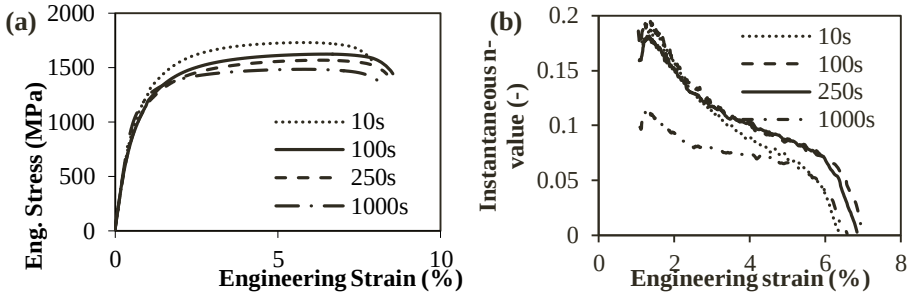

Figure III-18: (a) Engineering stress-strain curves and (b) instantaneous n-value versus engineering strain (%) of Q&P steel quenched to 224°C and partitioned at 300°C for 10s, 100s, 250s and 1000s

In the first 100s, stabilization of 5% austenite resulted in a flatter instantaneous n-value curve compared to 10s due to TRIP assisted deformation behaviour. Although more austenite was stabilized after 250s, the transformation of low-C austenite happened mainly in the beginning and no significant difference was observed with the curve of 100s. After 1000s, the austenite is more stable due to its higher C-content. As a consequence, the n-value at small strains is lower because of less transformation in the beginning and a more continuous transformation at larger strains, cfr. Figure III-18(b). The partitioning time to stabilize an austenite grain of 1µm in diameter was calculated to be 163min, based on the average diffusion distance (cfr. Figure III-15). Hence, at 300°C, very long partitioning times are needed for C-diffusion, stabilization and C-enrichment of the austenite.

A similar trend can be observed for partitioning at 350°C, cfr. Figure III-17 and Figure III-19. The total elongation increased until 100s due to stabilization of high-C austenite but decreased again after partitioning for 250s. Even though the highest retained austenite fractions were obtained after partitioning for 250s and 500s, C-diffusion at this temperature was not sufficient to have mechanical stabilization of the austenite. After partitioning for 1000s, the C-content increased to 1.5% with a decrease in retained austenite fraction due to its decomposition into bainite, which is reflected in the lower total elongation.

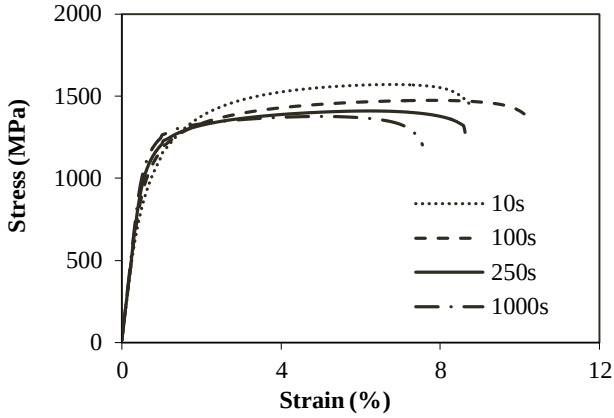

Figure III-19: Engineering stress-strain curves of Q&P steel quenched to 224°C and partitioned at 350°C for 10s, 100s, 250s and 1000s

The best time for annealing at 400°C was 500s because of the retained austenite fraction and the C-content of the austenite, and as a consequence the total elongation of the samples were the highest. The elongations after partitioning between 50s and 250s remained similar. Although the retained austenite fraction increased with longer partitioning times, its C-content decreased significantly. However, after 500s, the C-content increased simultaneously with the retained austenite fraction resulting in the highest ductility and continuous austenite to martensite transformation during plastic deformation, cfr. Figure III-20. In this condition, the diffusion coefficient of carbon (D_γ = 293 nm²/s) is high enough to have in 250s (from 250s to 500s) both a high C-content and retained austenite fraction. After 1000s partitioning at 400°C, the austenite fraction and its C-content decreased, probably due to the onset of austenite decomposition to ferrite and carbides, cfr. Figure III-13 (a).

The optimum time for partitioning at 450°C was 100s since at longer partitioning times the austenite started to decompose.

The time for partitioning should be determined first of all by the amount of retained austenite needed and secondly by the C-content required to give the desired mechanical stability of the retained austenite in the condition of absence of competing reactions.

The ultimate tensile strength was lower for higher partitioning temperatures due to progressive tempering of the martensite. Increasing the partitioning time softened the martensite further, resulting in a decreased strength, except for partitioning at 450°C after 250s due to decomposition of austenite.

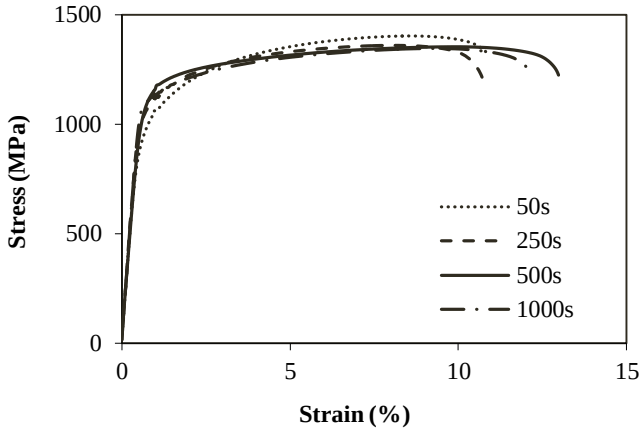

Figure III-20: Engineering stress-strain curves of Q&P steel quenched to 224°C and partitioned at 400°C for 50s, 250s, 500s and 1000s

III.5.3.2 The partitioning kinetics and mechanical properties at different quenching temperatures

The influence of the quenching temperature on the evolution of the total elongation and ultimate tensile strength is limited for Q&P steels partitioned at 400°C, which was the partitioning condition without competing reactions (cfr. Figure III-21).

The ultimate tensile strength (cfr. Figure III-21(b)) is not influenced by the quenching temperature and for all temperatures the decay is very similar, demonstrating that martensite tempering controls the ultimate tensile strength of Q&P steels.

The total elongation evolved towards 12%, whereby the time required to reach this depends on the quenching temperature. The samples quenched to 244°C reached their optimum retained austenite fraction faster than the samples quenched to 224°C, cfr. Figure III-21(c). As mentioned before, the time limiting step in partitioning is the diffusion of carbon in austenite [32]. At 244°C more austenite is available. Hence, in the same time frame a larger fraction can be stabilized by carbon pile-ups along the austenite/martensite grain boundaries [39], whereas the central part of the austenite will transform to fresh martensite during the final quenching. If the austenite fraction at the quenching temperature is lower, the carbon needs to diffuse a longer distance inside the austenite grains to stabilize the same amount. Hence, if all the austenite grains at the quenching temperature need to be stabilized completely, the required path length of carbon in austenite becomes larger and more time is needed, cfr.

Figure III-15. Similarly, the carbon content of the steel quenched to higher temperatures reached the maximum C-content faster (cfr. Figure III-21(d)).

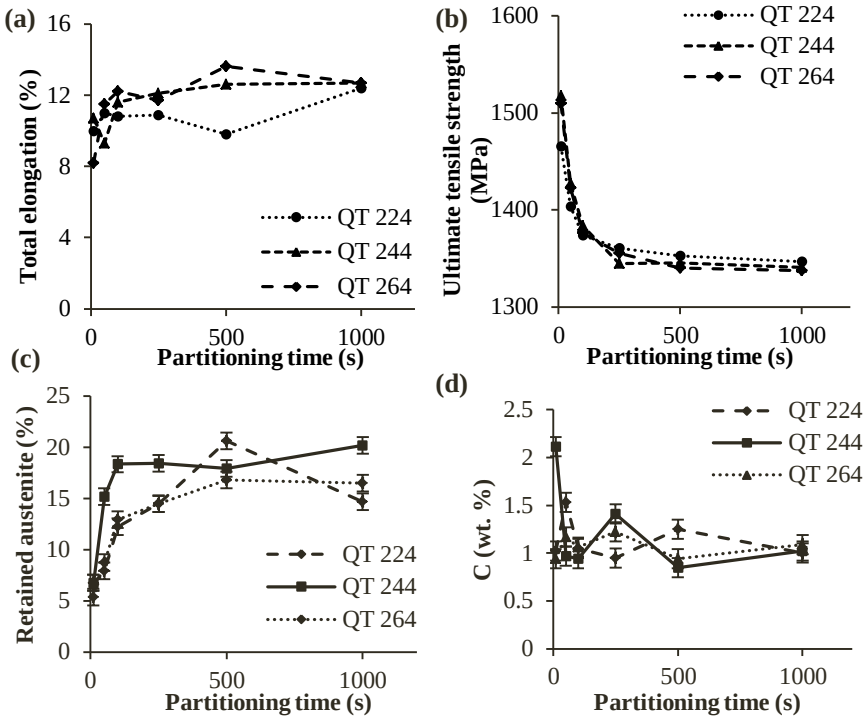

Figure III-21: (a) Total elongation (%) (b) ultimate tensile strength (MPa) (c) retained austenite fraction (%) and (d) C-content (wt.%) of RA versus partitioning time for Q&P steel quenched to different temperatures: 224°C - 244°C - 264°C and partitioned at 400°C

If the austenite fraction at the quenching temperature is too large (cfr. 264°C), the C-flux is lower due to the presence of less martensite. Thus it requires more time to deplete the martensitic matrix sufficiently to have austenite stabilization at the boundaries.

If the partitioning temperature is changed, the influence of the quenching temperature on the total elongation versus partitioning time becomes more substantial (cfr. Figure III-22).

Partitioning at 300°C (cfr. Figure III-22(a)) resulted in the strongest increase in elongation after quenching at 244°C. After quenching to 224°C, a small increase in elongation is observed after 50s partitioning, while at 264°C the elongation only starts to increase after longer partitioning times. At 300°C the carbon diffusion in austenite is very slow, cfr. Figure III-15. Consequently, for the lowest quenching temperature a limited fraction close to the martensite grain boundaries can be stabilized. By increasing the austenite fraction at the

quenching temperature, the stabilized portion increased. However, if the austenite fraction to be stabilized is too high, the time for the formation of these C pile-ups is larger, thus resulting in a very slow increase in stabilized austenite.

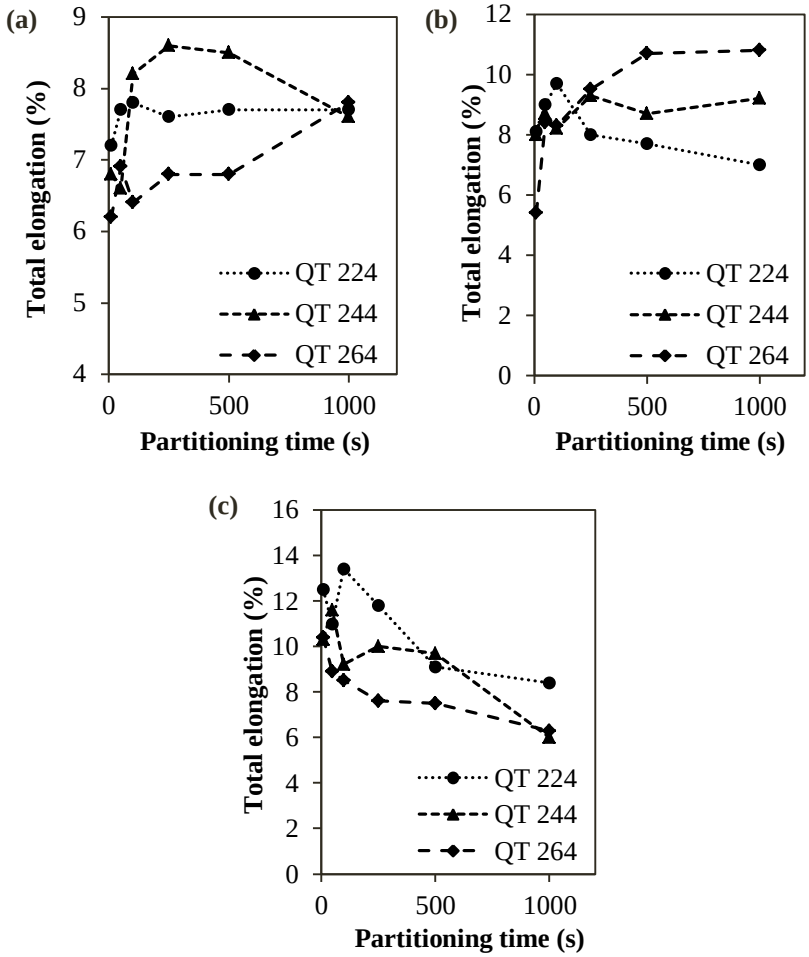

Figure III-22: Total elongation (%) versus partitioning time (s) for different quenching temperatures: 224°C - 244°C - 264°C and partitioning at (a) 300°C (b) 350°C (c) 450°C

For partitioning at 350°C (cfr. Figure III-22(b)), the total elongation peaks at 100s and 250s for quenching temperatures of 224°C and 244°C respectively. At longer partitioning times, the elongation drops again due to the formation of bainite. At 264°C, the stabilization of austenite can occur simultaneously with decomposition of part of the austenite into bainite, exhibiting much higher total elongation.

After partitioning at 450°C (cfr. Figure III-22 (c)), the total elongation decreases due to austenite decomposition. This process develops faster after quenching to higher quenching temperatures due to a larger possible decomposable austenite fraction.

III.5.3.3 Evolution of yielding behaviour as a function of the Q&P parameters

In Table III-2, the n-values and yield stresses of samples with varying quenching temperatures, partitioning temperatures and times are given. Figure III-23 (a) and (b) illustrate the yield stress evolution as a function of partitioning time for quenching temperatures 224°C, 244°C and 264°C and partitioning temperatures 300°C, 350°C, 400°C and 450°C respectively.

Table III-2: N-values and yield strength values for different quenching temperatures, partitioning temperature and times

PT = 400°C, Pt = 100s			QT = 224°C, Pt = 100s			QT = 224°C, PT = 400°C		
QT (°C)	n-value	YS (MPa)	PT (°C)	n-value	YS (MPa)	Pt (s)	n-value	YS (MPa)
224	0.132	1025	300	0.224	1007	10	0.143	963
244	0.135	1027	350	0.171	970	50	0.164	956
264	0.155	942	400	0.132	1025	100	0.132	1025
			450	0.209	833	250	0.121	1054
						500	0.073	1092
						1000	0.108	1095

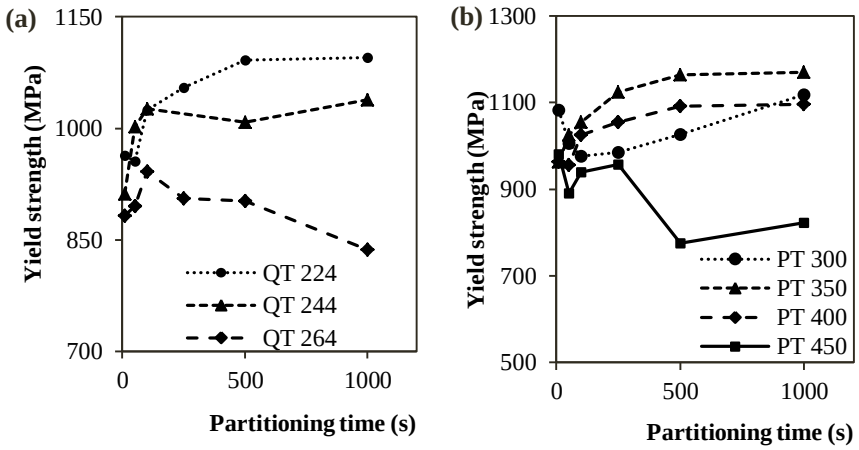

Figure III-23: (a) Yield strength as a function of partitioning time for quenching temperatures: 224°C - 244°C - 264°C and a partitioning temperature of 400°C (b) yield strength as a function of partitioning time for quenching to 224°C and partitioning temperatures: 300°C - 350°C - 400°C - 450°C

First, the influence of the quenching temperature on the yield strength and strain hardening behaviour is discussed. Increasing the quenching temperature to 264°C compared to 244°C and 224°C resulted in a slightly higher n-value and lower yield strengths as can be observed from Table III-2, the evolution of the yield strength versus partitioning time in Figure III-23(a) and the stress-strain curves in Figure III-24.

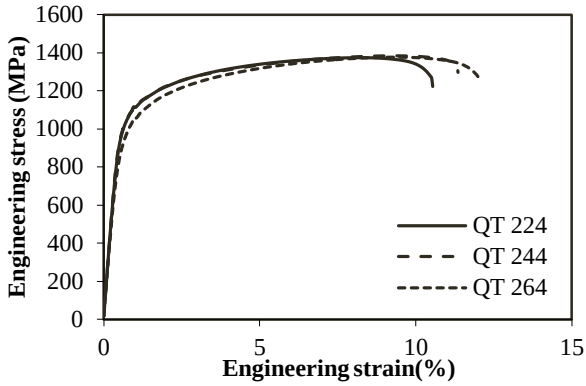

Figure III-24: Stress-strain curves for partitioning at 400°C for 100s with different quenching temperatures: 224°C – 244°C – 264°C

After quenching the samples to 224°C and partitioning for 100s, the n-values for partitioning at 300°C, 350°C, 400°C and 450°C were 0.224, 0.171, 0.132 and 0.209 respectively. Consequently, higher partitioning temperatures resulted in lower n-values except for 450°C since at this temperature austenite decomposition occurred. The stress-strain curves indicate a transition from continuous yielding to a higher, more discrete yield point, a decreasing strength and higher elongation with higher partitioning temperatures, cfr. Figure III-25.

If the partitioning time increased, the n-values decreased and yield strength increased together with a higher total elongation and lower ultimate tensile strength, cfr. Figure III-26. At shorter partitioning times the yielding is continuous due to the presence of mobile dislocations formed during the martensitic transformation [40]. As the partitioning time increases, these mobile dislocations may be pinned by interstitial atoms resulting in a higher, discrete yield strength.

The change in yield points and n-values with partitioning conditions is attributed to the presence of different fractions of phase and constituents. Austenite transformation gives strain hardening during plastic deformation. If fresh martensite is present in the microstructure prior to straining, this martensite locally causes stress concentrating effect and fast

transformation of austenite giving a lower yield point and initially higher n-value. If the austenite transforms continuously over the entire plastic regime, the yield point is higher and the strain hardening behaviour lower. Q&P samples with higher quenching temperatures, lower partitioning temperatures and shorter partitioning times have fresh martensite and as a consequence lower yield points and higher strain hardening behaviours.

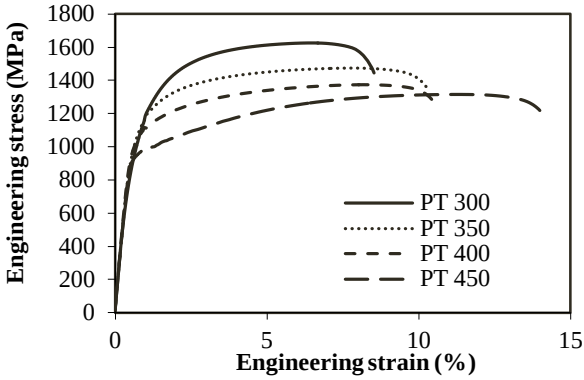

Figure III-25: Stress –strain curves for quenching to 224°C and partitioning to different temperatures: 300°C – 350°C – 400°C – 450°C for 100s

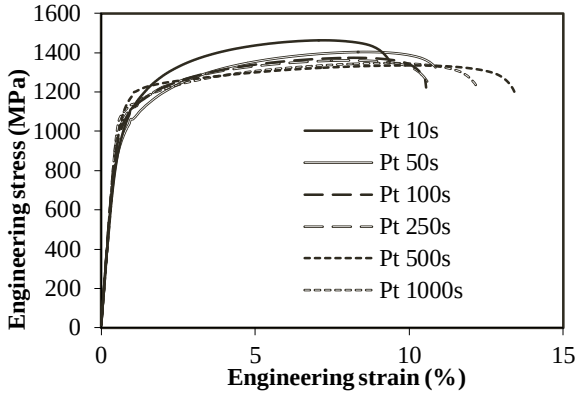

Figure III-26: Stress –strain curves for quenching to 224°C and partitioning to 400°C for different times: 10s, 50s, 100s, 250s, 500s and 1000s

III.5.3.4 The Koistinen-Marburger relationship

The Koistinen-Marburger equation was verified experimentally by varying the quenching temperature and conducting partitioning at 400°C for different times, cfr. Figure III-27. The retained austenite fractions determined experimentally with X-ray diffraction reached higher values than what was predicted from the theoretical equations.

At QT 264°C, 500s to 1000s were required to stabilize 16.8% retained austenite. This fraction is lower than the stabilised amount at lower quenching temperatures for the same time. At 224°C, 20.6% austenite was retained after partitioning for 500s while at 244°C, 20.2% was stabilized after 1000s holding at 400°C. If the quenching temperature is too high, the amount of C available in the martensite is insufficient to stabilize all the austenite. However due to kinetic effects i.e. pile-up formation in austenite at the grain boundary due to slow C-diffusion in austenite, 16.8% austenite was stabilized while parts of austenite grains with insufficient C-stabilisation transformed to high carbon martensite.

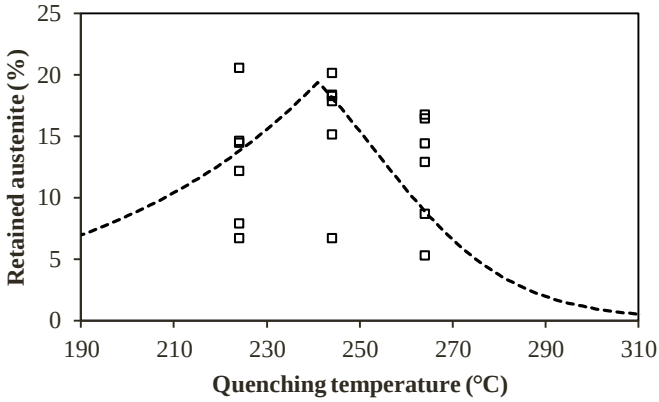

Figure III-27: Theoretical Koistinen-Marburger predictions with experimental data points after quenching at three temperatures 224°C, 244°C and 264°C, partitioning at 400°C for different times

Apparently, the retained austenite fraction is not really dependent on the quenching temperature if the partitioning step is well designed. However, not only the attainable retained austenite fraction determines the properties of the steel. Its carbon content [33, 41, 42] and the presence of fresh martensite [43-46] control the transformation stability and TRIP efficiency of the available austenite. Hence, 20% retained austenite is only effective if the austenite C-content is high enough to ensure chemical stability and if the deformation is not constrained by hard constituents in the matrix.

III.5.3.5 Relationship retained austenite fraction - mechanical properties

The total elongation increases and ultimate tensile strength decreases with higher retained austenite fractions (cfr. Figure III-28 (a) and (b)). This enhanced elongation is a result of the transformation of more retained austenite to martensite during straining, which is referred to as the transformation induced plasticity (TRIP) effect. The ultimate tensile strength

levels decrease due to stronger martensitic tempering after long partitioning heat treatments at higher temperatures to obtain high retained austenite fractions.

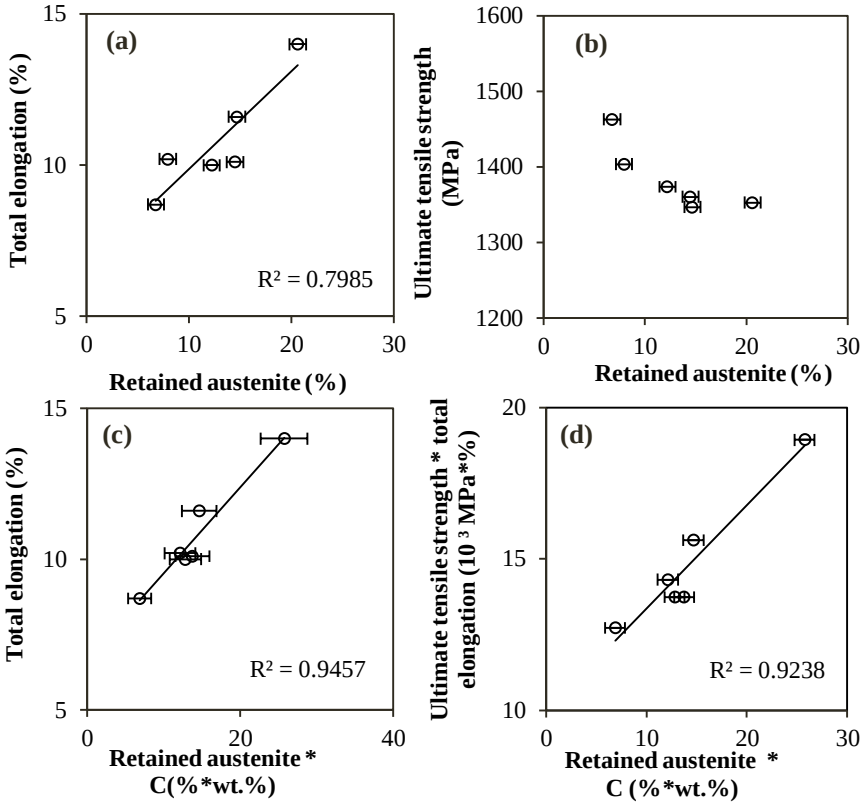

Figure III-28: (a) Total elongation (%) versus retained austenite fraction (%), (b) ultimate tensile strength (MPa) versus retained austenite fraction (%) and (c) total elongation (%) versus retained austenite fraction multiplied with its carbon content (%*wt.%) and (d) ultimate tensile strength multiplied with total elongation (MPa*%) versus retained austenite fraction multiplied with its carbon content (%*wt.%) for QT = 224°C

Additionally, the carbon content in the austenite determines its chemical stability influencing the mechanical properties. Therefore the retained austenite fraction multiplied with the C-content predicted the evolution of the total elongation of Q&P steel better (cfr. Figure III-28(c)) than only the retained austenite fraction. The fit between the product of ultimate tensile strength and total elongation, and the retained austenite fraction and carbon content is also excellent (cfr. Figure III-28 (d)).

III.5.3.6 Microstructural characterization

The microstructures for different partitioning temperatures and times were investigated by scanning electron microscopy. The quenching temperature was kept constant, 224°C and the partitioning times were selected as 50s, 100s and 500s.

In Figure III-29, the SEM micrographs after partitioning at 300°C are given. In all conditions, tempered martensite with small lath-shaped carbides was present. After 50s, cfr. Figure III-29 (a), the retained austenite cannot be resolved from the fresh martensite. However after longer partitioning times, small retained austenite grains can be observed whereby islands consisting partially of retained austenite and fresh martensite appear due to partial stabilisation of austenite at this partitioning temperature.

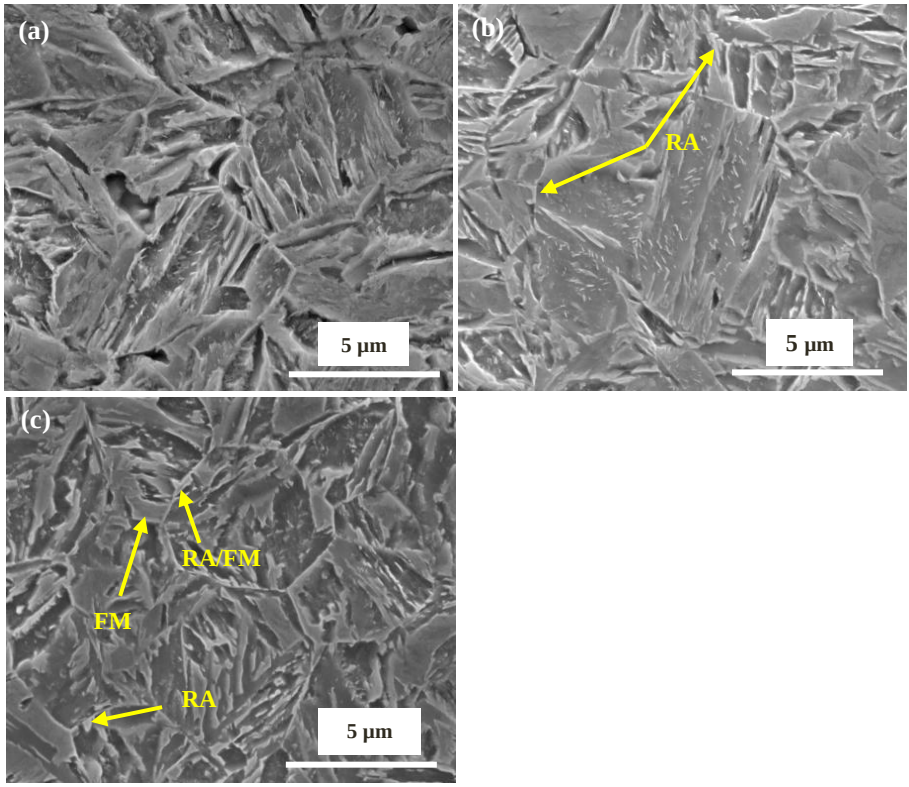

Figure III-29: SEM images of Q&P steel after quenching to 224°C and partitioning at 300°C for (a) 50s (b) 100s and (c) 500s – RA : retained austenite, FM: fresh martensite

In all the scanning electron micrographs of Q&P steel after partitioning at 350°C, retained austenite and fresh martensite constituents could be detected, cfr. Figure III-30. No signs of austenite decomposition into 'carbide-free' bainite could be observed.

After partitioning at 400°C for 50s, cfr. Figure III-31(a), a lot of fresh martensite blocks were detected. With increasing partitioning time, this fraction decreased by replacement with stabilized austenite, cfr. Figure III-31 (b-c). The optimal partitioning condition regarding the maximum amount of retained austenite without the presence of fresh martensite was identified as partitioning at 400°C for 500s, hence in Figure III-31(c) no fresh martensite could be observed.

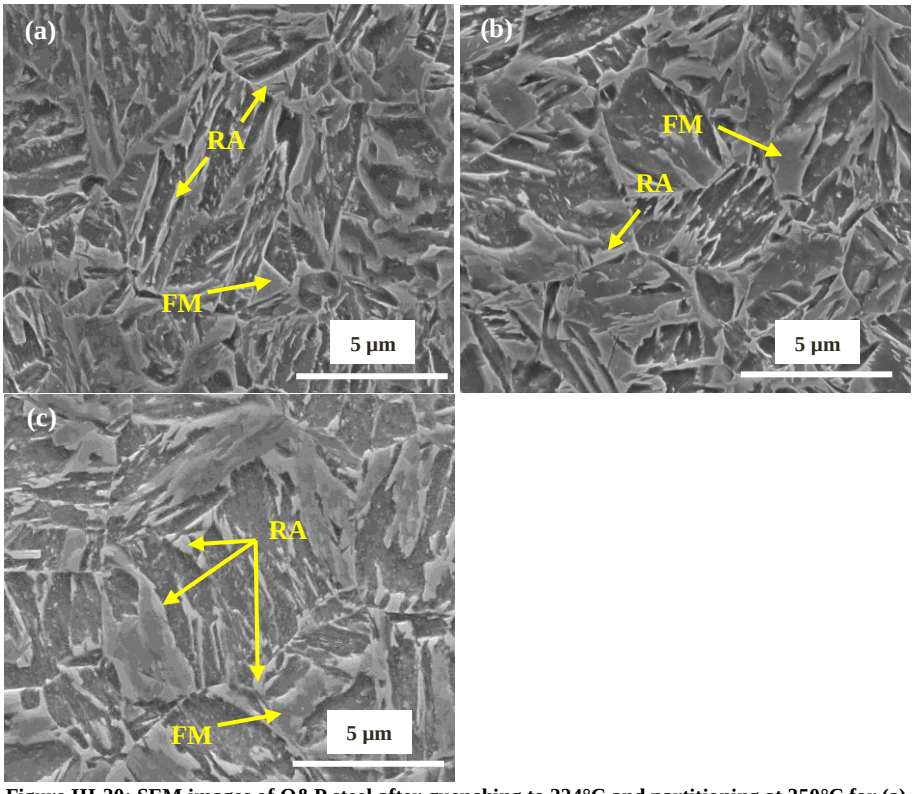

Figure III-30: SEM images of Q&P steel after quenching to 224°C and partitioning at 350°C for (a) 50s (b) 100s and (c) 500s – RA : retained austenite, FM: fresh martensite

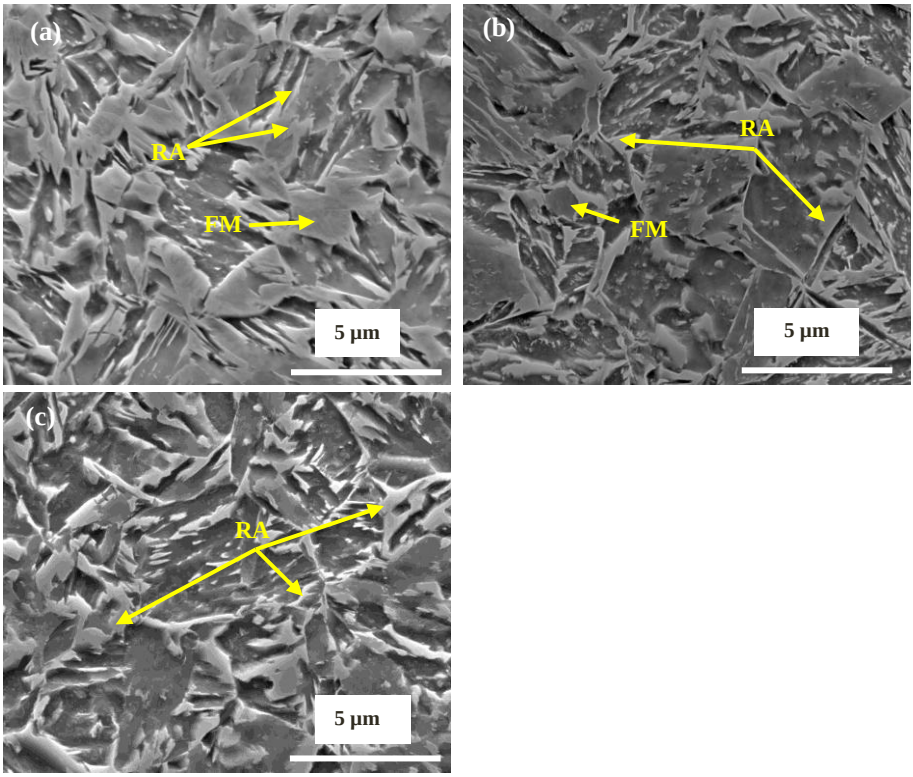

Figure III-31: SEM images of Q&P steel after quenching to 224°C and partitioning at 400°C for (a) 50s (b) 100s and (c) 500s – RA : retained austenite, FM: fresh martensite

After short partitioning times at 450°C, the microstructure consists of retained austenite and fresh martensite, cfr. Figure III-32(a). The optimal condition for these parameters were partitioning for 100s, cfr. Figure III-32(b) and as a consequence only retained austenite is present in this microstructure. After longer partitioning times, the retained austenite started to decompose into ferrite and carbides. This can be observed in the micrograph after 500s, cfr. Figure III-32(c). Part of the austenite is still retained while the other part transformed to a ferritic phase, as is illustrated by the grains indicated by DA (decomposed austenite). Moreover, the lath-structure which originated from stabilization of austenite grains in between the martensite laths mostly disappeared presumably due to their decomposition.

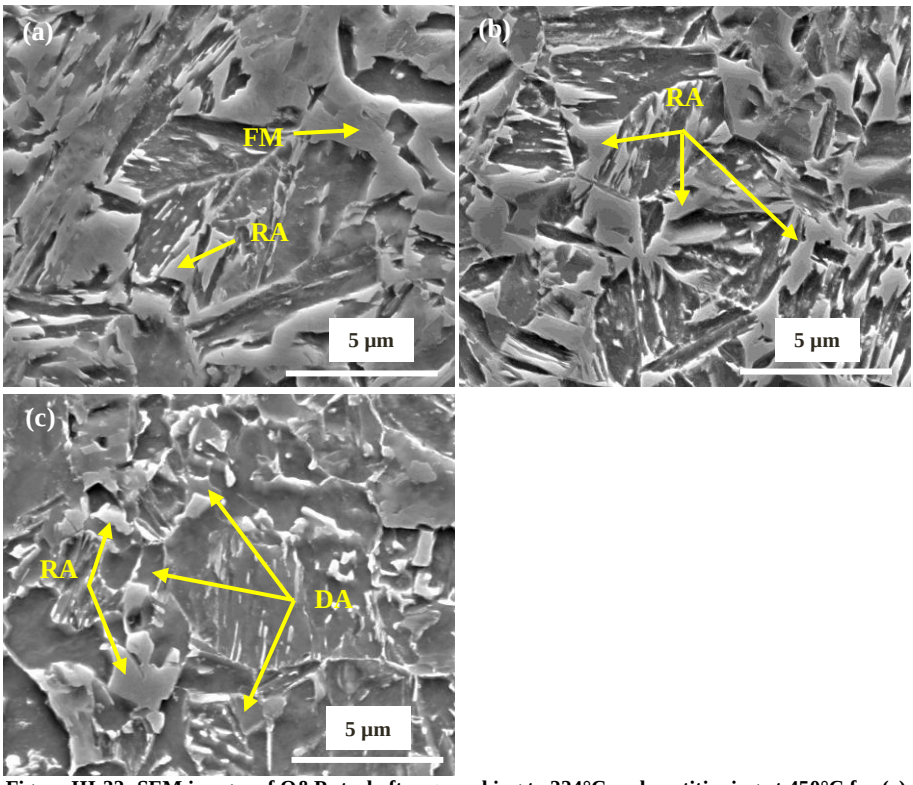

Figure III-32: SEM images of Q&P steel after quenching to 224°C and partitioning at 450°C for (a) 50s (b) 100s and (c) 500s – RA : retained austenite, FM: fresh martensite, DA: decomposed austenite

The influence of the heat treatment parameters on the microstructures was studied more in detail using EBSD. The image quality maps with the austenite grains in green for different heat treatment conditions are given in Figure III-33. The fresh martensite fraction was calculated using grain average low image quality points. Any distortions to the crystal lattice within the diffracting volume will produce lower quality (more diffuse) diffraction patterns. This enables the IQ parameter to be used to give a qualitative description of the strain distribution in the microstructure. The quantification of the phases is summarized in Table III-3.

The influence of the quenching temperature is illustrated in Figure III-33 (a-b-c) for partitioning conditions: 400°C for 500s. At higher quenching temperatures, the retained austenite fraction remained the same however due to an increasing austenite fraction at the quenching temperature, the fresh martensite fraction enlarged (cfr. Table III-3). These results were also obtained previously from the XRD data.

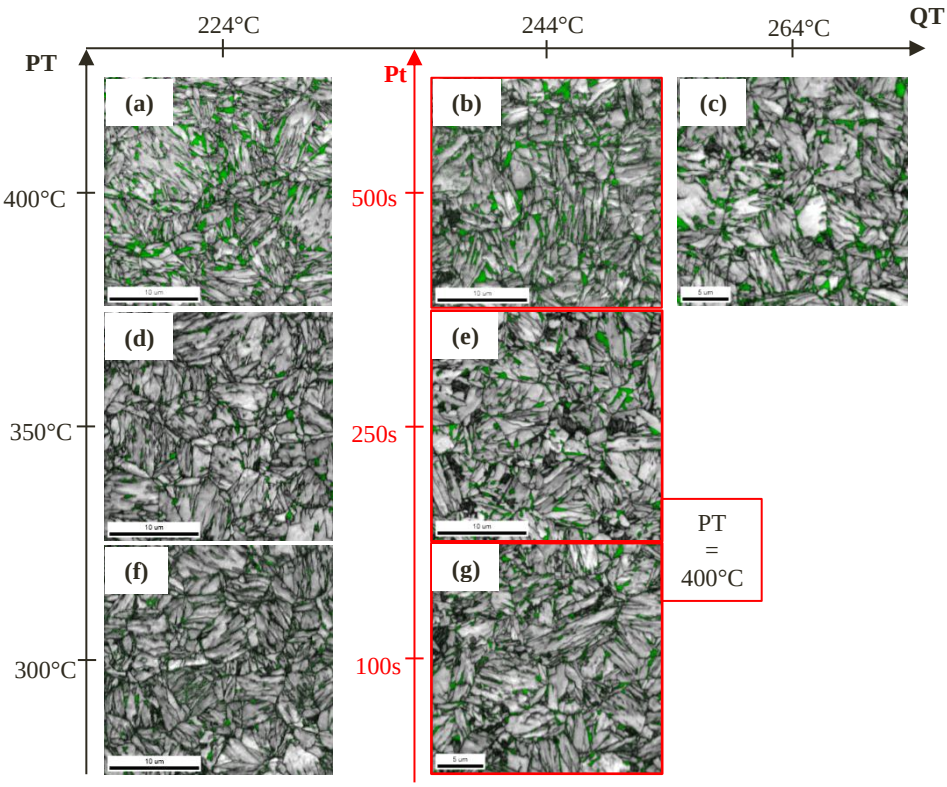

Figure III-33: Image quality maps of Q&P heat treated samples with austenite in green at different quenching temperatures (a) 224°C, (b) 244°C and (c) 264°C for partitioning at 400°C for 500s; different partitioning temperatures (a) 400°C, (d) 350°C and (f) 300°C for quenching to 224°C and partitioning for 500s; different partitioning times (b) 100s, (e) 250s and(g) 500s for quenching to 244°C and partitioning at 400°C

Table III-3: Retained austenite and fresh martensite fractions obtained from EBSD scans of Q&P heat treated samples with different quenching temperatures 224°C, 244°C and 264°C for partitioning at 400°C for 500s; with different partitioning temperatures for quenching to 224°C and partitioning times of 500s; with different partitioning times (100s, 250s and 500s) for quenching to 244°C and partitioning at 400°C

	RA	FM		RA	FM	RA	FM
PT (Pt = 500s)	**224°C**		**Pt (PT = 400°C)**	**244°C**		**264°C**	
400°C	14.1	2.3	**500s**	14	7.8	12.4	10
350°C	12.4	3.9	**250s**	10.6	12.3		
300°C	9.2	7.5	**100s**	11.4	11.6		

Lowering the partitioning temperature results in more fresh martensite and less retained austenite at the same quenching temperature and same partitioning times, cfr. Figure

III-33 (a-d-f). By increasing the partitioning time, cfr. Figure III-33 (b-e-g), the retained austenite fraction increased and fresh martensite fraction decreased as the partitioning has proceeded longer. These results are inherently connected to the kinetics of C-diffusion controlling the partitioning stage.

Part of the austenite cannot be resolved with EBSD. Therefore TEM is required to study the fine austenite grains in between the martensite laths. These grains, illustrating a Kurdjumov-Sachs orientation relationship in the diffraction pattern, have width dimensions of 20 to100 nm, cfr. Figure III-34.

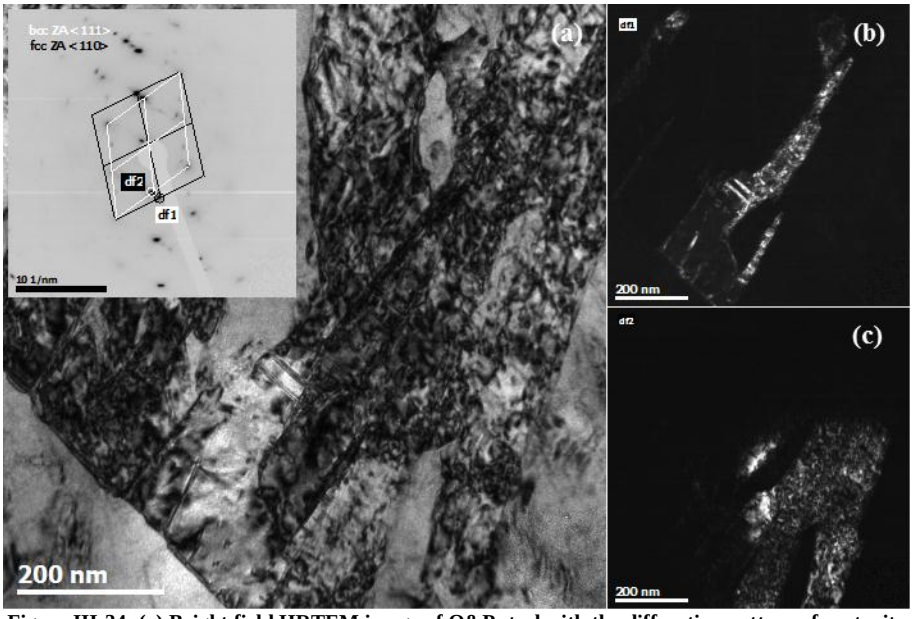

Figure III-34: (a) Bright field HRTEM image of Q&P steel with the diffraction pattern of austenite and martensite (b) dark field image of df1 illustrating an interlath austenite grain (c) dark field image of df2 being martensite

Kozeschnik et al. [47] reported that Si strongly suppresses carbide precipitation in austenite, but it is less effective in ferrite (or martensite) because the driving force for precipitation is too high due to the low solubility of carbon in ferrite.

Scanning electron images of the quenched sample and Q&P samples at different partitioning temperatures were studied to detect the presence of carbides, cfr. Figure III-35.

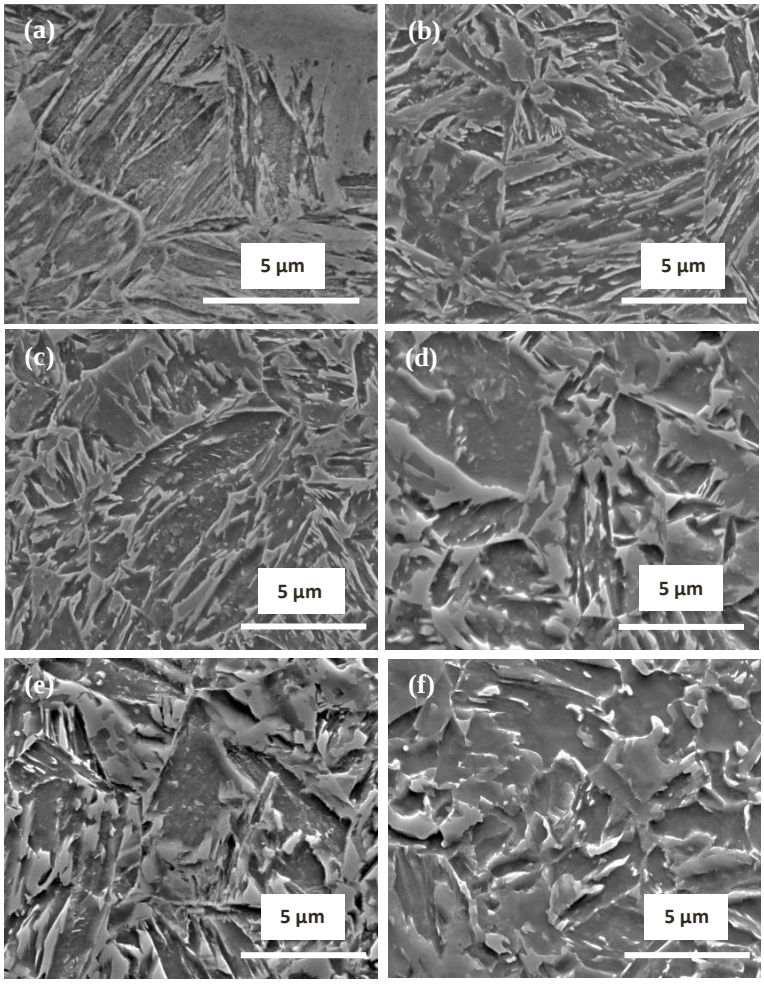

Figure III-35: SEM images of (a) quenched sample, Q&P heat treated samples quenched to 224°C, partitioned at (b) 300°C for 500s, (c) 350°C for 500s, (d) 400°C for 500s, (e) 450°C for 100s and (f) 450°C for 500s

In Figure III-35(a), the SEM picture of a hot rolled sample austenitized and quenched at 20°C/s to room temperature illustrates that no carbides were formed during cooling. A substructure which is related to an etching effect rather than the effect of real carbides was seen inside the martensite grains. After partitioning at all temperatures except at 450°C for 500s, a small fraction of lath-carbides were detected, cfr. Figure III-35 (b-e). No significant fraction of precipitates was formed and no change in fraction was observed for different conditions. At 450°C, these carbides were also present before the decomposition, cfr. Figure III-35 (e) however after 500s, no lath-carbides were found, cfr. Figure III-35 (f).

Nevertheless large, globular carbides were detected as was expected from the tempering behavior of the martensite.

As a conclusion we can say that although not predicted with DSC, some small lath-type carbides were present in the material. Nevertheless, the remaining C-content in the matrix was still sufficiently high to stabilize 20% retained austenite. Hence, the presence of these carbides did not interfere with the aim of the Q&P heat treatment cycle.

TEM measurements on tempered martensite in Q&P heat treated samples revealed different lattices or substructures in the diffraction patterns, cfr. Figure III-36. A martensite (110) lattice and two cementite lattices with zone axes of (125) and (013) were distinguished. The dark field images illustrated two types of carbides: large lath-type (in the range of 100 nm length) and small round (8.07 nm² averaged) carbides. The lath-type carbides were identified with energy dispersive spectroscopy (EDS) on a carbon replica as Fe_3C whereas the small round carbides contained manganese besides iron and carbon, cfr. Figure III-37.

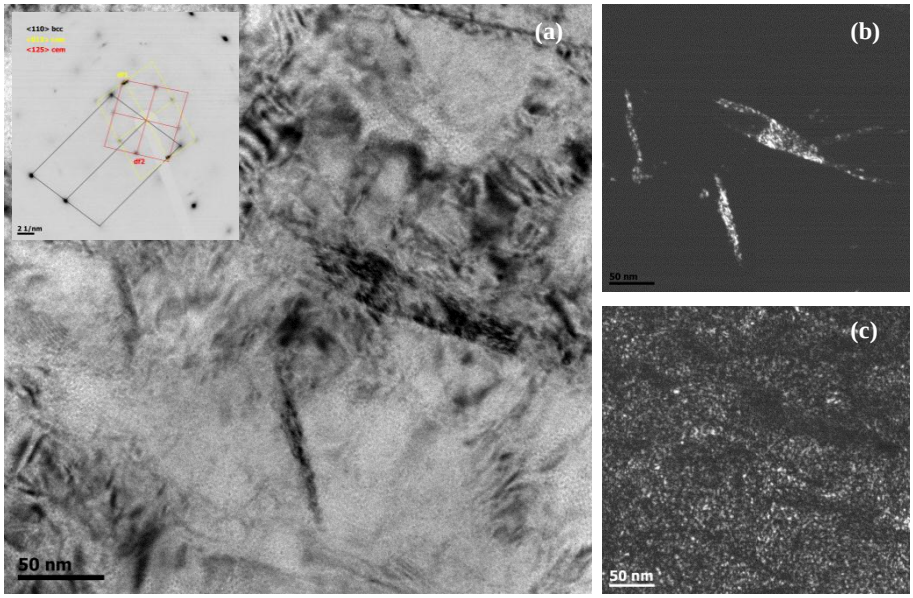

Figure III-36: (a) Bright field image with diffraction pattern of bcc and cementite and corresponding the dark field images of cementite by (b) df1 and (c) df2 of a Q&P sample heat treated by quenching to 224°C and partitioning et 400°C for 500s

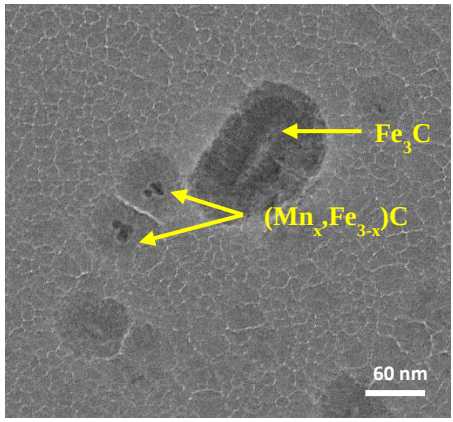

Figure III-37: STEM image of a carbon replica with larger and smaller carbides identified as Fe_3C and $(Mn_xFe_{3-x})C$ respectively

III.6. Conclusions

0.25C1.5Si3Mn steel was subjected to Q&P heat treatment cycles which were designed with the aid of dilatometric and DSC experiments. The influence of the quenching temperature, partitioning temperature and times on the mechanical properties of Q&P steel were studied and the results could by summarized in the following conclusions:

Influence of the quenching temperature: The stabilization of the same retained austenite fraction occurred faster with a larger austenite fraction formed at a higher quenching temperature. This is due to kinetic effects probably related to the formation of C pile-ups near the martensite-austenite grain boundaries. However, if the austenite fraction is too high, the stabilization is slower due to a lower available C-content in the martensitic matrix.

Influence of the partitioning temperature: Partitioning below 300°C resulted in the formation of ε-carbides depleting the available carbon for partitioning. Between 300°C and 370°C (B_s), the formation of low-carbide bainite after 100s caused a decrease of the retained austenite fraction but an increase in the C-content. Partitioning between 370°C and 400°C was the optimum partitioning temperature range, which enhanced C-diffusivity without competing reactions. Above 400°C, decomposition of austenite and tempering of martensite forming cementite occurred, decreasing strongly the RA fraction and total elongation.

Influence of the partitioning time: The time required for partitioning is determined by two factors: the retained austenite fraction and its required C-content to give mechanical stability. If the partitioning temperature is lower, the time to obtain a high fraction of retained austenite with high C-content is longer. Long partitioning times are limited by competing

reactions. The peak temperature for austenite decomposition was 450°C. Hence, partitioning at this temperature was still possible although it was limited to 100s for the studied composition.

These observations were additionally confirmed by EBSD analysis on selected samples. The presence of cementite was confirmed however it was not detrimental for Q&P processing with the stabilization of considerable amounts of retained austenite.

A linear correspondence could be found between the total elongation and retained austenite fraction multiplied with the C-concentration, indicating the importance of both high retained austenite fraction and sufficient C-content. The ultimate tensile strength of Q&P steels depends mainly on martensite tempering. The yielding behaviour was continuous at short partitioning times but changed to yield point elongation for longer times due to martensitic tempering. The presence of fresh martensite caused an initial higher strain hardening due to substantial austenite transformation at low strains.

III.7. Acknowledgements

This research was partly funded by the governmental institute for the Promotion of Innovation by Science and Technology in Flanders (IWT) and was supported by European project “RFCS-CT-2011-00017 “New advanced high strength steels by quenching and partitioning process (NewQ&P)”.

References

1. J. G. Speer, D. K. Matlock, B. C. De Cooman, and J. G. Schroth: 'Carbon partitioning into austenite after martensite transformation', *Acta Materialia*, 2003, **51**, 2611-2622.

2. J. G. Speer, D. V. Edmonds, F. C. Rizzo, and D. K. Matlock: 'Partitioning of carbon from supersaturated plates of ferrite, with application to steel processing and fundamentals of the bainite transformation', *Materials Science*, 2004, **8**, 219-237.

3. J. G. Speer, F. C. R. Assunção, D. K. Matlock, and D. V. Edmonds: 'The “quenching and partitioning” process: Background and recent progress', *Materials Research*, 2005, **8**, 417-423.

4. C. Y. Wang, J. Shi, W. Q. Cao, and H. Dong: 'Characterization of microstructure obtained by quenching and partitioning process in low alloy martensitic steel', *Materials Science and engineering*, 2010, **527**, 3442-3449.

5. A. J. Clarke, J. G. Speer, M. K. Miller, R. E. Hackenberg, D. V. Edmonds, D. K. Matlock, F. C. Rizzo, K. D. Clarke, and E. D. Moor: 'Carbon partitioning to austenite from martensite or bainite during the quench and partition process: A critical assessment', *Acta Materialia*, 2008, **56**, 16-22.

6. H. Y. Li, X. W. Lu, X. C. Wu, Y. A. Min, and X. J. Jin: 'Bainitic transformation during the two-step quenching and partitioning process in a medium carbon steel containing silicon', *Materials Science and engineering*, 2010, **527**, 6255-6259.

7. D. Kim, J. G. Speer, and B. C. De Cooman: 'Isothermal transformation of a cmnsi steel below the ms temperature', *Metallurgical and Materials Transactions A*, 2010, **42**, 1575-1585.

8. D. Kim, J. G. Speer, and B. C. De Cooman: 'The isothermal transformation of low-alloy low-c cmnsi steels below ms', *Materials Science Forum*, 2010, **654-656**, 98-101.

9. M. J. Santofimia, L. Zhao, and J. Sietsma: 'Overview of mechanisms involved during the quenching and partitioning process in steels', *Metallurgical and Materials Transactions A - Physical Metallurgy and Materials Science*, 2011, **42A**(12), 3620-3626.

10. D. A. Porter, K. E. Easterling, and M. Sherif: 'Phase transformations in metals and alloys, third edition (revised reprint)', 2009, Taylor & Francis.

11. A. Grajcar, M. Kaminska, M. Opiela, P. Skrzypczyk, B. Grzegorczyk, and E. Kalinowksa-Ozgowicz: 'Segregation of alloying elements in thermomechanically rolled medium-mn multiphase steels', *Journal of Achievements in Materials and Manufacturing Engineering*, 2012, **55**(2), 259-264.

12. M. J. Santofimia, T. Nguyen-Minh, L. Zhao, R. Petrov, I. Sabirov, and J. Sietsma: 'New low carbon q&p steels containing film-like intercritical ferrite', *Materials Science and engineering*, 2010, **527**, 6429-6439.

13. W. Li, L. Wenjuan, and F. Weijun: 'Industry trials of c-si-mn steel treated by q&p concept in baosteel', SAE 2010 World Congress & Exhibition, Detroit, Michigan, USA, 2010.

14. D. Hauserová, M. Duchek, J. Dlouhý, and Z. Nový: 'Properties of advanced experimental cmnsimo steel achieved by qp process', *Procedia Engineering*, 2011, **10**, 2961-2966.

15. N. Zhong, X. Wang, Y. Rong, and L. Wang: 'Interface migration between martenisite and austenite during quenching and partitioning (q&p) process', *Materials Science and Technology*, 2006, **22**(6), 4.

16. W. S. Owen: 'The effect of silicon on the kinetics of tempering', *Trans. ASM*, 1954, **46**, 812-828.

17. E. De Moor, J. G. Speer, D. K. Matlock, J.-H. Kwak, and S.-B. Lee: 'Effect of carbon and manganese on the quenching and partitioning response of cmnsi steels', *ISIJ International*, 2011, **51**, 137-144.

18. Mathew Peet and H. K. D. H. Bhadeshia: 'Www.Msm.Cam.Ac.Uk/map/steel/programs/mucg83.Html'.

19. K. Nakase and I. M. Bernstein: 'The effect of alloying elements and microstructure on the strength and fracture resistance of pearlitic steel', *Metallurgical Transactions A*, 1988, **19**(11), 2819-2829.

20. B. D. Cullity: 'Elements of x-ray diffraction', 1956, New Jersey, USA, Addison-Wesley Publishing Company, Inc.

21. C. Suryanarayana and M. G. Norton: 'X-ray diffraction: A practical approach', 1998, New York, Plenum Publishing Corporation.

22. E. J. Mittemeijer: 'Analysis of the kinetics of phase transformations', *Journal of Materials Science*, 1992, **27**(15), 3977-3987.

23. D. P. Koistinen and R. E. Marburger: 'A general equation prescribing extend of austenite-martensite tranformation in pure fe-c alloys and plain carbon steels', *Acta Materialia*, 1959, **7**, 59.

24. S. M. C. van Bohemen: 'The bainite and martensite start temperature calculated with an exponential carbon dependence', *Materials Science and Technology*, 2012, **28**(4), 487-495.

25. J. Wu, P. J. Wray, C. I. Garcia, M. Hua, and A. J. Deardo: 'Image quality analysis: A new method of characterizing microstructures', *ISIJ International*, 2005, **45**(2), 254-262.

26. M. J. Santofimia, R. H. Petrov, L. Zhao, and J. Sietsma: 'Microstructural analysis of martensite constituents in quenching and partitioning steels', *Materials Characterization*, 2014, **92**(0), 91-95.

27. M. J. Santofimia, L. Zhao, R. Petrov, C. Kwakernaak, W. G. Sloof, and J. Sietsma: 'Microstructural development during the quenching and partitioning process in a newly designed low-carbon steel', *Acta Materialia*, 2011, **59**, 6059-6068.

28. D. V. Edmonds, K. He, F. C. Rizzo, B. C. D. Cooman, D. K. Matlock, and J. G. Speer: 'Quenching and partitioning martensite—a novel steel heat treatment', *Materials Science and engineering*, 2006, **438-440**, 25-34.

29. F. L. H. Gerdemann: 'Microstructure and hardness of 9260 steel heat-treated by the quenching and partitioning process', Aachen University of Technology, Germany, 2004.

30. E. De Moor, C. Föjer, J. Penning, A. J. Clarke, and J. G. Speer: 'Calometric study of carbon partitioning from martensite into austenite', *Physical Review B*, 2010, **82**, 104-210.

31. Cheng Liu, C.M. Brakman, B.M. Korevaar, and E. J. Mittemeijer: 'The tempering of iron-carbon martensite; dilatometric and calorimetric analysis', *Metallurgical Transactions A*, 1988, **19**(A), 2415-2426.

32. M. J. Santofimia, J. G. Speer, A. J. Clarke, L. Zhao, and J. Sietsma: 'Influence of interface mobility on the evolution of austenite–martensite grain assemblies during annealing', *Acta Materialia*, 2009, **57**, 4548-4557.

33. N. H. van Dijk, A. M. Butt, L. Zhao, J. Sietsma, S. E. Offerman, J. P. Wright, and S. van der Zwaag: 'Thermal stability of retained austenite in trip steels studied by synchrotron x-ray diffraction during cooling', *Acta Materialia*, 2005, **53**, 5439-5447.

34. R. Blondé, E. Jimenez-Melero, L. Zhao, J. P. Wright, E. Brück, S. van der Zwaag, and N. H. van Dijk: 'High-energy x-ray diffraction study on the temperature-dependent mechanical stability of retained austenite in low-alloyed trip steels', *Acta Materialia*, 2012, **60**(2), 565-577.

35. C. Zhao, D. Tang, H.-T. Jiang, S.-S. Jhao, and H. Li: 'Process simulation and microstructure analysis of low carbon si-mn quenched and partitioned steel', *Journal of Iron and Steel Research, International*, 2008, **15**(4), 82-85.

36. P. V. Morra, A. J. Böttger, and E. J. Mittemeijer: 'Decomposition of iron-based martensite: A kinetic analysis by means of differential scanning calorimetry and dilatometry', *Journal of Thermal Analysis and Calorimetry*, 2001, **64**, 905-914.

37. S. T. Wardle, L. S. Lin, A. Cetel, and B. L. Adams: 'Orientation imaging microscopy: Monitoring residual stress profiles in single crystals using an image-quality parameter, iq', 52nd Annual Meeting of the Microscopy Society of America, San Fransisco, 1994, San Francisco Press, 680-681.

38. T. Gladman: 'The physical metallurgy of microalloyed steels', 1997, London, England, Institute of Materials.

39. M. Gouné, F. Danoix, S. Allain, and O. Bouaziz: 'Unambiguous carbon partitioning from martensite to austenite in fe–c–ni alloys during quenching and partitioning', *Scripta Materialia*, 2013, **68**(12), 1004-1007.

40. D.-W. Suh, S.-J. Park, T.-H. Lee, C.-S. Oh, and S.-J. Kim: 'Influence of al on the microstructural evolution and mechancial behaviour of low carobn, mangenese transformation-iduced plasticity steel', *Metallurgical and Materials Transactions A*, 2010, **41**, 397-408.

41. E. Jimenez-Melero, N. H. van Dijk, L. Zhao, J. Sietsma, S. E. Offerman, J. P. Wright, and S. van der Zwaag: 'The effect of aluminium and phosphorus on the stability of individual austenite grains in trip steels', *Acta Materialia*, 2009, **57**(2), 533-543.

42. E. Jimenez-Melero, N. H. van Dijk, L. Zhao, J. Sietsma, S. E. Offerman, J. P. Wright, and S. van der Zwaag: 'Characterization of individual retained austenite grains and their stability in low-alloyed trip steels', *Acta Materialia*, 2007, **55**(20), 6713-6723.

43. I. B. Timokhina, P. D. Hodgons, and E. V. Pereloma: 'Effect of microstructure on the stability of retained austenite in transformation-induced-plasticity steels', *Metallurgical and Materials Transactions A*, 2004, **35**, 2331-2340.

44. D. De Knijf, R. Petrov, C. Föjer, and L. A. I. Kestens: 'Effect of fresh martensite on the stability of retained austenite in quenching & partitioning steel', *Materials Science and engineering A*, 2014, **615**(0), 107-115.

45. P. J. Jacques, J. Ladriere, and F. Delannay: 'On the influence of interactions between phases on the mechanical stability of retained austenite in transformation-induced plasticity multiphase steels', *Metallurgical and Materials Transactions A - Physical Metallurgy and Materials Science*, 2001, **32**(11), 2759-2768.

46. J. Chiang, B. Lawrence, J. D. Boyd, and A. K. Pilkey: 'Effect of microstructure on retained austenite stability and work hardening of trip steels', *Materials Science and Engineering: A*, 2011, **528**(13–14), 4516-4521.

47. E. Kozeschnik and H. K. D. H. Bhadeshia: 'Influence of silicon on cementite precipitation in steels', *Materials Science and Technology*, 2008, **24**(3), 343-347.

CHAPTER IV

IN-SITU AUSTENITE-MARTENSITE INTERFACE MOBILITY STUDY DURING PARTITIONING

Extended version of

D. De Knijf, M. J. Santofimia , H. Shi, V. Bliznuk, C. Föjer , R. Petrov and W. Xu: 'In-situ austenite-martensite interface mobility study during annealing', Acta Materialia, 2015, 90, 161-168.

IV. IN-SITU AUSTENITE-MARTENSITE INTERFACE MOBILITY STUDY DURING PARTITIONING

IV.1. Introduction

In literature, indirect proves of grain boundary movement by SEM and TEM images were observed by Zhong *et al.* and addressed to Fe-diffusion [1]. Santofimia *et al.* [2] modelled grain boundary movement and its influence on the retained austenite fraction and its carbon content for different activation energies. In this chapter, two methods were used to study grain boundary movement by *(i)* using the experimental evolution of the retained austenite fraction and its C-content and compare these with the predictions of the model, *(ii)* HR-TEM experiments with a heating stage to simulate the partitioning stage and follow the grain boundary movement of an austenite-martensite interface in-situ.

IV.2. Experimental kinetic results compared with modelled evolutions with different grain boundary mobilities

Since in literature no experimental observations of grain boundary movement existed, several well-chosen activation energies were assigned to the boundary mobility for modelling the partitioning stage [2]. For an immobile grain boundary, an infinite activation energy was used whereas for a semi-mobile interface an arbitrary activation energy of 180kJ/mol was employed. To have an idea about the nature of the austenite-martensite grain boundary, the results of the volume fraction and C-content versus partitioning time were compared with experimental values. The samples were heat treated by quenching to the corresponding temperature (QT = 244°C) i.e. an equal amount of martensite formed during quenching, and by the same partitioning conditions (PT = 400°C).

The experimental evolution of the C-content and retained austenite fraction are plotted on top of the modelled curves with a scaling factor of 10 and 50 respectively (cfr. Figure IV-1). This scaling factor suggests that in reality partitioning proceeds slower than predicted by the model. The modelled evolution with a semi-mobile grain boundary predicts the experimental evolution of retained austenite fraction in Figure IV-1(b). The modelled plateau in the retained austenite fraction versus partitioning time is also observed experimentally. C-diffusion stabilizes austenite to some extent, being about 16% in this case.

Afterwards, time is required to enrich this austenite with carbon as can be seen in Figure IV-1(a).

The modelled evolution of the C-content corresponds not entirely with the experimental values. In the beginning it follows the semi-mobile boundary model however after 250s the C-content drops to the values predicted with the immobile model. This is related with the fact that the retained austenite fraction increases to higher levels without further enrichment in C.

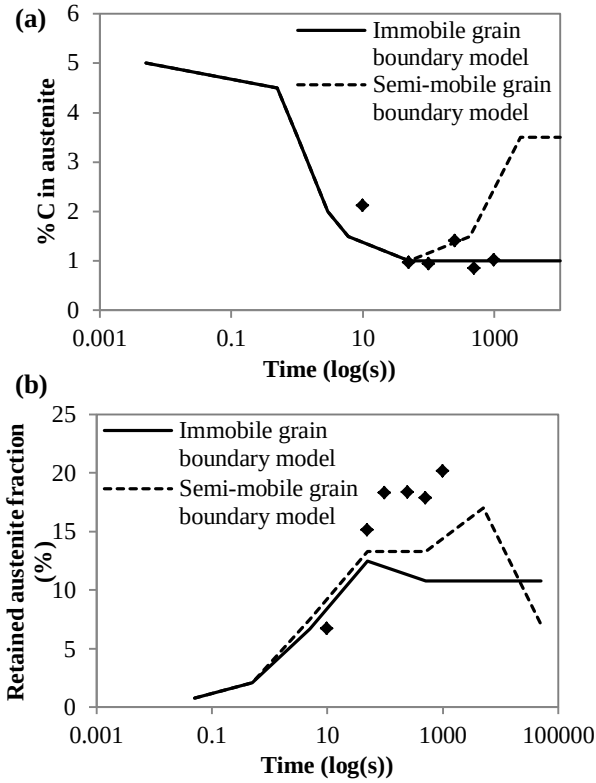

Figure IV-1: (a) %C in the austenite and (b) the austenite fraction after quenching to 244°C and partitioning at 400°C for different times experimentally, modelled with immobile and semi-mobile grain boundary mobility (0.25C-Fe)

The experimental values of quenching to 224°C were also compared with the modelled curves, cfr. Figure IV-2. In this case, the scaling factor for the retained austenite fraction and C-content were only 5 and 1 respectively.

Concerning the evolution of the C-content, the same tendency can be observed as for quenching to 244°C, cfr. Figure IV-2(a). Figure IV-2(b) illustrates that the partitioning

time for increasing the austenite fraction to significant levels is longer than for 244°C. This is related with the lower austenite fraction present at the quenching temperature. As a consequence, carbon needs to diffuse a longer distance *inside* the austenite grains, with slow C diffusion kinetics, to stabilize the same amount. Hence if all the available austenite grains at the quenching temperature need to be stabilized completely, the C path-length in austenite enlarges and more diffusion time is required. The shape of the semi-mobile modelled curve corresponds best with the experimental observed points.

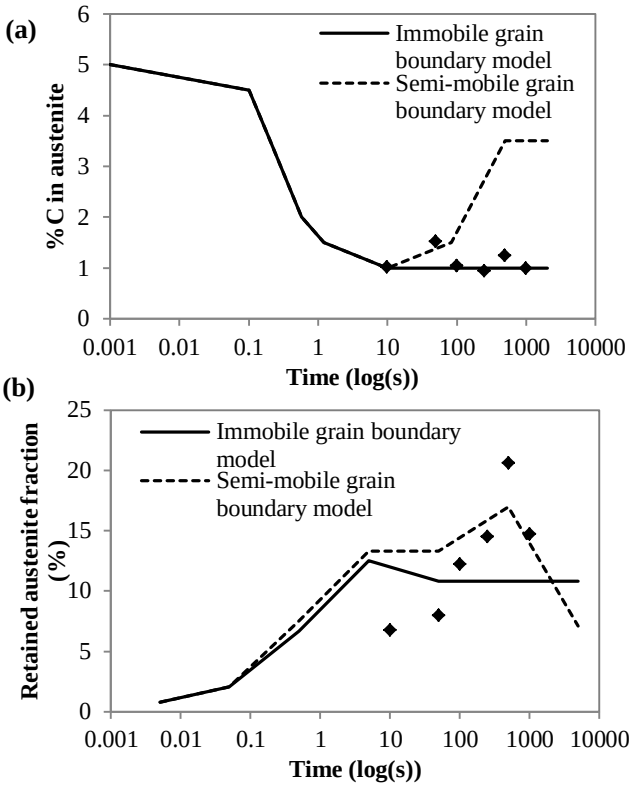

Figure IV-2: (a) %C in the austenite and (b) the austenite fraction after quenching to 224°C and partitioning at 400°C for different times experimentally, modelled with immobile and semi-mobile grain boundary mobility (0.25C-Fe)

The experimental values imply that the grain boundary is not immobile since the modelled evolution of the retained austenite fraction corresponds with the experimentally observed shape. The evolution of the C-content in the assumption of a semi-mobile interface cannot be explained. The C-content follows the curve modelled with a semi-mobile interface to a certain partitioning time and afterwards drops to the level predicted with an immobile interface.

IV.3. In-situ partitioning TEM experiments

A heating stage in TEM gives the opportunity to follow the Quenching and Partitioning process in-situ. The austenite-martensite grain boundary movement can be monitored during the partitioning stage. Several attempts were made to study the heat treatment cycle in-situ: *(i)* conducting the complete cycle in TEM, and *(ii)* study only the partitioning stage of newly designed high-C steel to have a sufficient amount of retained austenite at room temperature prior to the partitioning stage in TEM.

IV.3.1. Complete Q&P partitioning cycle in TEM

The first try-out was focused on conducting the complete heat treatment cycle in TEM. Hereby the following procedure was aimed at: full austenitisation, quenching (max 10°C/s), finding an austenite-martensite interface and reheating to the partitioning temperature to track the changes of the interface. However some difficulties were related with this experiment: *(i)* controlling the temperature of the heating stage at its limits (950°C); *(ii)* finding an austenite-martensite interface fast to avoid isothermal transformation products [3, 4]; and *(iii)* following this interface during the partitioning stage.

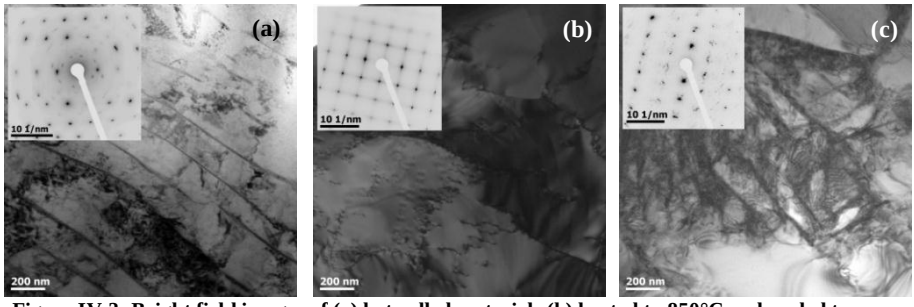

Figure IV-3: Bright field images of (a) hot rolled material; (b) heated to 850°C and cooled to room temperature; (c) heated to 950°C and cooled to room temperature

A TEM foil of the hot rolled material shown in Figure IV-3(a), was reheated to a target temperature of 850°C with the aim to austenitise the sample. It was however clear from the diffraction pattern that the material was still bcc-phase although it was recrystallized, cfr. Figure IV-3 (b).

After cooling down, the shape of the hole was changed (cfr. Figure IV-4), suggesting that the thinnest parts of the foil were lost inside the TEM. As a second attempt, the same sample was reheated again to the highest limits (950°C) of the reheating system

giving a partially austenitic microstructure without further material loss. At room temperature, the formation of martensite could be observed but no austenite could be detected.

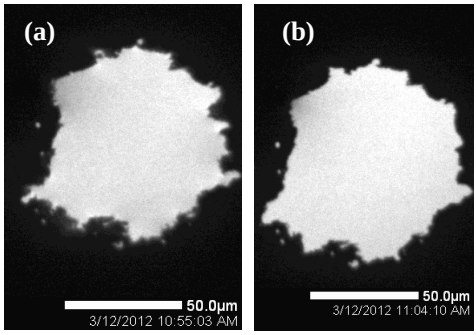

Figure IV-4: Low magnification image of the whole of the TEM sample (a) before heating (b) after heating to 850°C and cooling to room temperature

Both the material loss and the inability to reach the austenite region during austenitisation were problems for this experiment. Also, controlling the quenching temperature with the heating stage was not feasible. Hence in the attempt to study grain boundary movement in TEM, the austenitisation step needed to be omitted by creating Q&P steel with austenite retained at room temperature prior to partitioning. Consequently, the first step of the heat treatment cycle could be conducted in a dilatometer and the second step after sample preparation inside the TEM.

IV.3.2. Partitioning heat treatment in TEM

IV.3.2.1 Abstract

A 1C3Mn1.5Si steel was partially transformed into martensite by quenching to room temperature after full austenitisation. A partitioning treatment was applied in-situ in a high resolution transmission electron microscope. The width of an austenite grain in between martensite constituents was followed as a function of the annealing time. Migration of the martensite-austenite interfaces was quantitatively measured and compared with results from a model for carbon partitioning from martensite to austenite involving interface motion. The kinetics of the observed movement suggests that the interface has a semi-coherent nature. This work shows that grain boundary mobility of the martensite-austenite interfaces during annealing may play an important role in the microstructure development during the process of Quenching and Partitioning in steels.

IV.3.2.2 Introduction

A recent concept for processing advanced high strength steel was proposed by Speer *et al.* [5] in 2003 as a method to produce low carbon high strength steels with a mixed microstructure of martensite and retained austenite: "Quenching and Partitioning" (Q&P). Additions of silicon and aluminium in the steel compositions were used to inhibit cementite precipitation, opening the possibility to obtain carbon-enriched austenite at room temperature (i.e. with improved stability) by carbon partitioning from supersaturated martensite [5-7]. The process involves an initial partial or full austenitization, followed by quenching to a temperature between the martensite start (M_s) and finish (M_f) temperature to create a controlled fraction of martensite. Then, the steel is held isothermally or reheated to a higher temperature to allow carbon diffusion from martensite into the remaining austenite. During this partitioning step, it is intended to enrich the austenite with sufficient carbon to aim for its stabilization at room temperature after final quenching. The resulting microstructure consists of retained austenite, ferrite (for intercritical annealing) and possibly two types of martensite: the one formed during the first quench, "tempered" or "primary" martensite, and possibly the one formed during the final quench, "fresh" or "secondary" martensite [8].

A thermodynamic model to predict the endpoint of complete or *ideal* partitioning at a given temperature was described by the "Constrained Carbon Equilibrium" (CCE) condition [5-7, 9, 10]. This is defined by absence of iron or substitutional diffusion, and the freedom of carbon to migrate over distances greater than the unit cell. The difference with paraequilibrium [11] is that grain boundary movement is precluded by short-range iron or substitutional diffusion.

There are however experimental observations which question the immobility of the austenite-martensite grain boundary. The occurrence of interface migration was proposed by Zhong *et al.* [1] to explain changes in the curvature of austenite grains before and after partitioning, without nucleation of bainite at the interfaces. They stated that "the endpoint of the CCE model is the startpoint of Fe-diffusion or interface migration. Santofimia *et al.* [12] and Toji *et al*. [13] conducted atom probe tomography experiments on Q&P steels and observed that a small amount of manganese partitioned from martensite into austenite, most probably during the partitioning step. This could be explained by two mechanisms: partitioning of Mn from martensite to austenite, which would be a process with a much slower kinetics compared with the process of carbon partitioning or to solute drag due to the movement of the interface during the partitioning step. Santofimia *et al.* [12] observed that

such Mn enrichment was not a general result observed in all martensite/austenite interfaces in the same material, which shows that the process of Mn partitioning may be related with the particular character of every single martensite/austenite interface. If Mn partitioning is a process linked with the migration of martensite/austenite interfaces, this means that possibly not all martensite/austenite interfaces "migrate" during the partitioning step and this result is probably related with the characteristics of each interface.

Expected motion of the interface during partitioning, due to a chemical potential difference of iron, was qualitatively examined by Speer *et al.* [14] and quantitatively by Santofimia *et al.* [15] illustrating a bidirectional movement of the interface. The latter calculations were made under the assumption of an incoherent interface irrespective of their semi-coherent nature [16]. Later on [2], different grain boundary mobilities related to the activation energy for iron migration to simulate the microstructural evolution during partitioning were assumed: (1) completely immobile with an infinite activation energy, (2) limited mobile representing a semi-coherent interface with an activation energy of 180 kJ/mol, and (3) highly mobile demonstrating an incoherent interface with an activation energy of 140 kJ/mol. The studied composition was a binary Fe-0.25C (wt. %) alloy with an alternating morphology of martensite and austenite. The input microstructure was formed by a single lath of martensite sharing the interface with a film of austenite. Mirror conditions were assumed in the calculations. The martensite lath was considered to have a fixed width of 0.2 μm [17] whereas the austenite film width changed according to varying quenching temperatures.

In general, calculations obtained by Santofimia *et al.* [2, 15] resulted in a sharp increase of the carbon content in the austenite near the austenite/martensite interface for short partitioning times, stabilizing a small austenite fraction with a high C-content. If the partitioning time increased, this peak was progressively reduced while the overall carbon content of the austenite increased.

An immobile interface resulted in an equivalent behaviour as reported for CCE, which means that partitioning of carbon from martensite to austenite continues until the chemical potential of carbon is the same through the whole system under the restriction of a fixed martensite/austenite interface. For an activation energy of 180 kJ/mol, which was an arbitrary chosen value for a semi-coherent interface, the carbon concentration profiles were similar to those for an immobile interface for short partitioning times. However, longer partitioning times lead to the initiation of interface migration and enrichment of carbon at the interface until full equilibrium was reached. The way in which the system reached equilibrium

involved the martensite/austenite interface migration at longer partitioning times, and the direction of this migration depended on the initial relative sizes of the austenite and martensite grains. For example, for a very low quenching temperature, which corresponds with a small austenite grain size at the beginning of the partitioning process, the equilibrium involved the growth of austenite, whereas the opposite result was obtained in the case of high quenching temperatures. For an incoherent interface which was represented by an activation energy typical for reconstructive austenite to ferrite transformations, the carbon profiles and evolution of the interface were coupled during the partitioning process leading to a bidirectional movement of the interface prior to achieving equilibrium. Carbon partitioning started with an increase of the carbon content in the austenite which was compensated by an interface movement from the austenite to the martensite. Once the carbon content was lower than the equilibrium value, the interface reversed its direction if that was required in order to reach full equilibrium in the system.

Phase field simulation was addressed by Takahama *et al.* [18] to show details of the carbon redistribution as well as possible interface migration. When the calculated local carbon peak in the austenite in the vicinity of a martensite grain was higher than the paraequilibrium value, a driving force for interface movement was created, causing growth of austenite.

In summary, the revised literature shows experimental evidences suggesting the migration of martensite/austenite interfaces during annealing at relatively low temperatures such as 400°C. These migrations may not occur in all martensite/austenite interfaces, but on specific ones having particular characteristics. These experimental observations are well supported by thermodynamical and kinetics models, showing that the coherency of the martensite/austenite interfaces may play a role in the mobility of these interfaces during annealing. This work reports for the first time the in-situ migration of an austenite-martensite grain boundary during annealing. Experimental values were used as input for the model proposed by Santofimia *et al.* [2, 15] to fit the activation energy characterizing the mobility of the studied interface.

IV.3.2.3 Experimental procedure

To conduct the partitioning heat treatment in-situ in TEM we have to start with an adequate microstructure consisting of austenite and martensite at room temperature. Therefore, a chemical composition to retain sufficient austenite at room temperature after full austenitisation was selected: 1C3Mn1.5Si (wt.%).

According to literature [1, 19-21], 1.5wt.% silicon is enough to suppress cementite formation during the partitioning step by formation of a kinetic barrier to the growth of cementite [22, 23]. Manganese is an austenite stabilizing element and increases the hardenability during cooling [24]. Though, high concentrations result in segregation banding [25] and thus the Mn-content was limited to 3wt.%. Hence, the carbon content was adapted to retain sufficient austenite at room temperature. According to the Koistinen-Marburger equation, 50% retained austenite would be retained at room temperature for steel with a M_s temperature of approximately 80°C. By employing its relationship with the chemical composition as proposed by van Bohemen *et al.* [26], 1wt.%C would result in a calculated M_s temperature of 82°C retaining approximately 50% austenite at room temperature after cooling.

The first part of the heat treatment was carried out in a Bähr DIL 805 A/D dilatometer on hot rolled rectangular samples with dimensions of 2.5 x 3.5 x 10 mm. The sample was fully austenitized at 950°C for 60s and cooled to room temperature at 20°C/s with N_2-gas.

EBSD analysis was conducted in a FEI Quanta™ 450-FEG-SEM equipped with a Hikari detector controlled by the EDAX-TSL OIM-Data Collection software. The EBSD data were acquired on a hexagonal scan grid using an accelerating voltage of 20kV, a working distance of 16mm, a tilt angle of 70° and a step size of 60nm. The orientation data were post-processed with TSL-OIM Analysis 6.2® software.

Transmission Kikuchi diffraction data were acquired in SEM (TKD-SEM) with a spot size of 5, an accelerating voltage of 30kV, a working distance of 6mm and a tilt angle of -10° in a FEI Quanta™ 450-FEG-SEM. The step size used in this work was 10nm and the orientation data were post-processed with TSL-OIM Analysis 6.2® software.

From the dilatometer specimen, a FIB-sample was prepared using a SMI 3050TB triple beam FIB/SEM system from SII NanoTechnology Inc. The equal thickness of the sample was 80nm to minimize magnetic effects, to have a better temperature homogeneity during in-situ partitioning and to enhance the sharpness of the grain boundary by reducing the possibility of a non-perpendicular interface. It is known from literature [27, 28] that interface movement is influenced by externally applied stresses. Therefore, stresses resulting from thermal gradients in samples with thickness gradients can also affect the interface movement. To avoid such side-effects the sample for TEM study was prepared by using focussed ion beam milling (FIB) and a foil with a constant thickness of 80 nm was prepared. Besides, the

interface analysis was conducted in the centre of the foil to assure an equal resistance of the surrounding material. A JEOL JEM-2200FS high resolution hot stage-TEM was used for conducting the in-situ partitioning experiment at a heating voltage of 3.5mV corresponding with a partitioning temperature of 400°C.

IV.3.2.4 Results

Dilatometry Analysis

The pre-partitioning heat treatment namely austenitisation and quenching to room temperature was conducted in a dilatometer. The change in length (µm) versus temperature (°C) is shown in Figure IV-5. The sample was heated at 20°C/s to 950°C for 60s to ensure full austenitisation. The M_s temperature was determined experimentally as 79°C resulting in an undercooling of approximately 54°C upon further cooling to room temperature at 20°C/s.

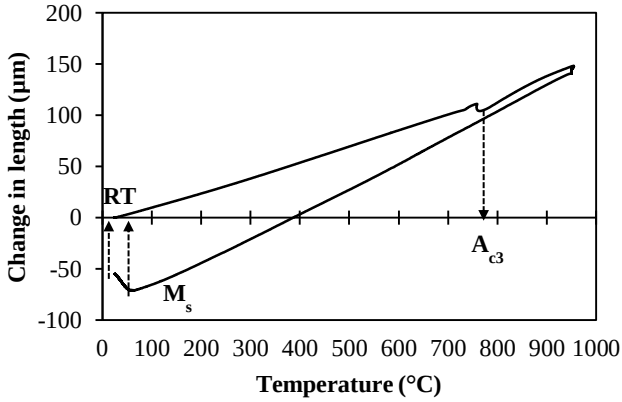

Figure IV-5: Change in length (µm) versus temperature (°C) for the austenitisation and quenching treatment prior to in-situ partitioning in TEM

Starting Material

The starting material after full austenitisation and quenching contained 39% austenite at room temperature as can be observed from red phase in the EBSD phase map given in Figure IV-6(a). The image quality map in Figure IV-6(b) reveals the austenite as high image quality grains and resolves the internal structure of the martensite grains with both lath and/or twinned morphologies.

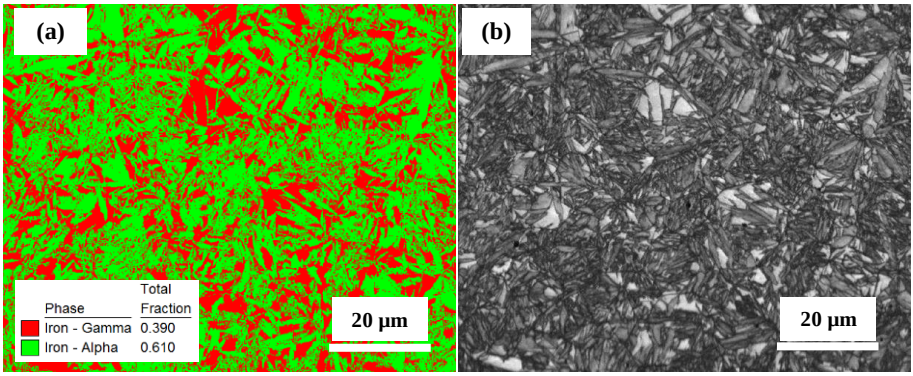

Figure IV-6: (a) Phase map with austenite in red and martensite in green (b) image quality of 1C3Mn1.5Si after full austenitisation and quenching to room temperature

Selection of Area for the In-Situ Annealing

The microstructural evolution focussing on interface migration between martensite and austenite was studied in-situ during partitioning. This experiment requires the selection of an adequate area fulfilling the following criteria:

(1) The austenite grains need to be small to allow detection of the entire grain with such resolution that the visualisation of grain boundary movement is possible.

(2) The morphology of the austenite grains is preferably lath-type. Measuring the size of a polygonal grain is less straightforward compared to a lath morphology where basically the distance between two straight lines needs to be measured. By this we also eliminate the effect of curvature on diffusion and grain boundary movement.

Combining criterion (1) and (2) suggests that an alternating structure of martensite laths and film-like austenite grains will provide the best microstructure to study in-situ partitioning. Besides, this microstructure of a single lath of martensite sharing the interface with a film of austenite is the input of the model proposed in [2, 15].

An area which satisfied these criteria is illustrated in the boxed area of the SEM micrograph in Figure IV-7(a). The corresponding EBSD phase map in Figure IV-7(b) with martensite in green and austenite in red reveals a lath-type alternating austenite-martensite microstructure.

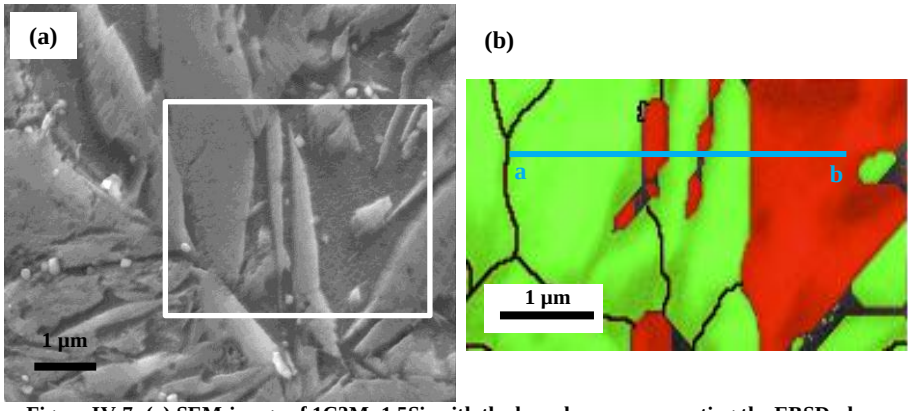

Figure IV-7: (a) SEM-image of 1C3Mn1.5Si with the boxed area representing the EBSD phase map in (b) with martensite is green and austenite in red, the line a-b represents the edge of the FIB-sample

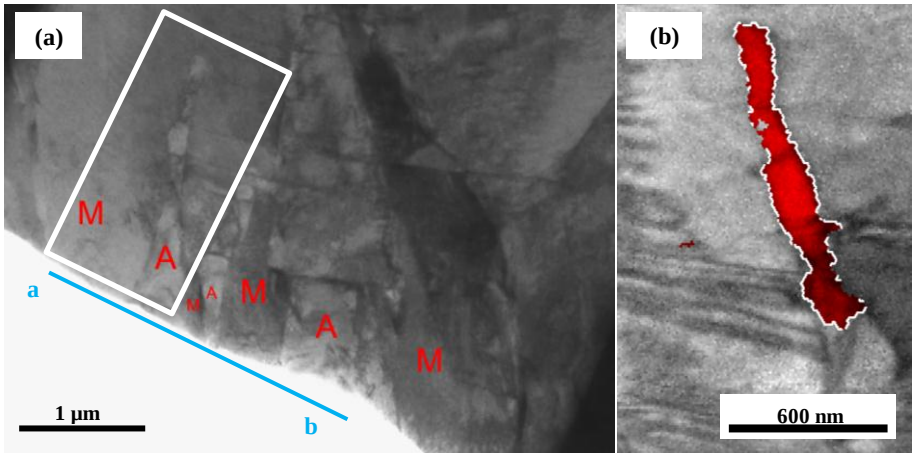

Figure IV-8: (a) STEM image of the FIB-sample with austenite (A) and martensite (M), the line a-b indicates the same position as in Figure IV-7(b); (b) image quality map superimposed with the austenite phase in green and the Kurdjumov-Sachs orientation relationship by the white line

The line indicated with a-b in Figure IV-7(b) shows the area of interest for FIB sample preparation. A layer of FIB-deposited tungsten was placed over this line to prevent milling from damaging the surface of the TEM specimen cross-section. Next, two trenches were milled on either side of the line and the central part was lift out [29, 30]. Consequently, the FIB sample shows the interior of Figure IV-7(b) along line a-b which is now the edge of the sample, cfr. the STEM image of the foil in Figure IV-8 (a). The identification of the phases was additionally controlled by diffraction patterns in TEM. Besides, Figure IV-8(b) displays the TKD-SEM image quality map superimposed with the austenite phase in red of the white boxed area in Figure IV-8(a). The Kurdjumov-Sachs orientation relationship between the

austenite grain and the martensitic matrix, shown by the white line, illustrates the reliability of the phase indexation with TKD.

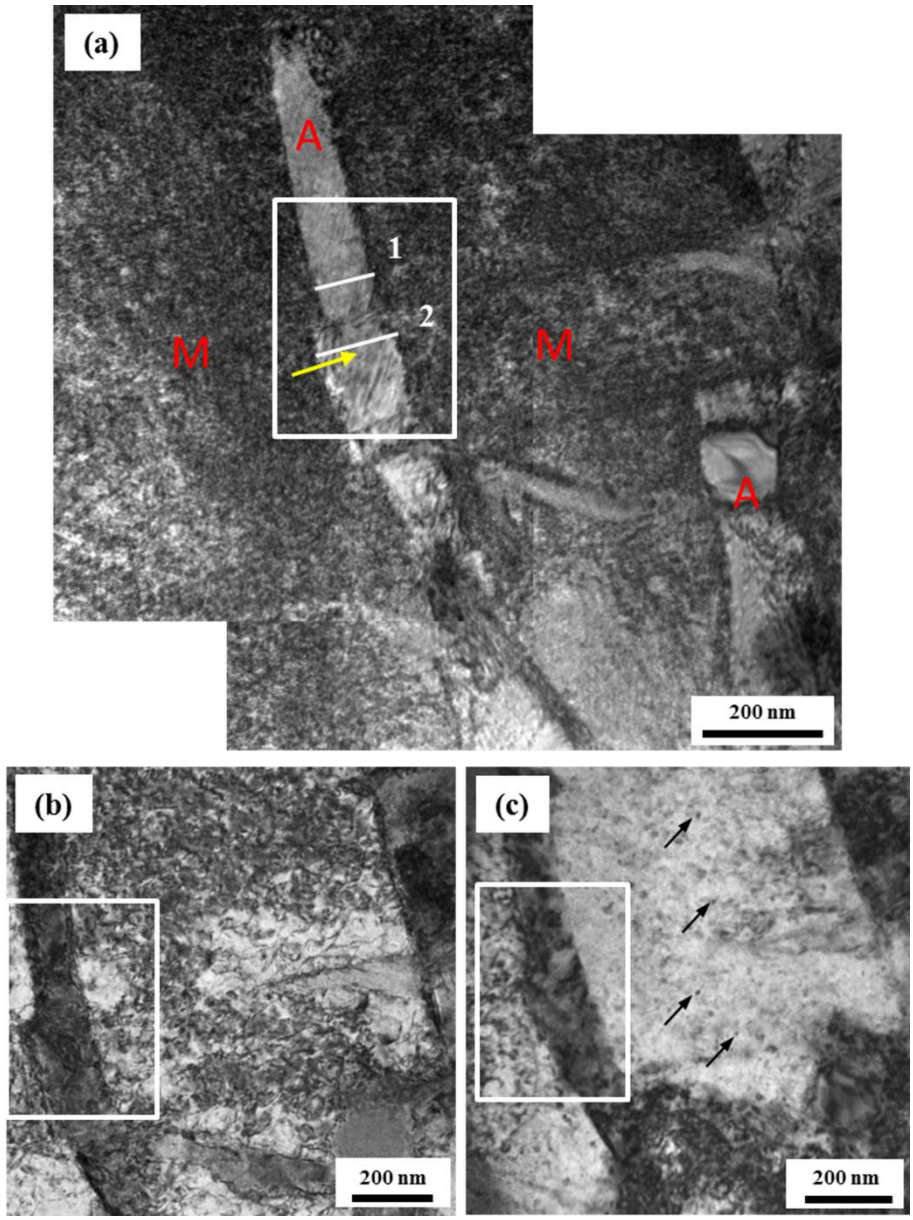

Figure IV-9: (a) TEM image before partitioning (b) during partitioning (after 32min) (c) after partitioning for 1h and cooling to RT

A TEM image of the same starting austenite grain is given in Figure IV-9(a). The lines numbered 1 and 2 represent the two positions where the change in width was measured

during partitioning. Figure IV-9(b) shows the image after partitioning for 32 min at 400°C. After 60 min at 400°C, the sample was slowly cooled down to room temperature resulting in the final microstructure illustrated in Figure IV-9(c).

Evolution of the Interface During Annealing

The width change of the austenite grain as a function of partitioning time is given in Figure IV-10(a) for line 1 and in Figure IV-10(b) for line 2.

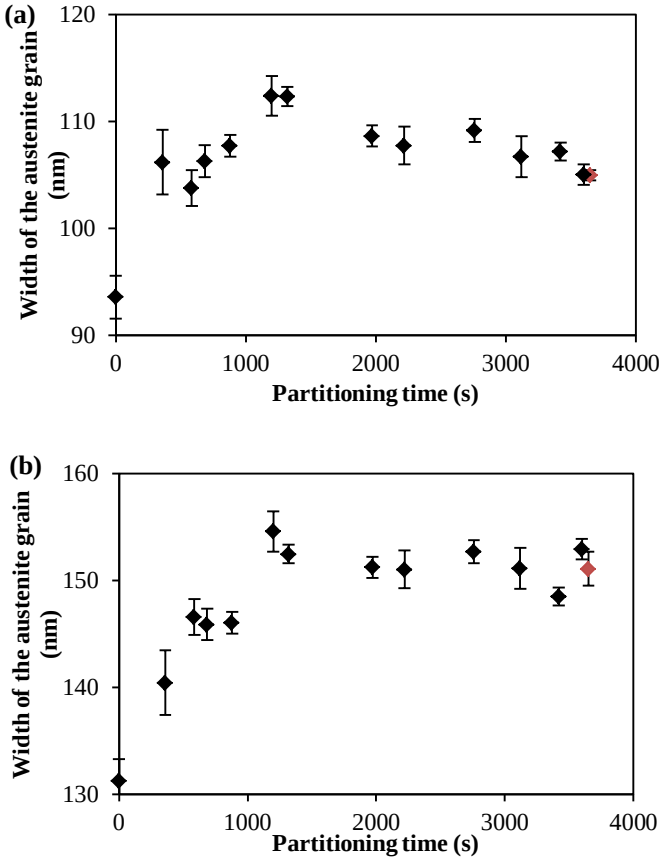

Figure IV-10: Change in austenite grain width during partitioning for (a) position 1 (b) position 2 as highlighted in Figure IV-9 (a). The final size after cooling is given by the red data point. The error bars were obtained from measuring the width three times independently

The starting width at position 1 was 94 ± 2 nm which increased fast to 106 ± 3 nm after 360s partitioning at 400°C. After 20 min a maximum value of 112 ± 2 nm was reached, being approximately 20 nm larger than the starting width. Afterwards, the width decreased to a final thickness of 105 ± 1 nm after cooling to room temperature as shown by the red data

point in Figure IV-10(a). The final thickness difference was approximately 11 nm. A similar behaviour can be observed for position 2 in Figure IV-10(b). The width increased from 131 ± 2 nm to 151 ± 2 nm after cooling as shown by the red data point in Figure IV-10(b), resulting in a growth of approximately 20 nm. The calculated linear thermal expansion [31] of the measured austenite grain upon heating/cooling to 400°C is less than 1 nm. This value lies in the range of the experimental error.

Compositional Analysis Across the Interface after Annealing

An Energy Dispersive X-ray Spectroscopy (EDX) element analysis across the martensite-austenite grain boundary after in-situ partitioning at position 2 along the yellow arrow in Figure IV-9was conducted to characterise the distribution of C (cfr. Figure IV-11) and substitutional elements Mn and Si (cfr. Figure IV-12).

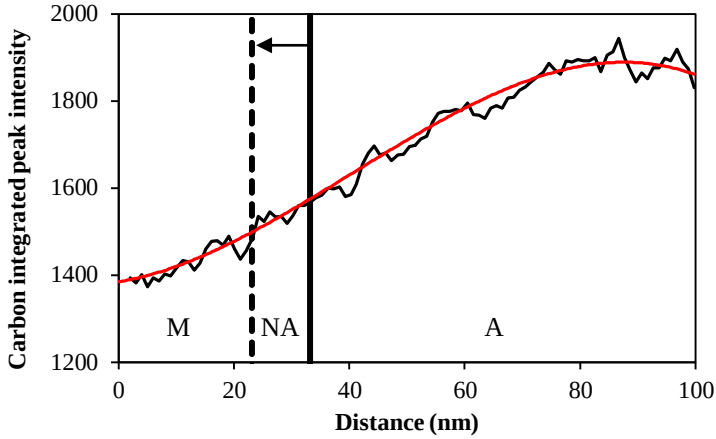

Figure IV-11 Carbon peak intensity (%) across the austenite (A) martensite (M) grain boundary at position 2 going from the martensite to the austenite grain with increasing distance as illustrated by the yellow arrow in Figure IV-9 – the full and dotted line indicate the original and moved grain boundary with newly stabilized austenite (NA)

The changes of the integrated intensity of the C-peaks were used to monitor the relative change of the C-distribution along the interface. Carbon showed a continuous evolution being lowest inside the martensite (M) and highest inside the austenite (A) grain. The C-content of the newly stabilized austenite (NA) after grain boundary movement - the full and dotted lines indicate the original and moved grain boundary respectively with the arrow illustrating the direction of movement- lies in between the C-contents of the depleted martensite and enriched, original austenite.

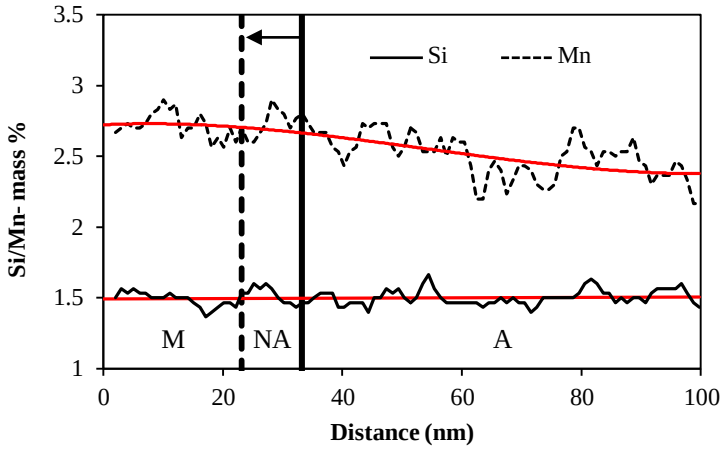

Figure IV-12: Mass% of Si and Mn across the austenite (A)-martensite (M) grain boundary at position 2 going from the martensite to the austenite grain with increasing distance as illustrated by the yellow arrow in Figure IV-9 – the full and dotted lines indicate the original and moved grain boundary with newly stabilized austenite (NA)

Figure IV-12 illustrates that the silicon level remained the same over the studied region across the martensite-austenite interface. The average Mn-content in the original martensite matrix was constant as seen by the interpolation of the EDX data from the matrix (at a distance of 0 nm) until the original martensite-austenite grain boundary represented by the full line (at 33 nm). A subsequent decrease with the highest rate near the interface in the Mn-concentration with increasing distance inside the austenite grain was observed. After partitioning, the new position of the grain boundary is given by the dotted line (at 23 nm) and no changes in the Mn-content with respect to the original martensite grain were observed. This means that, after the partitioning step, there is a gradient of Mn within the austenite grain.

IV.3.2.5 Discussion

A high-C Q&P steel was subjected to in-situ partitioning in TEM after full austenitisation and quenching to room temperature. The width of an austenite grain in between two martensite grains was monitored at 2 different positions resulting in an increase in width of 12% and 15% for positions 1 and 2 respectively.

Indirect prove of grain boundary movement during partitioning was observed in literature [1] by a change in the austenite/martensite interface appearance from straight to curved. In this work, no difference in the shape of the austenite lath was observed before and after partitioning, cfr. Figure IV-9. Besides grain boundary movement, the dislocation density

in the martensite decreased during annealing [32, 33] as can be detected from the consecutive TEM bright field images in Figure IV-9 (a-b and c). In Figure IV-9 (c), small globular carbides marked by arrows can be observed as darker spots in the martensitic matrix, but not in the close vicinity of the studied interface. The possible interaction between the tempering of the surrounding martensite and movement of the interface cannot be excluded. This suggestion is supported by the fact that the mobility of the interface practically finished in the first 1500s to 2000s.

EDX element analysis of the C-content after annealing indicates that C-partitioning effectively occurred from the martensitic matrix into the austenite grain, and illustrates that the stabilized austenite fraction after partitioning by grain boundary movement has a continuous C-content evolution with values in between the C-enriched austenite and C-depleted martensite [13]. The stabilized austenite has the same Mn-content as the martensite before grain boundary movement which indicates that the newly stabilized austenite acquired the Mn concentration that was originally in the martensite grain. On the other hand, there was a slight increase of the Mn-content in the austenite after annealing near the interface with respect to the martensite phase. The variations in the Mn-concentration over larger distances is most probably related to inhomogeneity (Mn segregation) in the hot band microstructure since its diffusion distance in austenite at 400°C for 1h was calculated to be only 0.016nm [34]. Although zones of clear Mn enrichment thinner than 5nm were observed with 3D-APT in [12, 13], they were not detected in this study because of the detection limit of the EDX technique. Moreover, Santofimia *et al.* [12] observed these zones of Mn enrichments in approximately half of the martensite-austenite interfaces, even when carbon partitioning was clearly observed.

The relative width change as a function of partitioning time was calculated using the model proposed in [2, 15]. The input parameters of the model were a partitioning temperature of 400°C, a starting austenite thickness of 131 nm corresponding with position 2 and a starting martensite thickness of 750 nm and 1195 nm respectively corresponding with the neighbouring martensite grains. The initial chemical composition of martensite and austenite was set equal to the overall composition. Their equilibrium C-contents at the annealing temperature of 400°C (x_{CFCC} = 0.154 and x_{CBCC} = 8.57 10^{-4}) were calculated with Thermocalc™ with a TCFE7 database assuming paraequilibrium conditions. The activation energy for grain boundary mobility was altered between 150kJ/mol and 190kJ/mol as shown in Figure IV-13 and Figure IV-14 for a neighbouring martensite thickness of 750 nm and 1195 nm respectively since the model assumes a symmetric input microstructure.

For this particular steel, austenite grain and interface characteristics, an activation energy of 165 kJ/mol was obtained as the best fit for the relative width change kinetics for both martensite grain thicknesses. This value of activation energy is higher than the value corresponding to austenite-ferrite phase transformations in Fe-Mn alloys [35, 36], which means that the migration kinetics of the studied martensite-austenite interface is slower than observed in diffusional austenite-ferrite transformations. The interpretation of this result can be based on the coherency of the studied martensite-austenite interface.

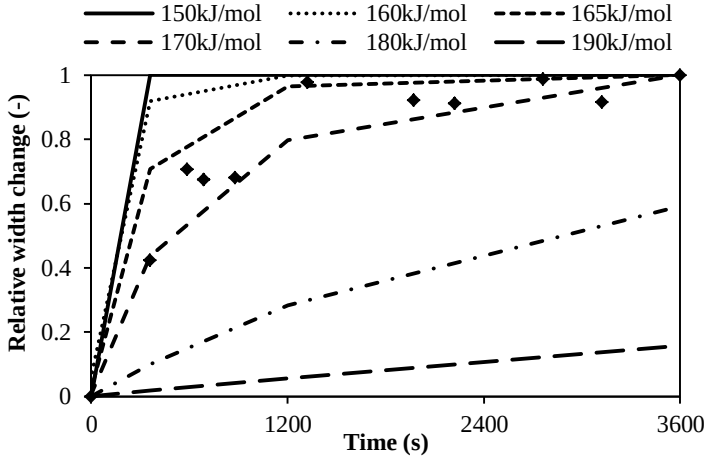

Figure IV-13: Relative changes in width observed experimentally and modelled with different activation energies ranging from 150kJ/mol to 190kJ/mol for a symmetric microstructural input with a neighbouring martensite grain with a width of 750nm

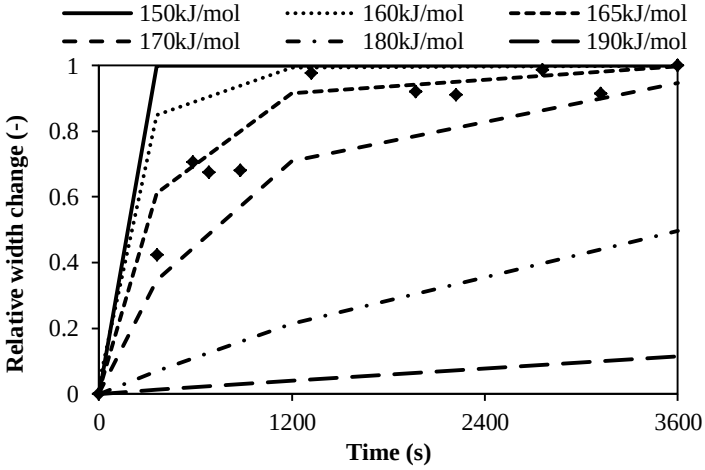

Figure IV-14: Relative change in width observed experimentally and modelled with different activation energies ranging from 150kJ/mol to 190kJ/mol for a symmetric microstructural input with a neighbouring martensite grain with a width of 1195nm

Thus, the migration of ferrite-austenite interfaces in Fe-Mn alloys is a thermally activated diffusional process preferentially occurring in highly mobile incoherent interfaces. However, the studied martensite-austenite interface is more likely semi-coherent and with a reduced mobility with respect to austenite to ferrite transformations. This semi-coherent nature of the martensite-austenite interface is well-known after martensitic transformations [16] and can explain the experimentally observed evolutions of the retained austenite fraction during partitioning [10, 37, 38].

Observations made in this article show that the mobility of the martensite-austenite interfaces during annealing may play an important role in the microstructure development of Q&P steels during processing, affecting volume fraction of phases further than calculated applying CCE conditions. In this work, it has been assumed that the difference in chemical potential of iron during the partitioning step acts as a driving force for the interface migration. However, other phenomena taking place during the partitioning step may also play a role in the migration of the austenite–martensite interface, such as recovery and carbide precipitation [39] in the martensite structure, or strain accommodation at the interface. The model used in this work did not take into account cementite precipitations in martensite since they were only observed after 1200s which is after the initial and largest stage of grain boundary movement, cfr. Figure IV-13 and Figure IV-14. Besides, no direct evidences of carbide precipitations were observed in the close vicinity of the studied region of the austenite-martensite interface. Therefore, a local CCE condition was assumed for the calculations of the grain boundary movement kinetics. However, we do not exclude that the presence of small carbides can interfere with the kinetics at longer partitioning times due to grain boundary pinning.

IV.3.2.6 Conclusions

A high-C steel was subjected to in-situ partitioning inside a hot-stage HR-TEM. The width of an austenite grain with a film-like morphology as a function of partitioning time was followed during partitioning. Compositional investigations across the interface after annealing proved that C-partitioning effectively occurred. The migration kinetics of the studied martensite/austenite interfaces was slower than in diffusional austenite to ferrite transformations due to its semi-coherent nature. Consequently, motion of the austenite/martensite interface during partitioning will affect the microstructural evolution of Q&P steels.

IV.3.2.7 Acknowledgements

This research was funded by the governmental institute for the Promotion of Innovation by Science and Technology in Flanders (IWT) and was carried out under the frame of the project "RFCS-CT-2011-00017 "New advanced high strength steels by quenching and partitioning process (NewQ&P)". Maria J. Santofimia acknowledges the funding received from the European Research Council under the European Union's Seventh Framework Programme (FP/2007-2013) / ERC Grant Agreement n. [306292].

References

1. N. Zhong, X. Wang, Y. Rong, and L. Wang: 'Interface migration between martenisite and austenite during quenching and partitioning (q&p) process', *Materials Science and Technology*, 2006, **22**(6), 4.

2. M. J. Santofimia, J. G. Speer, A. J. Clarke, L. Zhao, and J. Sietsma: 'Influence of interface mobility on the evolution of austenite–martensite grain assemblies during annealing', *Acta Materialia*, 2009, **57**, 4548-4557.

3. D. Kim, J. G. Speer, and B. C. De Cooman: 'Isothermal transformation of a cmnsi steel below the ms temperature', *Metallurgical and Materials Transactions A*, 2010, **42**, 1575-1585.

4. D. Kim, J. G. Speer, and B. C. De Cooman: 'The isothermal transformation of low-alloy low-c cmnsi steels below ms', *Materials Science Forum*, 2010, **654-656**, 98-101.

5. J. G. Speer, D. K. Matlock, B. C. De Cooman, and J. G. Schroth: 'Carbon partitioning into austenite after martensite transformation', *Acta Materialia*, 2003, **51**, 2611-2622.

6. J. G. Speer, D. V. Edmonds, F. C. Rizzo, and D. K. Matlock: 'Partitioning of carbon from supersaturated plates of ferrite, with application to steel processing and fundamentals of the bainite transformation', *Materials Science*, 2004, **8**, 219-237.

7. J. G. Speer, F. C. R. Assunção, D. K. Matlock, and D. V. Edmonds: 'The "quenching and partitioning" process: Background and recent progress', *Materials Research*, 2005, **8**, 417-423.

8. C. Y. Wang, J. Shi, W. Q. Cao, and H. Dong: 'Characterization of microstructure obtained by quenching and partitioning process in low alloy martensitic steel', *Materials Science and engineering*, 2010, **527**, 3442-3449.

9. A. J. Clarke, J. G. Speer, M. K. Miller, R. E. Hackenberg, D. V. Edmonds, D. K. Matlock, F. C. Rizzo, K. D. Clarke, and E. D. Moor: 'Carbon partitioning to austenite from martensite or bainite during the quench and partition process: A critical assessment', *Acta Materialia*, 2008, **56**, 16-22.

10. A. J. Clarke, J. G. Speer, D. K. Matlock, F. C. Rizzo, D. V. Edmonds, and M. J. Santofimia: 'Influence of carbon partitioning kinetics on final austenite fraction during quenching and partitioning', *Scripta Materialia*, 2009, **61**, 149-152.

11. M. Hillert and J. Agren: 'On the definitions of paraequilibrium and orthoequilibrium', *Scripta Materialia*, 2004, **50**, 697-699.

12. M. J. Santofimia, L. Zhao, I. Povstugar, P. Choi, D. Raabe, and S. J.: 'Carbon redistribution in a quenched and partitioned steel analysed by atom probe tomography', 3rd int symp steel sci, Kyoto: The Iron and Steel Institute of Japan, 2012, 155.

13. Y. Toji, H. Matsuda, M. Herbig, P.-P. Choi, and D. Raabe: 'Atomic-scale analysis of carbon partitioning between martensite and austenite by atom probe tomography and correlative transmission electron microscopy', *Acta Materialia*, 2014, **65**(0), 215-228.

14. J. G. Speer, R. E. Hackenberg, B. C. De Cooman, and D. K. Matlock: 'Influence of interface migration during annealing of martensite/austenite mixtures', *Philosophical Magazine Letters*, 2007, **87**(6), 379-382.

15. M. J. Santofimia, L. Zhao, and J. Sietsma: 'Model for the interaction between interface migration and carbon diffusion during annealing of martensite–austenite microstructures in steels', *Scripta Materialia*, 2008, **59**(2), 159-162.

16. J. W. Christian: 'Chapter 21 - characteristics of martensitic transformations', in 'The theory of transformations in metals and alloys', (ed. J. W. Christian), 961-991; 2002, Oxford, Pergamon.

17. C. A. Apple, R. N. Caron, and G. Krauss: 'Packet microstructure in fe-0.2c pct c martensite', *MT*, 1974, **5**(3), 593-999.

18. Y. Takahama, M. J. Santofimia, M. G. Mecozzi, L. Zhao, and J. Sietsma: 'Phase field simulation of the carbon redistribution during the quenching and partitioning process in a low-carbon steel', *Acta Materialia*, 2012, **60**(6–7), 2916-2926.

19. M. J. Santofimia, T. Nguyen-Minh, L. Zhao, R. Petrov, I. Sabirov, and J. Sietsma: 'New low carbon q&p steels containing film-like intercritical ferrite', *Materials Science and engineering*, 2010, **527**, 6429-6439.

20. W. Li, L. Wenjuan, and F. Weijun: 'Industry trials of c-si-mn steel treated by q&p concept in baosteel', SAE 2010 World Congress & Exhibition, Detroit, Michigan, USA, 2010.

21. D. Hauserová, M. Duchek, J. Dlouhý, and Z. Nový: 'Properties of advanced experimental cmnsimo steel achieved by qp process', *Procedia Engineering*, 2011, **10**, 2961-2966.

22. W. S. Owen: 'The effect of silicon on the kinetics of tempering', *Trans. ASM*, 1954, **46**, 812-828.

23. L. Chang and G. D. W. Smith: 'The silicon effect in the tempering of martensite in steels', *Journal de Physique*, 1984, **45**, 397-401.

24. D. A. Porter, K. E. Easterling, and M. Y. Sherif: 'Phase transformations in metals and alloys'.

25. A. Grajcar, M. Kaminska, M. Opiela, P. Skrzypczyk, B. Grzegorczyk, and E. Kalinowksa-Ozgowicz: 'Segregation of alloying elements in thermomechanically rolled medium-mn multiphase steels', *Journal of Achievements in Materials and Manufacturing Engineering*, 2012, **55**(2), 259-264.

26. S. M. C. van Bohemen, M. J. Santofimia, and J. Sietsma: 'Experimental evidence for bainite formation below ms in fe–0.66c', *Scripta Materialia*, 2008, **58**(6), 488-491.

27. M. Winning, G. Gottstein, and L. S. Shvindlerman: 'Migration of grain boundaries under the influence of an external shear stress', *Materials Science and Engineering: A*, 2001, **317**(1–2), 17-20.

28. T. J. Rupert, D. S. Gianola, Y. Gan, and K. J. Hemker: 'Experimental observations of stress-driven grain boundary migration', *Science*, 2009, **326**, 1686–1690

29. L. A. Giannuzzi, B. W. Kempshall, S. M. Schwarz, J. K. Lomness, B. I. Prenitzer, and F. A. Stevie: 'Fib lift-out specimen preparation techniques', in 'Introduction to focused ion beams', (eds. L. Giannuzzi, et al.), 201-228; 2005, Springer US.

30. T. Ohnishi and T. Ishitani: 'Method for separating specimen and method for analyzing the specimen separated by the specimen separating method', 1993, Google Patents.

31. W. James R. , W. Charltes E., W. Robert E., and R. Gregory: 'Fundamentals of momentum, heat, and mass transfer', 2001, United Stated of America, John Wiley & Sons.

32. I. Tkalcec, C. Azcoïtia, S. Crevoiserat, and D. Mari: 'Tempering effects on a martensitic high carbon steel', *Materials Science and Engineering: A*, 2004, **387–389**(0), 352-356.

33. N. Zhong, Y. Wang, K. Zhang, and H. Rong: 'Microstructural evolution of a nb-microalloyed advanced high strength steel treated by quenching-partitioning-tempering process', *Steel Research International*, 2011, **82**(11), 1332 - 1337.

34. S. Sun and M. Pugh: 'Manganese partitioning in dual-phase steel during annealing', *Materials Science and Engineering: A*, 2000, **276**(1–2), 167-174.

35. M. G. Mecozzi, J. Sietsma, and S. van der Zwaag: 'Analysis of γ → α transformation in a nb micro-alloyed c–mn steel by phase field modelling', *Acta Materialia*, 2006, **54**(5), 1431-1440.

36. G. P. Krielaart and S. v. d. Zwaag: 'Kinetics of γ → α phase transformation in fe-mn alloys containing low manganese', *Materials Science and Technology*, 1998, **14**(1), 10-18.

37. D. De Knijf, E. Pinto Da Silva, C. Föjer, and R. Petrov: 'Study of heat treatment parameters and kinetics of quenching and partitioning cycles', *Materials Science and Technology*, 2014.

38. D. K. Matlock, V. E. Bräutigam, and J. G. Speer: 'Application of the quenching and partitioning (q&p) process to a medium-carbon, high-si microalloyed bar steel', *Materials Science Forum*, 2003, **426-432**, 1089-1094.

39. Y. Toji, G. Miyamoto, and D. Raabe: 'Carbon partitioning during quenching and partitioning heat treatment accompanied by carbide precipitation', *Acta Materialia*, 2015, **86**(0), 137-147.

CHAPTER V

MECHANICAL AUSTENITE STABILITY STUDY

SECTION 1

EFFECT OF FRESH MARTENSITE ON THE STABILITY OF RETAINED AUSTENITE IN QUENCHING AND PARTITIONING STEEL

D. De Knijf, C. Föjer, L. A. I. Kestens, and R. Petrov: 'Effect of fresh martensite on the stability of retained austenite in Quenching & Partitioning steel', Materials Science and Engineering A, 2014, 615, 107-115.

V.1. EFFECT OF FRESH MARTENSITE ON THE STABILITY OF RETAINED AUSTENITE IN QUENCHING AND PARTITIONING STEEL

V.1.1. Abstract

Restrictions on fuel consumption and safety in the automotive industry have stimulated the development of Quenching and Partitioning (Q&P) steel. This steel is expected to have very high strength in combination with acceptable ductility owing to its microstructure consisting of martensite with a considerable amount of retained austenite. The effect of retained austenite on the mechanical properties and its transformation stability were determined by stepwise uniaxial micro-tensile testing and subsequent Electron Backscatter Diffraction (EBSD) study of a pre-selected region. The austenite fraction evolution with increasing plastic deformation and the influence of fresh martensite on the local strain distribution were quantified based on the orientation data. The decrease of the retained austenite as a function of the applied strain was described by an exponential function with the pre-exponential and exponential factors related to the starting austenite fraction and its transformation stability respectively. It was proven that the presence of fresh martensite has a negative influence on this austenite transformation stability due to its constraining effect on the strain distribution. This affects the mechanical properties manifested by changes in the strain hardening behaviour and total elongation. The results suggest that the ductility of the Q&P steels can be improved by an appropriate design of the heat treatment schedule in order to ensure high retained austenite fractions without the presence of fresh martensite in the final microstructure.

V.1.2. Introduction

The development of advanced high strength steel (AHSS) grades has largely been driven by the demands of the automotive industry. Fuel consumption can be decreased, without compromising the safety of the passengers, by reducing the weight of the steel car body. This in turn, requires the use of thinner, stronger and more ductile materials. Such materials, which have a required balance of hard and ductile phases, can be obtained by employing new approaches for heat treatments. In conventional steel production processes carbon diffusion after displacive or martensitic transformations is not considered. There is

however, evidence that carbon partitioning occurs from martensite to austenite to thin interlath austenite films or isolated islands during cooling or isothermal holding [1]. Speer et al. [2, 3] assumed that carbon partitioning played an important role in stabilizing the remaining austenite if alloying elements which suppress carbide formation are added. They proposed a new heat treatment *Quenching and Partitioning (Q&P)*. Q&P appears promising with regards to the attainment of desired mechanical properties by control of the martensite fraction and carbon enrichment of the austenite.

The Q&P treatment starts with full austenitisation or intercritical annealing followed by quenching to a temperature below the martensite start temperature (M_s) and above the martensite finish temperature (M_f). At this temperature, the microstructure consists of controlled fractions of martensite and austenite. Carbon diffusion from the supersaturated martensite to the untransformed austenite (carbon partitioning) occurs during the isothermal holding between M_s and M_f or after increasing the temperature above M_s, and stabilizes the austenite during the final quench to room temperature. In case of partial austenitisation in the intercritical temperature interval i.e. between Ac_1 and Ac_3 the final microstructure after quenching and partitioning will consist of ferrite, retained austenite and possibly two types of martensite: the one formed during the first quench and the other formed during the final quench [4]. In case of complete austenitisation (heating above A_{C3}) the microstructure will consist only of martensite and retained austenite [5]. In the Q&P process, carbon partitioning and microstructure development are decoupled [6]. The phase fractions and morphologies are controlled by an athermal martensite transformation while partitioning is controlled in an isothermal stage. Such an approach creates a wide variety of microstructures and correspondingly large ranges of mechanical properties in Q&P steels. However, knowledge is still limited concerning the influence on the mechanical properties of the fraction, morphology, distribution and crystallographic texture of retained austenite and different types of martensite. This is an obstacle for better understanding of the microstructure development in order to obtain optimal combinations of strength and ductility by employing Q&P.

The microstructural dependency of their response to deformation must be studied in order to understand and optimize the mechanical properties of Q&P steels. In Transformation Induced Plasticity (TRIP) steel, experimental investigations showed that the transformation stability of austenite is affected by *(i)* the local carbon content in the austenite [7, 8]; *(ii)* the grain volume of the retained austenite [9]; *(iii)* the constraining effect from the phases surrounding the austenite [10, 11]; and *(iv)* the crystallographic orientation of the austenite with respect to the loading direction [8, 12, 13]. These effects are also expected to play an important

role in the transformation stability of the retained austenite in Q&P steels. Observations concerning the morphological dependency of austenite grains on the deformation behaviour in Q&P steel revealed that high-carbon blocky grains were less stable (i.e. transform easier under load) than the lath-type or film-like austenite grains, although the latter have the lower carbon content [14]. For intercritical annealed Q&P the strain distribution between different constituents and its influence on the mechanical properties was studied [15]. It has been shown that the presence of hard martensite constituents reduces the total elongation and toughness [16] however the effect of these constituents on the retained austenite stability has not been investigated so far.

The goal of this work is to contribute to a better understanding of the deformation response of the Q&P microstructure and the resulting mechanical properties. The emphasis is put on the reaction of the retained austenite with and without the presence of *fresh* martensite, i.e. martensite created during the final quench to room temperature. A combination of EBSD measurements and micro-tensile testing was employed in order to quantify the evolution of retained austenite fraction with applied strain.

V.1.3. Experimental

Steel with a nominal composition of 0.25C-1.5Si-3Mn (mass %), produced in a laboratory vacuum induction furnace was studied. Silicon prevents carbide precipitation during the partitioning step since the controlling reaction upon addition of silicon to plain carbon steels changes from carbon diffusion towards the diffusion of silicon away from the interface due to a low solubility in cementite [17]. The silicon forms a barrier around this cementite, representing a kinetic barrier to the growth of the carbide [18]. Manganese increases the hardenability during cooling, and hinders ferrite, pearlite or bainite formation [19]. This, in turn, ensures that sufficient carbon is present for the stabilization of austenite during the final quench.

After casting, the steel slabs were hot rolled to a final thickness of 2.5mm, accelerated cooled by water jets to 600°C and transferred to a furnace for coiling simulations at 560°C. The hot rolled plates were pickled and cold rolled to a thickness of 1mm imposing a total reduction in thickness of 60%. In order to investigate the stability of the austenite, strips of the aforementioned sheets were cut perpendicular to the rolling direction and subsequently subjected to two Q&P heat treatment cycles in the thermo-mechanical simulator Gleeble™ 3500, cfr. Figure V.1-1.

Sample A (the first sample) was fully austenitized at 850°C for 60s, quenched to 224°C for 5s and reheated to 400°C for 500s. The isothermal holding time at the quenching temperature was kept short to avoid isothermal transformation products below M_s [20, 21].

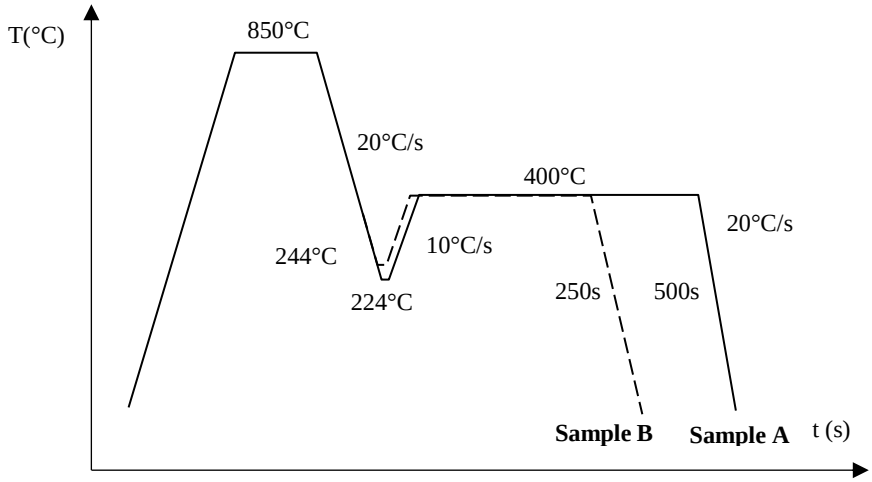

Figure V.1-1: Heat treatment cycles for sample A and B applied to the Q&P steel. The quenching temperature of sample A is lower than for sample B with longer partitioning times suggesting a lower fraction of martensite formed during the final quenching.

An optimal quenching temperature of 242°C was calculated for the current steel composition using the Koistinen-Marburger equation [22] modified with exponential carbon dependencies for the M_s and α-parameter [23]. By considering the experimental martensite fraction after the first quench, this calculation can be improved and results in an optimal quenching temperature of 244°C. The experimental value of the optimal quenching temperature differs by only 2°C from the calculated value suggesting that the theoretical prediction can be used to design Q&P heat treatments.

Sample A is therefore assumed to be completely partitioned as a result of the lower quenching temperature and enhanced partitioning conditions. Sample B (the second sample) was quenched to the optimal quenching temperature of 244°C resulting in a lower first formed martensite fraction compared to sample A. The partitioning time for sample B was half of that of sample A at the same partitioning temperature. Hence, owing to non-complete partitioning, a higher fraction of secondary formed martensite during the final quench is expected in sample B compared to sample A. By studying these two samples, the influence of different untempered or fresh martensite fractions on the microstructural response during deformation can be monitored.

Dog-boned A50 and micro-tensile samples were prepared by water jet cutting from the central area of the Gleeble™ specimens (assuring a well-controlled and known thermal cycle) and the tensile axis was kept perpendicular to the rolling direction of the steel sheet as shown in Figure V.1-2 (a). The dimensions of the small-size tensile specimens satisfy the ASTM standard conditions and to ensure that the specimen failed within the parallel length, the ratio of the grip width to the parallel width is equal or greater than 1.5 [24]. The actual micro-tensile specimen dimensions are given in Figure V.1-2 (b).

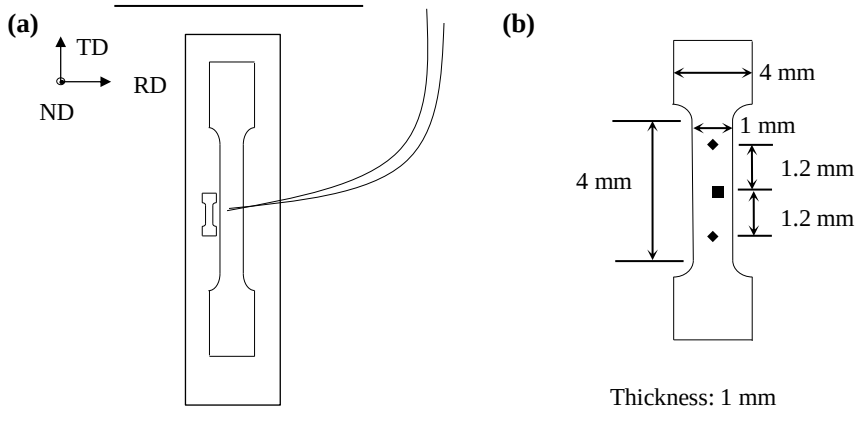

Figure V.1-2: Schematic representation of (a) the cold rolled plate, Gleeble specimen, A50 and micro-tensile specimen with a schematic drawing of the thermocouple; (b) a dog-boned micro-tensile specimen with the location of the Vickers indents (diamond symbols) and the EBSD scan (square symbol).

The A50 tensile tests were carried out on a Zwick Z250 tensile test machine at room temperature with two different speeds. First the position was determined with 20 MPa/s from start to the yield point, followed by an elongation rate of 0.006 mm/s from the yield point to fracture. The micro-tensile tests were conducted on a Deben Microtest 5000N® Tensile Stage device at a constant cross head speed of 0.5 mm/s. Microtest™ software was used for control of the test parameters and data acquisition. The results from the micro-tensile tests are not representative of the mechanical properties owing to uncontrolled effects of factors such as sample alignment, specimen geometry, level of fixing and slip in the grips [25]. Nevertheless, the plastic strains could be successfully evaluated by measuring the distance between outer micro-Vickers indents after each loading step.

Samples were mechanically prepared following the classical preparation route [26] and their microstructural response to deformation was evaluated by means of EBSD measurements. The samples were analysed by a FEI Quanta™ 450-FEG-SEM equipped with a Hikari detector controlled by the EDAX-TSL OIM-Data Collection version 6.2® software.

The EBSD data were acquired on a hexagonal scan grid using an accelerating voltage of 20 kV, a working distance of 16 mm, tilt angle of 70° and a step size of 60nm. Orientation data, acquired from the same selected region marked with a central Vickers indent (cfr. Figure V.1-2 (b)) after each loading step, were post-processed with TSL-OIM Analysis 5.1® software. All scans were performed at a distance of 200 µm from the central indent to avoid influences of its deformation zone on the microstructure.

The volume fractions of austenite at room temperature and the average carbon content were determined from X-ray diffraction (XRD) experiments performed on a Siemens Kristalloflex D5000 diffractometer equipped with Mo-K_α source operating at 40 kV and 40 mA. A 2θ-range of 0° to 45° was scanned using a step size of 0.02° and a dwell-time of 1s. This 2θ-range contains the (111), (200), (220) and (311) fcc reflections and the (110), (200), (211) bcc reflections. The data were post-processed by subtracting the background radiation and $K\alpha_2$ influence. Austenite fractions were calculated by the formula of Cullity [27] and the austenite lattice parameter a_γ is determined from the extrapolation function of the lattice parameter vs. $\cos^2(\theta)/\sin(\theta)$ of the (200), (220) and (311) austenite peaks [28]. The carbon concentration x_c was obtained from the following well-accepted equation [29]: $a_\gamma = 0.3556 + 0.00453x_C + 0.000095x_{Mn}$ where a_γ is the austenite lattice parameter in nm and x_C and x_{Mn} are the concentrations of carbon and manganese in austenite in wt.%. If paraequilibrium conditions are assumed, no diffusion of manganese during partitioning occurs and the average manganese content can be used. The equation does not include silicon since the literature contains limited data about its effect on the lattice parameter of austenite. Similarly, compared to carbon, silicon has negligible effect on the lattice parameter.

V.1.4. Results and discussion

V.1.4.1 Starting Microstructures (initial, undeformed microstructures)

Table V.1-1 lists the austenite fraction, carbon content, and fraction of secondary formed martensite of the microstructures of the heat treated samples which were analysed with X-ray diffraction and electron backscattered diffraction.

The austenite fraction and average carbon content determined by XRD are 20.6 ± 0.4% with 1.3 ± 0.1 wt. % C and 18.4 ± 0.4% with 1.4 ± 0.1 wt. % C for samples A and B respectively. Localized EBSD scans yield significantly lower austenite fractions of 13.6 ± 0.2% for sample A and 8.5 ± 0.3% for sample B illustrated in the phase map by the yellow

coloured grains in Figure V.1-3 (a) and (c) respectively. These discrepancies in austenite fraction between both techniques have been reported in the literature [30] and are attributed to the limits of the spatial resolution of the EBSD systems. Although the spatial resolution of the EBSD technique is reasonably high (step size is 60nm), the smallest austenite laths formed between the martensite plates, as observed with TEM, have sizes in the range of 20 to 100nm [14, 31, 32]. The laths can therefore not be resolved by EBSD but are detectable with XRD.

Table V.1-1: The retained austenite (RA) fractions of samples A and B measured with XRD and EBSD, its carbon content measured with XRD and the fraction of fresh martensite (FM) obtained from the volume fraction of the low image quality grains in the EBSD scan. The error on the carbon content and retained austenite fraction by XRD, and the fresh martensite fraction by EBSD was determined by repeated measurements on the same specimen whereas for analysis of the retained austenite fraction by EBSD two analysis methods to clean up and quantify the measurements were used.

Sample	XRD		EBSD	
	RA fraction (%)	C content (%)	RA fraction (%)	NM fraction (%)
A	20.6 ± 0.4	1.3 ± 0.1	13.6 ± 0.2	3.5 ± 0.6
B	18.4 ± 0.4	1.4 ± 0.1	8.5 ± 0.3	21.8 ± 1.4

The image quality maps of the starting, undeformed steels in Figure V.1-3 clearly reveal the difference in the microstructures of steels A and B. Owing to a less perfect bcc lattice, darker regions with a lower pattern quality are present in steel B (cfr. Figure V.1-3 (d)) but are practically absent in the microstructure of A (cfr. Figure V.1-3 (b)). These dark regions are associated with fresh martensite, formed during final quenching [5], which has a higher Kernel average misorientation (calculated for the 3rd nearest neighbour of each point and upper limit of 5°) than the rest of the microstructure (cfr. Figure V.1-3 (e)). The fresh martensite grains are located in close vicinity of the retained austenite grains, which makes the distinction between the fresh and old martensite by image quality difference reliable [33]. The fresh martensite fraction was found to be 3.5 ± 0.6 % and 21.8 ± 1.4 % for sample A and B respectively. These fractions correlate well with the partitioning conditions, illustrating that partitioning was less pronounced for sample B and hence part of the austenite transformed to martensite.

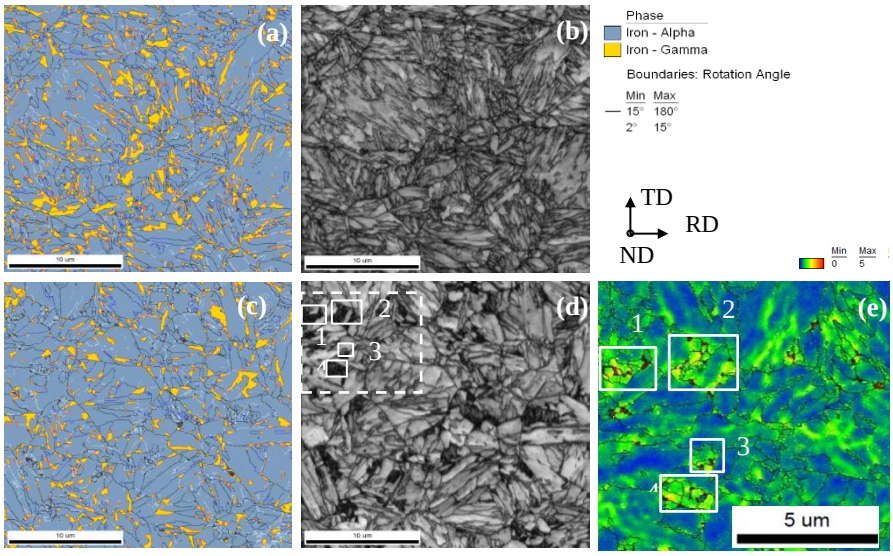

Figure V.1-3: Phase map (blue is martensite, yellow is austenite) for samples A (a) and B (c) with the image quality of the EBSD scans given in images (b) and (d) respectively. Image (e) represents the Kernel average misorientation calculated with the 3rd nearest neighbours of the white boxed area in map (d) to illustrate the presence of fresh martensite by both lower image quality and higher Kernel average misorientation.

Figure V.1-4 shows the crystallographic textures of retained austenite and martensite for samples A and B before tensile deformation. The textures of retained austenite (cfr. Figure V.1-4 (a) and (c)) are similar and rather weak, with maxima of 2.8 and 4 mrd (multiples of a random distribution) occurring for the {011}<112> Brass component in sample A and B respectively. Goss {110} <001>, Rotated Goss {110} <110>, S {123} <634> and Copper {211} <111> also occur in both steels while the weak rotated Cube {001} <110> is present in sample A only. The martensite has a crystallographic texture which is frequently observed after double α-γ-α transformation of cold deformed bcc phase in advanced high strength steels. Figure 4 (b) and (d) clearly represent the transformation products of the previously discussed austenite textures for samples A and B respectively.

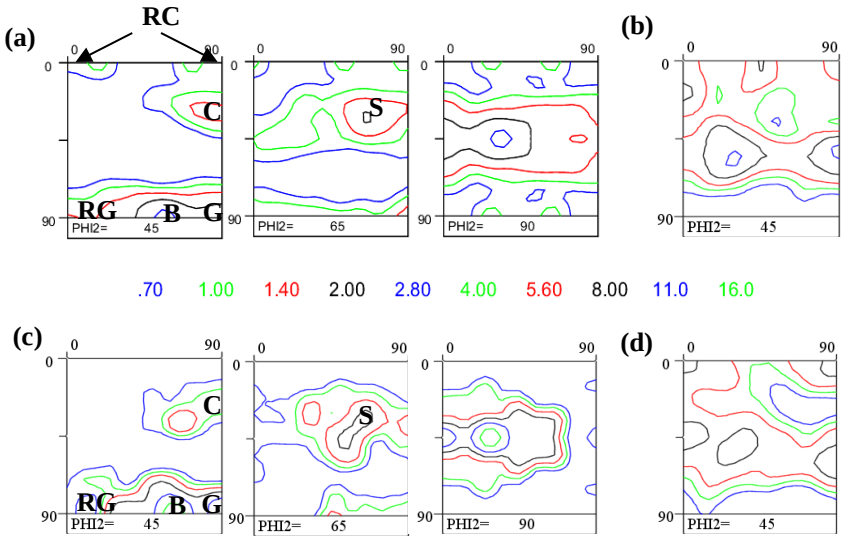

Figure V.1-4: Orientation distribution functions (ODFs) in φ2 = 45°, 65° and 90° sections for austenite in sample A (a) and sample B (c); and in φ2 = 45° for martensite of sample A (b) and sample B (d) in the material after hot rolling, cold rolling and Q&P heat treatment with RC = Rotated Cube, C = Copper, RG = Rotated Goss, B = Brass, G = Goss.

V.1.4.2 Plastic strain accommodation (during tension)

The relative changes in length of the central indent axis were used as a reference for local strain characterization. These differences were monitored as a function of the applied tensile strain. Dimensional changes of the axis parallel and perpendicular to the tensile axis direction respectively were calculated as a function of the total elongation, based on the distance between the outer indents. Figure V.1-5 plots the evolution in strain, as measured by the elongation and shrinkage of the central indent as a function of the total elongation. The length change is positive and linearly interpolated whereas the width change results in zero or negative values consistent with contraction due to narrowing. The interpolation of the indent length change for sample A has a slope of 1.03 indicating that the total elongation equals the local deformation in the studied zone. Interpolation of sample B on the other hand gives a slope of 0.79 and hence an overestimation of the local strain. Width reductions were observed starting from elongations of 4.3% and 3.7% for samples A and B respectively. This suggests that the volume change during the early stages of deformation was preserved by thinning (not observed in 2D characterization) rather than by narrowing. Hereafter, the local strain will be described by the projection of the total elongation corrected with a factor 0.79 for sample B.

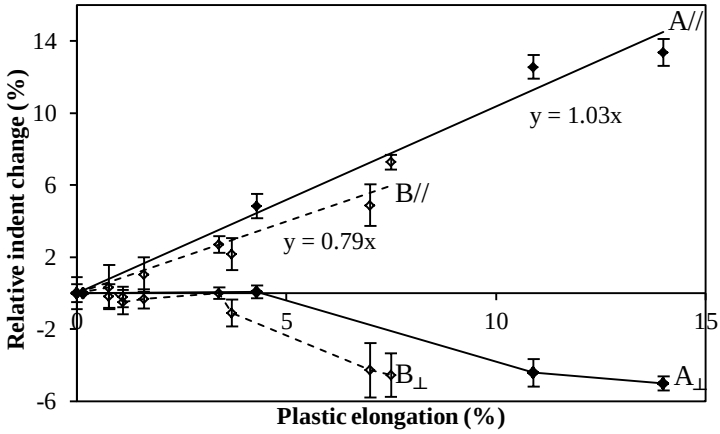

Figure V.1-5: Relative indent change as a function of the total elongation- the positive, interpolated values represent the length increase (axis parallel to the tensile direction) and the zero and negative values represent the width decrease (axis perpendicular to the tensile direction). The sum is not 0 because the thinning of the sample in the third dimension is not monitored. The measured length is the average of three length measurements on the same indent with the error bar related to the standard deviation.

V.1.4.3 Retained Austenite Fraction as a Function of the Elongation

Figure V.1-6 shows the decrease in retained austenite fractions, obtained from the EBSD phase maps, as a function of the total elongation at different stages of deformation. The EBSD data were always acquired from exactly the same area after removing the non-indexed points (by assigning a minimum confidence index value of 0.1). The initial retained austenite fraction in sample A was 13.6 ± 0.2 %. This value is reduced to 1.4 ± 0.2 % after 14% plastic deformation. In contrast, the fraction in sample B decreases from 8.5 ± 0.3 % to 0.5 ± 0.2 % after only 5.8% elongation. The differences in the total elongation and deformation behaviour, in general, can be attributed to the specific microstructures and, more precisely, to the fractions of retained austenite and fresh martensite. Sample B has lower retained austenite and higher fresh martensite fraction than sample A, which contributes to its decreased elongation at fracture. The evolution of the retained austenite fraction with plastic elongation can be fitted to an exponential function (cfr. Figure V.1-6). The pre-exponential factor of 13.6 for sample A and 8.5 for sample B are assigned as the initial austenite fractions whereas the exponential factors (0.178 for sample A and 0.445 for sample B) are related to features which influence the austenite stability. Hence, the austenite in sample B is more susceptible to strain-induced transformation compared to that of sample A.

Necking in sample A was observed after 14% elongation. However, the retained austenite fraction values measured in the pre-defined zone of sample A remained the same as in the previous loading step because no deformation was accommodated in the scanned zone which is located outside the necking area. EBSD scans were performed in the necking region in order to correct this and to verify the proposed exponential dependence. This, for calculations done under volume restrictions, yielded an average austenite fraction of 0.4% and a local elongation of 18.5% which, when incorporated into the plot (cfr. Figure V.1-6 point 18.5% elongation) follows the predicted exponential interpolation curve.

Matsumura et al. [34] suggested that the retained austenite fraction (F_{aust}) decreases with increasing strain (ε) according to an inverse relationship in which A and B are fitted by a least-squares method: $F_{aust} = \frac{1}{(A*\varepsilon+B)}$ where A and B have values of A = 0.020 and B = 0.074 for sample A, and A = 0.113 and B = 0.115 for sample B.

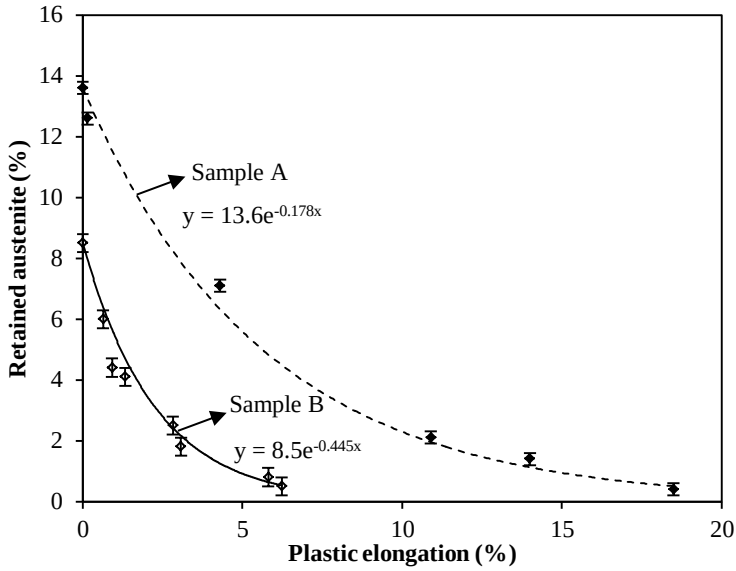

Figure V.1-6: Retained austenite fraction as a function of the elongation- sample A: filled symbols and sample B: open symbols. The experimental values are interpolated by an exponential curve with the pre-exponential factor set equal to the starting austenite fraction and the exponential factor representing the influences on the austenite stability. Error bars were calculated by two analysis methods to clean up and quantify the measurements.

In the exponential interpolation only one parameter needs to be fitted since the pre-exponential factor was set equal to the initial austenite fraction. Henceforth, the exponential fit will be used since it gives a satisfactory approximation and the relative differences in retained austenite profiles between both samples are most important. Using this fit omits the

influence of the starting austenite fraction on the stability of the austenite. All other contributory factors are therefore grouped in one parameter, the exponential factor, which can be seen as an austenite stability factor.

V.1.4.4 Different Factors Influencing the Austenite Stability

The transformation stability of austenite is affected by the carbon content (which may even vary inside the grain [35]) of individual austenite grains [7, 8], the grain size [9] and morphology [14], the constraining effect from the phases surrounding the austenite [10, 11] and the crystallographic orientation with respect to the loading direction [12, 13]. These effects were further considered in order to explain the difference in transformation stability between both samples. Although the local carbon content of the retained austenite cannot be measured the average values obtained by XRD were 1.3 ± 0.1 wt. % C and 1.4 ± 0.1 wt. % C for samples A and B respectively. Thus, in general, the austenite grains of both samples have the same chemical stability since the difference is within the experimental error. Nevertheless, these data give no information concerning the local carbon content inside specific austenite grains which determines the local stability of the (partial) austenite grain. The intragranular carbon content, and hence M_s temperature, can vary significantly due to the intrinsic mechanism of carbon diffusion, kinetics and austenite-martensite interface mobility during partitioning [35]. The difference in carbon diffusion in martensite and austenite results in a pile-up of carbon in the austenite grains at the interface [36]. Therefore, if the partitioning time is not sufficient to homogenize the carbon concentration, a carbon rich austenite edge with lower carbon content in the central part of the retained austenite will be formed.

The grain size can also influence the transformation stability of retained austenite. It is generally accepted that large austenite grains transform easily to martensite under strain [9]. However, in the current study, the undeformed A and B samples have both similar austenite grain size distributions and average diameter values of 0.62 µm and 0.60 µm, respectively.

The morphology of the austenite grains was quantified as the area fraction of grains with different major axis orientations. The austenite grains were considered as ellipsoidal volumes with a major and minor axis observed on a 2D section. Henceforth the area fraction distribution can be considered as a function of the angle between the major axis and the sample RD direction. Since the tensile direction is along TD (vertical in the EBSD maps), the grains with their long axis oriented 90° in the scan are parallel to the tensile axis whereas 0°

and 180° oriented grains in the map are perpendicular to the tensile direction. The distributions of area fractions are quite similar in the range of 0°- 108° (cfr. Figure V.1-7).

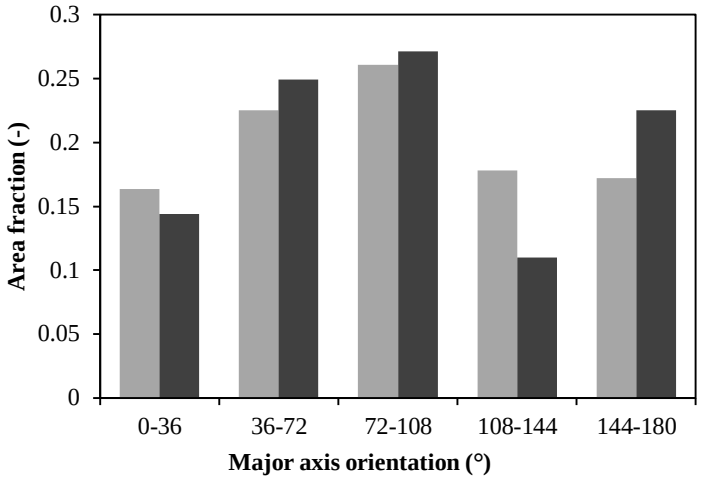

Figure V.1-7: The area fraction of different ranges of major axis orientations of the austenite grains of sample A in light grey and sample B in dark grey. 0° and180° represents RD whereas 90° is parallel to TD.

Grains with orientations between 108° and 144° have lower fractions in B while those in the range of 144°-180° occur with a higher fraction compared to sample A. Compared to A, this could result in less local accommodation of shear in sample B and more transformation of grains perpendicular to TD. All orientations are however present in both samples and can contribute to the accommodation of deformation by the TRIP effect for different strain modes.

As discussed previously, the starting texture of the austenite is very similar for both samples with the only difference being the presence of a weak rotated Cube component in sample A, which was not observed in B. The texture differences can therefore be ignored as factors which influence the deformation behaviour of samples A and B. However the influence of the crystallographic orientation on the transformation stability of the retained austenite is an important parameter which is documented in the literature for TRIP assisted steels [8, 37].

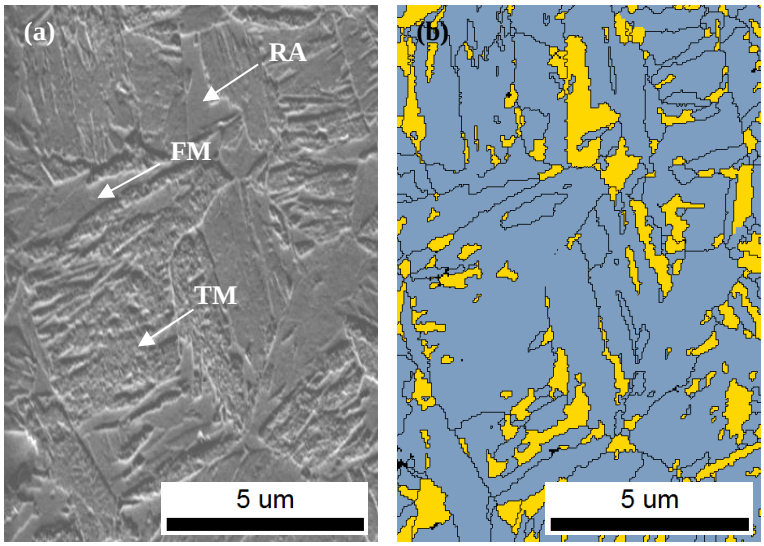

Figure V.1-8: (a) SEM image of a Q&P heat treated sample (QT = 244°C, PT = 400°C, Pt = 1000s) with tempered martensite (TM) with carbides, fresh martensite (FM) and retained austenite (RA). The phase map of the same area (b) reveals that the less etched blocks can be attributed to both fresh martensite and retained austenite.

In contrast, the fraction of fresh martensite differs significantly in both samples being on average 3.5% for sample A and 21.8% for sample B. The fresh martensite grains are less ductile and hence cannot easily accommodate the deformation [38]. As such, the interfaces between old and fresh martensite or between fresh martensite and austenite are potential nucleation sites for local damage (voids or cracks). In Figure V.1-8 (a) and (b) respectively a SEM image and phase map are shown with the austenite grains yellow and martensite grains blue of a Q&P heat treated sample. The unetched blocks are attributed to fresh martensite (FM) or retained austenite (RA) whereas the tempered martensite (TM) with carbides lies deeper in the microstructure because it etches more heavily [5]. SEM images (cfr. Figure V.1-9 (a)-(b)) were taken of samples A and B after tensile testing. After fracture, the homogeneous deformation zone consists of unetched rigid blocks and etched deformed grains. Since austenite transforms during the deformation, the austenite fraction will be small. The unetched blocks are therefore attributed to fresh martensite.

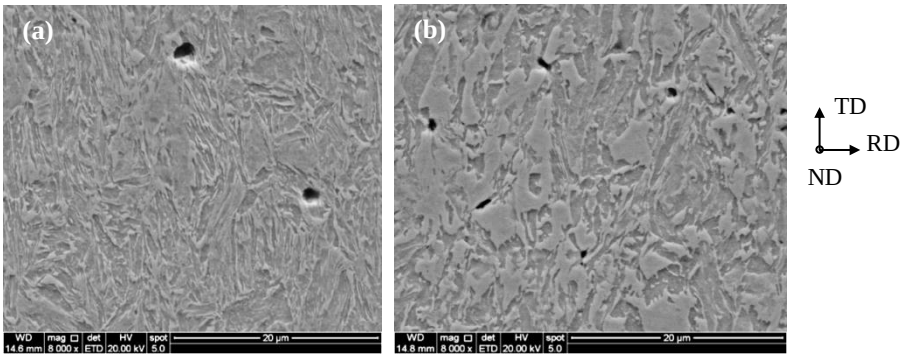

Figure V.1-9: SEM image in the homogenous deformation zone of (a) sample A and (b) sample B after 2% Nital etching with elongated tempered martensite grains; untempered, fresh martensite blocks and void formation at the fresh martensite interfaces in sample B.

Fresh martensite blocks are absent from sample A and the tempered martensite grains are deformed along the tensile direction. Sample B consists of many fresh martensite blocks which remain as rigid, undeformed components in the microstructure. Deformed, tempered martensite grains are observed between the fresh martensite blocks. Void formation at the interfaces of fresh and tempered martensite seems to be triggered by the presence of this fresh martensite owing to its constraining effect on the deformation resulting in stress concentrating areas in the surrounding microstructure. Figure V.1-10 compares the distribution of voids in samples A and B whereby the void fractions of sample A are calculated with respect to the total number of voids present in sample B in order to draw conclusions about the relative difference between both samples. Sample A, shown by the light grey bars, contains only about 25 % of the voids present in sample B. The difference is particularly striking for voids with sizes between 0.02 and 0.03 µm². This indicates that the fresh martensite changes the deformation mechanism. The fresh martensite blocks cannot easily accommodate the deformation and, as a result, more voids are generated at the interfaces.

The surrounding austenite grains try to accommodate the strain by transforming to high-C martensite. High-C martensite appears as non-indexed points in the EBSD map as for example in the case of grain I in Figure V.1-11.

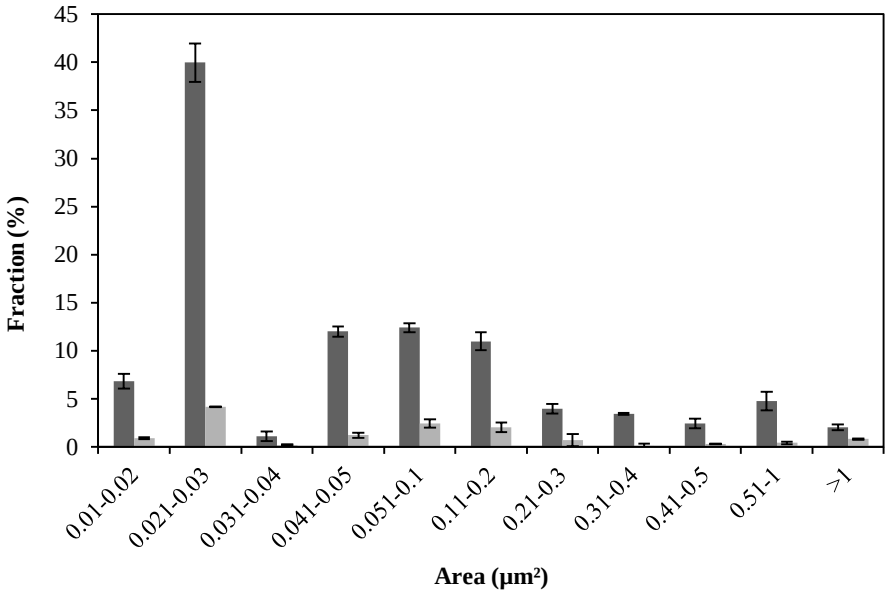

Figure V.1-10: Fraction of voids with different sizes (area) for sample A in light grey and sample B in dark grey whereby the distribution of sample A is rescaled to the total number of voids present in sample B to compare both distributions in a quantitative manner. For calculating the distributions several images representing a total area of 240µm x 240µm were used. Error bars were calculated by reanalysing the images and recalculating the distribution.

The high local misorientations in the fresh martensite blocks are identified by the darker grey colour in the image quality map. The fraction of non-indexed points due to the lattice distortion generated in subsequent deformation stages increases. For example, grain II in the starting material (cfr. Figure V.1-11 (b)) is fully indexed. However, after total elongations of 3.1% and 5.8% it evolves into a completely non-indexed or black grain (cfr. Figure V.1-11 (c)-(d)). Fresh martensite grains limit the strain accommodating capacity of the tempered martensite. This constraining effect gives rise to stress concentrations which, in turn, cause the austenite to transform at lower elongations.

Figure V.1-12 (a) and (b) show the Kernel average orientation maps (KAM) of the tempered martensite in the fractured A and B samples. The KAM was calculated with respect to the third nearest neighbours in regions located 1.4mm away from the fracture surface. Fresh martensite grains have lower KAM values because they are less deformed during tensile testing compared with the tempered martensite. Grains with image quality (IQ) lower than 1000 were excluded from the maps in order to investigate the deformation accommodating capacity of the tempered martensite. As evidenced by a higher fraction of blue-coloured

grains, the map of tempered martensite in sample B consists of more minimum KAM (in the range of 0-1°) values compared to sample A.

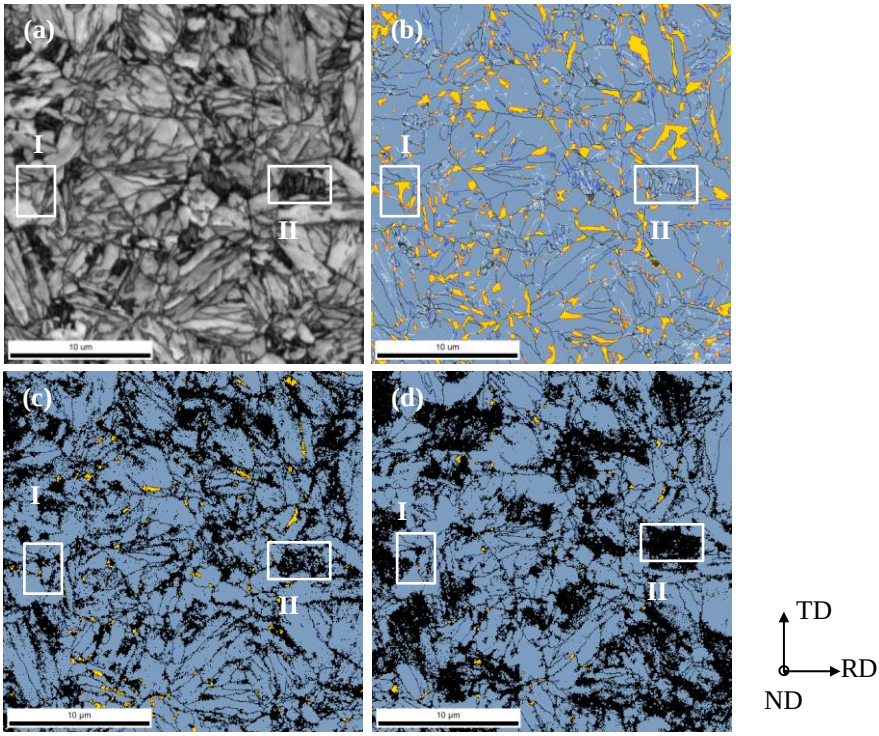

Figure V.1-11: Sample B - (a) image quality map of undeformed material (b) phase map of undeformed material (c) phase map after 3.1% and (d) after 5.8% elongation with yellow = austenite and blue = martensite. The black points in (c) are associated with austenite to martensite transformation and stress localization in/around fresh martensite.

Figure V.1-12 (c) plots the number fractions of the KAM in both samples. The distributions are similar but the curve of sample B (dark grey) is shifted to the left relative to that of sample A (light grey). This shift indicates that the tempered martensite of sample B accommodated less deformation compared to that of sample A. A lower average KAM value, 1.345 vs. 1.386, confirms that this is the case. The stress-concentrating effect in the new martensite blocks which remain as rigid, constituents results in less deformation accommodation in the tempered martensite matrix and a faster decay of retained austenite and consequently an overall lower total elongation.

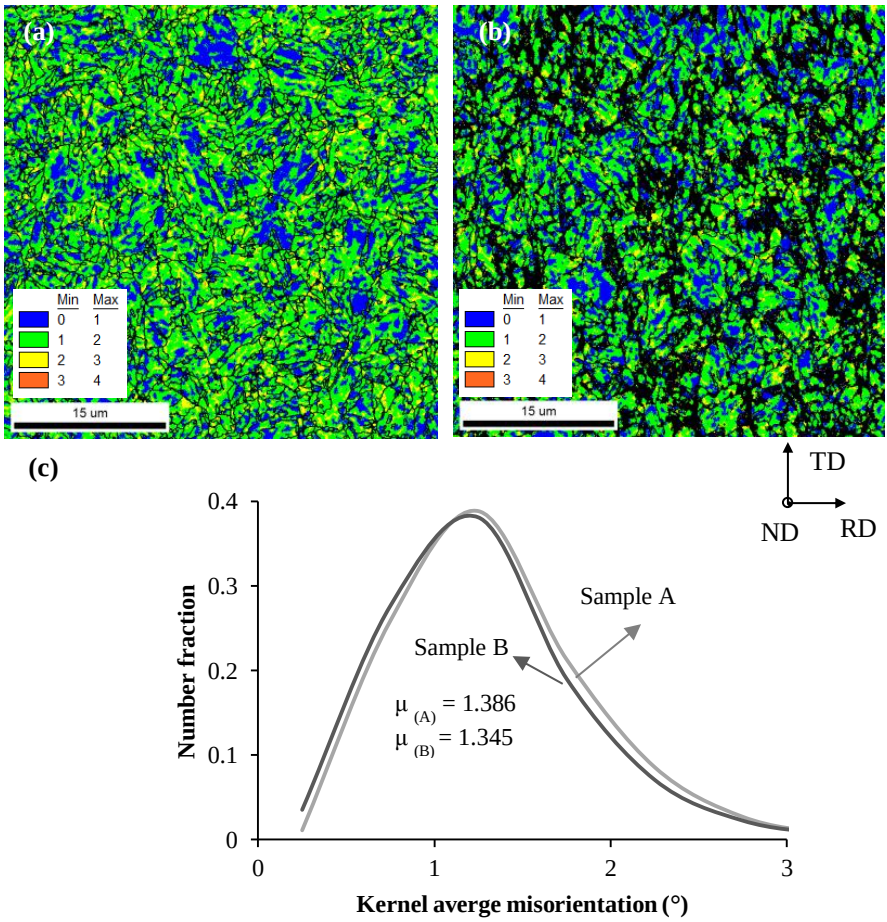

Figure V.1-12: Kernel average misorientation (KAM) with 3rd nearest neighbours superimposed on the image quality for (a) sample A (b) sample B. The fracture surface is located 1.4 mm above the images. Image (c) illustrates the number fraction of the KAM of the tempered martensite for sample A in light grey and sample B in dark grey relative to sample A.

The constraining effect of fresh martensite formed during the second quench of the Q&P heat treatment seems to play an important role in the transformability of austenite and hence, the mechanical properties.

Grains on the surface and those inside the bulk of the material exhibit different transformation behaviours. Since the spatial freedom of the grains at the surface is larger, they accommodate the shape changes associated with the austenite-to-martensite transformation more easily than their counterparts in the bulk. Therefore, during tensile testing the austenite grains near the surface are able to transform at lower strains than those in the bulk and this leads to a reduction in the exponential factor [30]. To verify this, EBSD measurements were

conducted on exactly the same area as before, but after polishing to remove the surface layer. The internal microstructure was examined at a distance of 7.7µm (a few grain diameters) below the surface of the micro-tensile experiment. After polishing, the austenite fraction for sample A was found to be 1.8% which is very similar to the 1.4% previously obtained at the surface. The internal EBSD scan for sample B shows that 0.5% retained austenite is left which is exactly the value found on the surface of the sample after 5.8% elongation. Such small difference between the austenite fractions at the surface and in the subsurface layers verifies that the previously discussed results are reliable predictors of the austenite fraction versus strain relationship.

V.1.4.5 Influence on the mechanical properties

The engineering stress-strain curve of sample A has a lower strain hardening rate, higher total elongation and yield point, and lower ultimate strength compared to sample B (cfr. Figure V.1-13 and Table V.1-2).

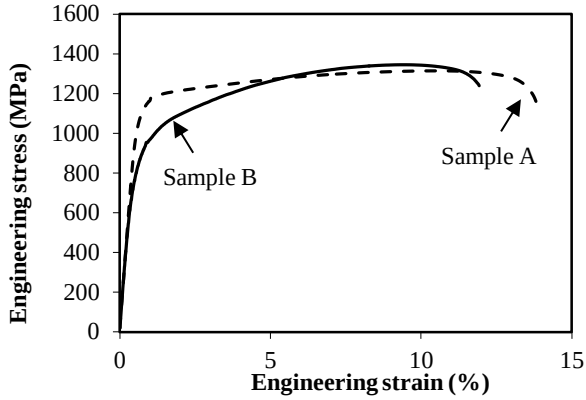

Figure V.1-13: Representative engineering stress-strain curves (A50) of samples A and B.

According to the above discussed experiments, the presence of fresh martensite results in locally higher stress levels in the vicinity of the fresh martensite blocks. In these areas, the austenite grains transform at lower stress levels, decreasing the overall austenite stability. Thus in sample B, larger austenite grains in the surrounding of the fresh martensite transformed fast in the first deformation stages at low overall stress-levels resulting in a low yield point and high strain hardening exponent. In sample A, the homogeneous strain distribution results in a higher yield point and the continuous TRIP effect contributes to a lower n-value. Besides this low n-value, longer partitioning time in sample A resulted in more tempered first formed martensite. The later contributes in lowering the ultimate tensile

strength. The slower transformation rate of the retained austenite (cfr. Figure V.1-6) explains its higher total elongation.

Table V.1-2: The n-values, yield stresses, ultimate tensile stresses and total elongations for samples A and B.

Sample	Yield Stress	Ultimate tensile stress	Total elongation	n-Value
	MPa	MPa	(%)	-
A	1092	1335	13.4	0.073
B	823	1345	11.9	0.196

V.1.5. Conclusions

Two heat treatments on specially designed Q&P steel were chosen to study the influence of fresh martensite on the mechanical response of the microstructure by combined micro-tensile testing with EBSD measurements on a pre-selected area. The fresh martensite was found to play a significant role on the strain distribution in the microstructure by inhibiting the amount of deformation that can be accommodated in the tempered martensite, and on the fracture mechanism by triggering void formation. This constraining effect decreases the austenite transformation stability, defined as the exponential factor of the retained austenite fraction versus strain interpolation. Consequently, a high retained austenite fraction with a low fresh martensite fraction will enhance the total elongation and decrease the strain hardening rate due to a continuous TRIP effect after yielding.

V.1.6. Acknowledgements

This research was funded by the governmental institute for the Promotion of Innovation by Science and Technology in Flanders (IWT) and was carried out under the frame of the project “RFCS-CT-2011-00017 “New advanced high strength steels by quenching and partitioning process (NewQ&P)”. Discussions with and comments from Dr. Maria Santofimia Navarro and Prof. Jilt Sietsma of the Materials Science and Engineering Department, Faculty 3mE, TU Delft, The Netherlands are greatly appreciated. We are furthermore grateful to TU Delft and F. Hajy Akbary for assistance and use of the micro-tensile test device.

SECTION 2

EVOLUTION OF THE RETAINED AUSTENITE FRACTION DETERMINED WITH EBSD AND XRD DURING UNIAXIAL TENSILE TESTING

with special thanks to Arnold Kolk for conducting the XRD experiments

V.2. EVOLUTION OF THE RETAINED AUSTENITE FRACTION DETERMINED WITH EBSD AND XRD DURING UNIAXIAL TENSILE TESTING

V.2.1. Introduction

The retained austenite fractions, as determined from EBSD and XRD measurements, differ owing to a difference in the spatial resolution of the techniques [30]. Therefore, XRD was used to measure the retained austenite fraction as a function of the total elongation of the same samples, which were previously measured with EBSD (see Chapter V.1). Sample A was quenched to 224 °C and partitioned at 400 °C for 500 s whereas sample B was quenched to 244 °C and partitioned at the same temperature for 250 s. These processing conditions resulted in the formation of fresh martensite in the starting material of sample B.

V.2.2. Experimental

The cold-rolled samples were cut into micro-tensile samples, whose geometry is shown in Figure V.2-1. To avoid scattering of the X-ray signals, the specimen surface was polished electrolytically after mechanical polishing.

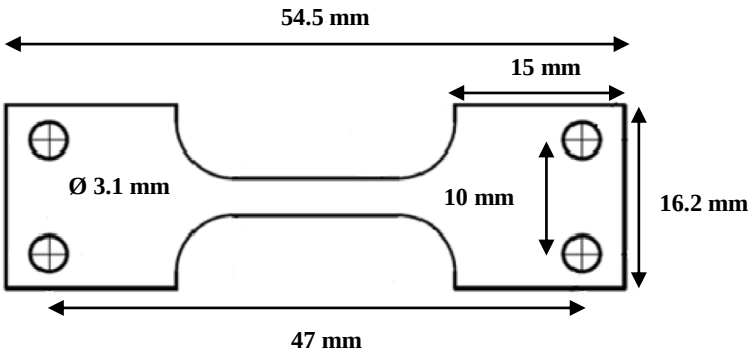

Figure V.2-1: Geometry of the micro-tensile sample for the in-situ XRD experiments

Tensile tests were performed in 100 MPa steps at a strain rate of 6 10^{-4} s^{-1} on a Microtest machine mounted inside a Bruker D8 X-ray diffractometer equipped with a Co-K_α source. At each stress step, a diffraction scan was performed for 2θ-angles of 55°-105°, a range which contains the {200} and {220} austenite as well as {200} and {211} martensite

peaks; a scan rate of 1 s per step and a step size of 0.05° were used for all measurements. The relative intensity change of the $\{220\}_{\gamma}$ to the $\{200\}_{\alpha'}$ was used to quantify the retained austenite fraction since they are related by the Kurdjumov-Sachs orientation relationship. Hence, austenite with a $\{220\}_{\gamma}$ orientation will transform to martensite with a $\{200\}_{\alpha'}$ orientation, thereby revealing the stability of this austenite crystallographic orientation.

V.2.3. Results

Figure V.2-2 and Figure V.2-3 show the profiles corresponding to samples A and B, respectively. As previously discussed in Chapter V.1, the data points can be interpolated by an exponential equation of the form:

$$RA\ (\varepsilon) = RA_f + \left(RA_0 - \ RA_f\right).\exp(-T_{RA}.\varepsilon)$$

where RA_f is the fraction of retained austenite remaining in the uniformly deformed area after fracture, RA_0 is the initial fraction of retained austenite, and T_{RA} is the stability-dependent transformation rate of the austenite.

For the profiles measured with EBSD, this equation is simplified to:

$$RA\ (\varepsilon) = RA_0.\exp(-T_{RA}.\varepsilon)$$

since the final detectable fraction with EBSD approached zero, as shown in Figure V.2-2 and Figure V.2-3.

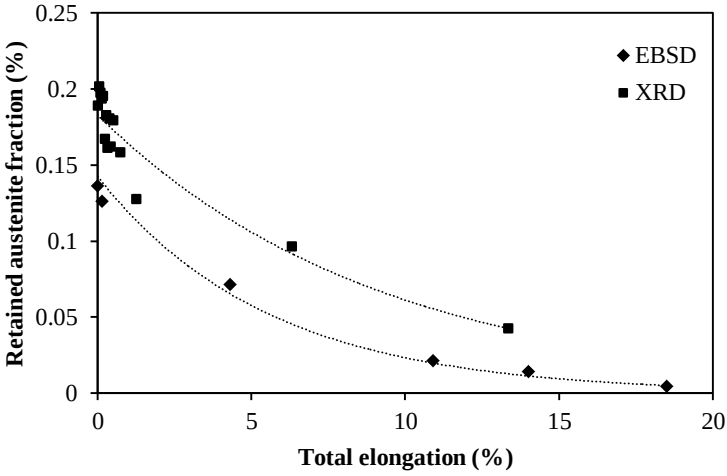

Figure V.2-2: Retained austenite fraction of sample A versus total elongation, as measured by EBSD and XRD

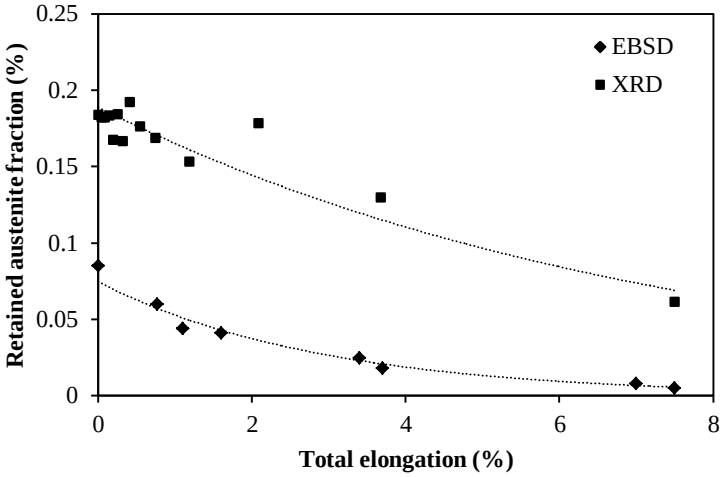

Figure V.2-3: Retained austenite fraction of sample B versus total elongation, as measured by EBSD and XRD

V.2.4. Discussion

Over the entire deformation range, the XRD-derived fraction of retained austenite differs by approximately the same amount from that determined via EBSD. This indicates that both techniques are reliable in predicting the austenite evolution during straining. For sample A, the ~4% difference in the retained austenite fractions is attributed to the small undetectable austenite grains, which are located between the martensite laths.

For sample B, the 8% difference stems from both undetectable austenite laths and the austenite grains stabilized inside the fresh martensite blocks [39]. Some traces of these austenite grains inside the fresh martensite blocks can be observed experimentally, as illustrated in the EBSD map shown in Figure V.2-4. The blocks are, however, poorly indexed owing to the low image quality of the surrounding high-C martensite. Although their fraction is underestimated by EBSD, the presence of these austenite grains was confirmed by the reliably indexed points obtained after the cleaning procedure; as Figure V.2-4 shows, the retained austenite grains (yellow regions) are present inside the fresh martensite (FM) blocks.

The XRD measurements were conducted in uniformly deformed areas, which exhibited uniform elongations of 13.3% and 7.5% and resulting retained austenite fractions of 4.3% and 6.2% (Figure V.2-2 and Figure V.2-3) for samples A and B, respectively. Since the

majority of these austenite grains is unresolvable with EBSD, a sufficient fraction of retained austenite may still be available for accommodating the strain after necking.

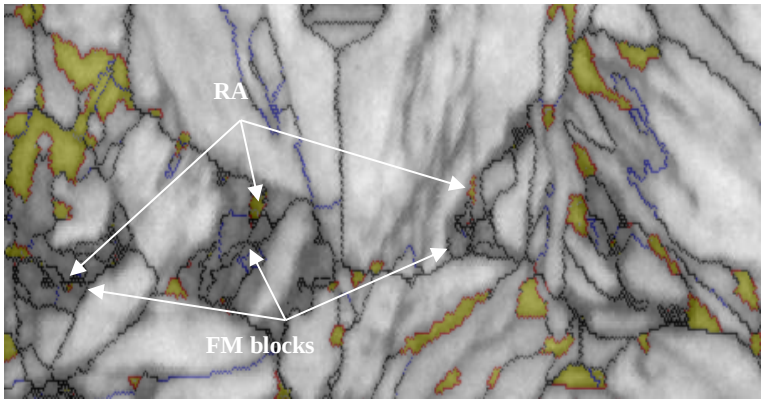

Figure V.2-4: Image quality map with retained austenite grains coloured in yellow: fresh martensite blocks are identified by the low image quality areas with small traces of retained austenite grains inside

In sample B, (cfr. Figure V.2-3) the small austenite grains inside the fresh martensite blocks are shielded by the high yield strength of the high-C martensite. This shielding results in a relatively high (6.2%) retained austenite fraction even after fracture. Consequently, the transformable fraction (12.2%) of retained austenite is smaller than the starting austenite fraction, thereby reducing the amount of TRIP-assisted deformation behaviour. In Chapter V.1, it was concluded that the presence of fresh martensite results in highly localized strains and rapid transformation of the detectable austenite grains.

On the other hand, sample A (cfr. Figure V.2-2) has a transformable austenite fraction of 14.7% in the uniformly deformed zone and exhibits homogenous transformation behaviour over the entire deformation regime. The last 4.3% which remained in this area detected with XRD is expected to contribute (partially) to necking, since the fraction determined via EBSD continued to decrease until 0.5% which is below the values measured at uniform strain levels.

V.2.5. Positioning versus literature

The profiles measured in this work are compared with data from previous studies, cfr. Figure V.2-5.

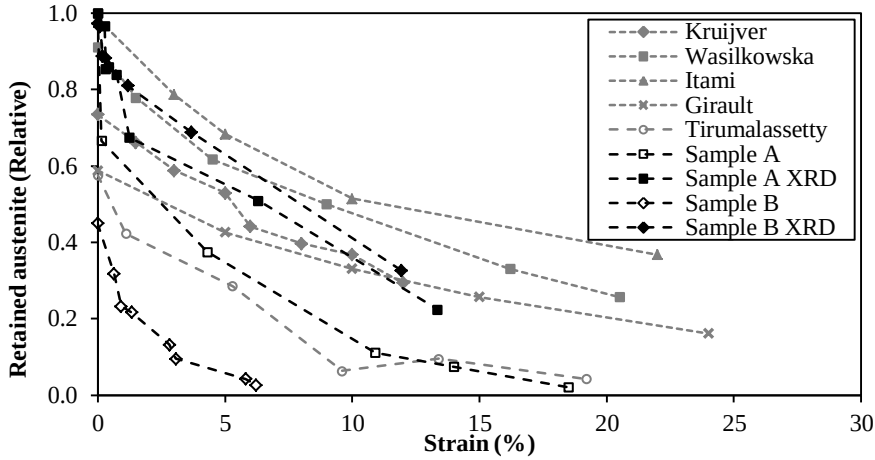

Figure V.2-5: Retained austenite fractions vs. strain for samples A and B studied in this work (EBSD and XRD measurements) compared with austenite stability in TRIP steel measured with diffraction by Kruijver [40], Itami [41], and Girault [42], with magnetic measurements by Wasilkowska[43], and with EBSD by Tirumalassetty [30]

The retained austenite profiles for samples A and B measured with EBSD and XRD are denoted by the black curves. The other profiles for TRIP steels [30, 40-43] were measured with different techniques: diffraction experiments, magnetometer experiments, and EBSD. The EBSD-measured profile of sample A concurs with that obtained by Tirumalassetty [30] measured via EBSD for TRIP-steel. Owing to limits in its detection resolution, the profiles obtained with other methods all lie in a higher range than those measured by EBSD.

V.2.6. Conclusion

In-situ tensile tests were conducted inside an XRD diffractometer in order to track the retained austenite fraction as a function strain and compare this evolution with the results obtained from EBSD. Two Q&P samples, with and without fresh martensite (FM), were tested. Over the entire deformation range, the XRD-derived fractions of RA differed by a constant value from those determined via EBSD. This value was larger for the sample with FM in the starting microstructure, compared to its non-FM-containing counterpart. The larger value stemmed from a less reliable indexation, via EBSD, of the RA patterns inside the FM blocks on top of the film-like austenite located between the tempered martensite laths, which are present in both samples. In addition, although both samples had a similar starting RA fraction, the transformable RA fraction until uniform deformation decreased, owing to shielding by the FM blocks.

SECTION 3

ORIENTATION DEPENDENCE OF THE MARTENSITE TRANSFORMATION IN A QUENCHED AND PARTITIONED STEEL SUBJECTED TO UNIAXIAL TENSION

D. De Knijf, T. Nguyen-Minh, R. Petrov, L. A. I. Kestens, and J. J. Jonas: 'Orientation dependence of the martensite transformation in a quenched and partitioning steel subjected to uniaxial tension', *Journal of Applied Crystallography*, 2014, 47

V.3. ORIENTATION DEPENDENCE OF THE MARTENSITE TRANSFORMATION IN A QUENCHED AND PARTITIONED STEEL SUBJECTED TO UNIAXIAL TENSION

V.3.1. Abstract

The orientation dependence of the austenite-to-martensite transformation during uniaxial tensile testing was modelled using the phenomenological theory of martensite crystallography and the mechanical driving force. It was validated experimentally by means of electron-backscattered diffraction measurements on a pre-defined zone of a quenched and partitioned steel during interrupted tensile tests. A close match is obtained between the predictions of the model and the experimental observations.

V.3.2. Introduction

Since the end of the last century TRIP steels have emerged on the market as they exhibit an excellent balance between strength and ductility. This combination of properties is a result of the transformation of retained austenite to martensite during straining, which is referred to as the transformation induced plasticity (TRIP) effect. The ability of the retained austenite to transform during deformation is affected by many factors, such as: (i) the local carbon content of the austenite [7, 8]; (ii) the grain size of the retained austenite [9]; (iii) its morphology [44]; (iv) the constraining effect of the phases surrounding the austenite [10, 11]; and (v) its crystallographic orientation [8, 12, 13, 45-47]. The influence of austenite orientation on transformation stability is generally attributed to an orientation dependent mechanical driving force [45, 48, 49]. Under mechanical load, austenite grains with the higher driving forces transform preferentially, which can be observed in the evolution of the austenite texture after deformation.

However, dislocation glide and mechanical twinning during deformation can also lead to rotation of the austenite grains [30], whereby the stored plastic energy may also contribute to the mechanical driving force. In this study, the dependence of the austenite-to-martensite transformation under tensile loading was investigated both by simulation and direct observation of the microstructural response. This was achieved by carrying out stepwise uniaxial micro-tensile tests along the transverse direction (TD) of a rolled steel sheet combined with EBSD measurements on a pre-selected region.

V.3.3. Experimental Procedure

The studied material contained 0.25 wt.% C, 1.5 wt.% Si and 3 wt.% Mn and it was Q&P heat treated. The Q&P (from Quenching and Partitioning) process is a two-step heat treatment. The first step (Quenching) consists of a full or partial austenitisation followed by quenching to a pre-determined temperature between the martensite start (M_s) and finish (M_f) temperatures. Immediately after quenching the microstructure consists of controlled fractions of martensite and austenite. The second step, referred to as the partitioning stage, consists either of isothermal holding at the quench temperature or at an increased temperature to promote carbon diffusion. This step induces carbon depletion of the martensite and diffusion into the untransformed austenite, resulting in its stabilization [3]. After final quenching to room temperature, the microstructure contains ferrite, in the case where the austenitisation occurred in the intercritical temperature interval, retained austenite and martensite. In the case where the austenitisation was complete, the microstructure contains only martensite and retained austenite.

After quenching and partitioning there are two different types of martensite - tempered martensite, obtained in the first quenching stage, which is tempered during the subsequent partitioning, and fresh martensite, which is formed during final quenching in the case of incomplete stabilization of the untransformed austenite. In this work, full austenitisation at 850°C for 1min, quenching to 224°C and partitioning at 400 °C for 500s, was applied in order to stabilize all the available austenite. This annealing treatment produced a microstructure consisting only of tempered martensite and 13.6% of retained austenite.

Controlled uniaxial deformation was applied on a Deben Microtest® 5000N tensile stage device at a constant crosshead speed of 0.5 mm/s, controlled with the Microtest™ software. The uniaxial extension was evaluated by measuring the distance between two micro-Vickers indents after each loading step using optical microscopy. Sample preparation consisted of mechanical grinding and polishing following the standard procedure for EBSD sample preparation [26]. The sample was analysed on an FEI Quanta™ 450-FEG-SEM equipped with a Hikari EBSD detector operated with the TSL-OIM® software. The data were acquired with an accelerating voltage of 20 kV, a working distance of 16 mm, a tilt angle of 70° and a step size of 60 nm on a hexagonal scan grid. The orientation data were post-processed with the TSL-OIM Analysis® version 6.2 software. The post processing of the raw orientation data can be followed step-by-step in the combined grey scale confidence index (CI) maps and colour coded phase maps (Figure V.3-1 (a-d)). In these maps, the martensite

appears in blue, retained austenite in yellow and all pixels are grey shaded with respect to their CI -in black if the CI is 0 and in white if the CI is 1.

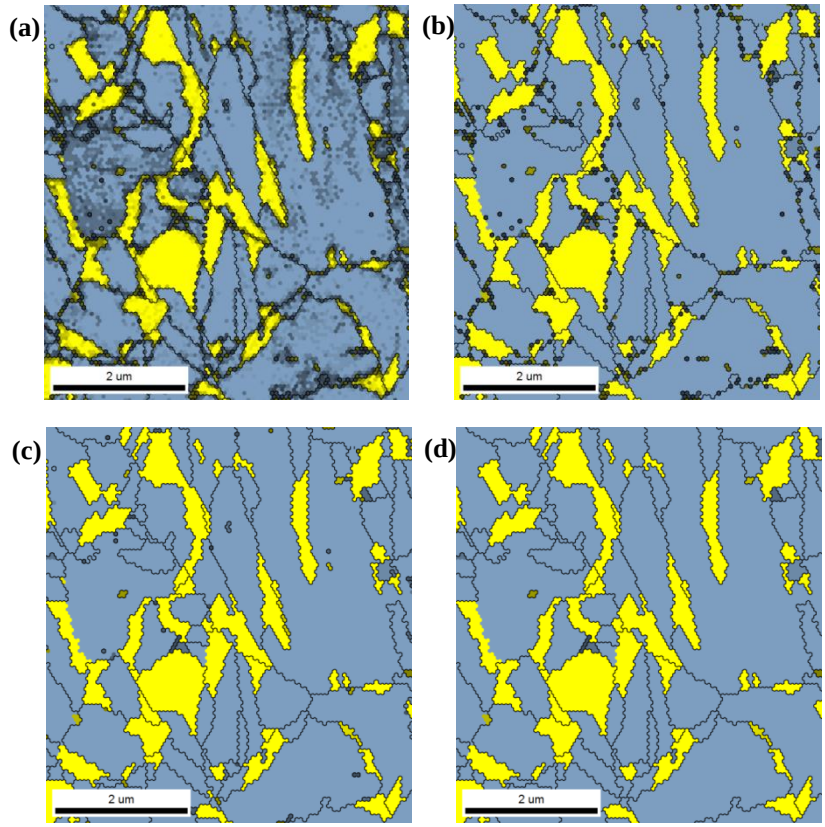

Figure V.3-1: Clean-up procedure illustrated with the phase map (austenite in yellow, martensite in blue) superimposed on the confidence index whereby the highest confidence index is transparent and the lowest confidence index is black. (a) Raw data, (b) after CI standardization with a grain tolerance angle of 5° and a minimum grain size of 4 pixels, (c) after neighbour CI correlation with a limitation of 0.1 and (d) after grain dilation with a grain tolerance angle of 5° and a minimum grain size of 4 pixels.

The raw orientation data are shown in Figure V.3-1 (a) whereas the changes in the orientation maps after each cleaning step are illustrated in Figure V.3-1 (b-d). First, a *CI standardization* with a minimum grain size of 4 pixels or 1.44 µm² was applied. This clean up algorithm changes the CI of all points in a grain to the maximum CI found among all points belonging to that grain, as illustrated in Figure V.3-1 (b). Afterwards, the *neighbour CI correlation* algorithm was employed, which implies that if a particular point has a CI below 0.1 then the CI of the nearest neighbours are checked to find the neighbour with the highest CI. The orientation and CI of the particular point are reassigned to match the orientation and

CI of the neighbour with the maximum CI, cfr. Figure V.3-1 (c). Finally, if the majority of neighbours of a particular grain smaller than 4 pixels with a grain tolerance angle of 5° belong to the same grain, then the orientation of the particular grain is changed to match that of the majority grain, i.e. a *grain dilation* algorithm was applied, cfr. Figure V.3-1 (d).

After applying these post processing steps, inverse pole figure maps of the retained austenite were plotted using a colour code that represents the crystallographic orientation of the sample transverse direction (TD). The inverse pole figures are derived from calculated ODFs, which were obtained by superimposing Gaussian peaks with half-widths of 5° on the orientation of each pixel in the scan. The series expansion method (with Lmax = 16) was employed for representing each ODF. The inverse pole figures indicate the crystal direction that is aligned with the TD of the sample reference direction, corresponding to the tensile axis.

V.3.4. Simulation Results

To simulate the transformation potential for different austenite orientations, the phenomenological theory of martensite crystallography (PTMC) [50-52] was employed to calculate the shape deformation associated with martensitic formation. According to this theory, the volume and shape changes are accomplished by a combination of three displacements: a lattice invariant shear, a Bain strain and a rigid body rotation. The model fully determines the crystallographic orientation relation between the parent austenite and the product martensite phase by the lattice invariant shear and the Bain strain. This implies that the orientation relationship is of an irrational nature and cannot be readily expressed as an ideal crystallographic relationship of the Kurdjumov-Sachs, Nishiyama-Wassermann, or Greninger-Troiano types.

The Bain strain results from the correspondence between the initial and final lattices and their lattice parameters. In this study, the Bain correspondence (i.e. $[100]_\gamma//[110]_\alpha$, $[010]_\gamma//[-110]_\alpha$ and $[001]_\gamma//[001]_\alpha$) was chosen, although a different correspondence relation [53] can be used as well. The lattice parameters of austenite (a_γ = 0.3591 nm) and martensite ($a_\alpha = c_\alpha$ = 0.2875 nm) were taken from experimentally measured data [54], which were used to simulate the formation of lath martensite [53, 55, 56].

The lattice invariant shear can take place by single or double shear [55, 57]. In the single shear mode, the (112)[11-1] shear system in the martensite lattice is considered. In the double shear mode, a pair of consecutive shears is allowed. Although the double shear mode

is more flexible and able to predict a wider range of transformations, only the single shear mode was employed in this study.

For any austenite orientation, because of cubic crystal symmetry, there are 24 variants of the product orientation. They are related to each other by symmetry operations [58]. Each of them has a habit plane (the invariant plane) with a normal unit vector ($\mathbf{p}^i$) and a displacement direction with a unit vector ($\mathbf{d}^i$) and magnitude (m). The shape deformation, therefore, can be expressed by a tensor:

$$F_i = I + m(d^i \otimes p^i) \tag{1}$$

The projection of the deformation vector ($m\mathbf{d}^i$) on the normal direction ($\mathbf{p}^i$) results in the dilatation part (ε_0 = 0.02636 in this work) whereas its projection onto the habit plane gives the shear part (γ_0 = 0.22421 in this work) of the shape deformation. In general, the shape strain of each transformation variant is calculated using the symmetric part of the displacement tensor:

$$\varepsilon_i = \frac{m}{2}(d^i \otimes p^i + p^i \otimes d^i) \tag{2}$$

The mechanical work of the transformation, which is dependent on the austenite orientation and the stress state, can be derived from the scalar product of the applied stress and shape strain tensors [45, 47-49]:

$$U_i = \sigma : \varepsilon_i \tag{3}$$

where σ and ε_i are the applied stress and the shape strain of each transformation variant.

In the present model, the material was assumed to behave as a polycrystalline Sachs aggregate, which implies that the local stress state on the crystal scale is identical to the macroscopically applied tensile stress. For simplicity, the macroscopic and isotropic yield stress of the material was applied to all austenite orientations. The magnitude of this applied stress was normalized to one, since the main focus of this study is on the *anisotropy* of the mechanical work with the purpose of differentiating between the behaviours of different crystal orientations. Among the 24 possible variants, the one with the highest value of the mechanical work was chosen as the one selected for transformation. Because of the normalization of the stress, the transformation potential P can be expressed as a dimensionless value:

$$P = max\{U_i | i = 1..24\} \tag{4}$$

To obtain the distribution of the mechanical driving force, the calculation procedure described above was applied to all possible crystallographic orientations of the austenite, ignoring the size and shape of the grains. The distribution of the mechanical driving force can then be represented by contour plots in orientation space. This distribution is illustrated in Figure V.3-2 for the case of uniaxial tension along the TD of a rolled sample by three sections $\varphi_2 = 0°$, $\varphi_2 = 45°$ and $\varphi_2 = 65°$ of Euler space. All the important orientations in rolled and annealed FCC materials can be found in these sections. Orientations with low potentials are less likely to undergo the transformation to martensite than those with high potentials. Orientations with the highest potentials are located in the vicinity of the Cube (0^o, 0^o, 0^o) and rotated Goss (0^o, 90^o, 45^o) components. Here, the driving forces are 0.121 and 0.134, respectively. The Cube orientation is frequently present in textures of FCC materials after conventional rolling and recrystallization annealing. By contrast, low potential orientations can be found near the Brass (35^o, 45^o, 0^o) and Copper (90^o, 35^o, 45^o) orientations, which are typical FCC rolling components. These exhibit the lowest driving forces (0.034 and 0.059 respectively). Thus, the rolling texture components are less likely to undergo martensitic transformation than the recrystallization texture components.

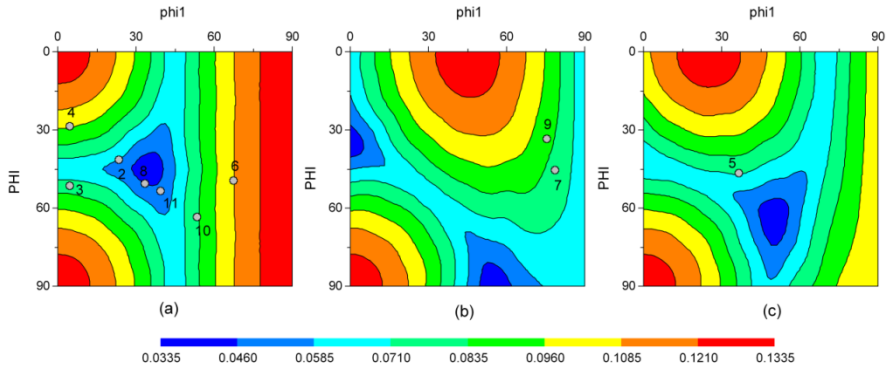

Figure V.3-2: Distribution of the mechanical driving force for martensitic transformation in orientation space (a) $\varphi_2 = 0^o$, (b) $\varphi_2 = 45^o$ and (c) $\varphi_2 = 65^o$ with 10 out of the 11 selected orientations projected on the transformation potential maps (orientation 1 is located in another cross-section). Low values of the modelled mechanical driving force correspond to low transformation potentials.

The high potential orientations all have in common that the <010> crystallographic direction is nearly parallel to TD, which was the loading axis of the present experiment (Figure V.3-2 (a)). Since the dilatation part only contributes 11.7% to the shape deformation, most of the work done by the transformation is carried out by the shear part on the habit plane. For the current martensitic transformation, the habit plane in the austenite reference system predicted by the model is (0.59424, -0.78271, 0.18507). This deviates less than 1°

from the (3 -4 1) austenite plane. The smallest angle between this habit plane and the [010] direction is 38.5°, whereas the maximum shear stress direction in tension is inclined at 45° to the loading axis. Therefore, austenite grains that have a <010> direction misaligned by 6.5° with respect to the tensile axis, have the greatest potential for transformation.

The calculation result for distribution of the transformation potential is similar to the ones obtained in previous studies [47, 48]. However, there is an essential difference between the present analysis and the ones reported earlier. In the previous investigations, the transformation potentials pertaining to austenitic stainless steels and TRIP steels were the main focus. They both assumed that twinned martensite was being formed and included a calculation of the volume fraction of each variant in the twinned structure during simulations. This assumption and its implementation are appropriate for twinned and lenticular martensite, but this mechanism is unlikely to operate in low carbon steels, where dislocated lath martensite is generally observed. Therefore, in the current study, the lattice invariant shear is assumed to take place entirely by dislocation glide. In this way, the volume fractions of the individual martensite variants were not evaluated as no spatial coordinates, morphologies or other local factors influencing the stability were taken into account. The model is essentially restricted to predicting the transformation stability of particular orientations.

V.3.5. Experimental Observations

The mechanical driving force for transformation during tensile testing associated with any austenite orientation can be readily derived from the model described above. The predictions of the model were evaluated by means of direct observations of transforming austenite orientations during interrupted tensile loading parallel to TD. By progressively increasing the strain at which the orientation measurements were made, the orientation dependent transformation rate was determined. As described above, the orientations with the highest mechanical driving forces were expected to transform first and the orientations with lower transformation potentials to transform later or not at all. Due to the nature of the model, the influence of local factors on the stability of the grains (which varies from grain to grain) was eliminated by studying all the grains of a given orientation and averaging the local effects in this way.

Inverse pole figure maps of the austenite grains in the starting material and of the same area after 4.7%, 8.6% and 12% tensile elongation are displayed in Figure V.3-3 (a-d),

respectively. The decrease in the total austenite area fraction from 13.6% to 2.1% after 12% plastic elongation is evident.

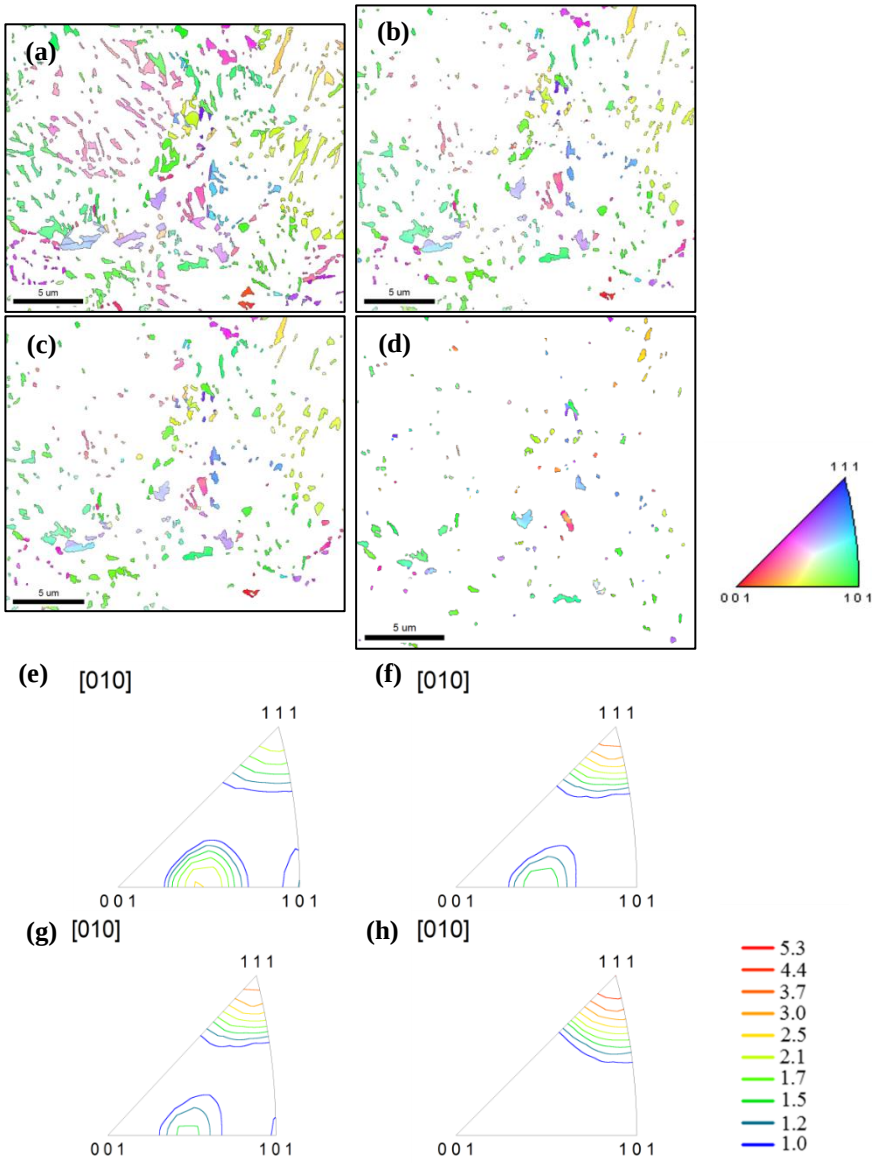

Figure V.3-3: ND- inverse pole figure maps (martensite in white) of (a) the starting material and the same site after plastic deformation to (b) 4.7% (c) 8.6% and (d) 12% with the corresponding TD-inverse pole figures (e)-(h). The scale of the inverse pole figure is the relative intensity compared to random texture.

The TD inverse pole figures of the austenite phase, corresponding to the maps of Figure V.3-3 (a–d), are illustrated in Figure V.3-3 (e-h).These reveal that the austenite orientations are plastically stable during tensile straining as they do not rotate drastically. This indicates that grain rotation only makes a minor contribution to the ductility of austenite compared to the martensitic transformation. Therefore, the original orientations of the austenite grains, as observed in the OIM scan prior to plastic deformation, can be employed for evaluation of the mechanical stability, i.e. for applied strains up to 12%.

To determine the transformation rate applicable to the various orientations, eleven representative austenite orientations (with a tolerance of 10°) were selected for monitoring the area fraction evolution as a function of increasing strain. According to this procedure, all austenite grains of a given orientation contribute to the determination of the stability of this orientation, without the need to take the precise space coordinates of each grain into account. This is, each specific crystal orientation is taken to represent the behaviour of all the grains of that orientation in the microstructure. The transformation rates were defined as the transformed volume fraction per unit of applied strain (dimensionless), which corresponds to the average slope of the volume fraction curves. The negative sign of the transformation rate originates from the *decrease* in austenite fraction inherent to the TRIP phenomenon

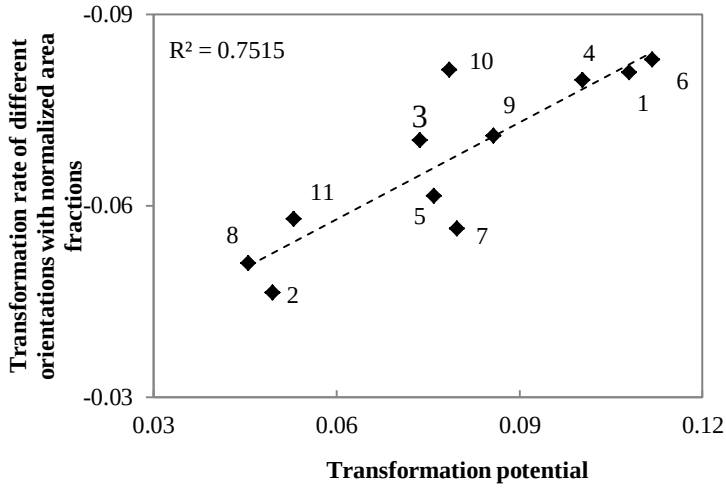

Figure V.3-4: Transformation potential versus experimental transformation rate of 11 randomly chosen orientations; the numbers identify the orientations which are projected onto the transformation potential map of Figure V.3-2.

The experimentally measured transformation rates are plotted vs. the calculated transformation potential in Figure V.3-4. The 11 orientations are numbered in the chart; these

were also identified on the transformation potential maps of Figure V.3-2. For example, orientation 6 is associated with the highest driving force (as can be seen by its projection in the orange area of Figure V.3-2) and the highest transformation rate. The actual average austenite orientations defined by their Euler angles, the calculated transformation potential values and the experimental transformation rates for the studied orientations numbered as displayed in Figure V.3-2, Figure V.3-3 and Figure V.3-4 are given in Table V.3-1.

Table V.3-1: The orientation number displayed in Figure V.3-2, the average orientation defined by its Euler angles, the calculated transformation potential value, and the experimental transformation rate.

Number of orientation	Orientation (Euler angles, °)			Transformation potential (model)	Transformation rate (experimental)
	$\phi 1$	Θ	$\phi 2$		
1	100.0	26.1	239.0	0.1080	-0.0809
2	21.5	40.1	8.8	0.0496	-0.0464
3	185.7	40.3	177.5	0.0737	-0.0702
4	356.8	26.7	358.5	0.1003	-0.0796
5	215.3	45.0	153.6	0.0760	-0.0615
6	256.8	43.2	81.8	0.1118	-0.0829
7	282.9	44.1	44.3	0.0798	-0.0564
8	328.4	39.9	359.0	0.0456	-0.0510
9	106.2	31.6	222.6	0.0857	-0.0709
10	128.2	27.6	269.9	0.0786	-0.0812
11	47.3	38.6	352.3	0.0530	-0.0578

It is apparent that a linear relationship with a correlation coefficient of approximately 0.75 is obeyed. For this experiment, the grains were selected solely on the basis of their orientations without considering other parameters that can affect local stability, such as local carbon content, grain size and morphology. The chosen orientations, however, include a range of austenite grain sizes and morphologies. Hence many of these *other* effects are expected to have been levelled out, although they may explain the remaining scatter. In spite of the observed scatter, the data demonstrate the significant effect of crystal orientation on the transformation behaviour of residual austenite during tensile loading. The role of other local parameters remains to be verified quantitatively along the lines of that of crystallographic orientation.

V.3.6. Acknowledgements

This research was partly funded by the governmental institute for the Promotion of Innovation by Science and Technology in Flanders (IWT) and was supported by European project "RFCS-CT-2011-00017 "New advanced high strength steels by quenching and partitioning process (NewQ&P)". We also would like to thank the Belgian Federal Science Policy Office for financial support via the Inter-University Attraction Poles (IAP) project P7/21. We are grateful to TUDelft and F. Hajy Akbary for assistance and use of the micro-tensile test device.

SECTION 4

MODELLING THE TEXTURAL EVOLUTION OF AUSTENITE DURING UNIAXIAL TENSION

with special thanks to Jurij Sidor for assistance with the model

V.4. MODELLING THE TEXTURAL EVOLUTION OF AUSTENITE DURING UNIAXIAL TENSION

V.4.1. Abstract

The evolution of deformation textures of austenite in Q&P steel is analysed via experimental measurements and numerical simulations. Specifically, the textural evolution of austenite during tensile testing is modelled with the visco-plasticity self-consistent model [59]. The modelled textural evolution was compared with that of the experimentally measured texture after 18.5% plastic deformation, in order to understand the textural response of austenite, i.e. the textural components that rotated or transformed to martensite under uniaxial tension were identified.

V.4.2. Introduction

Understanding the evolution of microstructural features, in this case the response of retained austenite to uniaxial tension is essential to controlling particular microstructure-related properties.

Most of the models, which describe the plastic deformation of polycrystalline materials and predict the deformation textures, consist primarily of two elements, namely: the microscopic model and a transition model, which as the name suggests, transitions from the microscopic to the macroscopic length scales.

The crystal plasticity theory (CP) can microscopically model the textural changes. This theory describes the relationship between the active slip processes and the microscopic velocity gradient. In austenite, the close-packed {111} planes and ⟨110⟩ directions constitute the 12 possible active slip systems.

In addition, several grain-interaction schemes can be used for the micro-macro transition. These schemes assume that each grain is a single crystal. The classical Taylor-Bishop-Hill [60-62] assumption of equal strain in every grain fulfils the compatibility condition but amounts to an extremely rigid interaction. A more realistic approach must account for the fact that the grain-matrix interaction is neither completely rigid nor fully compliant. In the Relaxed Constraints approach [63-65], one or two of the components of the local velocity

gradient tensor are 'relaxed' and may differ from the macroscopic velocity gradient tensor. The choice of the components to be relaxed remained, however, arbitrary depending on the interpretation of the microscopic stress/strain distribution. The visco-plastic self-consistent model proposed by Molinari *et al.* [59, 66] made this choice by considering an interacting cluster of grains, which are represented by anisotropic ellipsoidal inclusions and surrounded by a visco-plastic anisotropic Homogeneous Effective Medium (HEM).

V.4.3. Model

The VPSC model incorporates, explicitly, the interaction of a grain with its surroundings (i.e. grain interaction) and the plastic anisotropy of the grain and the matrix. The approach assumes that the HEM is characterized by an average constitutive behaviour of the entire polycrystalline aggregate. The stress applied to the outer boundary of the HEM induces local deviations of the strain rates in the vicinity of the grains. These deviations with respect to the macroscopic average are characterized by an interaction parameter in the constitutive law. Hence, the grain response is coupled to the overall response of the polycrystal and the grain deformation may differ from that of the polycrystal. Moreover, the stress equilibrium equation is solved for inclusions in the homogeneous medium; i.e. the stress tensor in each grain is defined via the Taylor approach, and then the visco-plastic compliance tensor is calculated and solved iteratively for the plastic compliance of the aggregate. This solution is then inserted into the interaction equation and the stress in each grain is determined. If the recalculated stress deviates from the guessed stress, then the calculation is repeated.

The applied strain tensor was defined as:

$$\sigma = \begin{bmatrix} -q & 0 & 0 \\ 0 & 1 & 0 \\ 0 & 0 & -(1-q) \end{bmatrix}$$ with q = 0.5 for uniaxial tension along TD

Deformation is accommodated by slip in the ⟨110⟩ directions and on the {111} crystallographic planes. Furthermore, the deformation of the austenite grains is not influenced by the local matrix, which is assumed to be a visco-plastic homogeneous medium.

V.4.4. Results, discussion and conclusions

The texture of austenite after Q&P processing consisted of rotated Cube {001}⟨110⟩, Copper {112}⟨11-1⟩, Brass {110}⟨-112⟩, S {123}⟨63-4⟩, Goss {110}⟨001⟩, and rotated Goss {110}⟨110⟩ components, cfr. Figure V.4-1 (a).

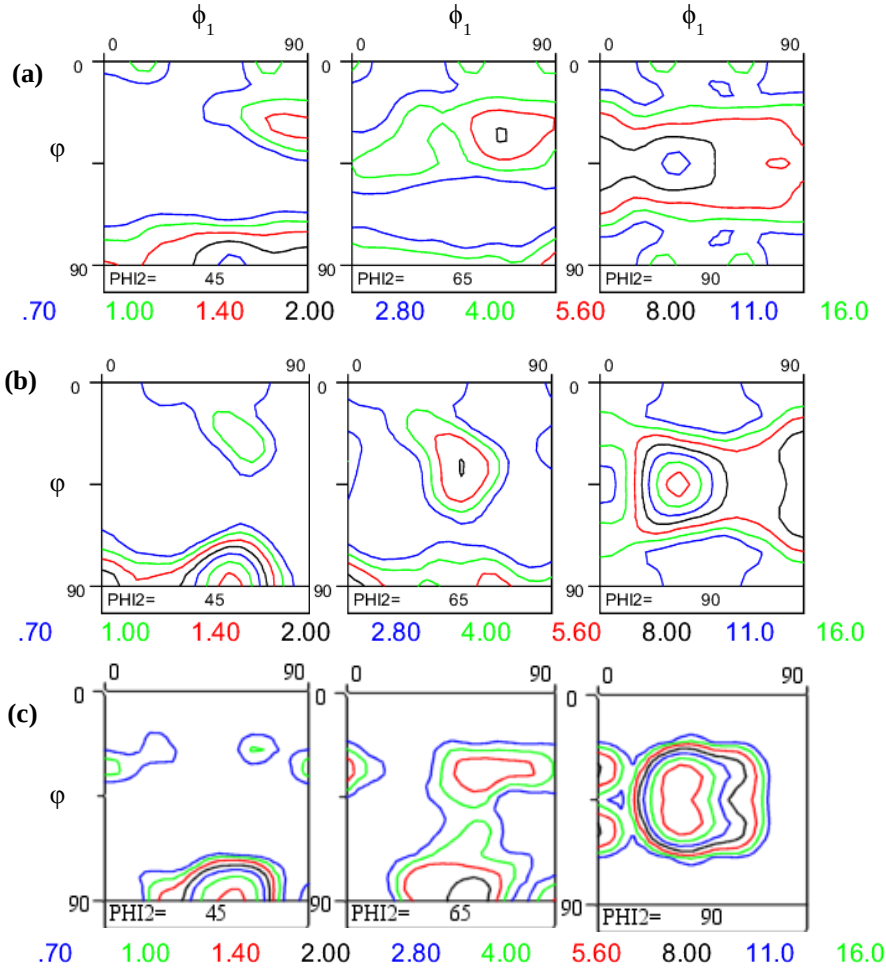

Figure V.4-1: φ_2 = 45°, 65°, and 90° sections showing the (a) starting (b) modelled, and (c) experimentally measured textures after a total elongation of 18.5%

The VPSC model predicted a rotation of the components towards rotated Goss, Brass, and S after a total imposed elongation of 18.5%, cfr. Figure V.4-1 (b). The Copper and rotated Cube components disappeared completely from the modelled ODF. In addition, the

experimentally measured texture after 18.5% elongation, Figure V.4-1 (c), consists primarily of the Brass and S components; the rotated Goss is absent from this texture.

Deformation-induced texture changes result from the *(i)* grain rotation and *(ii)* austenite-to-martensite transformation. The visco-plastic self-consistent model only predicts rotation of the austenite grains during deformation. Therefore, we can conclude that rotated Goss transformed to martensite. This is supported by the crystallographic transformation potential map for tensile testing along TD, as shown in Figure V.4-2. This potential is based on an orientation-dependent mechanical driving force [45, 48, 49] combined with a work criterion whereby the shape changes are based on the crystallographic theory of martensite [50-52]. As the figure shows, Brass has the lowest transformation potential of all the texture components, and hence requires the largest stress in order to transform to martensite.

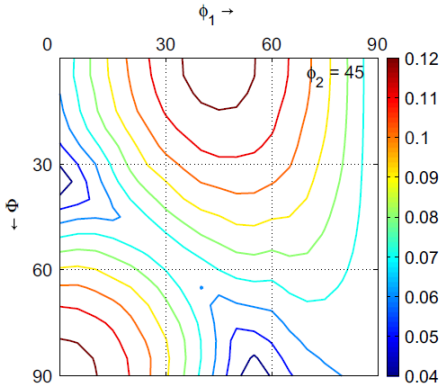

Figure V.4-2: Transformation potential of austenite grains for tensile testing along TD

Furthermore, the increase of its intensity from 2.8 mrd (multiples of a random distribution) to 5.6 mrd after 18.5% straining, and having the lowest transformation potential, renders Brass a stable orientation against martensitic transformation.

Rotated Cube, Copper, and Goss have a modelled average transformation potential of approximately 0.06-0.07 and, according to the VPSC model, their rotation towards Brass and rotated Goss resulted in their absence from the ODF. Therefore, their absence from the experimental texture after 18.5% elongation is attributed to partial transformation and partial rotation.

The model predicted an increase in the intensity of the rotated Goss; however this component had the highest transformation potential. Therefore, other orientations which rotated towards rotated Goss, transformed to martensite owing to its low transformation

stability; the low transformation stability results in the absence of this component from the experimentally measured texture.

In addition, the intensity of the S component decreased in the experimentally measured texture, although the model predicted that its intensity should remain the same. This indicates that this component transforms partially to martensite during straining.

V.4.5. Conclusion

The experimentally obtained texture was explained by combining a model that predicts the textural evolution of austenite during plastic deformation with its transformation potential. Rotation of other orientations towards the Brass component, which had the highest transformation stability, resulted in this component being the most stable. The evolution of the texture during tensile testing was resolved, as shown schematically in Figure V.4-3.

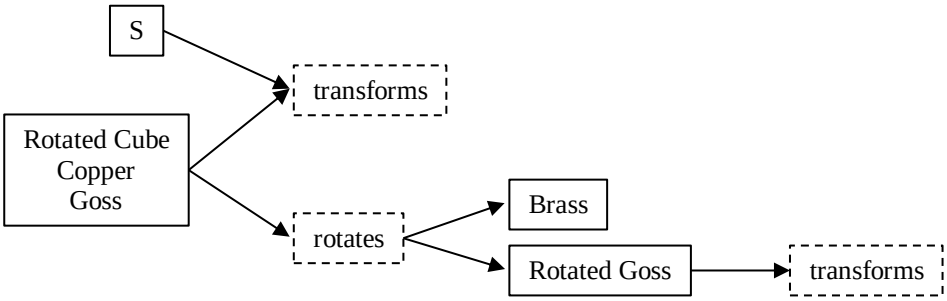

Figure V.4-3: Schematic overview of the evolution of texture components during tensile testing

SECTION 5

FACTORS INFLUENCING THE AUSTENITE STABILITY DURING TENSILE TESTING OF Q&P STEEL DETERMINED VIA IN-SITU EBSD

Submitted: D. De Knijf, R. Petrov, C. Föjer, and L. A. I. Kestens: 'Factors influencing the austenite stability during tensile testing of Quenching and Partitioning steel determined via in-situ EBSD', Materials Science and Engineering A, 2015, 219

V.5. FACTORS INFLUENCING THE AUSTENITE STABILITY DURING TENSILE TESTING OF Q&P STEEL DETERMINED VIA IN-SITU EBSD

V.5.1. Abstract

The effect of the microstructural characteristics of retained austenite on its transformation stability in steel after *Quenching and Partitioning* (Q&P) was studied via interrupted tensile tests and Electron Backscatter Diffraction measurements on a pre-determined zone of a micro-tensile test sample. The evolution of the retained austenite fraction was obtained as a function of the plastic strain. The dependence of the austenite transformation stability on the corresponding grain size, morphology, and local crystallographic orientation was discussed. Furthermore, the importance of the parameters on the austenite stability was analysed and it was shown that the austenite grains rotated, in addition to being transformed, constituting therefore an additional contribution to the ductility of Q&P steel.

V.5.2. Introduction

Attaining an optimum balance of hard and ductile phases, e.g. martensite and austenite, is one of the most promising approaches being explored for the production of new advanced high strength steels (AHSS). This type of microstructure can be achieved via a *Quenching and Partitioning (Q&P)* heat treatment, which was introduced by Speer *et al.* [1-3, 67, 68].

This heat treatment consists of austenitisation, followed by quenching to a temperature below the martensite start temperature (M_s), but above the martensite finish temperature (M_f), in order to partially transform the austenite to a controlled fraction of martensite. In the subsequent *partitioning* step, the steel is held isothermally between M_s and M_f or above M_s in order to promote carbon diffusion from the supersaturated martensite to the untransformed austenite. The austenite grains, which are sufficiently enriched in carbon, are retained at room temperature after final quenching; the other austenite grains transform to high-C martensite, often referred to as *fresh or untempered* martensite.

Various microstructures, and hence mechanical properties, can be obtained by varying the processing parameters. However, understanding the microstructure-mechanical

property relationship is crucial to designing appropriate heat treatments. Knowledge of the microstructural features that influence the transformation behaviour of retained austenite during deformation is also essential. A number of experimental studies performed on TRIP steels revealed that the transformation stability of austenite is affected by *(i)* the local carbon content in the austenite [7-9, 69]; *(ii)* the grain volume of the retained austenite [9, 10, 70, 71]; *(iii)* morphology [10, 72, 73], *(iv)* the constraining effect of the phases surrounding the austenite [11, 73-75] and *(v)* the crystallographic orientation [8, 12, 45] of the austenite with respect to the loading direction. In addition to transforming to martensite, austenite grains also rotate to accommodate plastic deformation [8, 30]. During straining of Q&P steel, the overall C-content of the remaining austenite is observed to increase due to transformation of austenite grains with low C-concentrations [76]. Intrinsic to the slow C-diffusion in austenite [35, 77], larger grains are generally linked with lower C-contents compared to the smaller counterparts with higher C-contents. This can be observed as well from their (partial) transformation to fresh martensite due to incomplete stabilisation during partitioning [78]. Recent investigations revealed however that stabilized blocky austenite grains were enriched more in C than their thin film-like counterparts [44, 79], which combined with the fact that larger, blocky austenite grains transform at lower strains [80, 81] suggests that size and morphology are strong determining factors in controlling the austenite stability.

The present work is aimed at understanding the transformation behaviour of retained austenite with uniaxial deformation using qualitative and quantitative information acquired by combining *in-situ* electron backscatter diffraction (EBSD) measurements with micro-tensile testing. The microstructural response was monitored via evolution of the austenite grain size, morphology, crystallographic orientation, and local strain; all these parameters were described as a function of the applied tensile strain. The matrix was aimed for tempered martensite to omit the effect of fresh martensite blocks on the deformation and the austenite stability. The local C content also influences the austenite stability [7-9, 69]. However, the local C content cannot be measured by the characterisation techniques used in this work and its effect was hence not included in the discussion.

V.5.3. Experimental

Steel with a nominal composition of 0.25C-1.5Si-3Mn (wt. %) was produced in a laboratory vacuum induction furnace. The steel slabs were hot rolled, coiled, and cold rolled to a final thickness of 1 mm. Strips of these sheets were cut perpendicular to the rolling direction and then subjected to a Q&P heat treatment cycle in the thermo-mechanical

simulator Gleeble™ 3500. The samples were fully austenitized at 850 °C for 60 s, quenched to 224 °C for 5 s , partitioned at 400 °C for 500 s was and subsequently quenched to room temperature.

Dog-bone-shaped micro-tensile samples were prepared by water jet cutting from the central area of the Gleeble™ specimens keeping the tensile axis perpendicular to the rolling direction, cfr. Figure V.1-2(a). The tests were conducted on a Deben Microtest™ 5000N Tensile Stage device at a constant cross head speed of 0.5 mm/s. Owing to the small sample size, the results from the micro-tensile tests are not considered representative of the mechanical properties of the samples [25]. Two Vickers indents were made at the end of the parallel section in order to accurately monitor the changes in the plastic strain. The distance between, and change in shape of, the indents were measured via optical microscopy after each loading step, cfr. Figure V.1-2 (b). In the EBSD images, the vertical direction corresponds to the tensile axis, which is parallel to TD, cfr. Figure V.1-2 (a).

Orientation imaging microscopy (OIM) was performed on mechanically ground and polished samples following the classical preparation route. The samples were analysed by using a FEI Quanta™ 450-FEG-SEM equipped with a Hikari EBSD detector controlled by the EDAX-TSL OIM-Data Collection version 6.2® software. The EBSD data were acquired on a hexagonal scan grid using an accelerating voltage of 20 kV, a working distance of 16 mm, tilt angle of 70°, and a step size of 60 nm. The raw orientation data, obtained at each loading step, were post-processed with TSL OIM Analysis 6.2© software and only the points with a confidence index (CI) higher than 0.1 and grains larger than 4 pixels, were considered in the scan.

V.5.4. Results and discussion

V.5.4.1 Evolution of the global retained austenite fraction with strain

The microstructure before deformation consisted of tempered martensite and 13.6% retained austenite, which are shaded in green in Figure V.5-1 (a). A small fraction of low image quality grains corresponding to 3% fresh martensite [33] were observed in the studied area of the undeformed material.This fraction is very low and no large, fresh martensite blocks were observed in the near surroundings of the austenite grains and therefore, it was assumed that they did not interfere with the deformation behavior and hence with the transformation stability of the retained austenite. Fresh martensite was reported [75] to play a

significant role in: *(i)* the strain distribution in the microstructure by inhibiting the amount of deformation that could be accommodated in the tempered martensite, and *(ii)* the fracture mechanism by triggering void formation. Hence, fresh martensite has a constraining effect on the strain accommodation that decreases the austenite transformation stability. In this work, the parameters that are inherently attributed to austenite and determine its stability were studied. Therefore, the fresh martensite fraction which alters the mechanisms triggering martensitic transformation, needed to be absent or very low in the matrix of the undeformed material.

The evolution of the retained austenite fraction with increasing strain was determined via EBSD measurements on the same area after consecutive straining of the micro-tensile sample, cfr. Figure V.5-1 (b). The decay can be fitted by an exponential function where the pre-exponential factor of 13.6 is associated with the starting austenite fraction and the exponential factor of 0.178 is related to features influencing the austenite transformation stability, i.e. grain size, morphology, crystallographic orientation and surrounding phases.

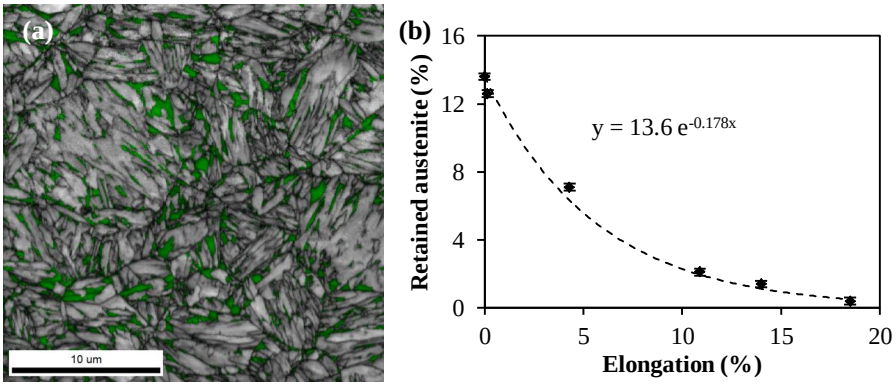

Figure V.5-1: (a) Image quality map of the starting (undeformed) microstructure, which consists mainly of tempered martensite and retained austenite (in green), (b) evolution of the retained austenite fraction with total elongation

V.5.4.2 Micromechanical behaviour of austenite grains during deformation

In this section, the individual effects of grain size, morphology (i.e. morphological orientation with respect to the tensile direction and grain shape), and crystallographic orientation on the micromechanical behaviour of the studied austenite grains are evaluated. The mechanical behaviour and transformation stability of the individual grains in the uniformly deformed area was investigated by analysing the following data acquired with

EBSD at consecutive strain levels: *(i)* grain diameter, *(ii)* major axis orientation (MAO) defined as the angle between the horizontal axis of the scan and the major axis of the ellipse surrounding the austenite grain, in order to evaluate the effect of morphological orientation, and *(iii)* grain shape aspect ratio (GSAR) defined as the length of the minor axis divided by the length of the major axis of the ellipse approximating the grain; and morphology; *(iv)* ND-inverse pole figure maps to analyse the influence of crystallographic orientations.

V.5.4.2-1 Evolution of the austenite grain size

During straining, the average grain diameter of the retained austenite decreased from 0.6 µm to 0.13 µm after 14% total elongation, cfr. Figure V.5-2, due to strain-induced transformation and grain fragmentation.

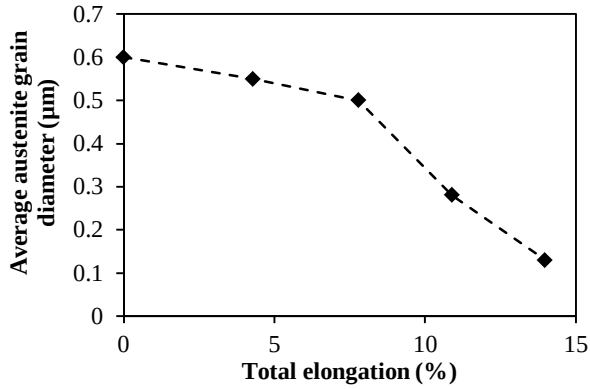

Figure V.5-2: Dependence of the average austenite grain diameter (µm) on the total elongation (%)

To study the influence of morphological orientation on the evolution of the austenite grain size, the average diameter was calculated for different major axis orientations (MAO), cfr. Figure V.5-3. The experimental data were linearly interpolated to determine the "rate" of grain size change.

The average size of the grains with their largest axis parallel to the tensile direction, and a MAO of 72°-108°, decreased at a rate of -0.0254 µm per % strain. In addition, grains oriented ± 45° with their longest axis parallel to the tensile axis have MAO of 108°-144°, whereas those, which are nearly perpendicular to the tensile axis have MAO of 144°-180°; the corresponding average austenite grain size evolves at rates of -0.0226 and -0.0283 µm per % strain, respectively. Therefore, the various morphological orientations exhibit similar rates of change in grain size indicating that the austenite stability is influenced more by the grain size

than by the morphology. The same conclusions were obtained for different ranges of grain shape aspect ratios: 0-0.3, 0.3-0.6, and 0.6-1 as can be seen in Figure V.5-4.

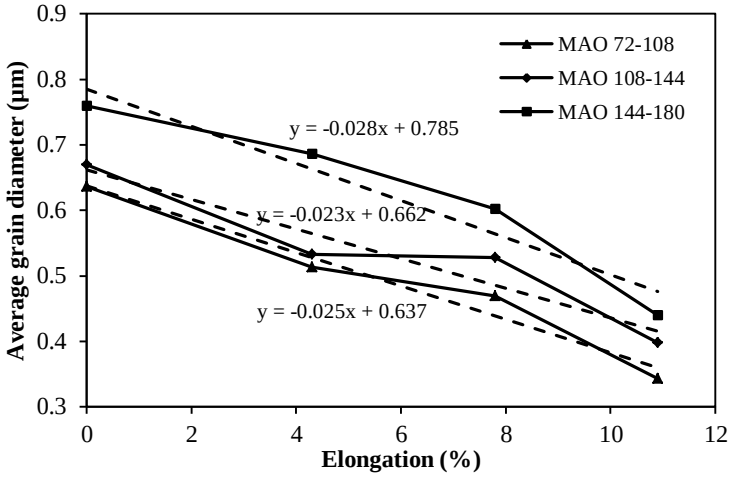

Figure V.5-3: Average grain diameter for different ranges of major axis orientations (MAO): (1) 72°-108°, (2) 108°-144°, and (3) 144°-180° correspond to austenite grains lying approximately (1) parallel, (2) < 45° with respect, and (3) perpendicular to the tensile direction

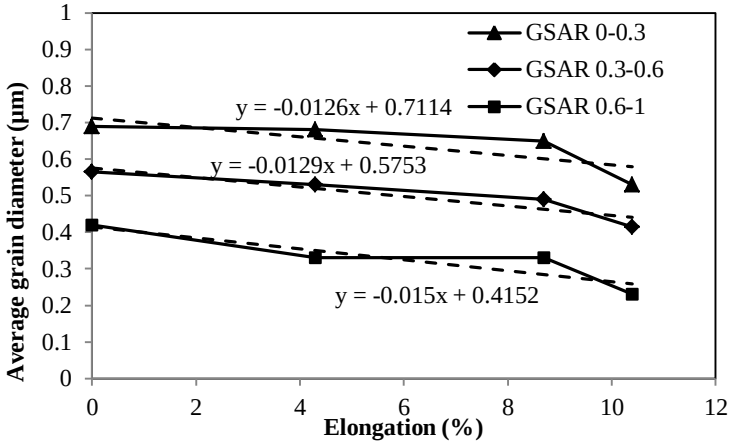

Figure V.5-4: Average grain diameter (µm) versus plastic elongation for different ranges of grain shape aspect ratio: (1) 0-0.3, (2) 0.3-0.6, (3) 0.6-1 which correspond to lamellar, elongated and globular austenite grains

Besides the overall evolution of the average grain diameter, individual transformation stabilities exist for each class of austenite grain size; these classes are obtained by dividing the entire range of sizes into intervals of 0.15 µm. The individual transformation rates were determined by evaluating seven grain size ranges (cfr. Figure V.5-6): 0.15-0.3 µm,

0.3-0.45 µm, 0.45-0.6 µm, 0.6-0.75 µm, 0.75-0.9 µm, 0.9-1.05 µm, and 1.35-1.5 µm for MAO values ranging from 72°-108° only.

Partial transformation of the austenite grains was observed during the experiment, cfr. Figure V.5-5. This effect was observed in previous TEM studies of TRIP steel [10]. Other studies reported a gradual transformation of austenite during cooling, as detected with synchrotron X-ray diffraction experiments, without direct microstructural evidence [9, 71]. However, a complete understanding of the mechanism governing this gradual transformation remains elusive. The transformation may be related to gradients in carbon, which result in local changes in the M_s and M_d temperatures inside individual austenite grains [9]. Another effect which is believed to contribute to the gradual transformation is the changed stress state due to the higher yield strength of fresh martensite (after the transformation) which can "shield" the austenite from plastic deformation [11, 82]. Large grains which are fragmented into small parts, due to partial transformation, were removed from the analysis since they would lead to an apparent increase in the fraction of austenite with a smaller grain size range, which would obscure the real influence of grain size on austenite stability. This is illustrated, for example, in Figure V.5-5 for the grain diameters of 0.6-0.75 µm. The original curve is given by the dotted line and after removing fragmented grains (1) and (2), the curve changed to those represented by the dashed and solid lines, respectively.

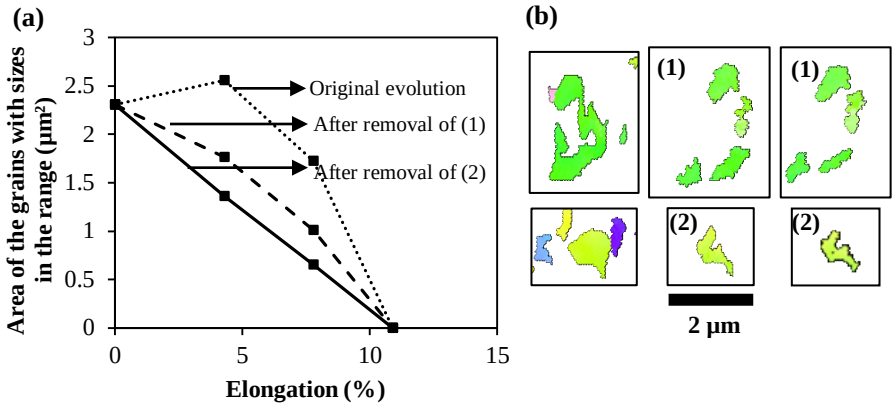

Figure V.5-5: (a) Area fraction of 0.6-0.75µm-sized austenite grains of as a function of the total elongation: the original evolution and after removal of the austenite grain parts, which persisted after partial transformation (b) the original austenite grains, with sizes greater than 0.6-0.75 µm before straining, which owing to partial transformation, were shifted to this interval. The area fractions were removed from the interval as illustrated in (a).

The corresponding transformation rates are obtained from the slopes of the linear interpolated curves (Figure V.5-6). Figure V.5-6 (a) suggests that for strains of up to 10.9%,

grains smaller than 0.15 µm did not transform to martensite, and hence did not contribute to the ductility.

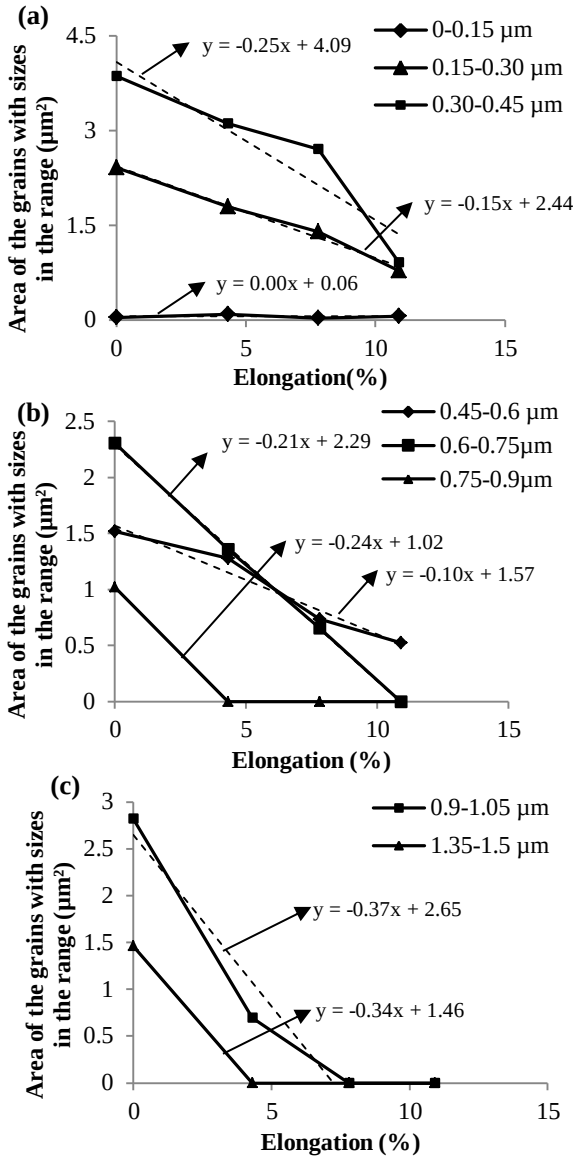

Figure V.5-6: Area of the grains in different size ranges of (a) 0-0.15 µm, 0.15-0.30 µm, 0.30-0.45 µm, (b) 0.45-0.6 µm, 0.6-0.75 µm, 0.75-0.90 µm, (c) 0.9-1.05 µm, 1.35-1.5 µm, as a function of total elongation; the original plots were linearly interpolated

This strain level lay within the uniform straining regime. However, in the later deformation stages (part of) these grains are believed to transform to martensite under

increased stresses stemming from strain localization in the necking region. Grains with diameters of 0.15 µm-0.45 µm transformed mainly after 7.8% total elongation, with an average, initial transformation rate of ± 0.15 µm² per % strain.

Austenite grains with diameters of 0.45 µm-0.75 µm transformed steadily with increasing elongation, cfr. Figure V.5-6 (b); those with sizes of 0.6 µm-0.75 µm were completely transformed after an elongation of 10.9%. Some of the grains with sizes of 0.15 µm-0.45 µm remained untransformed and were able to contribute to the ductility in the last 4% of uniform deformation and possibly to localized deformation during necking. Grains larger than 0.75 µm, cfr. Figure V.5-6 (b-c), disappeared at low strains indicating that these are least resistant against martensitic transformation and contribute only to strain hardening in the beginning of the stress-strain curve.

Summarizing the average transformation rates as a function of the grain size reveals the influence of the austenite grain diameter on the corresponding stability in Figure V.5-7.

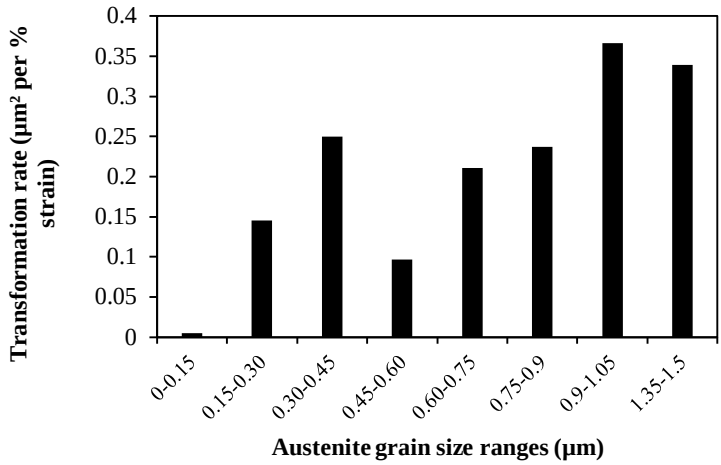

Figure V.5-7: Transformation rate as a function of the austenite grain diameter

Compared to small grains, large grains are less stable and transform to martensite in the initial stages of deformation. Grains with diameters of 0.15 µm-0.9 µm transform at a similar rate (cfr. Figure V.5-7) and, of all the grains, contribute most to sustaining plastic deformation of up to 10.9% elongation. At high strains, some of the grains which are smaller than 0.6 µm can still accommodate the final plastic strain. Compared to those required for large grains, smaller grains require pure geometrically larger macro-stresses to get the needed micro-stress for austenite to martensite transformation. In the current experiment, grains

smaller than 0.15 µm did not contribute significantly to TRIP-assisted behaviour since they are too stable to transform at the strain levels considered. However, it is believed that they play an important role at high uniform and localized strains.

If it is assumed that larger austenite grains have (locally) lower C-contents owing to its slower diffusion in austenite, then the effect of low C-content in large austenite grains re-enforces the influence of grain size on its transformation stability. In contrary, if small film-like austenite grains have lower C-contents than the larger, blocky grains [27, 28], then the (combined) effect of grain size and morphology on austenite stability exceeds that of the C-content.

V.5.4.2-2 Morphological evolutions

The morphological changes of the austenite grains during straining was evaluated via the major axis orientation (MAO) and the grains were divided into five groups, each corresponding to a MAO interval of 36°, thereby constituting a complete range of 0°-180°, cfr. Figure V.5-8 (a).

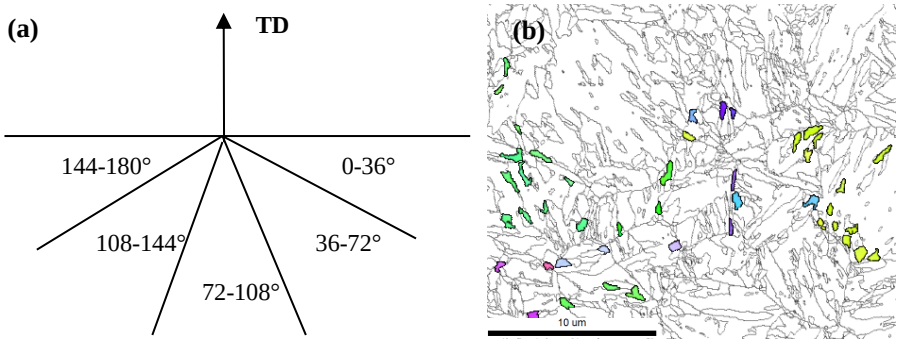

Figure V.5-8: (a) Schematic of the major axis orientations evaluated via (b) the ND-inverse pole figure of the austenite grains in the starting material which had transformation potentials lower than 0.105. The loading direction is parallel to TD, which is vertical in the image

To study the effect of morphology on the transformation stability, other factors controlling austenite stability should be kept constant. Therefore, only grains having sizes of 0.3 µm-0.75 µm and crystallographic orientations with transformation potential [48, 83] less than 0.105 were considered. The transformation potential, based on the phenomenological theory of martensite crystallography and the mechanical driving force, predicts the influence of the crystallographic orientation on the austenite transformation stability. An austenite grain with a high transformation potential should, therefore, have a low crystallographically based transformation stability. As such, in order to evaluate the effect of morphological orientation, the most *unstable* orientations (based on their transformation potential) were removed from

the data set. The grains remaining after applying these restrictions are shown in Figure V.5-8 (b).

The transformation stability of the austenite grains, originating from the same MAO range in the starting material, was tracked at consecutive strains. The transformation rate was calculated as the slope of the normalized area fractions vs. total elongation for three consecutive deformation stages, cfr. Figure V.5-9. Owing to symmetry, the ranges 0°-36° and 144°-180°; and 36°-72° and 108°-144° were considered together.

In the first deformation step, the grains with their longest axis under an angle of ± 45° were the least stable of all the orientations. Tensile deformation is accommodated by dislocation slip, which begins when the shear stress on the slip plane reaches its critical value [84]. The shear stress is maximal at an angle of 45° with respect to the loading axis. Hence, the grains with their longest axis parallel to this direction experience the highest shear component, and as a result, transform first. The austenite grains perpendicular to the tensile direction, represented by a MAO of 0°-36° and 144°-180°, also transformed at a relatively high rate of 0.075 transformed area fraction per % strain. For the grains with this morphology, the tensile stress component acts along the longest axis of the largest possible cross-section, thereby resulting in the highest total tensile force.

Due to the consumption of the 45°-oriented austenite grains, the strain in the subsequent deformation steps is accommodated mainly by transformation of the austenite grains having long axes parallel and perpendicular to the tensile axis.

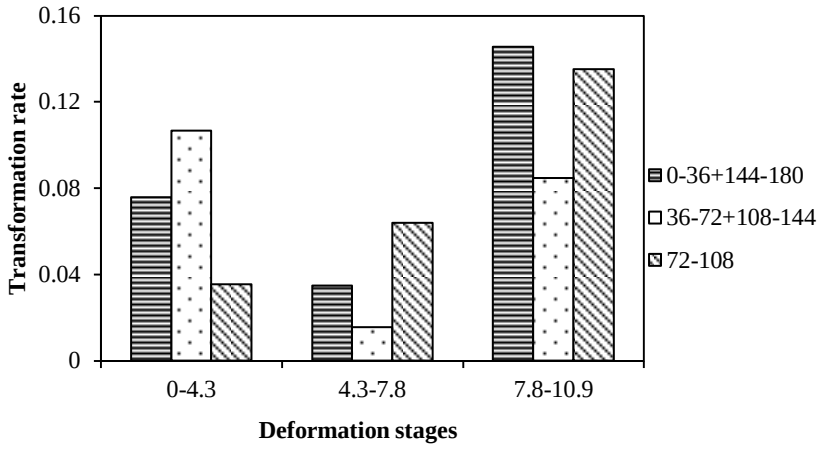

Figure V.5-9: Transformation rate of MAO ranges 0°-36°+144°-180°, 36°-72°+108°-144°, and 72°-108° at different deformation stages

The grains shape aspect ratio (GSAR) area distributions for grain sizes between 0.3 and 0.75µm and for consecutive strains of 0%, 4.3%, 7.8%, and 10.9% are given in Figure V.5-10.

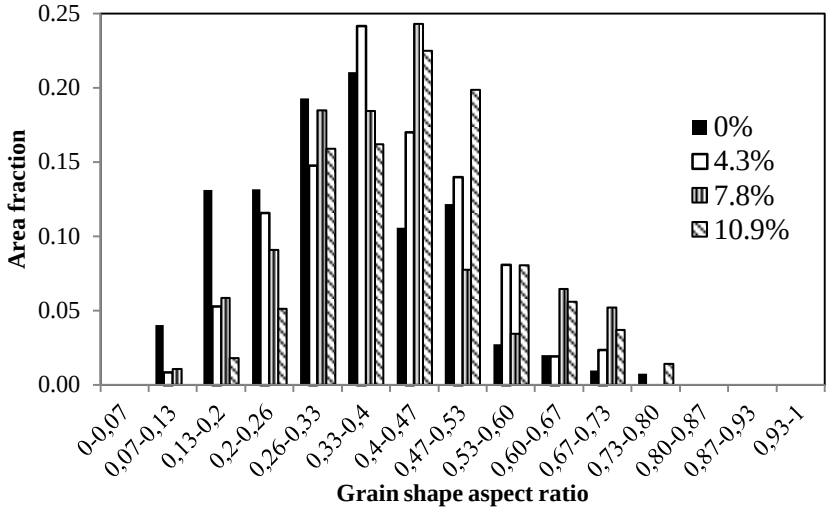

Figure V.5-10: Area fraction of austenite grains with different grain shape aspect ratios for 0%, 4.3%, 7.8%, and 10.9% elongation

The majority of the grains have a lamellar morphology with GSAR between 0.26 and 0.53. The distributions shifted to higher average values with increasing strain, cfr. Figure V.5-10. This indicates that lamellar grains with low grain shape aspect ratios or large differences between the length of the longest and smallest axis in 2D were found to be less stable compared to grains with smaller differences, i.e. more globular shape. They transformed completely or partially at lower strains which resulted in more globular austenite grains at higher strain levels.

V.5.4.2-3 Stability of the local crystallographic orientations and rotations during deformation

The stability is influenced by the crystallographic orientation of the austenite grains. Figure V.5-11 (a) and (b) show the inverse pole figures (IPF) of the austenite superimposed with the high angle grain boundaries of the matrix in the starting material and after 4.3% elongation. This deformation reduced the fraction of retained austenite by a factor of two and significantly changed the crystallographic orientations.

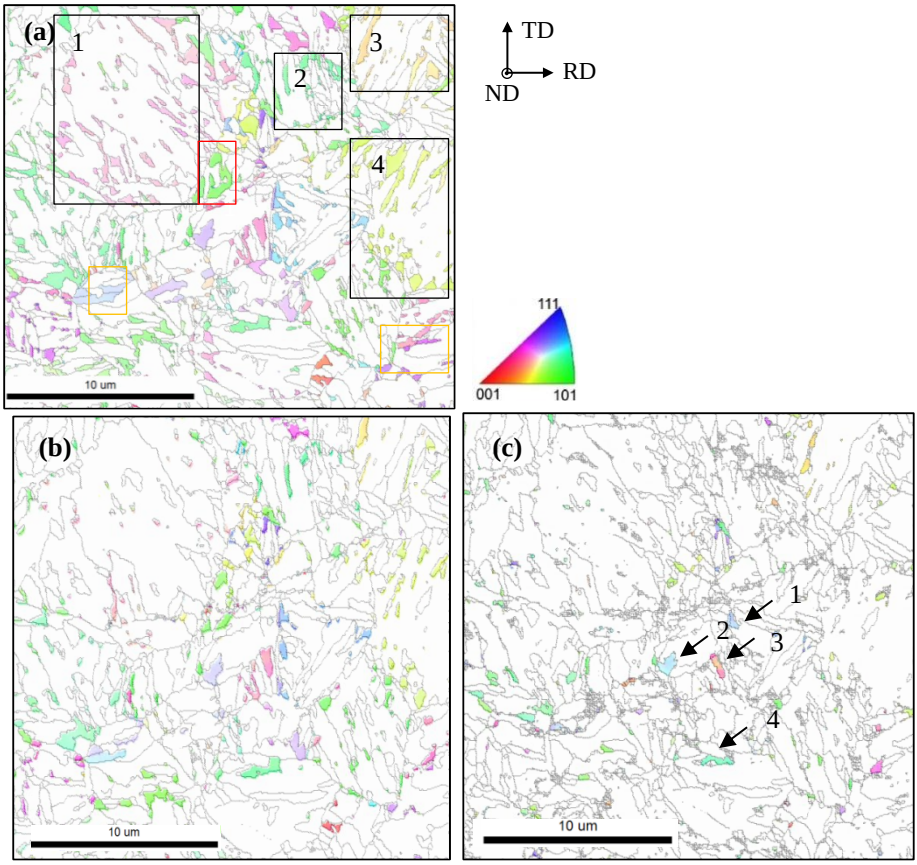

Figure V.5-11: ND-inverse pole figure of (a) the starting material and after elongations of (b) 4.3% and (c) 10.9%

Based on their transformation potentials of (1) 0.1132, (2) 0.1153, (3) 0.1195, and (4) 0.1054 [83], the grains in the black boxes should be relatively unstable. The transformation potentials of the austenite grains in the scanned area vary from 0.12- 0.045, where the highest transformation potentials indicate the lowest stability; i.e. for austenite grains with the same size and morphology, those with high transformation potential will transform first at a given strain. Approximately 60 % of the grains in these boxes transformed after 4.3% elongation. In square 2, however, some of the grains remained quite stable (more than what is predicted based on the transformation potential). The longest axis of these grains is parallel to the tensile axis, i.e. these grains have the most stable morphological orientation compared to those of other grains. Hence, we can conclude from this observation that, compared to orientation, morphology has a greater effect on the stability of the grains.

The large green grain in the red box has a transformation potential of 0.0511 and is one of the most stable orientations present in the scan. However, this grain transformed partially owing to its large size and rather unfavourable morphology.

The grains in the orange box represent (partially) transformed grains with medium crystallographic orientation stability (the transformation potentials are 0.088 and 0.085 for the purple and light-blue grains, respectively) but with their longest axes perpendicular to the tensile direction.

Therefore, the factors determining the local retained austenite stability in decreasing order of importance are: *(i)* grain size *(ii)* morphology, and *(iii)* crystallographic orientation. If all grains with the same crystallographic orientation are considered without limitations of the size or morphology, then a close correspondence between the orientation transformation rate and the predicted transformation potential is obtained since the effects of grain size and morphology are levelled out [83].

As in previous studies on TRIP-steels [30], it was observed that, some of the remaining austenite grains (indicated by the black arrows) rotate after a total elongation of 10.9%. Grains numbered 1, 2, and 4 rotated 4.1°, 4.4°, and 4.4°, respectively, with respect to their orientations after 4.3% elongation; however, grain 3 rotated (by 4.8°) only partially. Therefore, in addition to undergoing deformation and transformation, the austenite grains rotated to accommodate the strain. These rotations of the austenite grains, which act as a barrier to the movement of dislocations inside the martensite grains, may reduce the back-stress on dislocations and postpone the crack initiation process [84].

To study this rotation behaviour more quantitatively, the crystallographic orientations of 15 randomly selected grains were considered, cfr. Figure V.5-12 (a) and the rotation with respect to the starting orientation was calculated, as illustrated in Figure V.5-12 (b). Most of the austenite grains rotated between 2° and 6° except for grain 10, which rotated 11.1° with respect to its starting orientation. This grain remained stable against martensitic transformation but contributed to the ductility via its rotation. However, since the experiment was conducted on the surface of the sample, the austenite grains located there, have an additional degree of freedom compared to their counterparts in the bulk [30].

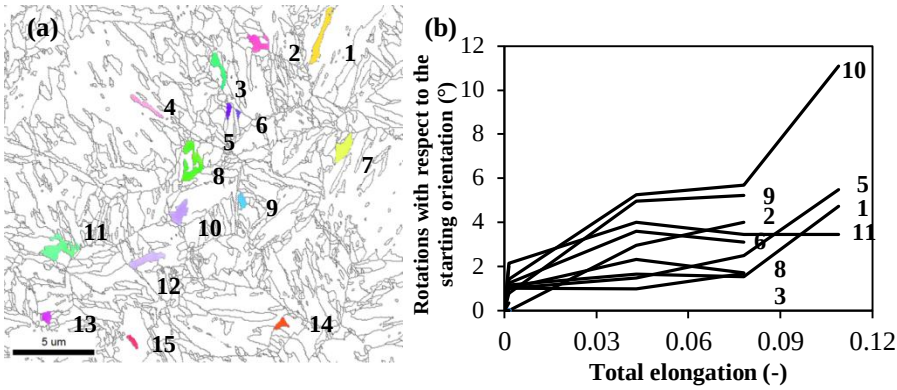

Figure V.5-12: (a) The ND-inverse pole figure of the 15 grains studied and (b) the rotation of austenite grains, with respect to the starting orientation, as a function of the total elongation. Grains 4-7-12-13-14-15 rotated by only 2° in the first deformation step after which they transformed

The measured rotation path of the tensile axis for the 15 grains is shown in black in the standard stereographic triangle, cfr. Figure V.5-13 (a). The starting- and endpoints are denoted by the red and green dots, respectively, and by the arrows. Grains with the same crystallographic orientation with respect to the straining direction experienced similar rotations [30], as is illustrated in Figure V.5-13 (b).

The rotations were compared with predictions of the classical Taylor model (in grey), which assumes that all of the grains are subjected to the same strain. The crystallographic grain rotations can be calculated by using the antisymmetric part of the strain tensor [85]. Grains 2, 5, 6, 9, 10, and 11 rotated, on average, in the same direction as that predicted by the model. They also have low transformation potentials and are stable against martensitic transformation. In contrast, grains 4, 7, 12, 13, 14, and 15, which have high transformation potentials, are transformed in the initial deformation stages without significant rotation. Grains 1, 3, and 8 rotated towards crystallographic orientations, which differed from those predicted by the Taylor model. These deviations from the Taylor model were observed previously in the case of copper [86].

The Taylor model is based on a single phase material but in our sample the austenite grains are embedded in a martensitic matrix. Moreover, the partial correspondence between the experimental data and the predictions indicates that the Taylor model is unable to fully predict the micro-deformation mechanisms.

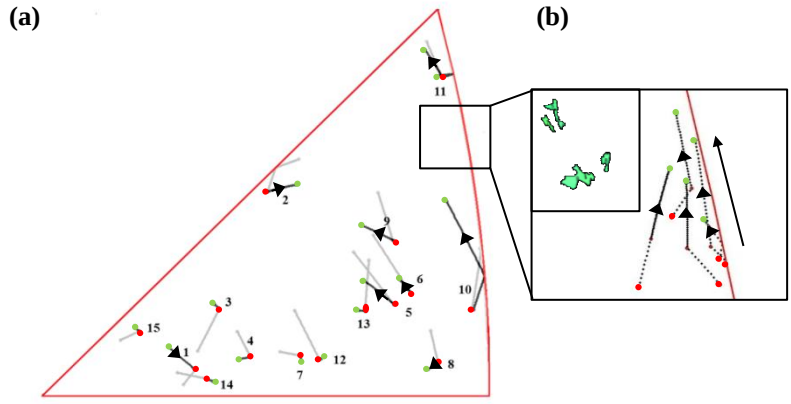

Figure V.5-13: (a) The rotation of the tensile axis of the 15 grains and the modelled orientation changes, predicted by the full-constraint Taylor model (in grey), projected in the TD- stereographic triangle and (b) orientation changes of austenite grains with the same starting orientation

V.5.4.3 Local deformation intake by Grain Reference Orientation Deviation

The grain reference orientation deviation (GROD) parameters were calculated in order to study the local deformation experienced by the austenite and martensite. The GROD represents the misorientation of each point of a grain from the average orientation of the grain. Both the average and the maximum GROD were evaluated since they provide information about the overall and local intake of deformation, respectively. The mechanisms of strain accommodation can be identified by combining the GROD with the change in the fraction of retained austenite. To obtain comparable results, the relative difference between different deformation steps per percentage elongation was evaluated, as shown in Figure V.5-14.

As the figure shows, throughout straining, the transformation of retained austenite contributed approximately the same amount to the deformation per percentage of elongation. The strain intake in the phases differed, however, from stage to stage. After elastic and 0.15% plastic deformation, the strain is accommodated mainly by local deformation in both the austenite and martensite phases, and globally in the austenite phase as can be observed from its higher difference in GROD. In the subsequent deformation stage, to 4.3% elongation, the local deformation remained similar due to partial relaxation of the grains after the austenite to martensite transformation in the highly strained regions. A portion of the deformation is also sustained by overall straining of the bcc phase. In addition, the transformation of retained austenite combined with the overall and local accommodation of strain in the martensitic

matrix occurred at total elongations of 4.3%-7.8%. In the final stage, the deformation was sustained mainly by the transformation of austenite.

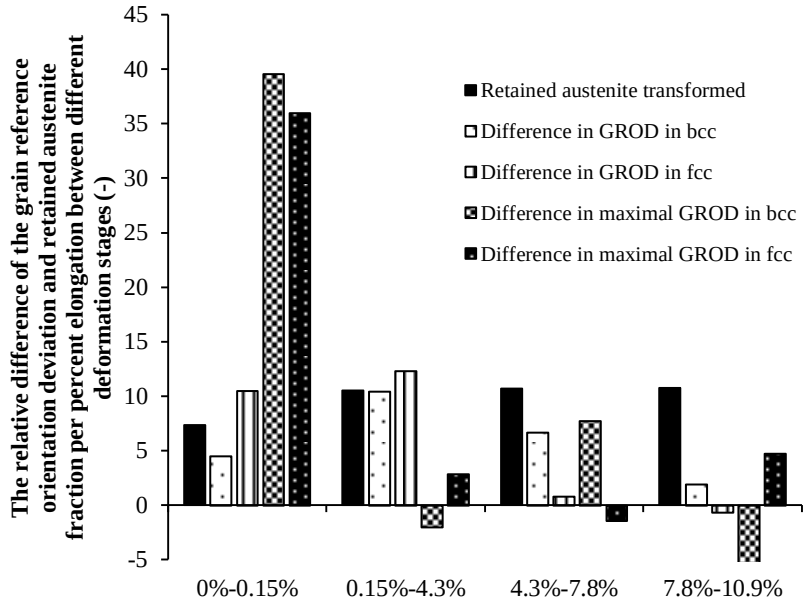

Figure V.5-14: The relative difference of the grain reference orientation deviation and retained austenite fraction per percentage elongation between different deformation stages

The evolution of the retained austenite fraction and the grain reference orientation deviation suggest that deformation accumulated in both phases; if the critical strain level is reached, then the transformation of austenite relieves the internal local strain. A combination of overall straining of the phases and phase transformation occurred thereafter and the latter became dominant to the former with increasing strain.

V.5.5. Conclusions

The austenite parameters influencing its stability against transformation to martensite under external load were investigated in 0.25C1.5Si3Mn Q&P steel. They can be listed in order of increasing importance as follows: *(i)* grain size, *(ii)* morphology and *(iii)* crystallographic orientation.

(i) The largest grains transformed rapidly upon plastic straining, whereas grains with intermediate diameters contributed the most to the transformation induced plasticity in

Q&P steel, all with different transformation rates; the small grains sustain plasticity at large strains. Owing to their high stability, the smallest detectable grains did not transform during uniform straining. They will, however, contribute to the plastic elongation when (local) strain levels increase.

(ii) The grains oriented perpendicular and under 45° with respect to the tensile direction transformed rapidly owing to the high force exerted on these grains by tensile and shear stresses, respectively.

(iii) Lamellar grains with a large difference between the length of the longest and smallest axis in 2D were found to be less stable compared to grains with smaller differences, i.e. more globular shape.

(iv) The dependence of the austenite crystallographic orientation on its stability is defined by the theory of martensite crystallography. This theory predicts the global transformation stability; however, compared to global factors local factors are more important in controlling the stability. Subsequent to transformation, the austenite grains rotate in order to accommodate the deformation. Orientations with high transformation potentials transform to martensite instead of rotating significantly. In contrast, orientations with low transformation potentials rotated mainly 2°-6° prior to the transformation.

In the initial stages of plastic elongation, the deformation is accommodated (locally) mainly in the martensite and austenite grains. After the critical strain for austenite transformation is reached, the austenite grains transform, thereby reducing the local, internal strain in the martensite grains. Strain accommodation in the martensite combined with the TRIP-effect occurs in the later stages of deformation, and the latter becomes dominant to the former with higher strains.

V.5.6. Acknowledgements

This research was funded by the governmental institute for the Promotion of Innovation by Science and Technology in Flanders (IWT) and was carried out under the frame of the project “RFCS-CT-2011-00017 “New advanced high strength steels by quenching and partitioning process (NewQ&P)”. Discussions with, and comments from, Dr. Maria Santofimia Navarro and Prof. Jilt Sietsma of the Materials Science and Engineering Department, Faculty 3mE, TU Delft, The Netherlands are greatly appreciated. We are furthermore grateful to TU Delft and Farideh Hajy Akbary for assistance with and use of the micro-tensile test device.

SECTION 6

INFLUENCE OF FRESH MARTENSITE ON THE PARAMETERS DETERMINING AUSTENITE STABILITY

V.6. INFLUENCE OF FRESH MARTENSITE ON THE PARAMETERS DETERMINING AUSTENITE STABILITY

V.6.1. Introduction

In Chapter V.5, the parameters of austenite influencing its stability against transformation to martensite under external load was investigated for a sample that consisted of only retained austenite embedded in a tempered martensitic matrix (sample A). In increasing order of importance, these factors were: *(i)* grain size, *(ii)* morphology, and *(iii)* crystallographic orientation. We observed in Chapter V.1 however, that fresh martensite changed the stress state and strain distribution in the microstructure, thereby reducing the overall austenite stability. This change in strain distribution and constraining effect are expected to affect the parameters and their order of importance. Therefore, the effect of fresh martensite on these parameters was studied by analysing sample B, which has a fresh martensite fraction of 21%.

V.6.2. Results and discussion

V.6.2.1 Micromechanical behaviour of austenite grains during deformation

For sample B, the same methods as those used to analyse sample A, cfr. Chapter V.5 paragraph V.5.4.2, will be used to determine the influence of fresh martensite on the aforementioned parameters.

V.6.2.1-1 The evolution of the austenite grain size

Figure V.6-1 shows the evolution of the average austenite grain diameter, which was initially 0.60 µm and decreased rapidly to 0.46 µm after only 0.6% plastic elongation. All grains larger than 1µm transformed during this first deformation stage, leading to the high transformation rates observed in Figure V.6-2. Due to stress concentration effects around the fresh martensite blocks combined with their unfavourable large size, these grains transformed at very low plastic strains. As a result, their contribution to the transformation induced plasticity (TRIP) effect was only minor, which resulted in high strain-hardening values at low plastic strains; this is frequently observed in the stress-strain curves of Q&P steels with incomplete stabilisation of austenite during partitioning [15, 75, 77]. The average austenite grain

size decreased only slightly (i.e. by 0.06 µm) from 0.46 µm to 0.40 µm at elongations of 0.6% to 3.1%.

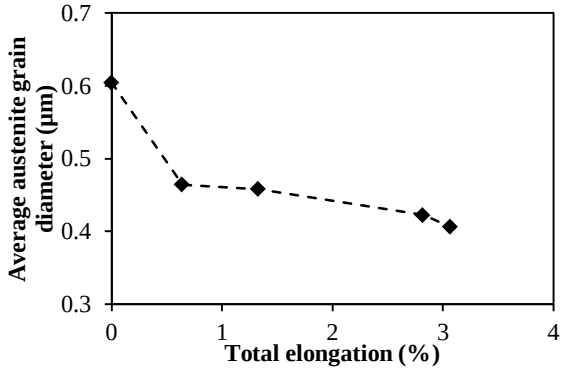

Figure V.6-1: Average austenite grain diameter (µm) as a function of the total elongation

Compared to the other grains, austenite grains with diameters of 0.2 µm-1 µm transformed at lower rates (cfr. Figure V.6-2), thereby sustaining plasticity at high strain levels, owing to a more continuous transformation to martensite. A fraction of the grains smaller than 0.8 µm persisted in the sample after 3.1% deformation and accommodated the final strain to fracture at 5.8%.

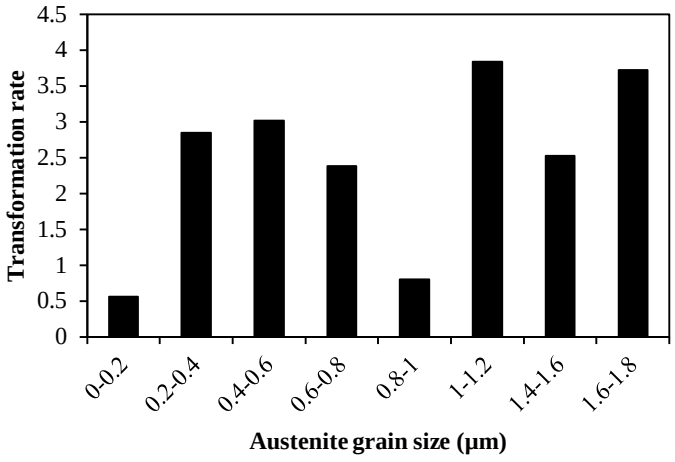

Figure V.6-2: Transformation rate as a function of the austenite grain size

Owing to their high stability, grains smaller than 0.2 µm did not transform at these low strain levels. This conclusion is the same as for the sample without fresh martensite, cfr.

Chapter V.5 paragraph V.5.4.2-1, indicating that the effect of grain size on austenite stability was not significantly altered by the presence of fresh martensite.

V.6.2.1-2 Morphology evolution

As in sample A, grains with sizes of 0.3 µm-0.75 µm and crystallographic-orientation-related transformation potential below 0.105 were considered in the analysis; as shown in Figure V.6-3 (a). These grains were subdivided according to their major axis orientation (MAO) into three groups, namely *(i)* 0°–36° and 144°-180°, *(ii)* 36°-72° and 108°-144°, and *(iii)* 72°-108°. The transformation rate of the austenite grains within a certain range of MAO and at different deformation stages is given in Figure V.6-3 (b).

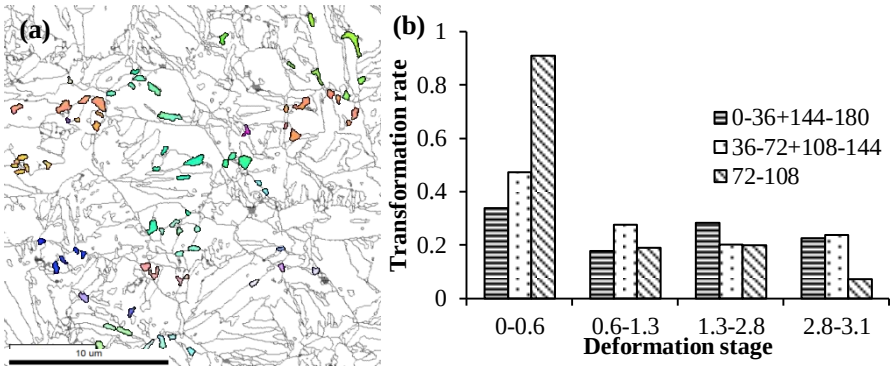

Figure V.6-3: (a) Austenite grains in the starting material, which have transformation potentials below 0.105 and grain sizes of 0.3-0.75 µm and (b) transformation rates of the MAO ranges at different deformation stages

The grains parallel to the tensile direction exhibited the highest transformation rate in the first deformation stage spanning elongations of 0% to 0.6%. Grains with their longest axis perpendicular to and under ± 45° with respect to the tensile axis sustained the deformation in the subsequent stages. As a consequence, the presence of fresh martensite changed the influence of morphology on the austenite stability compared to what was concluded from the sample in a homogeneous matrix without fresh martensite. In addition, the high stresses stemming from the tensile and shear component resulted in unstable grains perpendicular to and under ± 45°, respectively. Therefore, the presence of rigid martensite blocks changed the local stress state and hence modified the influence of morphology on austenite stability.

V.6.2.1-3 Stability of the local crystallographic orientations and rotations during deformation

The stability of austenite is influenced by the crystallographic orientation of the austenite grains. Figure V.6-4 (a) and (b), shows the respective inverse pole figures (IPF) of the austenite in the starting material and after 0.6% elongation.

The overall transformation potentials of all grains in the scan vary from 0.048-0.13, representing the most stable and unstable grains, respectively. The green grains in boxes 1 and 2 transformed (partially) in the first deformation stage owing to their high transformation potential of 0.1068 and large grain sizes. In contrast, the lamellar (part of the) grains, which are orientated parallel to the tensile direction, remained relatively stable.

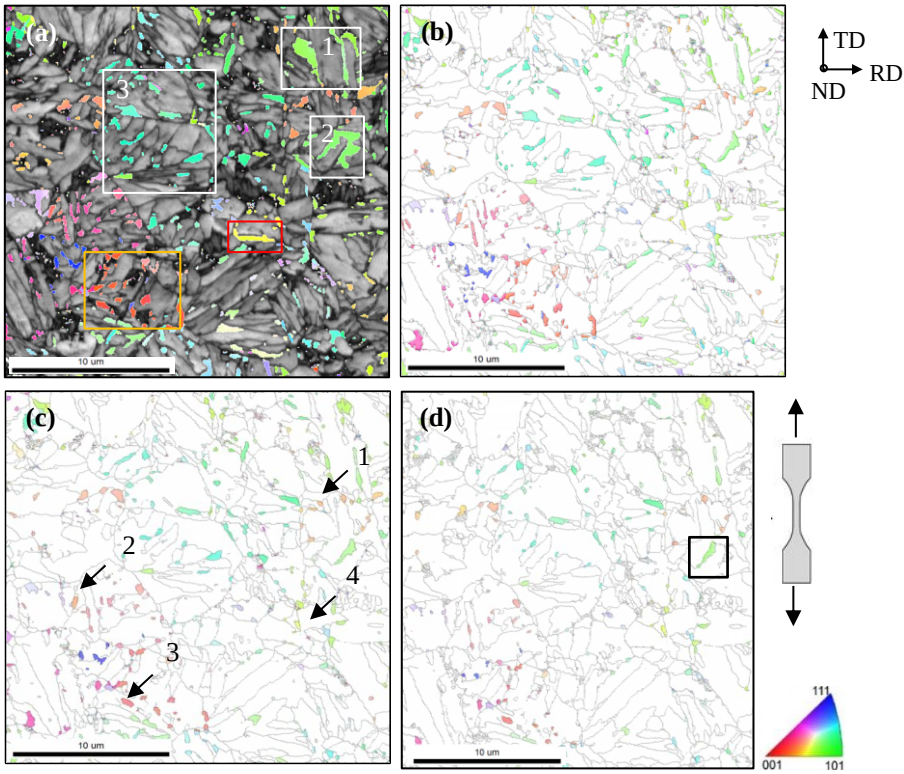

Figure V.6-4: ND-inverse pole figure of (a) the starting material superimposed with IQ and after (b)-(d) 0.6%, 1.3%, and 2.8% elongation, respectively

Owing to its unfavourable morphology and immediate neighbourhood of fresh martensite, the yellow grain in the red box transformed despite being crystallographically stable, as evidenced by a transformation potential of 0.067.

The grains in square 3 have a crystallographic orientation, which with a transformation potential of only 0.0597, is among the most stable orientations of all the grains. They are located in a tempered martensite matrix without stress-concentrating effects and hence, remained stable during tensile testing.

The grains surrounded by the orange frame have a transformation potential of 0.109, and have highly unstable orientations. Nevertheless, these grains remained stable and rotated as a result of their relatively small size, round morphology, and shielding by fresh martensite.

Figure V.6-4 (c) shows the IPF of the sample elongated to 1.3%; the end points of the rotated austenite grains are indicated by the black arrows. Grains 1, 2, and 3 rotated by 3°, 3.3°, and 0.6°, respectively, whereas grain 4 rotated by ~4°. During the subsequent deformation stage to 2.8% strain, the IPF in Figure V.6-4 (d) shows that part of the previously rotated grains transformed. A large austenite grain, shown by the black box in Figure V.6-4 (d) remained stable until fracture. This grain was part of the previously larger and partially transformed grain 2 in the white square. Hence, the high-C transformed martensitic region shielded the austenite, thereby inhibiting its transformation [11, 82].

The presence of fresh martensite, which partially shields the austenite grains located inside or near the fresh martensite blocks, resulted in a transformable austenite fraction that was lower than the starting fraction. The grains which could transform, transformed rapidly owing to a stress and strain-concentrating effect. Therefore, the influence of the parameters, which determined the austenite stability, was altered owing to the presence of fresh martensite.

As in sample A, the crystallographic orientation changes of 15 randomly selected austenite grains were monitored during deformation in order to accurately quantify the rotation. Figure V.6-5 (a) shows the rotation of these grains with respect to the starting crystallographic orientation; the grains rotated by only 3.5° prior to the transformation. Similar to the sample without fresh martensite (i.e. sample A), the grains rotated to accommodate the deformation.

The projection of the tensile axis on the TD-stereographic triangle with the modelled rotation path predicted by the full-constraint Taylor model, cfr. Figure V.6-5(b), illustrates that the direction of grain rotation cannot be reliably predicted. The Taylor model is based on the assumption of equal strain. However, the experimental conditions of this sample did not fulfil this requirement since the matrix changed the deformation behaviour.

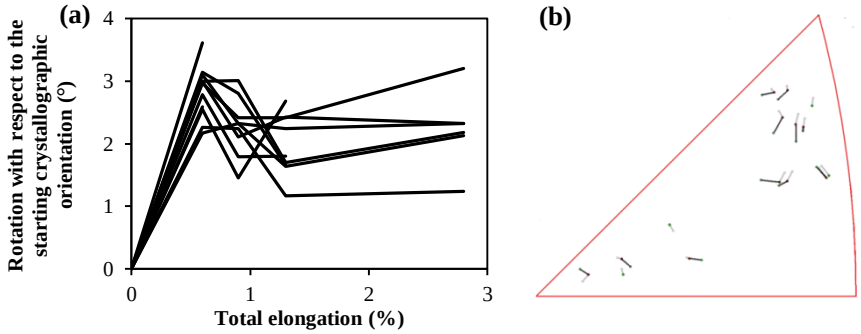

Figure V.6-5: (a) The rotations of 15 randomly selected austenite grains, with respect to the starting crystallographic orientation, as a function of the total elongation and (b) the rotation of the tensile axis of these grains and the orientation change modelled by the full-constraint Taylor model (in grey) projected on the TD-stereographic triangle

The overall influence of the crystallographic orientation on the austenite stability averaged over all grains with a specific orientation was modelled and determined experimentally for 10 orientations, cfr. Table V.6-1.

Table V.6-1: Euler angles of ten orientations and the corresponding modelled transformation potential as well as the experimentally determined transformation rate

Number of orientation	Orientation (Euler angles, °)			Transformation potential (model)	Transformation rate (experimental)
	ϕ1	Θ	ϕ2		
1	145.9	45.7	196.2	0.0659	-0.2254
2	312.1	19.2	28.8	0.1090	-0.1874
3	48.3	23.8	266.8	0.0626	-0.2025
4	32.6	7.2	349.8	0.1114	-0.1830
5	96.5	29.5	251.5	0.1238	-0.2296
6	118.1	53.3	222.6	0.0838	-0.1920
7	157.6	16.1	166.9	0.0792	-0.2114
8	111.9	17.7	286.0	0.0826	-0.2102
9	110.3	28.8	271.7	0.1125	-0.2252
10	39.5	41.0	278.4	0.0615	-0.1574

In contrast to sample A, the model could not predict the experimentally measured transformation rates, cfr. Figure V.6-6. The effects of grain size or morphology were levelled out when all of the grains with the same orientation were considered. Sample A exhibited close correspondence between the predicted and experimentally observed transformation behaviour of the crystallographic orientations. However, in sample B, the influence of fresh

martensite on the stress, and consequently strain distribution, controlled the austenite transformation behaviour.

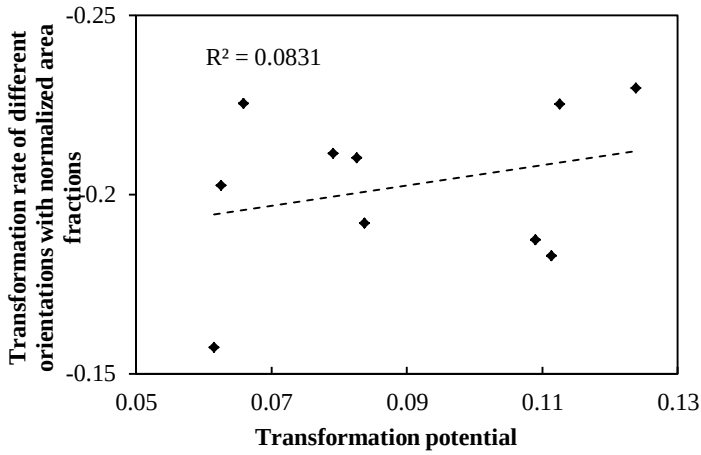

Figure V.6-6: Transformation potential vs. the experimental transformation rate of 10 randomly chosen orientations

V.6.2.2 Local deformation intake by Grain Reference Orientation Deviation

The mechanisms governing the accommodation of strain can be identified by using the relative difference, per percentage elongation between different deformation steps, of the average and maximal grain reference orientation deviation (GROD) and the change in the fraction of retained austenite fraction, cfr. Figure V.6-7. The GROD represents the misorientation between a given point inside a grain and the average orientation of the considered grain.

In the initial stage of deformation, the strain was accommodated by both the transformation of retained austenite and the deformation of martensite. In the subsequent deformation stage, to 0.9% deformation, a significant fraction of austenite transformed owing to the stress-concentrating effect of the fresh martensite. This transformation resulted in internal strain relief, as illustrated by a decrease in the maximum GROD of both martensite and austenite. At strains of 0.9%-2.8%, almost no austenite transformed and the strain was accommodated by deformation. However, the large, unshielded austenite grains transformed in the initial stages of deformation. The remaining transformable austenite grains were small and therefore transformed to martensite only at high strain levels, as reflected in the high transformation rate observed at strains of 2.8%-3.1%. During the final stage of straining, the plasticity was sustained by austenite transformation and strain localisation in the martensite.

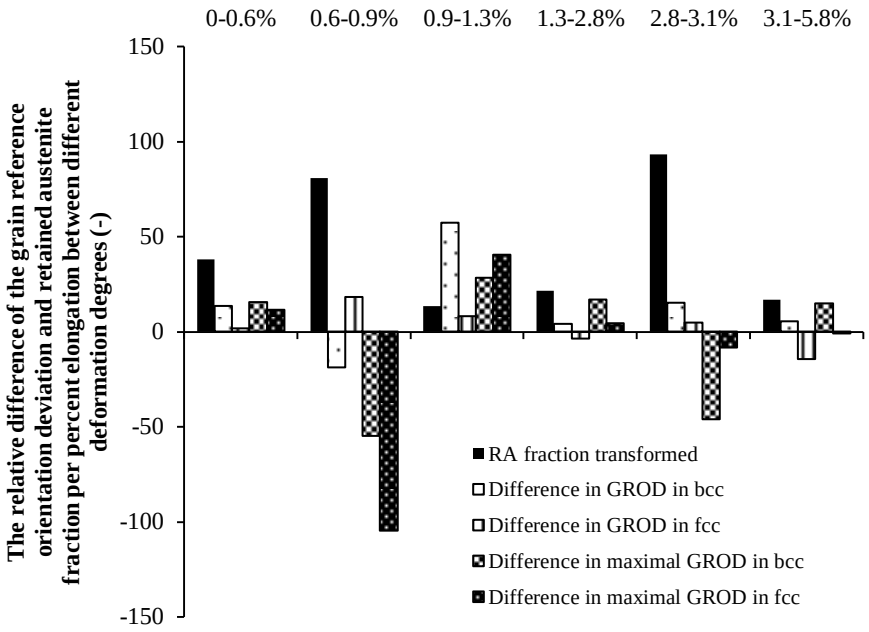

Figure V.6-7: The relative difference of the grain reference orientation deviation and the retained austenite fraction, per percentage elongation between different deformation stages

V.6.3. Conclusion

Fresh martensite altered the mechanisms controlling the austenite stability due to its constraining effect. This effect, on the one hand, reduced the stability of the transformable austenite grains owing to an increased local stress and strain state. These grains transformed at low strains resulting in a high n-value in the stress-strain curves at low strains. On the other hand, this effect shielded part of the austenite grains, which lie in or in the vicinity of the fresh martensite grains, thereby reducing the effectiveness of austenite as a TRIP-assisted component. The austenite grain size, which decreased during straining, was the only parameter that exhibited similar tendencies to those observed in Chapter V.5. The influence of morphology and crystallographic orientation on the stability was undermined by the presence of fresh martensite.

SECTION 7

DEFORMATION BEHAVIOUR AT THE FRACTURE SURFACE

V.7. DEFORMATION BEHAVIOUR AT THE FRACTURE SURFACE

V.7.1. Introduction

Three types of fracture (not taking fatigue into account) occur in steels: ductile, cleavage, and intergranular. Ductile materials usually fail as a result of the nucleation, growth, and coalescence of microscopic voids, which are initiated at inclusions and second phase particles. Cleavage fracture in metals proceeds via separation along the crystallographic planes, which have the lowest packing density, i.e. {100} for bcc. Although cleavage is often called brittle fracture, it can be preceded by large-scale plasticity and ductile crack growth. Intergranular fracture occurs when the grain boundaries are the preferred fracture path, as is the case of grain boundary segregation.

The fracture surfaces of Q&P steel have scarcely been studied and both brittle facets [87] and ductile dimples [88] have been reported. However, experimental data showing the influence of the microstructural components on the fracture behaviour have not been studied. Therefore, the fracture surfaces and deformation in the cross-section beneath the fracture surface of the two steels, with (referred to sample B) and without (referred to sample A) fresh martensite, previously mentioned in Chapter V.1-2, are examined; the effect of FM on the fracture mechanisms in these samples is also discussed.

V.7.2. Fracture surfaces

The fracture surfaces of samples A and B are given in Figure V.7-1 (a)-(b) and (c)-(d), respectively.

In sample A, a micro-void coalescence fracture mechanism is observed [89]. The fracture surface consists of dimples, which result from the growth of small neighbouring voids until the material between them is heavily deformed and finally ruptures. Small dimples are located at the grain boundaries of the parent austenite grain and are associated with transformed retained austenite grains, cfr. Figure V.7-1 (a). During deformation, the large austenite grains at the prior austenite grain boundaries transform to high-C martensite at relatively low strains and subsequently act as hard second phase particles, which initiate small voids. Neighbouring voids interact as the fraction and size of the voids increase. Moreover,

the tempered martensite located between the voids is plastically strained, thereby creating local instabilities and necking.

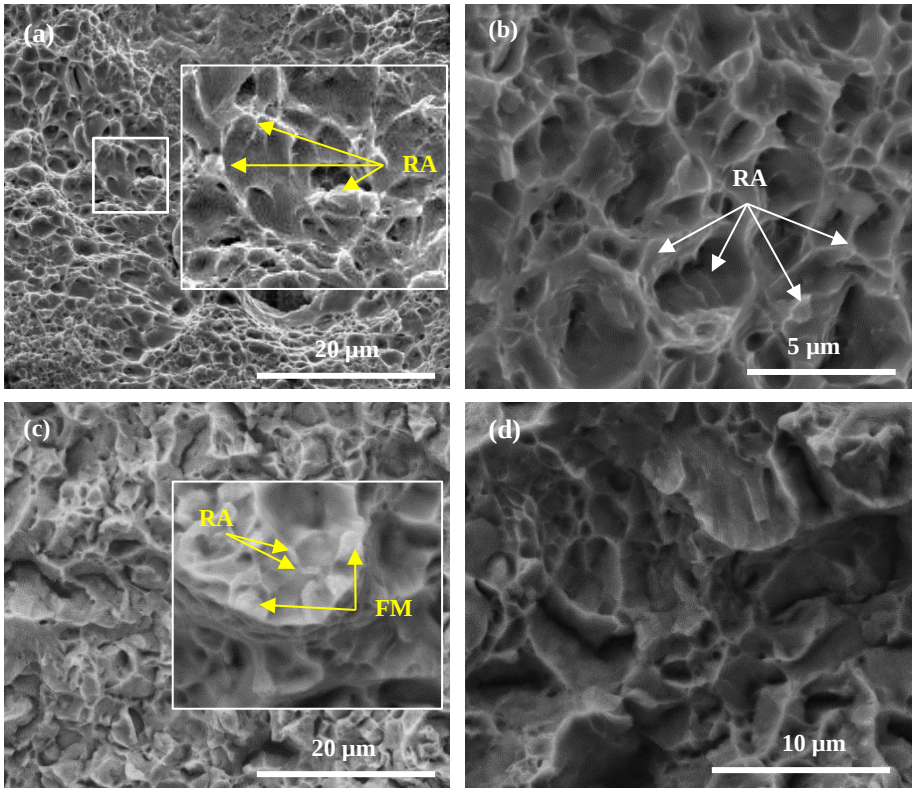

Figure V.7-1: Fracture surface of samples (a) – (b) A and (c) – (d) B; FM: fresh martensite and RA: retained austenite

Sample B exhibits mainly quasi-cleavage [89] and its fracture surface is significantly coarser than that of A. The cracks were initiated by micro-void coalescence at the transformed retained austenite grains and original fresh martensite blocks but ultimate failure occurred by brittle cleavage, as indicated from the smooth fracture facets. The cracks propagated along transgranular paths. Furthermore, the fresh martensite blocks acted as stress-concentrating points and the matrix, therefore, accommodated a substantial amount of deformation. Consequently, small dimples formed at these stress concentration points in the tempered matrix and via the transformation of retained austenite, whereas the neighbouring fresh martensite blocks fractured in a brittle manner.

V.7.3. Deformation behaviour close to the fracture surface

The deformed grains on the surfaces perpendicular to the fracture surface were revealed via SEM examination, cfr. Figure V.7-2. The tempered martensite grains in sample A, shown in figures (a) and (b), are elongated along and aligned 45° to the tensile axis. The lightly etched constituents are the transformed austenite grains since fresh martensite was not present in this undeformed Q&P sample. Their shape is indicative of co-deformation with the tempered martensite grains prior to the transformation. The large blocky austenite grains, indicated by the yellow squares, were less deformed than (for e.g.) the small lamellar grains enclosed in the white box. The large austenite grains transformed at low strains prior to significant straining whereas the thin austenite films accommodated more deformation prior to transformation. This difference stems from the differing influence of varying grain size and morphology on the stability of austenite. In addition, large, blocky austenite grains transform at lower strains than their small, lamellar counterparts [44].

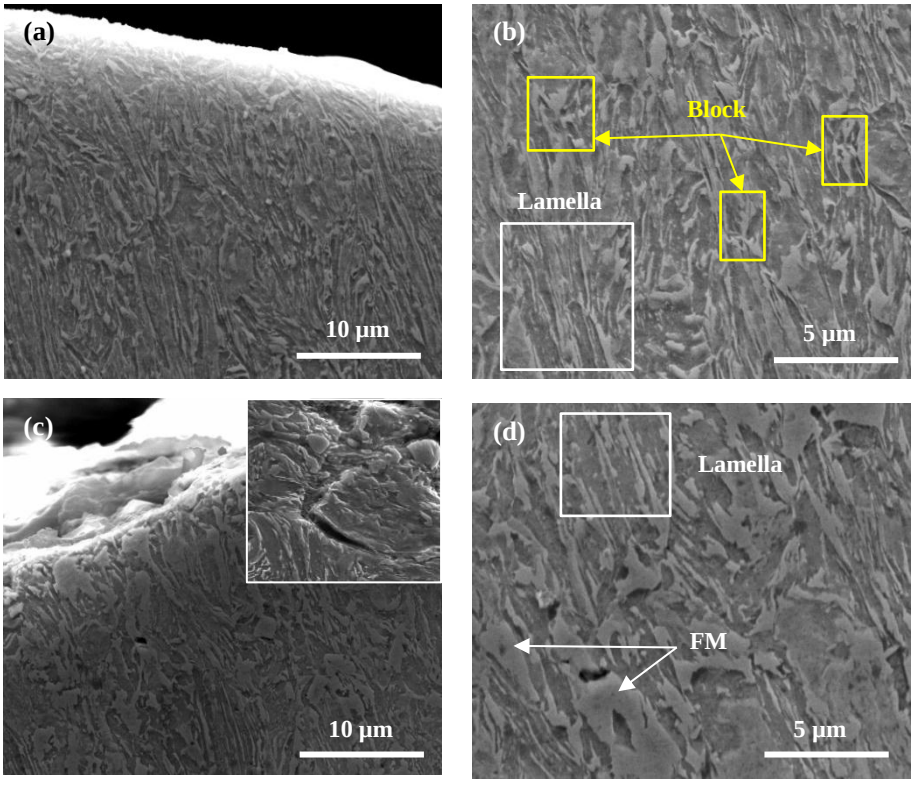

Figure V.7-2: Etched surface perpendicular to the fracture surface of samples (a) – (b) A and (c) – (d) B

Due to the presence of large, rigid blocks of fresh martensite, Figure V.7-2 (d), the deformed microstructure of sample B differs from that of A; the tempered martensite deformed around these FM blocks. Moreover, although the overall accommodated deformation was lower in sample B than in sample A, similar conclusions can be drawn regarding the retained austenite. Voids around the fresh martensite blocks, which account for void nucleation during straining, were previously mentioned in Chapter V.1. The inset of Figure V.7-2 (c) shows the decohesion of a prior austenite grain, thereby highlighting the importance of these boundaries in the fracture behaviour; similar observations were made from the fracture surfaces in Figure V.7-1.

V.7.4. Conclusions

The effect of FM on the fracture mechanisms was studied by analysing the fracture surface and deformed microstructure. The transformation of large retained austenite grains into high-C martensite induced hard second phase particles which are the nucleation sites for voids. A change from a micro-void coalescence to quasi-cleavage fracture behaviour was revealed by adding FM to a tempered martensite matrix with retained austenite. As indicated by their transformation at lower strains, RA blocks deformed less than the interlath lamellar austenite grains, owing to their lower mechanical stability. Moreover, the FM blocks remained as rigid constituents in the necking region triggering void formation by stress concentration, thereby reducing the overall strain via its constraining effect.

References

1. J. G. Speer, D. K. Matlock, B. C. De Cooman, and J. G. Schroth: 'Carbon partitioning into austenite after martensite transformation', *Acta Materialia*, 2003, **51**, 2611-2622.

2. J. G. Speer, D. V. Edmonds, F. C. Rizzo, and D. K. Matlock: 'Partitioning of carbon from supersaturated plates of ferrite, with application to steel processing and fundamentals of the bainite transformation', *Materials Science*, 2004, **8**, 219-237.

3. J. G. Speer, F. C. R. Assunção, D. K. Matlock, and D. V. Edmonds: 'The “quenching and partitioning” process: Background and recent progress', *Materials Research*, 2005, **8**, 417-423.

4. M. J. Santofimia, L. Zhao, R. Petrov, and J. Sietsma: 'Characterization of the microstructure obtained by the quenching and partitioning process in a low-carbon steel', *Materials Characterization*, 2008, **59**, 1758-1764.

5. M. J. Santofimia, L. Zhao, R. Petrov, C. Kwakernaak, W. G. Sloof, and J. Sietsma: 'Microstructural development during the quenching and partitioning process in a newly designed low-carbon steel', *Acta Materialia*, 2011, **59**, 6059-6068.

6. M. J. Santofimia, L. Zhao, and J. Sietsma: 'Overview of mechanisms involved during the quenching and partitioning process in steels', *Metallurgical and Materials Transactions A - Physical Metallurgy and Materials Science*, 2011, **42A**(12), 3620-3626.

7. N. H. van Dijk, A. M. Butt, L. Zhao, J. Sietsma, S. E. Offerman, J. P. Wright, and S. van der Zwaag: 'Thermal stability of retained austenite in trip steels studied by synchrotron x-ray diffraction during cooling', *Acta Materialia*, 2005, **53**, 5439-5447.

8. R. Blondé, E. Jimenez-Melero, L. Zhao, J. P. Wright, E. Brück, S. van der Zwaag, and N. H. van Dijk: 'High-energy x-ray diffraction study on the temperature-dependent mechanical stability of retained austenite in low-alloyed trip steels', *Acta Materialia*, 2012, **60**(2), 565-577.

9. E. Jimenez-Melero, N. H. van Dijk, L. Zhao, J. Sietsma, S. E. Offerman, J. P. Wright, and S. van der Zwaag: 'Characterization of individual retained austenite grains and their stability in low-alloyed trip steels', *Acta Materialia*, 2007, **55**(20), 6713-6723.

10. I. B. Timokhina, P. D. Hodgons, and E. V. Pereloma: 'Effect of microstructure on the stability of retained austenite in transformation-induced-plasticity steels', *Metallurgical and Materials Transactions A*, 2004, **35**, 2331-2340.

11. P. J. Jacques, J. Ladriere, and F. Delannay: 'On the influence of interactions between phases on the mechanical stability of retained austenite in transformation-induced plasticity multiphase steels', *Metallurgical and Materials Transactions A - Physical Metallurgy and Materials Science*, 2001, **32**(11), 2759-2768.

12. S. O. Kruijver, L. Zhao, J. Sietsma, S. E. Offerman, N. H. van Dijk, E. M. Lauridsen, L. Margulies, S. Grigull, H. F. Poulsen, and S. van der Zwaag: 'In situ observations on the mechanical stability of austenite in trip steel', *Journal de Physique*, 2003, **IV**(104), 499-502.

13. O. Muransky, P. Sittner, J. Zrnik, and E. C. Oliver: 'In situ neutron diffraction investigation of the collaborative deformation-transformation mechanism in trip-assisted steels at room and elevated temperatures', *Acta Materialia*, 2008, **56**(14), 3367-3379.

14. Xiong X.C., Chen B., Huang M.X., Wang J.F., and W. L.: 'The effect of morpholohy on the stability of retained austenite in a quenched and partitioned steel', *Scripta Materialia*, 2013, **68**(5), 321-324.

15. I. de Diego-Calderón, M. J. Santofimia, J. M. Molina-Aldareguia, M. A. Monclús, and I. Sabirov: 'Deformation behavior of a high strength multiphase steel at macro- and micro-scales', *Materials Science and Engineering: A*, 2014, **611**(0), 201-211.

16. E. Paravicini Bagliani, M. J. Santofimia, L. Zhao, J. Sietsma, and E. Anelli: 'Microstructure, tensile and toughness properties after quenching and partitioning treatments of a medium-carbon steel', *Materials Science and Engineering: A*, 2013, **559**(0), 486-495.

17. W. S. Owen: 'The effect of silicon on the kinetics of tempering', *Transactions of the ASM*, 1954, **46**, 812-828.

18. L. Chang and G. D. W. Smith: 'The silicon effect in the tempering of martensite in steels', *Journal de Physique*, 1984, **45**, 397-401.

19. D. A. Porter, K. E. Easterling, and M. Sherif: 'Phase transformations in metals and alloys, third edition (revised reprint)', 2009, Taylor & Francis.

20. D. Kim, J. G. Speer, and B. C. De Cooman: 'Isothermal transformation of a cmnsi steel below the ms temperature', *Metallurgical and Materials Transactions A*, 2010, **42**, 1575-1585.

21. D. Kim, J. G. Speer, and B. C. De Cooman: 'The isothermal transformation of low-alloy low-c cmnsi steels below ms', *Materials Science Forum*, 2010, **654-656**, 98-101.

22. D. P. Koistinen and R. E. Marburger: 'A general equation prescribing extend of austenite-martensite tranformation in pure fe-c alloys and plain carbon steels', *Acta Materialia*, 1959, **7**, 59.

23. S. M. C. van Bohemen: 'The bainite and martensite start temperature calculated with an exponential carbon dependence', *Materials Science and Technology*, 2012, **28**(4), 487-495.

24. M. Maringa: 'Dimensioning of dog bone specimens and numerical analysis of the effects of different fillet radii, clamp area and pinhole loading on the stresses in such specimens', *African Journal of Science and Technology* 2004, **5**(2), 60-72.

25. F. H. Akbary, M. J. Santofimia, and J. Sietsma: 'Specimen-size effects on the tensile behavior of various steels', International Conference SSTT (Small Sample Test Techniques), Ostrava, Czech Republic, 2012.

26. A. Guesnier: 'Preparation of ferrous metals for electron backscatter diffraction (ebsd) analysis', (ed. Struers), 2010, Copenhagen, Rosendahls.

27. B. D. Cullity: 'Elements of x-ray diffraction', 1956, New Jersey, USA, Addison-Wesley Publishing Company, Inc.

28. C. Suryanarayana and M. G. Norton: 'X-ray diffraction: A practical approach', 1998, New York, Plenum Publishing Corporation.

29. M. J. Santofimia, T. Nguyen-Minh, L. Zhao, R. Petrov, I. Sabirov, and J. Sietsma: 'New low carbon q&p steels containing film-like intercritical ferrite', *Materials Science and engineering*, 2010, **527**, 6429-6439.

30. G. K. Tirumalasetty, M. A. Van Huis, C. Kwakernaak, J. Sietsma, W. G. Sloof, and H. W. Zandbergen: 'Deformation-induced austenite grain rotation and transformation in trip-assisted steel', *Acta Materialia*, 2012, **60**, 1311-1321.

31. C. Y. Wang, J. Shi, W. Q. Cao, and H. Dong: 'Characterization of microstructure obtained by quenching and partitioning process in low alloy martensitic steel', *Materials Science and engineering*, 2010, **527**, 3442-3449.

32. H. Liu, X. Lu, X. Jin, H. Dong, and J. Shi: 'Enhanced mechanical properties of a hot stamped advanced high-strength steel treated by quenching and partitioning process', *Scripta Materialia*, 2011, **64**, 749-752.

33. M. J. Santofimia, R. H. Petrov, L. Zhao, and J. Sietsma: 'Microstructural analysis of martensite constituents in quenching and partitioning steels', *Materials Characterization*, 2014, **92**(0), 91-95.

34. O. Matsumura, Y. Sakuma, and H. Takechi: 'Trip and its kinetic aspects in austempered 0.4c-1.5si-0.8mn steel.', *Scripta Metallurgica*, 1987, **27**, 1301–1306.

35. M. J. Santofimia, J. G. Speer, A. J. Clarke, L. Zhao, and J. Sietsma: 'Influence of interface mobility on the evolution of austenite–martensite grain assemblies during annealing', *Acta Materialia*, 2009, **57**, 4548-4557.

36. H. Y. Li, X. W. Lu, X. C. Wu, Y. A. Min, and X. J. Jin: 'Bainitic transformation during the two-step quenching and partitioning process in a medium carbon steel containing silicon', *Materials Science and engineering*, 2010, **527**, 6255-6259.

37. R. Petrov, L. Kestens, A. Wasilkowska, and Y. Houbaert: 'Microstructure and texture of a lightly deformed trip-assisted steel characterized by means of the ebsd technique', *Materials Science and engineering A*, 2007, **447**(1-2), 285-297.

38. W. J. Dan, Z. Q. Lin, S. H. Li, and W. G. Zhang: 'Study on the mixture strain hardening of multi-phase steels', *Materials Science and Engineering: A*, 2012, **552**(0), 1-8.

39. G. Thomas, J. G. Speer, D. Matlock, and J. Michael: 'Application of electron backscatter diifraction techniques to quenched and partitioned steels', *Microscopy and Microanalysis*, 2011, **17**, 368-373.

40. S. Kruijver, L. Zhao, J. Sietsma, S. E. Offerman, N. H. Van Dijk, L. Margulies, E. M. Lauridsen, S. Grigull, H. F. Poulsen, and S. Van der Zwaag: 'Fundamental materials science of the trip phenomenon', International conference of TRIP-aided high strength ferrous alloys, 2002, Mainz.

41. A. Itami, M. Takahshi, and K. Ushioda: 'Plastic stability of retained austenite in the cold-rolled 0.14%c-1.9%si-1.7%mn sheet steel', *ISIJ International*, 1995, **35**(9), 1121-1127.

42. E. Girault, A. Mertens, P. Jacques, Y. Houbaert, B. Verlinden, and J. Van Humbeeck: 'Comparison of the effects of silicon and aluminium on the tensile behaviour of multiphase trip-assisted steels', *Scripta Materialia*, 2001, **44**(6), 885-892.

43. A. Wasilkowska, R. Petrov, L. A. I. Kestens, E. A. Werner, C. Krempaszky, S. Traint, and A. Pichler: 'Microstructure and texture changes in a low-alloyed trip-aided steel induced by small plastic deformation', *ISIJ International*, 2006, **46**(2), 302-309.

44. X. C. Xiong, B. Chen, M. X. Huang, J. F. Wang, and L. Wang: 'The effect of morpholohy on the stability of retained austenite in a quenched and partitioned steel', *Scripta Materialia*, 2013, **68**(5), 321-324.

45. P. Hilkhuijsen, H. J. M. Geijselaers, T. C. Bor, E. S. Perdahcıoğlu, A. H. vd Boogaard, and R. Akkerman: 'Strain direction dependency of martensitic transformation in austenitic stainless steels: The effect of', *Materials Science and Engineering: A*, 2013, **573**(0), 100-105.

46. T. Y. Liu, P. Yang, L. Meng, and F. Y. Lu: 'Influence of austenitic orientation on martensitic transformations in a compressed high manganese steel', *Journal of Alloys and Compounds*, 2011, **509**(33), 8337-8344.

47. P. Hilkhuijsen: 'The influence of texture on phase transformation in metastable austenitic stainless steel', University of Twente, Enschede, The Netherlands, 2013.

48. A. Creuziger and T. Foecke: 'Transformation potential predictions for the stress-induced austenite to martensite transformation in steel', *Acta Materialia*, 2010, **58**(1), 85-91.

49. S. Kundu and H. K. D. H. Bhadeshia: *Scripta Materialia*, 2007, **57**, 869 - 872.

50. J. S. Bowles and J. K. Mackenzie: 'The crystallography of martensite transformations i', *Acta Metallurgica*, 1954, **2**(1), 129-137.

51. J. K. Mackenzie and J. S. Bowles: 'The crystallography of martensite transformations ii', *Acta Metallurgica*, 1954, **2**(1), 138-147.

52. H. K. D. H. Bhadeshia: 'Geometry of crystals', 2001, London, Institute of Materials.

53. B. P. J. Sandvik and C. M. Wayman: 'Characteristics of lath martensite: Part iii. Some theoretical considerations', *Metallurgical Transactions A*, 1983, **14**(4), 835-844.

54. J. F. Breedis and C. M. Wayman: *Trans. TMS-AIME*, 1962, **224**, 1128-1133.

55. P. M. Kelly: *Materials Transactions JIM*, 1992, **33**, 235-242.

56. G. Miyamoto, A. Shibata, T. Maki, and T. Furuhara: *Acta Materialia*, 2009, **57**, 1120-1131.

57. N. D. H. Ross and A. G. Crocker: *Acta Metallurgica*, 1970, **18**, 405-418.

58. S. Kundu, K. Hase, and H. K. D. H. Bhadesia: *Proceedings of Royal Society A*, 2007, **463**, 2309-2328.

59. A. Molinari, G. R. Canova, and S. Ahzi: 'A self consistent approach of the large deformation polycrystal viscoplasticity', *Acta Metallurgica*, 1987, **35**(12), 2983-2994.

60. G. I. Taylor: 'Plastic strain in metals', *Journal of the Institute of Metals*, 1938, **62**, 307-324.

61. J. F. W. Bishop and R. Hill: 'Xlvi. A theory of the plastic distortion of a polycrystalline aggregate under combined stresses', *Philosophical Magazine Series 7*, 1951, **42**(327), 414-427.

62. J. Gil Sevillano, P. van Houtte, and E. Aernoudt: 'Large strain work hardening and textures', *Progress in Materials Science*, 1980, **25**(2–4), 69-134.

63. P. Van Houtte: 'A comprehensive mathematical formulation of an extended taylor-bishop-hill model featureing relaxed constraints, the renouard-winterberger theory and a strain rate sensitivity model', *Textures and Microstructures*, 1988, **8-9**, 313-350.

64. U. F. Kocks and H. Chandra: 'Slip geometry in partially constrained deformation', *Acta Metallurgica*, 1982, **30**(3), 695-709.

65. H. Honneff and H. Mecking: 'A method fot the determination of the active slip systems and orientation changes during single crystal deformation ', The 5th conference on textured materials (ICOTOM), 1978, 265-275.

66. R. A. Lebensohn and C. N. Tomé: 'A self-consistent anisotropic approach for the simulation of plastic deformation and texture development of polycrystals: Application to zirconium alloys', *Acta Metallurgica et Materialia*, 1993, **41**(9), 2611-2624.

67. A. J. Clarke, J. G. Speer, M. K. Miller, R. E. Hackenberg, D. V. Edmonds, D. K. Matlock, F. C. Rizzo, K. D. Clarke, and E. D. Moor: 'Carbon partitioning to austenite from martensite or bainite during the quench and partition process: A critical assessment', *Acta Materialia*, 2008, **56**, 16-22.

68. A. J. Clarke, J. G. Speer, D. K. Matlock, F. C. Rizzo, D. V. Edmonds, and M. J. Santofimia: 'Influence of carbon partitioning kinetics on final austenite fraction during quenching and partitioning', *Scripta Materialia*, 2009, **61**, 149-152.

69. E. Jimenez-Melero, N. H. van Dijk, L. Zhao, J. Sietsma, S. E. Offerman, J. P. Wright, and S. van der Zwaag: 'The effect of aluminium and phosphorus on the stability of individual austenite grains in trip steels', *Acta Materialia*, 2009, **57**(2), 533-543.

70. J. Wang and S. Van Der Zwaag: 'Stabilization mechanisms of retained austenite in transformation-induced plasticity steel', *Metallurgical and Materials Transactions A*, 2001, **32**(6), 1527-1539.

71. E. Jimenez-Melero, N. H. van Dijk, L. Zhao, J. Sietsma, S. E. Offerman, J. P. Wright, and S. van der Zwaag: 'Martensitic transformation of individual grains in low-alloyed trip steels', *Scripta Materialia*, 2007, **56**(5), 421-424.

72. K. Sugimoto, N. Usui, S. Kobayashi, and S. Hashimoto: *ISIJ International*, 1992, **32**(12), 1311-1318.

73. J. Chiang, B. Lawrence, J. D. Boyd, and A. K. Pilkey: 'Effect of microstructure on retained austenite stability and work hardening of trip steels', *Materials Science and Engineering: A*, 2011, **528**(13–14), 4516-4521.

74. Timokhina I.B., Hodgons P.D., and P. E.V.: 'Effect of microstructure on the stability of retained austenite in transformation-induced-plasticity steels', *Metallurgical and Materials Transactions A*, 2004, **35**, 2331-2340.

75. D. De Knijf, R. Petrov, C. Föjer, and L. A. I. Kestens: 'Effect of fresh martensite on the stability of retained austenite in quenching & partitioning steel', *Materials Science and Engineering A*, 2014, **615**(0), 107-115.

76. X. Tan, Y. Xu, X. Yang, Z. Liu, and D. Wu: 'Effect of partitioning procedure on microstructure and mechanical properties of a hot-rolled directly quenched and partitioned steel', *Materials Science and Engineering: A*, 2014, **594**(0), 149-160.

77. D. De Knijf, E. Pinto Da Silva, C. Föjer, and R. Petrov: 'Study of heat treatment parameters and kinetics of quenching and partitioning cycles', *Materials Science and Technology*, 2015, **31**(7), 817-828.

78. C. Y. Wang, J. Shi, W. Q. Cao, and H. Dong: 'Characterization of microstructure obtained by quenching and partitioning process in low alloy martensitic steel', *Materials Science and Engineering: A*, 2010, **527**(15), 3442-3449.

79. K. S. Choi, Z. Zhu, X. Sun, E. De Moor, M. D. Taylor, J. G. Speer, and D. K. Matlock: 'Determination of carbon distributions in quenched and partitioned microstructures using nanoscale secondary ion mass spectroscopy', *Scripta Materialia*, (0).

80. I. de Diego-Calderón, D. De Knijf, M. A. Monclús, J. M. Molina-Aldareguia, I. Sabirov, C. Föjer, and R. H. Petrov: 'Global and local deformation behavior and mechanical properties of individual phases in a quenched and partitioned steel', *Materials Science and Engineering: A*, 2015, **630**(0), 27-35.

81. Z. J. Xie, Y. Q. Ren, W. H. Zhou, J. R. Yang, C. J. Shang, and R. D. K. Misra: 'Stability of retained austenite in multi-phase microstructure during austempering and its effect on the ductility of a low carbon steel', *Materials Science and Engineering: A*, 2014, **603**(0), 69-75.

82. P. J. Jacques, Q. Furnémont, F. Lani, T. Pardoen, and F. Delannay: 'Multiscale mechanics of trip-assisted multiphase steels: I. Characterization and mechanical testing', *Acta Materialia*, 2007, **55**(11), 3681-3693.

83. D. De Knijf, T. Nguyen-Minh, R. Petrov, L. A. I. Kestens, and J. J. Jonas: 'Orientation dependence of the martensite transformation in a quenched and partitioning steel subjected to uniaxial tension', *Journal of Applied Crystallography*, 2014, **47**, 1261-1266.

84. G. E. Dieter: 'Mechanical metallurgy', 1988, New York: McGraw-Hill.

85. L. Margulies, G. Winther, and H. F. Poulsen: 'In situ measurement of grain rotation during deformation of polycrystals', *Science*, 2001, **291**(5512), 2392-2394.

86. K. H. Kim and Y. M. Koo: 'In-situ x-ray diffraction study of single-slip-conditioned copper single crystals during uniaxial deformations', *Philosophical Magazine A*, 2001, **81**, 479-488.

87. C. Zhao, D. Tang, H.-T. Jiang, S.-S. Jhao, and H. Li: 'Process simulation and microstructure analysis of low carbon si-mn quenched and partitioned steel', *Journal of Iron and Steel Research, International*, 2008, **15**(4), 82-85.

88. N. Maheswari, S. Ghosh Chowdhury, K. C. Hari Kumar, and S. Sankaran: 'Inluence of alloying elements on the microstructure evolution and mechanical properties in quenched and partitioned steels', *Materials Science and Engineering A*, 2014, **600**, 12-20.

89. T. L. Anderson: 'Fracture mechanics: Fundamentals and applications, second edition', 1994, Taylor & Francis.

CHAPTER VI

PREDICTION OF THE STRESS-STRAIN CURVE BY A MIXTURE LAW

with special thanks to Irene de Diego-Calderón for conducting the nano-indentation and DIC tests

VI. PREDICTION OF THE STRESS-STRAIN CURVE BY A MIXTURE LAW

VI.1. Introduction

Owing to a strain distribution between the interacting soft and hard constituents, classic macro-models cannot adequately describe the stress-strain response of Q&P steels. However micro-models are hindered by the determination of microstructural parameters. The main purpose of this chapter is to predict the stress-strain curve based on the rule of mixture whereby the micro-strain of the individual phases was governed by the macro-strain of the material.

VI.2. Theory of the model

VI.2.1. Strain distribution

To describe the strain distribution in multi-phase steels, Tomota *et al.* [1] proposed a concentration factor $M_i = \varepsilon_{ti}/\varepsilon_t$, where ε_{ti} is the mean strain in the i^{th} phase and ε_t is the total strain of a multi-phase steel. Digital image correlation (DIC) and in-situ tensile testing inside a scanning electron microscope revealed the strain distributions within the ferrite and martensite phases and indicated that their individual strains were higher and lower, respectively, than the overall strain. Therefore, the strain of an individual phase should be governed by the overall strain of the material ε via:

$$\varepsilon_i = b_i \varepsilon \tag{1}$$

where b_i is the strain coefficient of the individual phase.

VI.2.2. Mixture law

The macro stress-strain relationship of a multi-phase steel is given by [2]:

$$\sigma = \sum H_i f_i \sigma_{\varepsilon_i} \tag{2}$$

where H_i, f_i, and σ_{ε_i} are the respective slip activation coefficient, volume fraction, and stress at the strain levels of the individual phases. The slip activation coefficient represents the contribution of slip to the plastic deformation of the i^{th} phase and is defined as [2]:

$$H_i = 1 - \exp(-C_i \varepsilon_i) \quad (3)$$

where C_i is a material parameter. Owing to the degrading contribution of slip for retained austenite by the TRIP-effect, H_A equals 1. The C_i parameter for martensite was set to 99.72 [2], which was determined experimentally for TRIP-steel.

Consequently, the stress-strain model of Q&P steels is described by the mixture law, i.e.:

$$\sigma = f_A \sigma_{\varepsilon_A} + H_{FM} f_{FM} \sigma_{\varepsilon_{FM}} + H_{TM} f_{TM} \sigma_{\varepsilon_{TM}} \quad (4)$$

where the subscripts A, FM, and TM refer to austenite, fresh martensite, and tempered martensite respectively.

VI.3. Experimental

Two Q&P heat-treated materials were selected for modelling the stress-strain curve. The first sample was quenched to 244 °C and partitioned at 400 °C for 250 s (referred to as sample B). The second sample was quenched to 224 °C and partitioned at 400 °C for 500 s (referred to as sample A). The samples have different fractions of retained austenite, fresh, and tempered martensite and may therefore exhibit differing mechanical response to the deformation.

The stress-strain curve is defined by the mixture law if the evolution of the phase fractions, individual strain distributions as a function of overall strain, and individual stress-strain curves are known. Therefore, X-ray diffraction experiments, in-situ EBSD during tensile testing, nano-indentation, and digital image correlation experiments were performed.

VI.4. Phase fractions

The phase fractions at all strain levels are required. This was done by first determining the fractions of each microstructural constituent in the starting material. The fraction of austenite at the quenching temperature and the final retained austenite after partitioning were determined from dilatation data and X-ray diffraction experiments, respectively. As such, the austenite fraction that transformed to untempered martensite during final quenching, owing to insufficient C-stabilisation, was determined by subtracting the latter from the former.

The final microstructure of sample A consisted of 20.6% retained austenite, 0% initial fresh martensite, and 79.4% tempered martensite. In Sample B on the other hand,

18.4% austenite was stabilized, with 10% fresh martensite in a 71.6% tempered martensite matrix. EBSD measurements can also reveal the different phases present and their respective fractions; however, it is well-established that part of the retained austenite (grains between the martensite laths) is unresolvable by this technique [3-5] and hence EBSD underestimates the retained austenite fraction.

In Chapter V.1, an equation describing the evolution of the austenite fraction was obtained by in-situ EBSD measurements:

$$f_A(\varepsilon) = f_{A_0}\exp(-T_{RA}\cdot\varepsilon) \quad (5)$$

where $f_{A_0}$is the starting austenite fraction and T_{RA} is the transformation potential. In Chapter V.2, XRD measurements were used instead of EBSD, and a similar (albeit higher) transformation rate was obtained. The RA fraction at fracture was measured inside the uniformly deformed area by XRD whereas the evolution obtained by EBSD took the continuous decrease of RA inside the necking region into account. Therefore, we can assume that the RA fraction decreased to values lower than those measured at fracture inside the necking region, as indicated by equation (5). A transformation potential of T_{RA} = 0.178 and T_{RA}= 0.445 was found for samples A and B, respectively.

The total fraction of the different phases is equal to, 1 at all strain levels, i.e.:

$$1 = f_A(\varepsilon) + f_{TM}(\varepsilon) + f_{NM}(\varepsilon) \quad (6)$$

In addition, the tempered martensite fraction is constant during tensile testing:

$$f_{TM}(\varepsilon) = f_{TM_0} \quad (7)$$

Correspondingly, the fraction of fresh martensite was obtained from:

$$f_{FM}(\varepsilon) = f_{FM_0} + f_{A_0}(1-\exp(-T_{RA}\cdot\varepsilon)) \quad (8)$$

VI.5. Stress-strain curves of individual phases

VI.5.1. Nano-indentation

EBSD measurements were combined with nano-indentation experiments to determine the difference in mechanical properties of the constituent phases. The orientation data were acquired with a step size of 40 nm and the profile of the Berkovich indenter used can be approximated by a radius of 268.2 nm.

Oliver and Pharr [6] introduced a method for measuring the hardness and elastic modulus by nano-indentation techniques. The basic principle of the method can be summarized as follows:

(i) Take the load-displacement data obtained during one cycle of loading and unloading, as shown for e.g. in Figure VI-1. Measure the maximum load, P_{max}, the maximum displacement, h_{max}, and the elastic unloading stiffness, *S*, defined as the slope of the upper portion of the unloading curve during the initial stages of unloading.

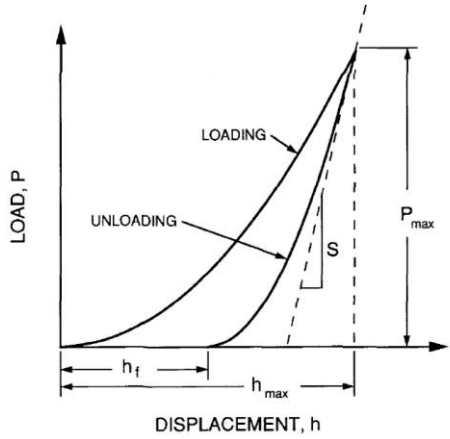

Figure VI-1: Example of load-displacement curve with P_{max}, h_{max}, and S indicated

(ii) Owing to pile-ups or sink-ins of the material around the indenter, determining the relationship between the indenter depth and the contact area is complicated. Assuming a pile-up at the contact periphery, the amount of sink-in is given by:

$$h_s = \varepsilon \frac{Pmax}{S} \tag{9}$$

where ε = 0.75 for a Berkovich indenter. The contact depth h_c is defined as the depth along which contact is made between the indenter and the specimen:

$$h_c = h_{max} - \varepsilon \frac{Pmax}{S} \tag{10}$$

(iii) The effective modulus, E_r, is given by:

$$E_r = \frac{\sqrt{\pi}}{2} \frac{S}{\sqrt{A}} \tag{11}$$

with $A = 24.5\ h_c^2$, which is the projected area for a Berkovich indenter.

The final elastic modulus of the steel, E, is then obtained from:

$$\frac{1}{E_r} = \frac{(1-\nu^2)}{E} + \frac{(1-\nu_i^2)}{E_i} \quad (12)$$

with $\nu_i = 0.07$ and $E_i = 1050$ GPa for a diamond indenter.

(iv) The hardness of the specimen H is estimated as:

$$H = \frac{Pmax}{A} \quad (13)$$

Figure VI-2 shows phase maps superimposed with on the image quality and the corresponding atomic force microscopy images with the locations of the indents.

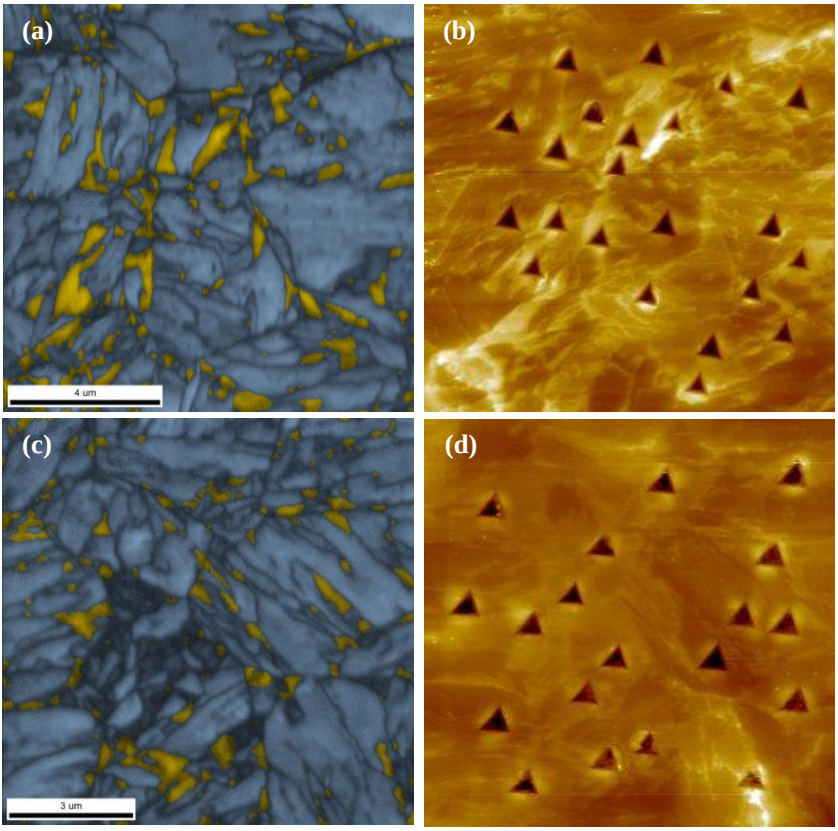

Figure VI-2: Phase map superimposed on the image quality of 0.25C1.5Si3Mn quenched to 244°C and partitioned at 400°C for (a) 1000s (c) 100s; (b) and (d) are the corresponding atomic force microscopy images with the indentation marks of (a) and (c) respectively

Figure VI-2 (a) and (b) shows the results of a Q&P steel heat-treated by quenching to 244 °C and partitioning at 400 °C for 1000 s. The austenite grains in this sample are large owing to long partitioning at a high temperature, which minimizes the effects of the surrounding phases and is therefore, conducive for conducting the nano-indentation

experiment. The other sample, whose micrographs are shown in Figure VI-2 (c) and (d), was heat-treated by quenching to 244 °C and partitioning at 400 °C for 100 s. This sample contains large fresh martensite blocks, as indicated by the low image quality areas. These large fresh martensite areas are required to obtain reliable hardness values.

Tempered martensite, retained austenite, and fresh martensite had average hardness values of 5.6 ± 0.4 GPa, 5.4 ± 0.5 GPa, and 8.4 ± 0.7 GPa, respectively. Hence we can conclude that the high-C fresh martensite is ~50% harder than the tempered martensite and retained austenite, which have similar hardness values.

Representative load-displacement curves of the three phases (Figure VI-3) reveal that the fresh martensite has a higher hardness and accommodates less plastic deformation than the tempered martensite and retained austenite. The pop-in in the curve of tempered martensite, at a load of 10 µN, is related to the generation or activation of pre-existing dislocations, which accommodate the plastic deformation [7-10]. Moreover, at an indentation depth of ± 80 nm, the pop-in the austenite curve at ± 1150 µN is related to its deformation-induced transformation to martensite [8, 10].

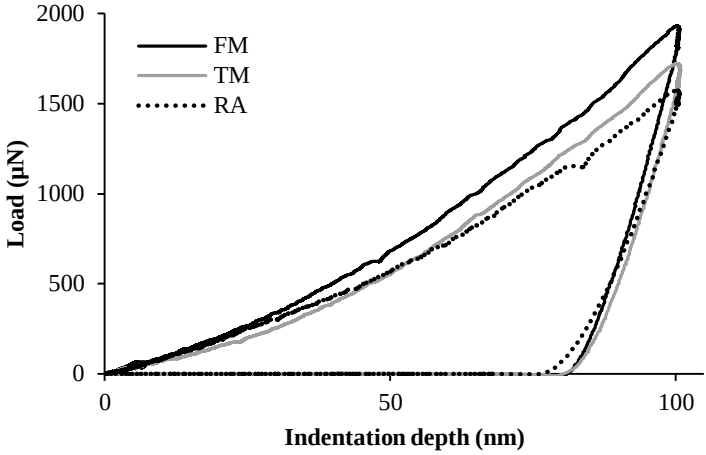

Figure VI-3: Load – displacement curves for fresh martensite (FM), tempered martensite (TM) and retained austenite (RA) in a Q&P steel

The stress-strain curves can be modelled from the indentation data, i.e. [11]:

$$\sigma = E.\varepsilon \quad \text{for} \quad \varepsilon < \varepsilon_y \tag{14}$$

$$\sigma = K\,(\varepsilon - \varepsilon_0)^n \quad \text{for} \quad \varepsilon > \varepsilon_y \tag{15}$$

with ε_y the yield point, n the strain hardening exponent, and E the elastic modulus. Assuming that the stress-strain curve and its first derivative are continuous, ε_0 and K can be obtained from:

$$\varepsilon_0 = (1 - n)\frac{\sigma_y}{E} \tag{16}$$

$$K = \sigma_y \left(n \frac{\sigma_y}{E}\right)^{-n} \tag{17}$$

The elastic modulus and E_r were determined by using equation (12) and (11), respectively; the actual indentation area, A_r, was measured by atomic force microscopy.

The n-value was also determined and the pile-up values of a rigid material, which does not deform elastically, were used [11].

Therefore, the pile-up of a rigid material, $c_{rig}\ (n)$, is given on one hand by:

$$c_{rig}\ (n) = \kappa\ (c - c_{el})\ \frac{W_{el}}{W_{pl}} + c \tag{18}$$

with $\kappa = 2$, $c_{el} = 2/\pi$, and W_{el} and W_{pl} the elastic and plastic work as calculated from the area underneath the force-displacement curve.

The pile-up coefficient, c, can be determined from:

$$c = \sqrt{\frac{A_r}{A_{max}}} \tag{19}$$

with A_r the real indentation area and A_{max} the area at the maximum indentation depth, h_{max}:

$$A(h) = 21.2141\ h^2 + 1593.2\ h - 499.63\ h^{1/2} \tag{20}$$

This equation is related to the Berkovich indenter equipment itself.

On the other hand, the pile-up of a rigid material can be written as a function of the n-value, i.e.:

$$c_{rig}\ (n) = 1.2725 - 1.277\ n + 1.6214\ n^2 - 1.0833\ n^3 \tag{21}$$

Hence by combining equations (18) and (21), the n-value can be solved for.

Finally to obtain the yield strength out of formula (17), another equation for the K-value is required:

$$K = \frac{2E}{1+n}\ \frac{W_{el}}{W_{pl}}\ {\varepsilon_p}^{1-n} \tag{22}$$

with ε_p = 0.028 [11], which is a fitting parameter that represents the effective plastic deformation of the Berkovich indenter; this K-value is determined by substituting the calculated elastic modulus, n-value, and the elastic and plastic work into the above equation.

Table VI-1 lists the average elastic moduli, yield strengths, and n-values of retained austenite, tempered martensite, and fresh martensite obtained from 24, 14, and 8 reliable nano-indentations, respectively. As the resulting stress-strain curves (Figure VI-4) show, the yield point and strength levels of fresh martensite are higher than those of tempered martensite and retained austenite. The modelled curves of the tempered martensite and retained austenite are similar and exhibit lower respective strain hardening exponents of 0.074 and 0.095 compared to that of the fresh martensite.

Table VI-1: E-modulus, yield strength, and n-values obtained from 24, 14, and 8 nano-indentations for retained austenite, tempered, and fresh martensite respectively

	RA	**TM**	**FM**
E (MPa)	158380	182520	186290
σ_y (MPa)	1348	1272	2183
n (-)	0.074	0.095	0.071

The modelled yield points are higher than those of the overall experimental stress-strain curves, where yielding starts at ~1000 MPa. The reliability of the nano-indents in the tempered martensite matrix is higher than in the retained austenite and fresh martensite where the influence of the surrounding phases plays a significant role. Therefore, the experimental stress-strain curves were used for modelling the overall curve.

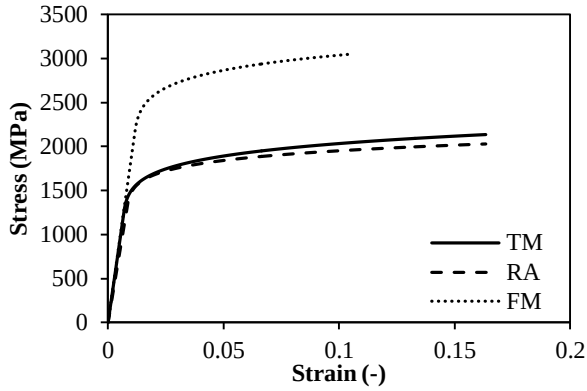

Figure VI-4: Modelled stress-strain curves from nano-indentation experiments for tempered martensite (TM),fresh martensite (FM), and retained austenite (RA)

VI.5.2. Experimental stress-strain curves

The stress-strain curves of untempered and tempered martensite were determined experimentally, as shown in Figure VI-5(a) and (b), respectively. The mechanical properties of fresh martensite were simulated by using samples, which were austenitized at 850 °C and quenched to room temperature to produce high-C untempered martensite; the resulting stress-strain curve indicates the brittle nature of this martensite, cfr. Figure VI-5 (a). To obtain the stress-strain curve of tempered martensite, an additional tempering heat treatment was conducted at 400 °C for 15 min, thereby enhancing the ductility as demonstrated in Figure VI-5 (b). For the austenitic phase, the stress-strain curve of a stainless steel grade was adopted from literature [12].

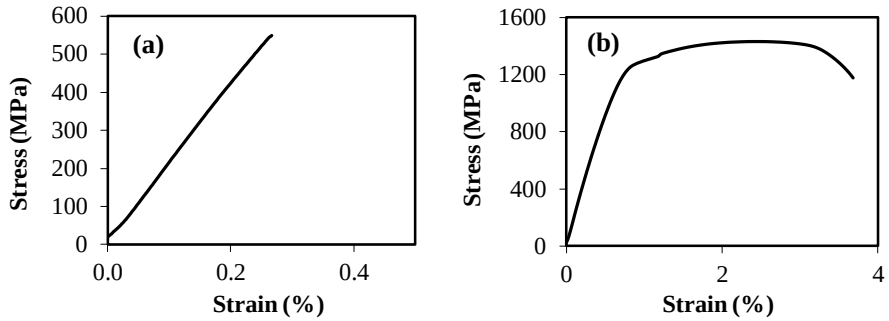

Figure VI-5: Stress-strain curve of (a) martensite formed after austenitisation without tempering reaction and (b) with additional tempering at 400°C for 15min

VI.6. 2D- finite element modelling (Abaqus)

Finite element modelling (FEM) is a discretization technique that is used in the field of structural mechanics. In the FEM, a structure is subdivided into non-overlapping spatial elements and the response of each element to a general input is expressed in terms of a finite number of degrees of freedom. These degrees of freedom are solved by differential equations, which minimize the differences at the nodal points. Hence, approximate solutions to boundary-value problems can be obtained. To determine the deformation behaviour of a structure, a strain increment is applied to all of the elements and the stresses are calculated based on the parameters of the material. If the stresses between two neighbouring elements differ significantly, then the values are recalculated until the mismatches are reduced.

The global deformation behaviour in a typical Q&P microstructure can be simulated via the FEM by assigning the individual stress-strain curves to the phases present. In this

work, the matrix was assumed to be homogenous tempered martensite without additional microstructural features as carbides or grain boundaries. Particles of austenite and fresh martensite were added to this matrix and rigid boundaries, which maintain their adhesion during tensile testing, were assumed; the grid was meshed automatically.

Figure VI-6 shows the stress and strain response upon 4.3% uniaxial deformation in the horizontal direction of a material without, Figure VI-6 (a)-(b), and with fresh martensite, Figure VI-6 (c)-(d). The tempered martensite in the sample without fresh martensite experiences relatively high stress levels (1312 MPa), with local stress localization (of up to 1414 MPa) between the austenite grains, which experienced the lowest stress levels (495 MPa). The strain is accommodated at an angle of 45° by the interconnecting retained austenite grains. However, this observation should be viewed with scepticism since substructures were not accounted for in the martensitic matrix. In reality, grain boundaries and original locally strained areas will also contribute to the accommodation of deformation, cfr. Figure VI-7. The model exhibits close correspondence to the experimental results only if one grain is considered at a time (cfr. Figure VI-7). The Kernel Average Misorientation (KAM) for the 5th neighbour revealed that the misorientation between two adjacent austenite grains, measured along the blue line, increased from 1.2° to 2.8° after the sample was deformed by 4.3%.

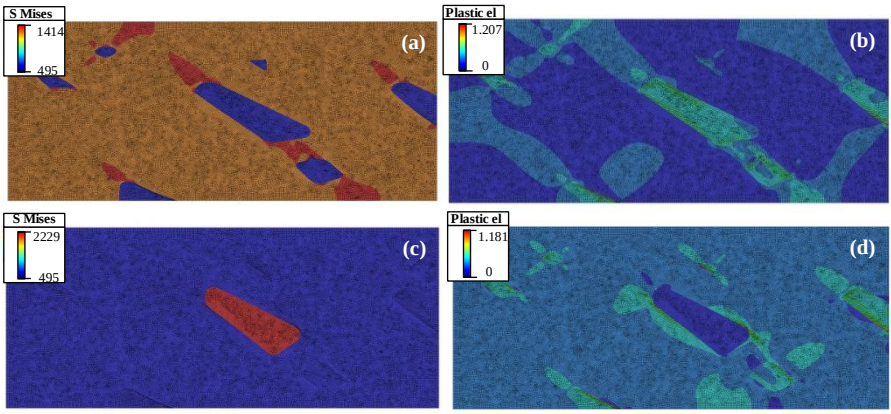

Figure VI-6: (a) Stress distribution (MPa) (b) plastic strain in a tempered martensite matrix with retained austenite grains (c) stress distribution (MPa) (d) plastic strain with a fresh martensite grain

The finite element simulation suggested that the tempered martensite deformed only 0.09% and exhibited local values of up to 0.27%, whereas the austenite deformed by ~0.65%. In this microstructure no rigid components were present and the austenite seemed to accommodate a significant part of the deformation with a small contribution of the tempered martensite.

If, on the other hand, fresh martensite is present (cfr. Figure VI-6(d)), then the tempered martensite is inhibited locally and, as a result, accommodates less deformation than in the case without untempered martensite. The fresh martensite did not deform plastically; this is expected since its stress-strain curve is consistent with that of brittle materials. In contrast, the stress in the fresh martensite block is very high (2229 MPa). Therefore, the stress concentration in the non-plastically deformed new martensite and the strain concentration around this new martensite grain results in the void formation observed in the microstructure after deformation. The overall deformation of austenite and tempered martensite was the same (i.e., 0.09% and 0.6%, respectively) as that of the microstructure without untempered martensite.

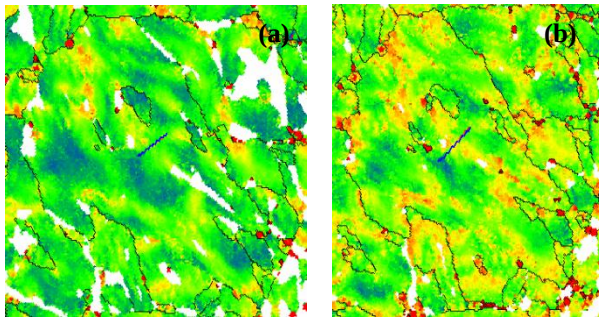

Figure VI-7: KAM 5th neighbour of (a) starting material with austenite in white (b) after 4.3% elongation showing that the misorientation between RA grains increases in one tempered martensite grain

After obtaining the aforementioned preliminary modelling results, a realistic microstructure was implemented in the finite element model, as shown schematically in Figure VI-8.

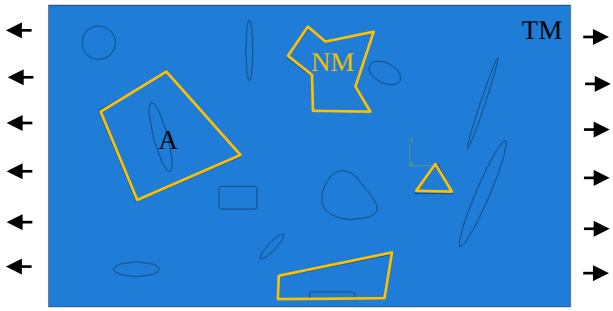

Figure VI-8: Schematic overview of the input for finite element modelling with a tempered martensite matrix, the black grains represent austenite grains with different morphologies; the yellow blocks denote the fresh martensite with morphologies, which are representative of the experimentally observed microstructures

Austenite grains with different sizes and shapes, representing blocky and lath-type morphologies were implemented. The untempered martensite grains were taken as blocks with and without retained austenite grains inside.

Figure VI-9 (a)-(b) and (c)-(d) show the stress-strain results of the simulation without and with fresh martensite, respectively. A total of 1% elongation was applied in the horizontal direction.

In the simulations without fresh martensite, the austenite grains experienced stress intensities ranging from 208-470 MPa. The tempered martensite on the other hand reached stress levels of 650-1268 MPa with the highest values occurring in the areas interconnecting the retained austenite grains. The austenite grains accommodated most of the deformation whereby the grain with its longest axis perpendicular to the tensile axis experienced the highest (2.1%) deformation levels. Hence, this morphology is most susceptible to martensitic transformation, as is expected from the influence of the austenite grain shape on its stability [3]. Austenite grains with their largest axis parallel to the loading direction experience the second highest level (0.5-1.25%) of deformation. Lath-type austenite grains oriented at angles of 30-70° with respect to the loading direction accommodated 0.17-0.83% strain, and were relatively stable under this uniaxial straining condition. Round austenite grains were most stable and were therefore, strained only 0.42- 0.83%.

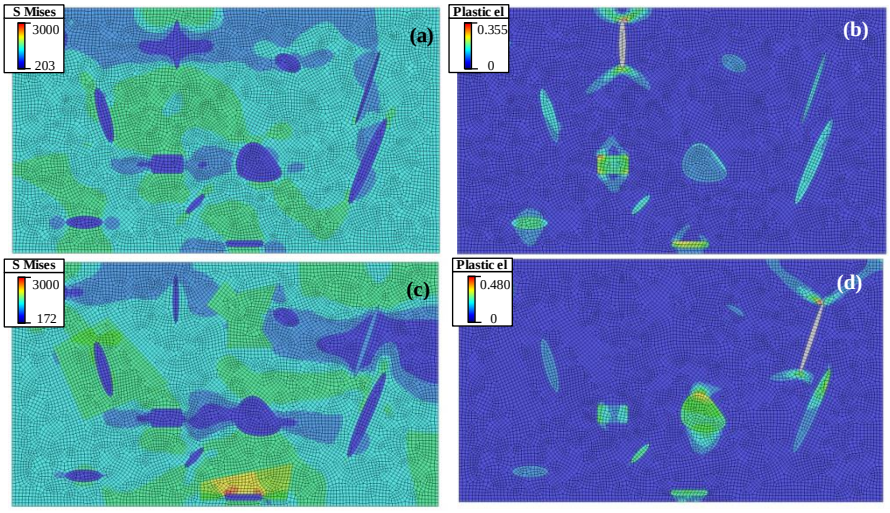

Figure VI-9: (a) Stress distribution (b) plastic elongation without fresh martensite (c) stress distribution (d) plastic elongation with fresh martensite for a simulation of 1% strain (tensile direction is horizontal)

Since the uniaxial tensile deformation is accommodated mainly via shear, which is not taken into account in this simulation, the order of the morphology-dependent transformation differs from that of the experiments. The maximum component of the pure uniaxial stress acts on grains, which have the largest surface perpendicular to the tensile axis. As a result, round-shaped grains are more stable than lath-shaped grains, and are hence, more strained as the surface perpendicular to the tensile direction increases.

The retained austenite grains experienced similar stress levels when the fresh martensite was added to the simulated microstructure. However, the local stress levels in the tempered martensite were higher compared to the case without fresh martensite. The fresh martensite acted as a stress-concentrating constituent resulting in stress levels of 1588-3000 MPa. The most important difference was revealed for the plastic elongation accommodated in the austenite grains; i.e. the order of transformation stability exhibited no morphological dependence. However, the fresh martensite changed the strain distribution substantially by shielding some of the austenite grains, which would deform at low strains based on their shape, while others were more heavily strained than expected, based on their morphology.

The simulation results confirmed, in general, the experimental trends described in Chapter V: fresh martensite altered the strain distribution resulting in more unstable austenite owing to locally higher strain levels (than the overall strain), stemming from the constraining effect of the fresh martensite blocks on deformation. The untempered martensite blocks experienced high stress levels and changed the stress distribution in the matrix. In the presence of fresh martensite, the stability of austenite was determined by the strain alteration rather than by the parameters, which influenced the stability of the individual austenite grains.

VI.7. Strain division with digital image correlation

The microscopic strain distribution of grains can be measured by digital image correlation (DIC) based on scanning electron microscope topography [13, 14]. DIC is an image analysis method, based on grey value digital images, that measures load-induced shifts in the datasets. Therefore, DIC can be used to measure, for e.g. internal, local strains.

A Q&P sample was etched with 2% Nital and then subjected to tensile testing in a SEM chamber. The displacement of the characteristic features, as indicated by the grey values of the pixels, was correlated with each deformation stage by using Vic-2D 2009 Digital Image Correlation software. Figure VI-10 (a) shows the starting microstructure in which fresh martensite (FM), tempered martensite (TM), and retained austenite (RA) are identified.

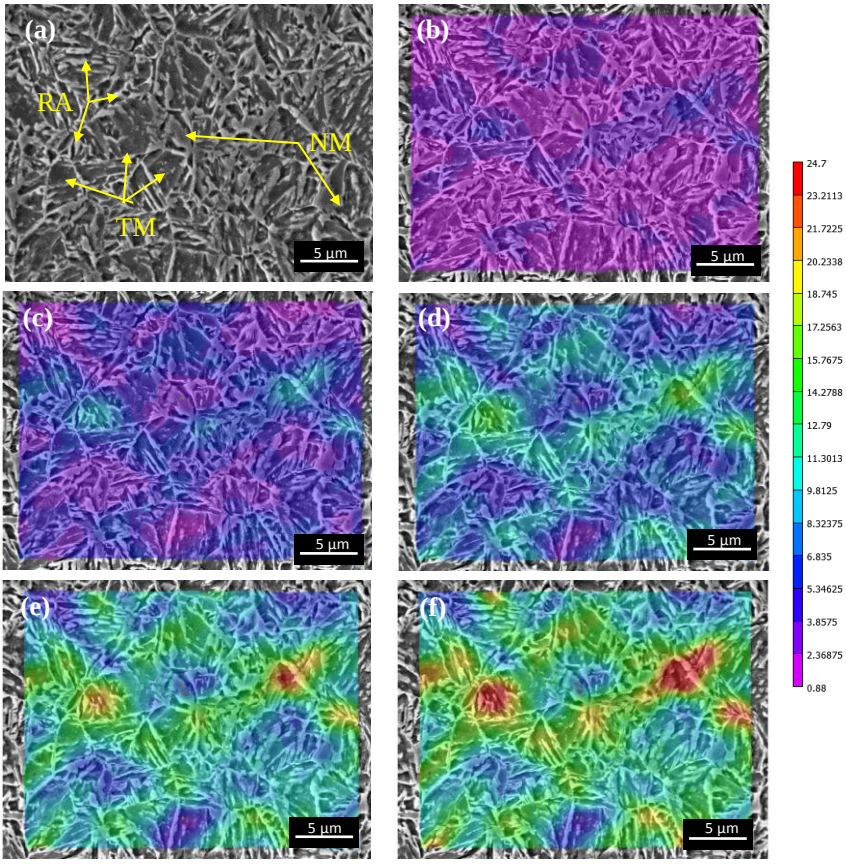

Figure VI-10: Sample B (a) Starting SEM image showing retained austenite (RA), tempered martensite (TM), and fresh martensite (FM); SEM image superimposed with strain distribution along the tensile direction after (b) 2.5% (c) 5% (d) 7.9% (e) 10.5% (f) 13% total elongation

The vertical axis corresponds to the loading direction during *in situ* tensile testing. The displacement, e_{yy}, for 2.5%, 5%, 7.9%, 10.5%, and 13% total elongation along the tensile direction is monitored, as shown by the colour map superimposed on the SEM images in Figure VI-10 (b-f). A network-like structure of interconnected bands of localized plastic flow, oriented at 45-60º with respect to the loading axis, is clearly observed, and a significant fraction of modestly deformed areas also persist. The local plastic strain is also strongly partitioned among the different phases. This network-like plastic deformation was also observed in the finite element modelling of a tempered martensite matrix without grain boundaries or defects and is similar to those previously reported for Q&P intercritically annealed steels [15], dual phase (DP) steels [16, 17], and metal matrix composites (MMCs) [18]. As the KAM-map in Figure VI-7 shows, the interconnection of the strain along the retained

austenite grains in a single tempered martensite grain, oriented 45° with respect to the tensile axis, occurred for macro-deformation of the entire microstructure as well.

The local strain values of the different constituents were determined by correlating the phases with the e_{yy} values of the same pixels after 13% elongation. The TM, FM, and RA have area-weighted average e_{yy} deformation values of 0.253, 0.152, and 0.306, respectively. These respective values are 1.05, 0.63 and 1.27 times the average value (0.24) of the entire image. As such, the relationship between the local deformation and global strain of the different phases can be expressed as:

$$\varepsilon_A = 1.3\,\varepsilon$$

$$\varepsilon_{FM} = 0.6\,\varepsilon$$

$$\varepsilon_{TM} = \varepsilon$$

According to digital image correlation, fresh martensite accommodates 0.6 times the overall strain. Nevertheless, its stress-strain curve exhibited fracture in the elastic regime, which suggests that fresh martensite blocks do not deform plastically. Moreover, SEM images in Chapter V.4 showed that tempered martensite deformed and voids formed between the fresh martensite blocks, which remained as rigid constituents in the microstructure of sample B. The DIC-experiments were performed at the surface of the specimen, hence the presence of a free surface provided an additional degree of freedom to the martensite blocks for the accommodation of the deformation [4]. This parameter was, therefore, fitted in the model of the stress-strain curve.

VI.8. Modelled stress-strain curve

As a first attempt, the strain accommodated in the fresh martensite was set at $\varepsilon_{FM} = 0.6\,\varepsilon$. The prediction of the stress-strain curve is denoted by the red line in Figure VI-11 (a). The figure shows that the modelled curve overestimates the stress-strain values. By fitting the curve to the experiment, a strain distribution parameter of 0.15, $\varepsilon_{FM} = 0.15\,\varepsilon$, was calculated. This concurs with the observation that these components experience only low strain; for e.g. a total elongation of 15%, results in an only 3% individual strain of fresh martensite, which behaves, in this case, as a rigid component. Figure VI-11 (b) shows the contribution of fresh martensite to the modelled stress-strain curve. The red curve simulates the curve of austenite combined with tempered martensite whereas the blue curve takes into account the presence of fresh martensite and its formation via TRIP-assisted deformation.

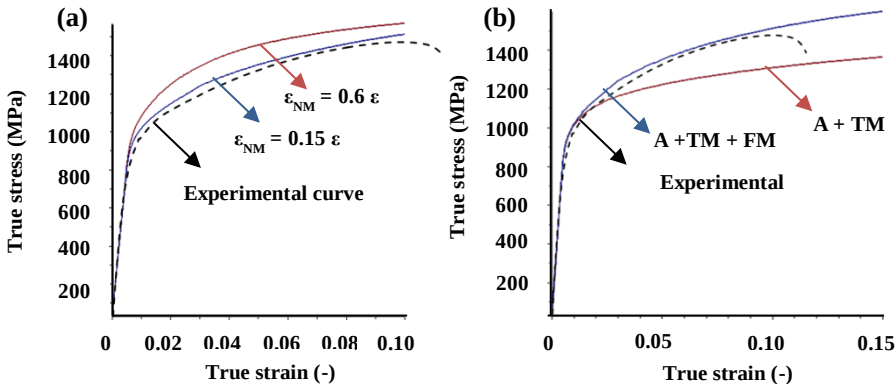

Figure VI-11: Stress-strain curves for sample B modelled with (a) a strain distribution in the fresh martensite such that red: ε_{FM} =0.6 ε - blue: ε_{FM} =0.15 ε and the experimental curve is denoted by the black dashed line (b) the contribution of fresh martensite (blue) separated from tempered martensite and retained austenite (red)

The model was evaluated by modelling the stress-strain curve of sample A (cfr. Figure VI-12); recall, the initial microstructure of this sample did not contain fresh martensite. As the figure shows, when an individual strain of $\varepsilon_{FM} = 0.15\,\varepsilon$ was imposed on the fresh martensite, the predicted strain hardening was larger than that observed experimentally.

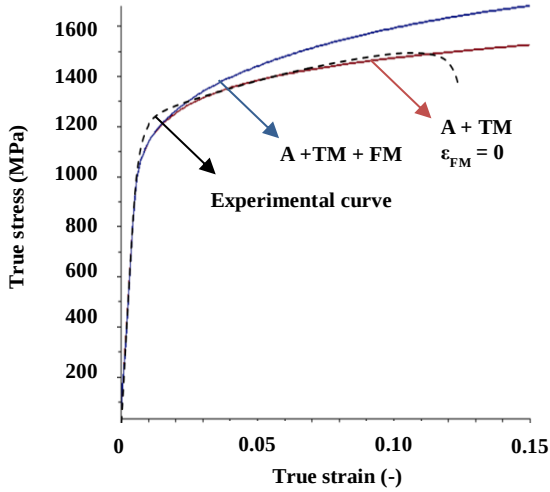

Figure VI-12: Modelled stress-strain curve of sample A showing the contributions of the fresh martensite (blue) and the tempered martensite and austenite (red); the black dotted line represents the experimental stress-strain curve

However, the modelled curve of unstrained fresh martensite ($\varepsilon_{FM} = 0$) exhibits close correspondence to the experimentally measured curve. The difference between the samples can be explained as follows: in the model, fresh martensite always experiences the

same individual strain irrespective of whether it was present in the starting material or formed by the TRIP-effect. In reality however, the untempered martensite grains formed during straining will initially be strain-free owing to the low levels of internal strain present immediately after its transformation.

If fresh martensite is initially absent, then the transformed austenite-to-martensite grains do not accommodate strain. However, if fresh martensite is present in the starting microstructure, its contribution (both from the starting and transformed fraction) is required in order to accurately predict the experimentally observed strain hardening, cfr. Figure VI-13; this contribution can be incorporated via a variable ε_{FM} .

The simple model employed here neglects void formation.

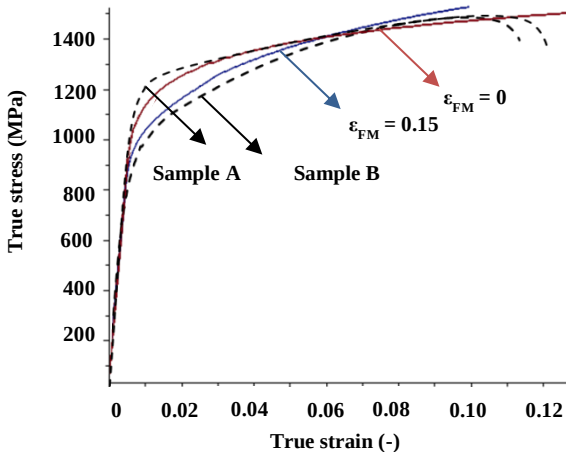

Figure VI-13: Modelled versus experimental stress-strain curves of sample A (modelled with $\varepsilon_{FM}=0$) and sample B (modelled with $\varepsilon_{FM}=0.15$)

VI.8.1. Prediction of elongation

The onset of necking was calculated as the intersection point of the modelled instantaneous n-value with the modelled stress-strain curve [2], cfr. Table VI-2.

If the fraction of retained austenite is increased in 5% steps from 5% to 20% without initial fresh martensite, then the necking is postponed to high elongations. However, the same results are obtained if the initial fresh martensite fraction is increased from a constant starting retained austenite fraction of 15%. This reflects the limitations of the model, as it relates to

the straining of fresh martensite formed as a result of the TRIP effect. Therefore, this method cannot predict the onset of necking.

Table VI-2: Values at the onset of necking as predicted from the intersection of the stress-strain curve with the n-value

0% FM		**15% RA**	
5% RA	0.1123	**5% FM**	0.1276
10 % RA	0.1190	**10% FM**	0.1315
15 % RA	0.1252	**15% FM**	0.1358
20 % RA	0.1311	**20% FM**	0.1400

The influence of the phase fractions on the elongation can also be predicted by taking the TRIP-phenomenon into account. The material strain hardens when austenite transforms to martensite, thereby suppressing strain localisation and enhancing formability. However, after strain localisation, the remaining austenite grains, which were too stable to transform under uniform strain levels, experienced high deformation levels thereby resulting in a continuous decrease of the retained austenite fraction to 0.5%. The corresponding experimental observations were described in Chapter V; i.e., in-situ tensile experiments were described in which the samples broke when the local austenite fraction reached a value of 0.5%, cfr. Figure VI-14.

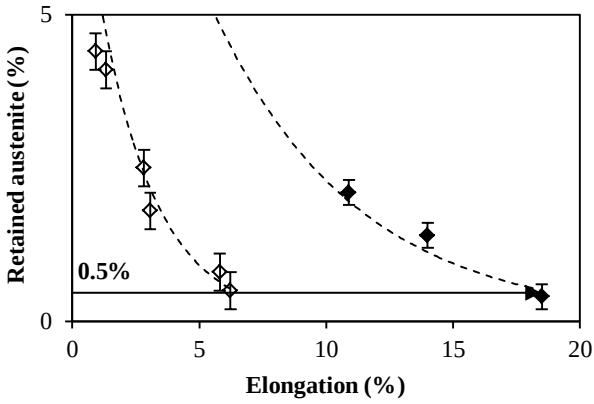

Figure VI-14: Retained austenite fraction (%) as a function of the elongation of samples A (open symbols) and B (closed symbols), as described in Chapter V.

Assuming that the samples fracture when most of the retained austenite transformed to martensite leaving only a low fraction (for e.g. 0.5%) of small austenite grains, then the elongation at fracture is defined as:

$$\varepsilon_{fr} = -\frac{\ln(\frac{0.005}{f_{A_0}})}{280\, f_{FM_0} + 16.5} \tag{23}$$

where f_{A_0} and f_{FM_0} are the fractions of initial austenite and fresh martensite, respectively.

The elongation at fracture is plotted as a function of the initial austenite and fresh martensite fraction in Figure VI-15. As Figure VI-15 (a) shows, the ductility increases exponentially with increasing fractions of starting retained austenite. Therefore, increasing the fraction of initial retained austenite by up to 10-20% should result in a significant enhancement of the ductility. This contribution decreases thereafter, as indicated by the first derivative in Figure VI-15 (c). The total elongation decreases substantially, cfr. Figure VI-15 (b-d), with increasing amounts of initial fresh martensite. As such, minimizing the fraction of starting fresh martensite and optimizing the amount of initial retained austenite results in the highest elongation.

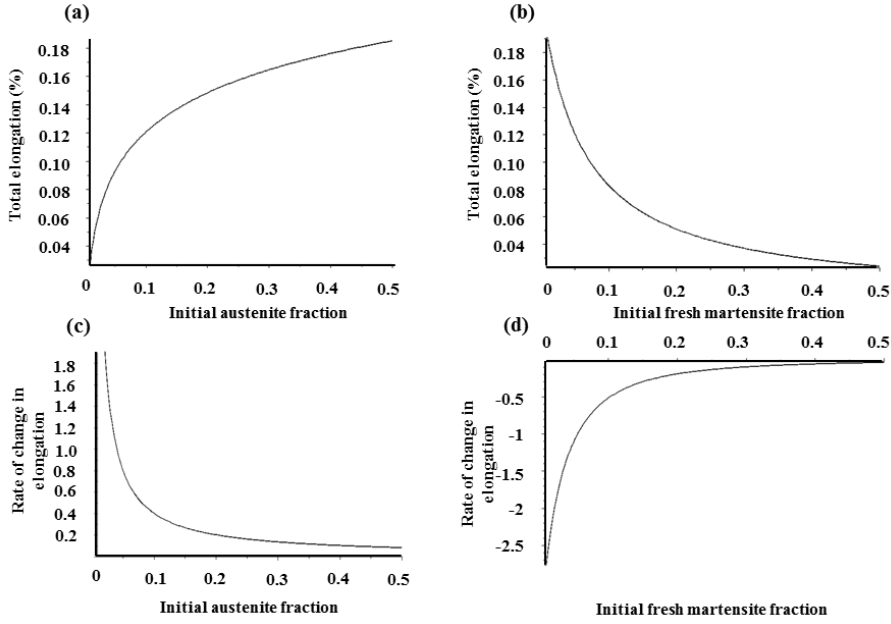

Figure VI-15: Elongation versus (a) initial austenite fraction with 3% initial fresh martensite (b) initial fresh martensite fraction with 20% initial austenite and the (c)-(d) first derivatives of (a) and (b) respectively

VI.9. Conclusions

Owing to the strain distribution between the interacting constituents, classic macro-models cannot describe the stress-strain response of Q&P steels. Therefore, a simple rule of mixture of the micro-strains of the different phases was used; these micro-strains were proportional to the overall strain.

The phase fractions were determined experimentally and the evolution of the retained austenite fraction with overall strain was described by an exponential relationship wherein the transformation stability was related to the initial fresh martensite fraction.

The mechanical characteristics of the individual constituents were determined by nano-indentation. However for the simulation, experimental stress-strain curves of large-scale specimens of tempered and untempered martensite were employed.

The relationship between the local and global strain for the different phases was obtained with DIC. This result revealed that retained austenite and tempered martensite accommodated strains that were 1.3 times and equal to the overall strain, respectively. The strain distribution coefficient of fresh martensite was fitted by the model. However, one weakness of the model is that regardless of its origin, the fresh martensite is always strained by the same amount, which is related to the overall strain. Therefore, there is limited correspondence between the model and experiments and hence the model must be modified to account for strain variations in fresh martensite.

A new relation was proposed for determining the total elongation and the material fractured when the retained austenite fraction decreased to a low, fixed value of for e.g. 0.5%. The evolution of the total elongation with fractions of retained austenite and fresh martensite was examined. The ductility increased with increasing fraction of retained austenite; however, the enhancement of the ductility became less pronounced with further increases in the austenite fraction. This calculation suggested that increasing the austenite fraction by more than ~20% would not improve the ductility significantly. In contrast, increasing the amount of fresh martensite, even very slightly, resulted in substantial deterioration of the ductility, although the effect is less pronounced in experimental observations than in the model. Therefore, the formation of fresh martensite must be suppressed, in order to make a Q&P steel with a combination of high strength and ductility.

References

1. Y. Tomota, M. Umemoto, N. Komatsubara, A. Hiramatsu, N. Nakajima, A. Moriya, T. Watanabe, S. Nanba, G. Anan, K. Kunishige, Y. Higo, and M. Miyahara: 'Prediction of mechanical properties of multi-phase steels based on stress-strain curves', *ISIJ International*, 1992, **32**(3), 343-349.
2. W. J. Dan, Z. Q. Lin, S. H. Li, and W. G. Zhang: 'Study on the mixture strain hardening of multi-phase steels', *Materials Science and Engineering: A*, 2012, **552**(0), 1-8.
3. X. C. Xiong, B. Chen, M. X. Huang, J. F. Wang, and L. Wang: 'The effect of morpholohy on the stability of retained austenite in a quenched and partitioned steel', *Scripta Materialia*, 2013, **68**(5), 321-324.
4. G. K. Tirumalasetty, M. A. Van Huis, C. Kwakernaak, J. Sietsma, W. G. Sloof, and H. W. Zandbergen: 'Deformation-induced austenite grain rotation and transformation in trip-assisted steel', *Acta Materialia*, 2012, **60**, 1311-1321.
5. C. Y. Wang, J. Shi, W. Q. Cao, and H. Dong: 'Characterization of microstructure obtained by quenching and partitioning process in low alloy martensitic steel', *Materials Science and engineering*, 2010, **527**, 3442-3449.
6. W. C. Oliver and G. M. Pharr: 'An improved technique for determining hardness and elastic modulus using load and displacement sensing indentation experiments', *Journal of Materials Research*, 1992, **7**(06), 1564-1583.
7. P. S. Phani, K. E. Johanns, E. P. George, and G. M. Pharr: 'A stochastic model for the size dependence of spherical indentation pop-in', *Journal of Materials Research*, 2013, **28**(19), 2728-2739.
8. R. D. K. Misra, P. Venkatsurya, K. M. Wu, and L. P. Karjalainen: 'Ultrahigh strength martensite–austenite dual-phase steels with ultrafine structure: The response to indentation experiments', *Materials Science and Engineering: A*, 2013, **560**(0), 693-699.
9. B. B. He, M. X. Huang, Z. Y. Liang, A. H. W. Ngan, H. W. Luo, J. Shi, W. Q. Cao, and H. Dong: 'Nanoindentation investigation on the mechanical stability of individual austenite grains in a medium-mn transformation-induced plasticity steel', *Scripta Materialia*, 2013, **69**(3), 215-218.
10. T. H. Ahn, C. S. Oh, D. H. Kim, K. H. Oh, H. Bei, E. P. George, and H. N. Han: 'Investigation of strain-induced martensitic transformation in metastable austenite using nanoindentation', *Scripta Materialia*, 2010, **63**(5), 540-543.
11. J. Alkorta: 'Materiales nanocristalinos producidos por spd y su caracterización mediante nuevos métodos de nanoindentación', University of Navarra, 2005.
12. M. F. Hassanein: 'Imperfection analysis of austenitic stainless steel plate girders failing by shear', *Engineering Structures*, 2010, **32**(3), 704-713.
13. J. Kang, Y. Ososkov, D. Embury, and D. S. Wilkinson: 'Digital image correlation studies for microscopic strain distribution and damage in dual phase steels', *Scripta Materialia*, 2007, **56**, 999-1002.
14. H. Ghadbeigi, C. Pinna, S. Celotto, and J. R. Yates: 'Local plastic strain evolution in a high strength dual-phase steel', *Materials Science and engineering A*, 2010, **527**, 5026-5032.
15. I. de Diego-Calderón, M. J. Santofimia, J. M. Molina-Aldareguia, M. A. Monclús, and I. Sabirov: 'Deformation behavior of a high strength multiphase steel at macro- and micro-scales', *Materials Science and Engineering: A*, 2014, **611**(0), 201-211.
16. M. Kapp, T. Hebesberger, and O. Kolednik: 'A micro-level strain analysis of a high-strength dual-phase steel', *International Journal of Materials Research*, 2011, **102**(6), 687-691.

17. Q. Han, Y. Kang, P. D. Hodgson, and N. Stanford: 'Quantitative measurement of strain partitioning and slip systems in a dual-phase steel', *Scripta Materialia*, 2013, **69**(1), 13-16.

18. O. Kolednik and K. Unterweger: 'The ductility of metal matrix composites - relation to local deformation behavior and damage evolution', *Engineering Fracture Mechanics*, 2008, **75**(12), 3663-3676.

CHAPTER VII

THE INFLUENCE OF ULTRA-FAST ANNEALING PRIOR TO QUENCHING AND PARTITIONING ON THE MICROSTRUCTURE AND MECHANICAL PROPERTIES

D. De Knijf, A. Puype, C. Föjer, and R. Petrov: 'The influence of ultra-fast annealing prior to Quenching and Partitioning on the microstructure and mechanical properties', ***Materials Science and Engineering A*** **627, 2015, 182-190.**

VII. THE INFLUENCE OF ULTRA-FAST ANNEALING PRIOR TO QUENCHING AND PARTITIONING ON THE MICROSTRUCTURE AND MECHANICAL PROPERTIES

VII.1. Abstract

The microstructural evolution of a Quenching and Partitioning (Q&P) steel after ultra-fast annealing (UFA) was studied and correlated with the obtained mechanical properties. The shift of the transformation temperatures with increasing heating rates was shown by dilatometric experiments. The influence of the heating rate on the carbide precipitation and texture was evaluated. A remarkable refinement of the prior austenite grain size is observed resulting in a better combination of strength, ductility and fracture behaviour compared to conventionally used heating rates.

VII.2. Introduction

The classical development of advanced high strength steels (AHSS) is usually based on special combinations of alloying elements or on controlling the cooling rate. Nowadays non-conventional, novel process techniques have been developed to refine the microstructure and to improve both strength and toughness. Recent publications [1, 2] suggested that rapid transformation annealing cycles applied to cold rolled AHSS can result in substantial grain refinement. The degree of refinement is influenced by the interaction between recrystallization and ferrite-to-austenite phase transformation [1]. Recrystallization in cold rolled AHSS is delayed to higher temperatures with increasing heating rate and possibly even to temperatures above $A_{c1.}$ Hence α-γ phase transformation starts in a non-recrystallized matrix with a large number of nuclei which results in remarkable grain refinement [1, 3]. Carbon and alloying elements play an important role in controlling the grain size in conditions of fast and ultrafast heating. The effect of grain refinement is clearly pronounced in C-Mn steels whereas for interstitial-free and low carbon steel, the grain structure and recrystallization texture were not significantly altered by applying higher heating rates or shorter soaking times [4-7].

It was reported that at heating rates as high as 3000°C/s, the phase transformation is primarily located in the subgrain boundaries of the recovered matrix [8, 9]. During recovery, the dislocations in the cold deformed matrix are re-arranged in subgrain boundaries forming cells (polygons) with dislocation walls. These dislocation cells play an important role as carbon

diffusion channels in the transformation process. Faster carbon diffusion in the cell walls leads to local increase of the C-concentration and formation of fine carbides which pin the dislocations, suppress their movement and therefore inhibit growth of the recrystallized grains. Hence according to [8, 9], a very important parameter for grain refinement during ultra-fast annealing is the distribution and size of the iron carbides in ferrite. A homogeneous distribution of small carbides impedes the coarsening of recrystallized ferrite grains as well as a homogeneous nucleation and growth of very small austenite grains. If the carbides are coarse or in the "carbide free" zones of not uniformly distributed carbides, the growth of the recrystallized ferrite grains during annealing is not inhibited. Moreover, non-uniformly distributed zones of fine austenite grains can develop where the initial carbides were present.

The aim of the present work is to bring insight into the possibilities of refining the microstructure of Q&P steels prior to the partitioning stage of the Q&P heat treatment and the corresponding influence on the final mechanical properties.

VII.3. Experimental

Hot and cold rolled steel with a nominal composition of 0.25C-1.5Si-3Mn (wt.%) was studied in this work.

VII.3.1. Heat treatments

To determine the variation of the transformation temperatures as a function of heating rate, experiments were carried out in a Bähr DIL 805 A/D dilatometer on hot rolled rectangular samples with dimensions of 2.5 x 3.5 x 10 mm, with the longest axis parallel to the plate rolling direction. The samples were heated with different heating rates of 10 °C/s, 150 °C/s, 500 °C/s, and 1000 °C/s up to 1000 °C which is in the austenitic region and cooled at 20 °C/s to room temperature.

Strips of 80% cold-rolled sheets (100 x 10 x 0.5 mm) were cut parallel to the rolling direction and subsequently subjected to ultra-fast heating Q&P cycles in the Gleeble™ thermo-mechanical simulator (cfr. Figure VII-1). The cold rolled strips were reheated to 850°C without isothermal holding at three different heating rates of 10°C/s, 500°C/s and 1000°C/s. An additional heat treatment was performed with a heating rate of 10°C/s to 850°C at which the sample was kept isothermally for 5min to simulate a conventional Q&P cycle. Subsequently, the samples were cooled at 20°C/s to 270 ± 10°C. The used quench rate of 20°C/s was higher than the critical cooling rate to avoid ferrite, pearlite or bainite formation

during cooling, which for this steel composition was determined to be 10°C/s. Afterwards the samples were reheated at 10 °C/s to 400 °C for 50s to complete the partitioning step and finally cooled with N_2-gas to room temperature.

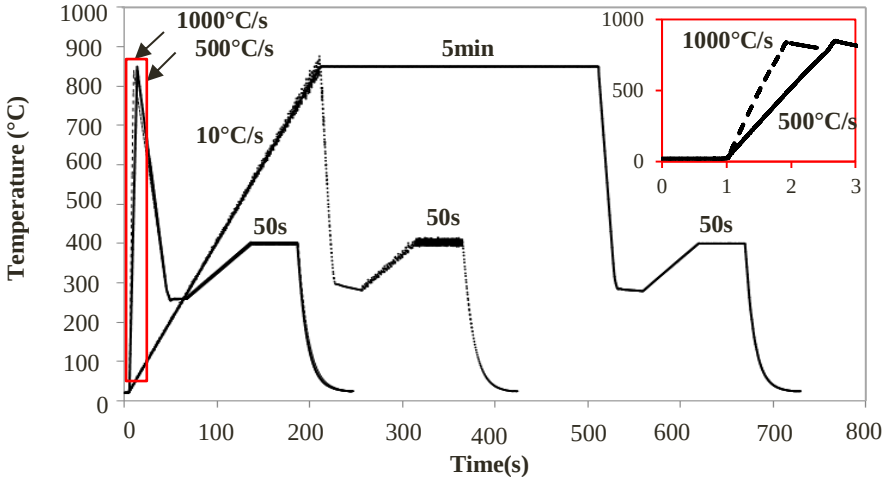

Figure VII-1: Heat treatment cycles performed in Gleeble on the cold rolled material, upper right corner insert is a zoom of the first 3s of heating time

VII.3.2. Microstructural characterization

For microstructural characterization, the samples were mechanically ground and polished following the classical preparation route.

SEM images and EBSD maps were obtained by a FEI Quanta™ 450-FEG-SEM equipped with a Hikari EBSD detector controlled by the EDAX-TSL OIM-Data Collection software. The EBSD data were acquired on a hexagonal scan grid using an accelerating voltage of 20 kV, a working distance of 16 mm, tilt angle of 70° and a step size of 60 nm. The orientation data were post-processed with TSL-OIM Analysis 6.2® software and only the points with a confidence index higher than 0.1 were considered in the scan. Average grain sizes were determined on the base of a grain definition of minimum 4 pixels per grain and a misorientation angle of 15°.

The austenite volume fractions were determined at room temperature with XRD experiments performed on a Siemens Kristalloflex D5000 diffractometer equipped with Mo-K_α source operating at 40 kV and 40 mA. A 2θ-range of 25° to 45° was scanned using a step size of 0.01°, dwell-time of 2 s and rotation speed of 15 rpm. The data were post-processed by subtracting the background radiation and $K\alpha_2$ influence. The retained austenite volume

fractions were determined with the formula of Cullity [10] using the intensity of the $(220)_\alpha$, $(311)_\alpha$, $(200)_\gamma$ and $(211)_\gamma$ reflections.

VII.3.3. Mechanical testing

Tensile tests were performed at room temperature on A25 tensile test samples (ASTM E8/E8M) on a MTS819 tensile test machine at two strain rates - 0.083 mm/s until an elongation of 2.5 mm followed by a strain rate of 0.208 mm/s until fracture.

VII.4. Results

VII.4.1. Dilatometer experiments on hot rolled material

VII.4.1.1 Shift of the transformation temperatures

Samples of the hot rolled steel were heated in the dilatometer up to a full-austenisation temperature of 1000 °C, with heating rates of 10 °C/s, 150 °C/s, 500 °C/s and 1000 °C/s. Analysis of the dilatation records illustrates that both the A_{C1} and A_{C3} temperatures increased with higher heating rates, cfr. Figure VII-2.

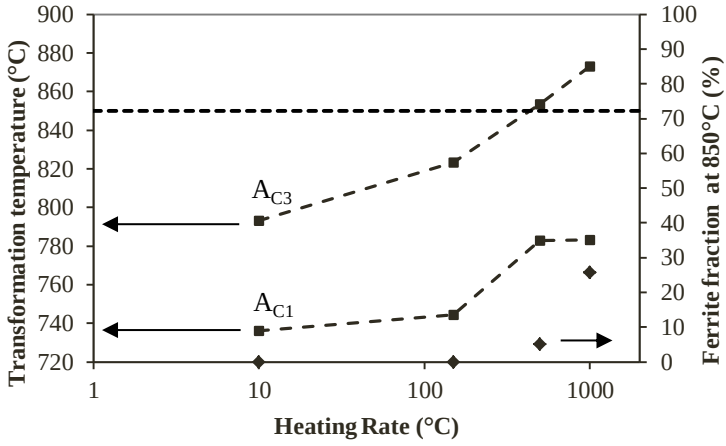

Figure VII-2: Shift of the transformation temperatures A_{c1} and A_{c3} with heating rate together with the theoretical calculated ferrite fraction upon heating to 850°C

The A_{C1} and A_{C3} temperature increased from 736 °C to 783 °C and 793 °C to 873 °C respectively upon changing the heating rate from 10 °C/s to 1000 °C/s. The ferrite fractions at 850 °C (which was the reheating temperature for the cold rolled samples) were calculated by the lever rule as shown in Figure VII-2. After reheating the sample with 500

°C/s to 850 °C, the steel is almost completely austenitized, however, after reheating at 1000 °C/s and subsequent quenching about 25 % ferrite remains in the material. The reheating experiments confirm the well-known fact that the A_{C3} is more sensitive to the heating rate then the A_{C1} temperature (as can be seen from the slope change of the curves in Figure VII-2).

VII.4.1.2 Carbide precipitation conditions

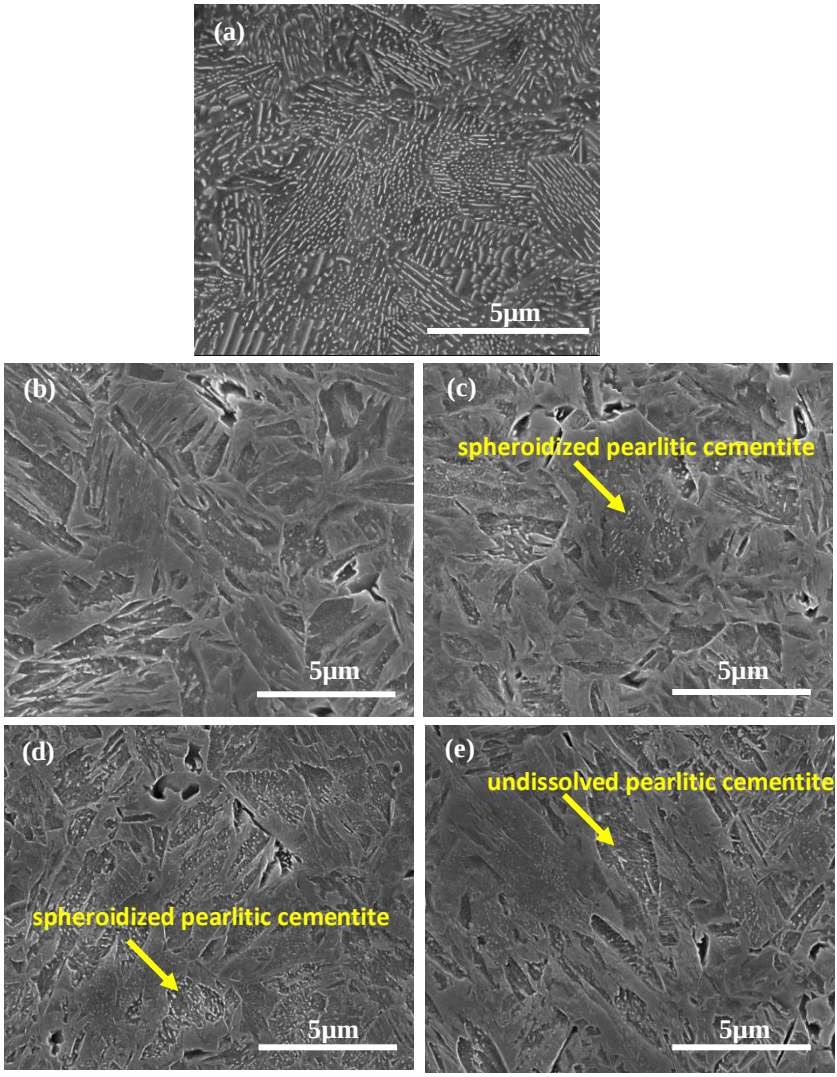

Figure VII-3: SEM images of (a) hot rolled material and quenched samples which were reheated at 1000°C with (b) 10°C/s, (c) 150°C/s , (d) 500°C/s and (e) 1000°C/s. The arrows show typical appearance of characteristic features however they appear in the entire microstructure.

The influence of UFA prior to Q&P on the microstructure and mechanical properties

In Figure VII-3 (a-e), the carbide precipitation conditions were studied by scanning electron microscopy in the hot rolled sample and the quenched samples which were heated at different rates.

The pearlitic microstructure of the hot rolled material is given in Figure VII-3 (a). After conventional flash heating with 10 °C/s and quenching, a very small fraction of carbides is detected in the microstructure, cfr. Figure VII-3 (b). An increase of the heating rate to 150 °C/s leads to an increasing fraction of undissolved carbides which are present in the microstructure as (partially) spheroidized pearlitic cementite, cfr. Figure VII-3 (c). At a heating rate of 500 °C/s a smaller part of the carbides is dissolved as can be observed in Figure VII-3 (d). The shape of the original cementite in the pearlite is more distinctly visible which implies that the carbides are partially spheroidized cementite. After reheating with 1000 °C/s, the remaining carbides are finer and with well pronounced lath-shape (cfr. Figure VII-3 (e)) with similar morphology to the cementite lamellas in pearlite (cfr. Figure VII-3 (a)) which is an indication that they are undissolved pearlitic cementite.

VII.4.2. Gleeble Q&P heat treatments with ultra-fast heating

VII.4.2.1 Microstructural characterization

The scanning electron microscopy images of the Q&P heat treated samples illustrate that the microstructure becomes more finely dispersed after UFA as shown in Figure VII-4.

A lot of large, fresh martensite blocks are present in the sample heated with 10 °C/s and isothermally held for 5 min, cfr. Figure VII-4 (a). After reducing the isothermal holding time to a flash process (cfr. Figure VII-4 (b)), the microstructure refines significantly and the average bcc grain diameter decreases from 2.5 µm to 2 µm (see also Figure VII-7(b)). Increasing the heating rate to 500 °C/s (cfr. Figure VII-4 (c)) and 1000 °C/s (cfr. Figure VII-4 (d)) alters the microstructure in such a way that the martensite blocks have less lath-shaped morphology and coarser, undissolved carbides are present.

The fresh martensite fraction can be determined with EBSD as the fraction of low image quality grains. Any distortions to the crystal lattice within the diffracting volume will produce lower quality (more diffuse) diffraction patterns. This enables the IQ parameter to be used to give a qualitative description of the lattice distortion of the microstructural constituents in an EBSD scan. Since the fresh martensite has more dislocations, its lattice is

more distorted resulting in lower image quality grains[11]. The retained austenite is highlighted in green in the maps in Figure VII-5.

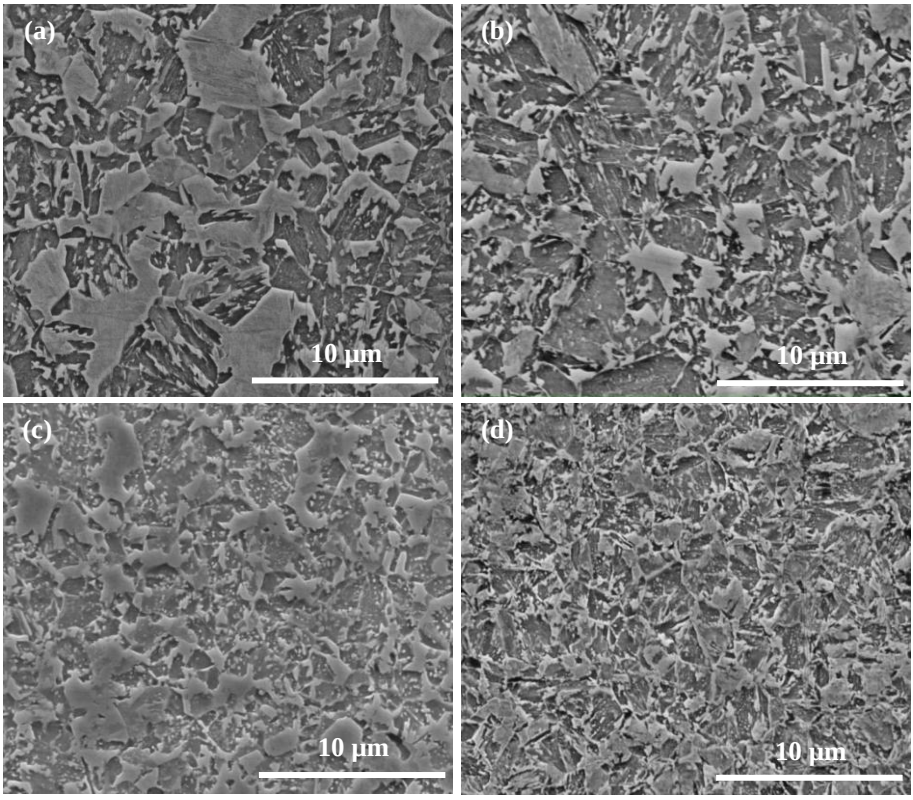

Figure VII-4: SEM images after Q&P heat treatments with different heating rates prior to full austenitisation (a) 10°C/s + soak (b) 10°C/s (c) 500°C/s (d) 1000°C/s

As was observed previously from the SEM images, the martensite grains in the conventionally Q&P heat treated sample are rather large (average grain diameter of 2.5 µm) with 14.1 % fresh martensite blocks, cfr. Figure VII-5 (a). If a flash process is conducted instead of an isothermal holding at 850 °C, the microstructure refines and the average grain diameter of the martensite reduces to 2 µm, cfr. Figure VII-5 (b). In this flash heat treatment the α-γ phase transformation started in a recrystallized bcc matrix and is completed, however there was no time for all of the austenite grains to grow which resulted in a bimodal grain size distribution. Similar conclusions can be drawn after analysing the microstructures obtained with a heating rate of 500 °C/s, cfr. Figure VII-5 (c). If the heating rate increased from 500 °C/s to 1000 °C/s, the fresh martensite fraction decreased significantly due to the presence of 25 % ferrite, cfr. Figure VII-5 (d). The average bcc grain diameter reduced to 1.4 µm and the retained austenite grains became smaller and more homogenously distributed.

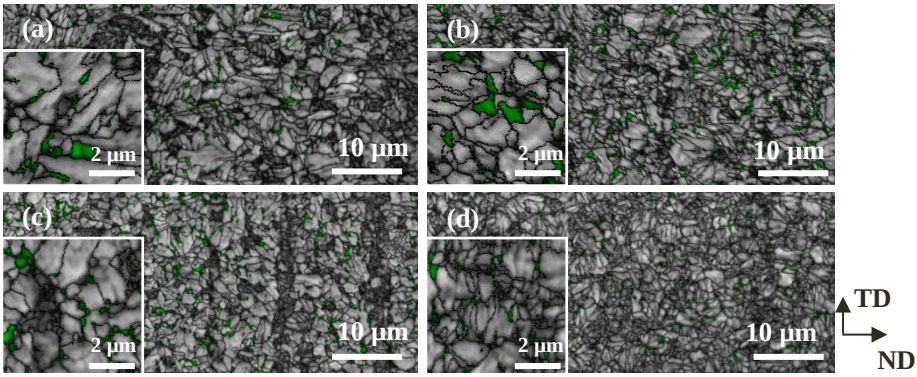

Figure VII-5: EBSD image quality maps with the austenite grains highlighted in green for (a) 10°C/s + soak (b) 10°C/s (c) 500°C/s (d) 1000°C/s

From the EBSD data, the approximate prior austenite grain (PAG) size can be determined by plotting the rotation angles between 21.1° and 47.1° [12]. After revealing the possible former austenite grain boundaries according to the methodology proposed in [12] the grain boundary maps were build and plotted (an example is shown in Figure VII-6).

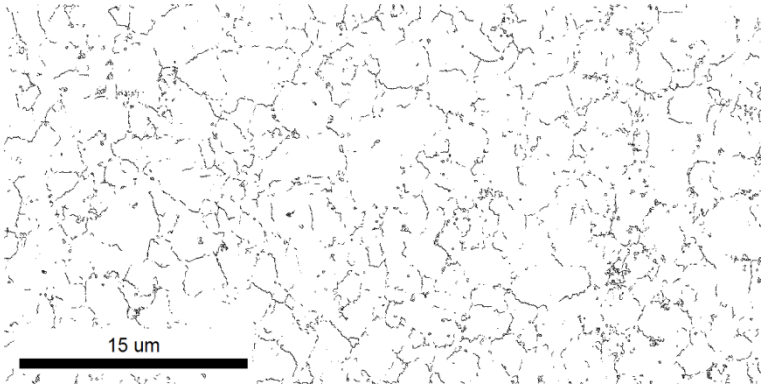

Figure VII-6: Former austenite grain boundaries for the UFA-Q&P with a heating rate of 1000°C/s by plotting the rotation angles between 21.1° and 47.1° according to a methodology proposed in [12]

The linear interception method was used to determine the average prior austenite grain size for the Q&P samples as illustrated in Figure VII-7 (a). The average austenite grain diameter in the material after heating at 10 °C/s and isothermal soaking is 4.8 µm and decreases to 2.9 µm without isothermal soaking. With a higher heating rate, the PAG diameter decreased to 1.7 µm for 1000 °C/s. After the Q&P heat treatment cycle without soaking, the austenite and ferrite grain sizes decreased from 0.6 µm to 0.3 µm and 2 µm to 1.4 µm respectively as the heating rate is increased from 10 °C/s to 1000 °C/s, cfr. Figure VII-7 (b).

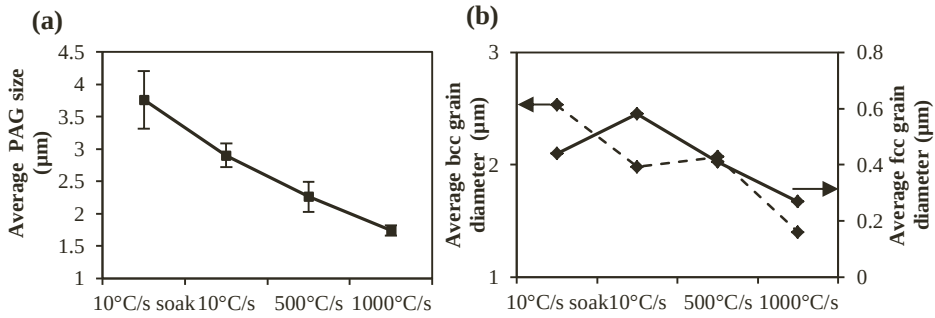

Figure VII-7: (a) Average prior austenite grain (PAG) size for the different Q&P cycles and the hot rolled material (b) average final bcc and fcc grain diameters of the Q&P heat treated samples

A remark should be made concerning the retained austenite fraction and its size determined with EBSD. Although the spatial resolution of the EBSD technique is reasonably high, it is well-known that the austenite grains could have sizes in the range of 100 nm which is below the detection limit. Hence, the retained austenite fractions as obtained with EBSD underestimate the real value. The retained austenite fractions from the XRD measurements are shown in Figure VII-8 and they remain similar (around 9%) for all heat treatment cycles except for 10°C/s without soaking for which 13% retained austenite was stabilized.

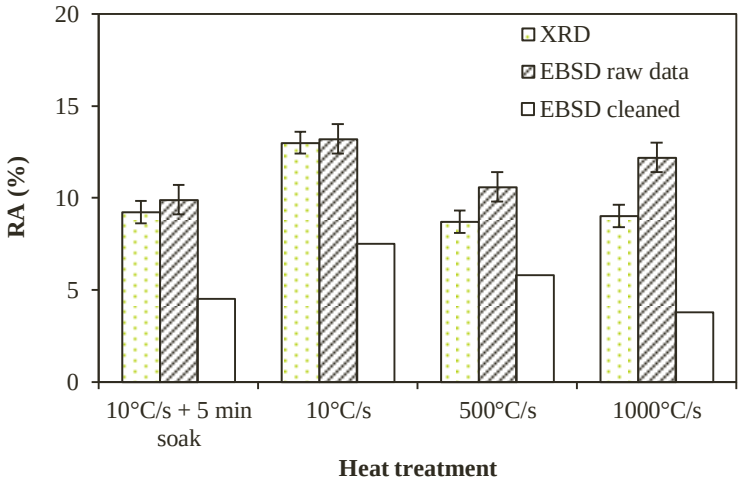

Figure VII-8: Retained austenite fraction obtained with XRD, EBSD raw data and EBSD cleaned data for different heat treatment conditions

The EBSD raw data are also included, since the fcc indexation of 1 point with a step size of 60 nm might be a real austenite grain in between martensite laths. The EBSD raw data correspond very well with the XRD data for a heating rate of 10 °C/s. If the heating rate increases, the quality of the EBSD measurement reduces due to a finer microstructure, making

the difference between the XRD and raw EBSD data larger. From this we can conclude that approximately 9% retained austenite was stabilized after conventional Q&P processing and after ultrafast heating at 500°C/s and 1000°C/s prior to partitioning although the size of the austenite grains decreased.

VII.4.2.2 Textural evolution

The textures of the samples were calculated from Electron Backscattered Diffraction data. Figure VII-9 displays the changes in the crystallographic textures as a function of the reheating rates represented by the orientation distribution function (ODF).

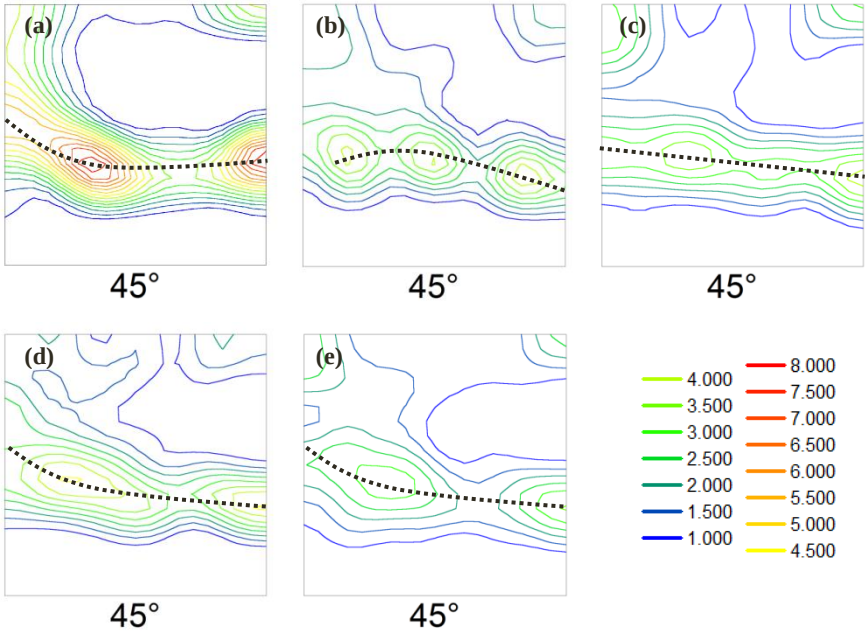

Figure VII-9: Orientation distribution figure at a cross-section of φ_2 = 45° of (a) cold rolled material and quenched samples after heating at (b) 10°C/s with soaking (c) 10°C/s without soaking (d) 500°C/s (e) 1000°C/s

The texture of the cold rolled sample is characterized with an RD-ND fibre texture with a maximum of 8 mrd (multiples of a random distribution) on the {111}<112> texture component and a weaker rotated cube {100}<110> with an intensity of 4 mrd, cfr. Figure VII-9 (a). The texture shows a convex curvature of the ND fibres which is typical for cold rolled low carbon steels.

After reheating the cold rolled sample with 10 °C/s and isothermal soaking, the cold rolling texture changes to a recrystallization type texture which is characterized by a strong

ND-fibre texture with a concave curvature and the disappearance of the RD-fibre component [13], cfr. Figure VII-9 (b). Flash processing at 10 °C/s changes the curvature of the ND-fibre from concave to straight as shown in Figure VII-9 (c).

After increasing the heating rate to 500 °C/s (cfr. Figure VII-9 (d)) and 1000 °C/s (cfr. Figure VII-9 (e)), the texture starts to resemble the original cold rolled texture with a convex curvature of the ND-fibres but with much lower intensity of 4 mrd. Due to a texture memory effect i.e. the martensite phase inherits the texture of the untransformed ferrite, we can conclude that this ferrite was not recrystallized but possible only recovered [14]. Similar effects were reported by Senuma *et al*. [5] and Petrov *et al*. [3] in rapidly annealed cold-rolled extra low carbon and advanced high strength steel sheets respectively.

VII.4.2.3 Mechanical properties

A representative example of the stress-strain curves of the conventionally heat treated Q&P sample and the ones heated at 10°C/s, 500°C/s and 1000°C/s without soaking are given in Figure VII-10. The corresponding characteristic values are given in Table VII-1.

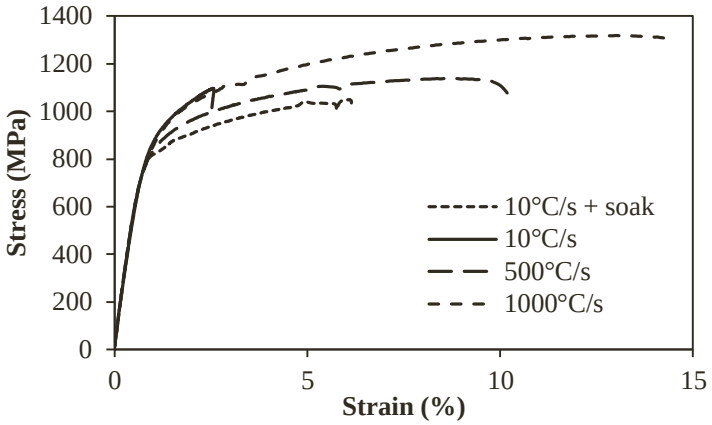

Figure VII-10: Stress-strain curves of the normal Q&P heat treated sample with soaking, the sample heated at 10°C/s without soaking, and the samples after ultrafast annealing at 500°C/s and 1000°C/s

The conventionally Q&P heat treated sample has an uniform elongation of 6.1 % with a yield strength and ultimate tensile strength of 782 MPa and 1050 MPa respectively. For the sample without isothermal soaking after heating at 10°C/s, the uniform elongation decreased to 2.6% with higher yield and ultimate tensile strengths of 837MPa and 1097MPa respectively. Increasing the heating rate to 500 °C/s results in an uniform elongation of 8.6 % with an ultimate tensile strength of 1138 MPa and a heating rate of 1000 °C/s results in an

uniform elongation of 12.8 % with an increased yield and ultimate tensile strength of 811 MPa and 1318 MPa respectively. The ratio of yield strength to ultimate tensile strength decreases with higher heating rates without soaking, cfr. Table VII-1. The n-values were also calculated as 0.241 for a heating rate of 10 °C/s, 0.167 for 500 °C/s and 0.245 for 1000 °C/s.

Table VII-1: Uniform elongation, yield strength, tensile strength, yield strength to tensile strength ratio and n-values for the stress-strain curves in Figure 9

	10°C/s + soak	**10°C/s**	**500°C/s**	**1000°C/s**
ε_u (%)	6.1	2.6	8.6	12.8
YS (MPa)	782	837	792	811
UTS (MPa)	1050	1097	1138	1318
YS/UTS	0.745	0.763	0.696	0.615
n-value	0.193	0.241	0.167	0.245

The fracture surface of the conventionally Q&P treated and the sample heated at 10°C/s without soaking is quasi-cleavage. Figure VII-11 (a) reveals some dimples but fracture propagated mostly by cleavage resulting in a mixed ductile-brittle fracture mode. After ultra-fast heating the fracture resulted in a ductile fracture surface with large dimples, cfr. Figure VII-11 (b-c).

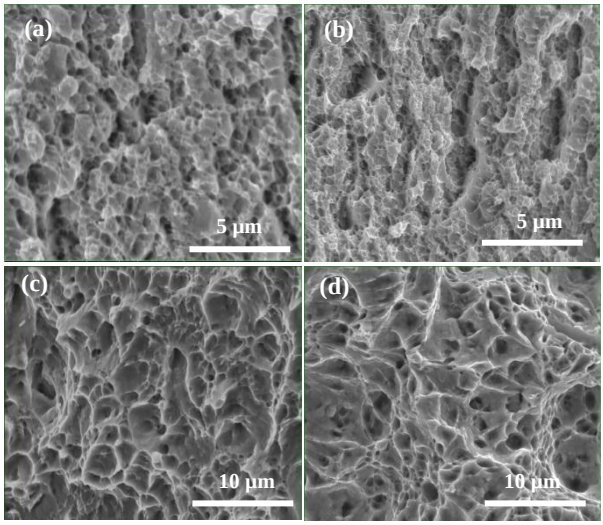

Figure VII-11: Fracture surface of (a) conventional Q&P after heating at 10°C/s and soaking, after flash heating at (b) 10°C/s, (c) 500°C/s, and (d) 1000°C/s

VII.5. Discussion

Ultrafast annealing changes the sequence of the mechanisms occurring during typical heat treatments of steel. After ultra-fast reheating the austenite formation starts in the deformed, partially recovered matrix as is illustrated by the unchanged texture after ultrafast heating compared with the starting cold rolled texture. This interaction between recovery, recrystallization and phase transformation results in a decrease of the prior austenite grain size. On the other hand, it also alters the carbide precipitation conditions. With a heating rate of 10 °C/s, practically all carbides were dissolved, resulting in high-C martensite after quenching to room temperature. However, if the heating rate was increased to 150 °C/s, some carbides were visible in the microstructure of the quenched material suggesting that they weren't dissolved completely during heating. The morphology of the carbides was oval shaped with their longest axis lying along the cementite lamellae of the original pearlite. After heating the samples with 500 °C/s, more partially spheroidized carbides compared to the previous condition, were present. After heating the material at 1000 °C/s, the carbides were lying more in the original lath-type morphology of the pearlite indicating that the spheroidization process was even suppressed during this fast heating. These carbides pin the grain boundaries and retard grain growth on one hand, while its effect on Q&P processing is the production of a tempered low-C martensitic matrix.

In conventional Q&P heat treatments, carbides are unwanted since they reduce the available carbon for enriching the austenite during partitioning. It seems that the carbon content in our material was still high enough to reach and maintain retained austenite levels up to about 10 %. The morphology of the retained austenite grains changed with the increase of the heating rate from blocky and lamellar to possibly film-like retained austenite which was difficult to detect with conventional EBSD.

By combining the XRD data for the retained austenite fractions, the EBSD data for the fresh martensite by low image quality bcc grains, and dilatometric data for the ferrite fractions, a balance of all phases present in our samples could be obtained, cfr. Figure VII-12. It seems that the fresh martensite which was present in the samples at lower heating rates is replaced by ferrite in the sample heated at 1000 °C/s.

The conventional Q&P heat treatment cycle with soaking resulted in a microstructure consisting of fresh martensite blocks, retained austenite and tempered martensite. If the isothermal soaking time was reduced to a flash process, the prior austenite grains refined from 3.8µm to 2.9µm and the martensite grain size reduced from 2.5µm to

2µm. This decrease in grain size caused the observed increase in yield strength from 782MPa to 837MPa. By changing the isothermal holding to a flash process, the stabilized retained austenite fraction increased from 9% -with an average size of 0.44µm- to 13% -with an average diameter of 0.58µm. As a consequence, these larger austenite grains are less stable [15] and transform at lower strains giving a higher strain hardening behaviour in the stress-strain curve at small elongations. This can be observed by a higher n-value for the flash process 0.241 compared to 0.193 for the conventional treatment. Besides, this reduced the uniform strain from 6.1% to 2.6%.

The combination of mechanical properties obtained after ultra-fast annealing is better than after conventional Q&P when the heating is 10 °C/s and includes a soaking stage at the austenitisation temperature. The total elongation increased from 6.1 % to 10.2 % with an increase in yield strength from 782 MPa to 792 MPa and ultimate tensile strength from 1138 MPa to 1318 MPa going from a normal Q&P heat treatment to a flash process with 500 °C/s. Hence, by altering the heating rate from 10 °C/s to 500 °C/s, an increase in total elongation of 67 % was obtained with a simultaneous increase in ultimate tensile strength of 16 %. The fractions of the different constituents in the microstructure are similar for both samples. The largest differences between both samples are related with martensite grain refinement from 2.5 µm to 2.1 µm diameter and with the carbide precipitation conditions. The martensite of the normal Q&P is tempered high-C martensite due to the dissolution of the carbides prior to quenching, whereas in the ultra-fast heated sample, the martensite is tempered and low-C. The higher n-value in the sample flash heated at 10°C/s compared to 500°C/s can be explained by a larger average austenite grains size and hence lower mechanical stability. It could be hypothesized that higher-C martensite due to carbide dissolution at slow heating and a similar martensite grain size could be associated with a higher yield strength but similar ultimate tensile strength.

The major difference between the microstructures obtained after heating with 500 °C/s and 1000 °C/s is the fraction of fresh martensite which is replaced by ferrite as well as the reduction of the prior austenite grain size from 2.3 µm to 1.7 µm. This replacement and grain refinement resulted in a higher total elongation from 10.2 % to 14.3 % with an increase in yield and ultimate tensile strength from 792 MPa to 811 MPa and from 1138 MPa to 1318 MPa respectively. The presence of fresh martensite islands has a negative influence on the mechanical properties of Q&P since they act as stress-concentrators decreasing the austenite stability and the overall ductility [16].

The ultimate strength levels increased 26% from 1050MPa to 1318MPa with a simultaneous increase in total elongation of 134% from 6.1% to 14.3% changing the conventional Q&P process by a flash austenitisation with a heating rate of 1000°C/s. Moreover, the yield strength increased and the ratio of yield strength to tensile strength reduced from 0.745 to 0.615 due to a larger strain hardening behaviour with n-values of 0.19 and 0.25 respectively. Besides, the overall bcc grain size decreased 44% from 2.5µm to 1.4µm. The effect of altering the heating rate from 10°C/s to 500°C/s resulted in an increase in uniform elongation from 2.6% to 8.6% with similar ultimate tensile strength levels, whereas a heating rate of 1000°C/s improved the ductility further to 12.8% with a simultaneous increase in ultimate tensile strength from 1097MPa to 1318MPa. These effects originate from the mixture of 10 % retained austenite laths and small grains in a fine matrix of low-C tempered martensite and the replacement of fresh martensite with small recrystallized ferrite grains at the highest heating rate.

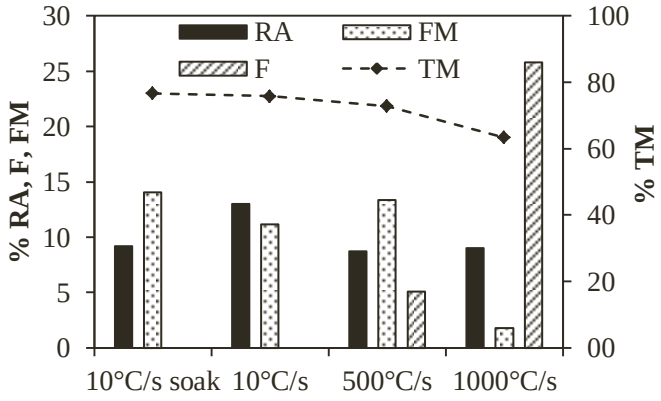

Figure VII-12: The fractions of retained austenite (RA), ferrite (F), fresh martensite (FM) and tempered martensite (TM) in the Q&P heat treated samples heated at 10°C/s with and without soaking and heated at 500°C/s and 1000°C/s

This combination of microstructural features explains the change in fracture behaviour from cleaved facets to ductile dimples. In a conventional Q&P, the austenite grains accommodate the plastic deformation resulting in the dimpled areas in the fracture surface whereas the martensite fractures with cleavage facets. After ultrafast heating the homogeneous distribution of small island of retained austenite, the possible existence of interlath austenite [17] and a matrix of low carbon martensite create a combination which changes the fracture mode from mixed (dimples and cleavage) to ductile.

VII.6. Conclusions

The result of experiments on Q&P heat treatment cycles executed in conventional and in the condition of fast and ultra-fast heating without isothermal soaking can be summarized as follows:

Dilatometric experiments on hot rolled 0.25C-3Mn-1.5Si Q&P material demonstrated the increase of both the A_{C1} and A_{C3} temperatures with increasing heating rate. It was shown that the A_{C3} temperature is more sensitive than the A_{C1} temperature to the heating rate. An incomplete dissolution of carbides at high heating rates was observed. With a heating rate of 10°C/s, with and without isothermal soaking almost no carbides were present in the quenched sample. However, flash heating at 500°C/s resulted in spheroidized carbides in a prior pearlitic cementite morphology and after heating with 1000°C/s, the pearlite structure was still visible after quenching with less significant carbide spheroidization.

The prior austenite grains, which originated from an non-recrystallized bcc matrix, refined significantly with higher heating rates. The stabilisation of around 9% retained austenite after ultrafast heating at 500°C/s and 1000°C/s and partitioning was realized.

The tempered martensite contained less carbon in comparison to the one in conventionally Q&P treated samples due to the non-complete dissolution of carbides in the heating stage and the presence of fine, recrystallized ferrite at the highest heating rate.

The mechanical properties of the UFA-Q&P samples with heating rates of 500°C/s and 1000°C/s without isothermal soaking are better than in the conventionally Q&P samples combining an increase in strength up to 26% and ductility up to 134%. The fracture surface changes from quasi-cleavage in conventionally heat treated samples to ductile dimples in the fast heated ones.

VII.7. Acknowledgements

This research was partly funded by the governmental institute for the Promotion of Innovation by Science and Technology in Flanders (IWT) and was supported by European project “RFCS-CT-2011-00017 “New advanced high strength steels by quenching and partitioning process (NewQ&P)”.

References

1. R. Petrov, F. Hajyakbary, J. Sidor, M. J. Santofimia, S. J., and L. A. I. Kestens: 'Ultra-fast annealing of high strength steel'.
2. T. Lolla, G. Cola, B. Narayanan, B. Alexandrov, and S. S. Babu: 'Developement of rapid heating and cooling (flash processing) process to produce advanced high strength steel microstructures', *Materials Science and Technology*, 2011, **27**(5), 863-875.
3. R. Petrov, J. Sidor, and L. A. I. Kestens: 'Texture formation in high strength low alloy steel reheated with ultrafast heating rates', *Materials Science Forum*, 2012, **702-703**, 798-801.
4. A. Lucas, A. De Paepe, H. Petitgand, C. Colin, L. Chapuis, and J. M. Artimez: 'Production of high quality formable grades in an ultra short annealing processing line', 2007.
5. T. Senuma, K. Kawasaki, and Y. Takemoto: 'Recrystallization behavior and texture formation of rapidly annealed cold-rolled extralow carbon steel sheets', *Materials Transactions*, 2006, 1769-1775.
6. M. Atkinson: 'Bifurcation of thermal restoration processes in deformed iron and steel', *Materials Science and Engineering*, 1999, 33-38.
7. V. Massardier, A. Ngansop, D. Fabrègue, and J. Merlin: 'Microstructure and mechanical properties of low carbon al-killed steels after ultra-rapid annealing cycles'.
8. R. Petrov, L. Kestens, W. Kaluba, and Y. Houbaert: 'Recrystallization and austenite formation in a cold rolled trip steel during ultra fast heating', in 'Steel Grips', 289-294; 2003.
9. R. Petrov, F. Hajyakbary, j. Sidor, M. J. Santofimia, J. Sietsma, and L. Kestens: 'Ultra-fast annealing of high strength steel', *MTM International Virtual Journal*, 2012(11), 72-81.
10. B. D. Cullity: 'Elements of x-ray diffraction', 1956, New Jersey, USA, Addison-Wesley Publishing Company, Inc.
11. M. J. Santofimia, R. H. Petrov, L. Zhao, and J. Sietsma: 'Microstructural analysis of martensite constituents in quenching and partitioning steels', *Materials Characterization*, 2014, **92**(0), 91-95.
12. N. Bernier, L. Bracke, L. Malet, and S. Godet: 'An alternative to the crystallographic reconstruction of austenite in steels', *Materials Characterization*, 2014, **89**, 23-32.
13. L. A. I. Kestens, K. Verbeken, and J. J. Jonas: 'Orientation selection by nucleation and growth in highly strained low carbon steels ', 1st Joint International Conference on Recrystallization and Grain Growth Aachen, Germany, 2001, Recrystallization and grain growth, 695-706.
14. N. Yoshinaga, H. Inoue, K. Kawasaki, L. A. I. Kestens, and B. C. De Cooman: 'Factors affecting texture memory appearing through alpha ->gamma ->alpha transformation in if steels ', *Materials Transactions*, 2007, **48**(8), 2036-2042.
15. W. C. Jeong, D. K. Matlock, and G. Krauss: 'Observation of deformation and transformation behavior of retained austenite in a 0.14c-1.2si-1.5mn steel with ferrite-bainite-austenite structure', *Materials Science and Engineering: A*, 1993, **165**(1), 1-8.
16. D. De Knijf, R. Petrov, C. Föjer, and L. A. I. Kestens: 'Effect of fresh martensite on the stability of retained austenite in quenching & partitioning steel', *Materials Science and engineering A*, 2014, **615**(0), 107-115.
17. F. Maresca, V. G. Kouznetsova, and M. G. D. Geers: 'On the role of interlath retained austenite in the deformation of lath martensite', *Modelling and Simulation in Materials Science and Engineering*, 2014, **22**.

CHAPTER VIII

SUMMARY, CONCLUSIONS AND SUGGESTIONS FOR FUTURE WORK

SUMMARY, CONCLUSIONS AND SUGGESTIONS FOR FUTURE WORK

The automotive industry supports the development of advanced high strength steel (AHSS) grades to enhance fuel economy and to satisfy with the increasing demands for safety and performance. To reduce the car body weight, steel products must be made thinner and therefore, compared to those currently available, steel with higher strength and similar ductility and formability is required.

Quenching and Partitioning (Q&P) steel is one of the currently investigated steel grades of the third generation AHSS. This generation aims to cover the property range between the first, ferritic-based and the second, austenitic-based AHSS grade generations. A Q&P microstructure consists typically of ductile austenite particles in a hard martensite matrix and exhibits, therefore, a favourable combination of both high strength and ductility. In the current work, this microstructure was created by full austenitisation, quenching between the martensite start temperature (M_s) and the martensite finish temperature (M_f), and reheating to a higher temperature to promote carbon diffusion from the supersaturated martensite to the austenite. In an ideal Q&P cycle, the quenching temperature is chosen such that the present austenite is just completely stabilized during partitioning without the occurrence of competing reactions. This results in a microstructure with the highest possible fraction of retained austenite, which depends on the concentration of C available, in a tempered martensite matrix without fresh martensite.

The results of the current study are given in seven chapters and summarized in Chapter VIII of this work.

In Chapter I, a literature overview, which focussed on carbon partitioning, competing reactions during Q&P processing, and parameters that influence the stability of austenite during TRIP-assisted deformation behaviour was presented. The current literature revealed no clear relationship between Q&P microstructures and mechanical properties. Moreover, in contrast to TRIP-steels for which parameters such as carbon content, grain size, and crystallographic orientation, are known to influence the austenite stability, relatively little is known about Q&P steel. Although studies on the influence of the austenite carbon content, grain size, and morphology are on-going, the effect of the surrounding phases on the microstructural response on austenite stability has been scarcely studied. Furthermore, ex-situ research was conducted on the movement of the austenite-martensite interface during partitioning but no experimental evidence was provided. Such evidence would provide

fundamental information regarding the activation energy for grain boundary motion and hence the underlying mechanisms of partitioning.

Chapter II explained the production of the 0.25C1.5Si3Mn and 1C1.5Si3Mn steels and the experimental techniques used in this work to characterize the microstructures and the mechanical properties.

The influence of the processing parameters on the final microstructures and ensuing mechanical properties was described in Chapter III. Understanding this link between microstructures and mechanical properties is essential to the efficient design of Q&P heat treatment cycles. In Chapter III, the 0.25C1.5Si3Mn steel was subjected to Q&P heat treatment cycles, which were designed with the aid of dilatometric and DSC experiments. Dilatometry data were used to reconstruct part of the CCT diagram from which the critical cooling rate to avoid ferrite/pearlite and bainite formation was derived. Additional Q&P experiments with long isothermal partitioning treatments at 300 °C, 350 °C, and 400 °C were performed in order to study isothermal transformations via the length change. At 400 °C, the decrease in length was associated with martensitic tempering and possible growth of existing austenite by interface movement, whereas at 300 °C and 350 °C the increase in length was attributed to competing reactions such as bainite formation. With DSC experiments, the partitioning temperature range without carbide precipitation was identified. Two exothermal peaks were observed, one at temperatures of 150-300 °C and the other at 400-525 °C, which stemmed from the formation of epsilon-carbides and cementite, respectively.

Based on this information, partitioning temperatures of 300-450 °C were selected; the lowest temperature, 300 °C, is only slightly higher than the ε-carbide dissolution temperature. In addition, the partitioning was performed at 350 °C in order to determine the effect of bainite formation on the partitioning kinetics and mechanical properties. The decrease in length and a high fraction of retained austenite determined with EBSD during and after partitioning, respectively, suggested that 400 °C was the optimum partitioning temperature, resulting in the highest C-diffusivity without competing reactions. Moreover, 450 °C was chosen to study the effect of austenite decomposition, to ferrite and coarse cementite, on the mechanical properties. The quenching temperatures were varied up to 20 °C above and below 244 °C. The influence of the quenching temperature, partitioning temperature and times on the fraction and C-content of retained austenite, and the resulting mechanical properties were studied.

Kinetic effects, possibly related to the formation of C pile-ups near the martensite-austenite grain boundaries could explain the limited influence of the quenching temperature on the retained austenite fraction. The stabilization of the same retained austenite fraction occurred faster with a larger austenite fraction formed at higher quenching temperatures. However, if the austenite fraction at the quenching temperature was too high, the stabilization was slower owing to a lower available amount of C in the martensitic matrix.

Competing reactions such as precipitation, bainite formation, and decomposition determined the best partitioning temperature range. For example, partitioning below 300 °C resulted in the formation of ε-carbides, which depleted the amount of carbon available for partitioning. At 300-370 °C (Bs), the formation of low-carbide bainite after 100 s resulted in a decrease in the fraction of retained austenite but an increase in the C-content owing to expulsion from low-carbide bainite. The optimum partitioning temperature range of 370-400 °C, resulted in enhanced C-diffusivity without competing reactions. Above 400 °C, cementite was formed owing to the decomposition of austenite and tempering of martensite; this cementite formation led to a significant decrease in the fraction of retained austenite and hence, the total elongation.

The time required for partitioning was determined by two factors namely, the fraction and C-content of retained austenite. The C-content provides mechanical stability and if the partitioning temperature is lower, the time to obtain a high fraction of retained austenite with a high C-content is longer. Long partitioning times are limited by competing reactions.

The total elongation exhibited a linear dependence on the product of the retained austenite fraction and the C-concentration, indicating the importance of both high retained austenite fraction and sufficient C-content. Furthermore, the yielding behaviour was continuous at short partitioning times but, owing to martensitic tempering, changed to a higher and more discrete yield point at longer times. The evolution of the ultimate tensile strength was also attributed to this tempering.

Furthermore, more fundamental questions regarding the austenite-martensite interface movement during partitioning were partially answered in Chapter IV. In this chapter, the austenite-martensite interface migration during partitioning was studied by using a heating stage in a HR-TEM. The complete heat treatment cycle could not be performed successfully because of two reasons: the inability to reach the austenitisation temperature and loss of material at high temperatures. Therefore, a high-C steel was developed in order to reduce the quenching temperature to room temperature. Consequently, only the partitioning heat

treatment after full austenitisation and quenching in a dilatometer needed to be conducted inside the TEM. After selecting an appropriate region with an alternating structure of lath martensite and interlath austenite, partitioning was conducted inside the TEM on a FIB-foil at 400 °C. The width of an austenite grain was monitored as a function of partitioning time. This width increased owing to grain boundary migration, which was modelled with a partitioning model that takes grain boundary movement into account. An activation energy of 165 kJ/mol was found to be the best fit for the kinetics of width change for the current chemical composition, austenite grain, and interface characteristics. This activation energy is higher than that of austenite-ferrite phase transformations, which indicates that the migration kinetics of the studied martensite-austenite interface is slower than that of diffusional austenite-ferrite transformations stemming from the semi-coherent nature of the interface. Determination of the composition across the interface after annealing confirmed the occurrence of effective C-partitioning.

The reaction of Q&P microstructures upon uniaxial deformation with the main focus on austenite to martensite transformation (TRIP-effect) was studied in Chapter V. The influence of fresh martensite on the strain distribution, austenite transformation and fracture behaviour was revealed and the factors inherently connected to retained austenite stability under external load were addressed. In this chapter the transformation stability of austenite during micro-tensile testing combined with EBSD measurements on a pre-selected area was studied.

Two heat treatments on specially designed Q&P steel were outlined in section V.1; these treatments were performed as part of the study on the influence of fresh martensite on the mechanical response of the microstructure. By inhibiting the amount of deformation that could be accommodated in the tempered martensite and by triggering void formation, the fresh martensite was found to play a significant role in the strain distribution in the microstructure and on the fracture mechanism, respectively. This constraining effect decreased the austenite transformation stability; i.e. the exponential factor of the retained austenite fraction versus strain interpolation. Consequently, compared to the fresh-martensite-free microstructure, fresh martensite resulted in an initially higher strain hardening owing to substantial austenite transformation at low strains. In-situ tensile tests were also conducted inside an x-ray diffractometer, as described in section V.2, in order to track the retained austenite fraction versus strain and compare the evolution with the results presented in section V.1. Both techniques predicted that the retained austenite evolved with a constant difference-value. This value was, however, larger for the sample with fresh martensite, compared to that without, in the starting microstructure; this higher value resulted from a less reliable

indexation of retained austenite patterns inside the fresh martensite blocks besides the difficult-to-detect film-like austenite between the tempered martensite laths, which were present in both samples. In addition, the transformable retained austenite fraction until uniform deformation decreased owing to the shielding by the fresh martensite blocks; nevertheless, both steels had a similar starting fraction of retained austenite.

In section V.3, the orientation dependence of the austenite-to-martensite transformation, modelled using the phenomenological theory of martensite crystallography and the mechanical driving force, was validated experimentally. This theory predicted the global transformation stability accurately. However, as described in section V.5, other factors such as the grain size and morphology, control the stability, locally. In this section, the EBSD data from the sample without fresh martensite were analysed in detail in order to separately study the influence of grain size, morphology, and crystallographic orientation on the stability of austenite.

Grains larger than 1 µm transformed rapidly upon plastic straining, whereas grains with diameters of 0.15-1 µm contributed most to the transformation induced plasticity in the Q&P steel; these grains transformed at different speeds and, compared to their large counterparts, the small grains sustained plasticity for larger strains. Grains smaller than 0.1 µm in diameter did not transform during straining of up to 10.9% because they were too stable to transform. However, they are believed to contribute to the total elongation when (local) strain levels increase.

The grains oriented perpendicular and at 45° with respect to the tensile direction transformed rapidly under the action of high tensile and shear stresses, respectively. Lamellar grains with a large difference between the length of the longest and smallest axis in 2D were found to be less stable compared to grains with smaller differences, i.e. with more globular shapes.

In addition, the austenite grains tend to rotate to accommodate the deformation. Austenite grains with crystallographic orientations with high transformation potentials did not rotate significantly but transformed to martensite instead, whereas those with low transformation potentials rotated mainly between 2°-6° before transforming to martensite.

From these data, an order of importance of the factors influencing the austenite stability could be determined as (1) grain size, (2) morphology, and (3) crystallographic orientation if no fresh martensite was present in the microstructure.

Fresh martensite altered the mechanisms controlling the austenite stability, due to its constraining effect as described in section V.6. The austenite grain size, which was reduced during straining, was the only parameter that exhibited the tendencies observed in section V.5. The influence of morphology and crystallographic orientation on the stability was undermined by the presence of fresh martensite.

As described in section V.7, the influence of fresh martensite on the fracture mechanisms was studied by analysing the fracture surface and deformed microstructure. The transformation of detectable, large retained austenite grains into high-C martensite induced hard second phase particles, which were nucleation sites for voids. A change from a micro-void coalescence to quasi-cleavage fracture behaviour was obtained by adding fresh martensite to a tempered martensite matrix with retained austenite. Less deformation of retained austenite blocks revealed that they transformed at lower strains due to a lower mechanical stability compared to the interlath lamellar austenite grains. The fresh martensite blocks remained as rigid constituents in the necking region, thereby triggering void formation by stress concentration and reducing the overall strain by its constraining effect.

In Chapter VI, a simple rule of mixture of the micro-strains of the different phases, which was used to model the overall stress-strain curve, was described; these micro-strains are proportional to the overall strain. The phase fractions were obtained experimentally and the evolution of the retained austenite fraction with overall strain was described by an exponential relationship, wherein the transformation stability was related to the initial fraction of fresh martensite. The mechanical characteristics of the individual constituents were determined by nano-indentation. However, for the simulation, experimental stress-strain curves of large-scale specimens of tempered and untempered martensite were employed. The relationship between the local and global strain of the different phases, obtained with DIC, showed that 1.3 times the overall strain was accommodated in retained austenite while tempered martensite strained to the same amount as the overall strain. The strain distribution coefficient of fresh martensite was fitted by the model and a value of 0.15 was obtained. The weakness of the model is that independent of the time of its formation, fresh martensite was strained to the same individual strain level, which was proportional to the overall strain. Therefore, the correspondence between the model and experiments was limited and must be modified to account for the strain in fresh martensite.

To determine the total elongation, a new relation was proposed wherein the material fractured if the retained austenite fraction decreased to a low, fixed value of for e.g. 0.5%. Independent of the actual value, the evolution of the total elongation with fraction of retained austenite and

fresh martensite was obtained; this evolution indicated that the ductility increased with increasing fraction of retained austenite. The change in ductility was largest for small additions of austenite and this enhancement became less pronounced with further increases in the austenite fraction. This calculation suggests that increasing the fraction above ~20% will not increase the ductility significantly. In contrast, the ductility deteriorated with even very small additions of fresh martensite, although the effect is less pronounced in experimental observations than in the model. Therefore, the formation of fresh marteniste must be suppressed in order to make a Q&P steel with a combination of high strength and ductility.

In Chapter VII, the ultra-fast annealing performed prior to Q&P was used as an option to refine the microstructure and enhance the mechanical properties beyond those obtained with conventional heating rates. Dilatometric experiments demonstrated the increase of both the A_{C1} and A_{C3} temperatures with increasing heating rate. The prior austenite grains, which originated from a non-recrystallized bcc matrix, became significantly refined with higher heating rates without influencing the stabilized austenite fraction after partitioning. The tempered martensite contained less carbon than that produced in conventionally Q&P treated samples, owing to the non-complete dissolution of carbides in the heating stage. At a heating rate of 10 °C/s, with and without isothermal soaking, almost no carbides were present in the quenched sample. However, flash heating at 500 °C/s resulted in spheroidized carbides in a prior pearlitic cementite morphology; after heating at 1000 °C/s, the pearlite structure was still visible after quenching and carbide spheroidization was not significant. Fine, recrystallized ferrite was present at the highest heating rate. The mechanical properties obtained at heating rates of 500 °C/s and 1000 °C/s without isothermal soaking were better than those resulting from the conventional Q&P samples; i.e. increases in strength of up to 26% and ductility of up to 134% were obtained. The fracture surface changed from quasi-cleavage in conventionally heat treated samples to ductile dimples in the rapidly heated ones.

The first suggestion for future work would be to fully exploit the possibilities of Q&P steels. From the knowledge gained and new concepts, the combination of both high strength and ductility of Q&P steel could be further improved by altering the heat treatment cycles.

e.g. - Ductility could be enhanced through the formation of small fractions of ferrite in the microstructure. Hence the question that still needs to be answered is: if intercritical annealing is applied such that a partial ferritic microstructure results, how will this influence the mechanical properties?

- Another option that could be investigated is the creation of a microstructure where bainite formation is allowed. The main issue here is to control the heat treatment cycle in such a way that bainite forms in a controlled manner leaving sufficient retained austenite after cooling.

- The strength and toughness could be further improved by reducing the prior austenite grain size and hence reducing the size of the final microstructure e.g. by UFA, pre-heat treatments, etc…

- Other variations in the heat treatment cycle which would create a microstructure with different austenite grain sizes and C-contents without fresh martensite to produce a material with a more continuous TRIP-effect during straining. This could be done e.g. by stepped quenching and partitioning heat treatment to consecutive lower temperatures or by a tempering heat treatment after Q&P.

The chemical composition can be further optimized e.g. by adding Nb to refine the microstructure and enhance precipitation hardening, by replacing Si with Al to improve galvanisability, by adding Mo to reduce the segregation banding behaviour, by adding Ni to enhance austenite stabilisation, etc…

Another unanswered question regards the 3D morphology of the microstructure. Therefore, 3D-EBSD could be employed to study the interconnectivity of retained austenite in samples with similar retained austenite fractions but different mechanical properties. In addition to its grain size and morphology, the interconnectivity of austenite is believed to play an important role in the effectiveness of austenite as a TRIP-assisted component. A martensitic microstructure with an interconnected network of retained austenite is expected to accommodate strain effectively by a smearing effect. The transformation of retained austenite cannot, by itself, explain the observed increase in ductility with increasing fraction of retained austenite; this increase in ductility is believed to result from the strain distribution and strain hardening effect. An interconnected network could distribute the strain and harden somewhat homogenously over the entire sample, thereby enhancing the overall ductility.

Fundamental questions concerning the observed austenite-martensite interface movement could be suggested. One of the essential questions concerns the influence of the grain boundary characteristics, such as coherency and curvature, on the mobility. Other parameters which could influence the mobility are related to the austenite morphology, grain size, and crystallographic orientation. In addition, the effect of the nearest neighbourhood e.g.

tempering behaviour of martensite resulting in precipitates and a reduction of strain next to the interface cannot be excluded.

This work provided the answers to several questions, which existed in the field of Q&P, and also formulated new ones that will hopefully be answered in the near future.